THE UNIVERSITY *of* EDINBURGH

Molecular Imaging Of Calcification And Inflammation in Aortic Valve Disease and Atherosclerosis

Alexander T Vesey

MB/ChB, FRCS

Thesis submitted in fulfilment of the requirements for the Degree of Doctor of Philosophy in the Faculty of Medicine

Department For Cardiovascular Science

College of Medicine and Veterinary Medicine

University of Edinburgh

2019

For my wife, Dr Hazel Miller, and my daughters, Iris and Stella.

Abstract

Introduction. Calcific aortic valve disease (CAVD) and atherosclerosis are important public health problems. Our ability to allocate patients to treatment strategies optimally and monitor progression is limited. Hybrid positron emission and computed tomography (PET/CT) is able to demonstrate both anatomy (CT) and molecular processes (PET) *in vivo.* The 18F-sodium fluoride (18F-fluoride) isotope has shown promise in early cardiovascular studies. The purpose of this thesis was to elucidate the mechanisms of cardiovascular 18F-fluoride uptake and define how 18F-fluoride PET/CT might play a role in the assessment of CAVD and atherosclerosis.

Methods. Three cohorts were recruited constituting patients with: CAVD, coronary atherosclerosis and carotid atherosclerosis. Using *in vitro*, *ex vivo* and *in vivo* techniques, a model of the mechanism of 18F-fluoride uptake and its pharmacology was elaborated. In observational clinical studies, 18F-fluoride and 18F-FDG uptake in aortic valvular, coronary and carotid arterial tissue was assessed. Techniques for uptake quantification were evaluated for accuracy and reliability. Tissue uptake was related to established clinical and image-based variables as well as prospectively gathered clinical outcome data.

Results. In the CAVD cohort, 121 volunteers were recruited. 18F-fluoride PET/CT correlated with tissue markers of active calcification and predicted the genesis of new areas of calcification within the aortic valve. 18F-fluoride uptake was associated with disease progression and clinical events.

In the coronary cohort, 80 volunteers were recruited. In patients with acute myocardial infarction the highest coronary 18F-fluoride uptake was seen in the culprit plaque (median maximum tissue-to-background ratio: culprit 1·66 [IQR 1·40–2·25] *versus* highest non-culprit 1·24 [1·06–1·38], p<0·0001). In patients with stable angina, plaques with focal 18F-fluoride uptake were associated with more high-risk features on intravascular ultrasound than those without uptake.

In the carotid cohort, 38 volunteers were recruited (26 +12, separate studies). 18F-fluoride plaque uptake was associated with neurovascular symptoms (log_{10} mean standardized uptake value 0.29±0.10 *versus* 0.23±0.11, P=0.001) as well as image and tissue derived features of high-risk plaque. 18F-fluoride selectively highlighted areas of pathologically high risk nascent microcalcification and was proven to have pharmacological properties highly favourable for PET imaging.

Conclusions. 18F-fluoride PET/CT is a valuable tool for exploring pathobiology in CAVD and atherosclerosis may represent an attractive method for assessing response to novel therapies.

Lay Summary

Narrowing of the aortic valve (aortic stenosis) and hardening of the arteries (atherosclerosis) are related diseases responsible for a huge burden of death, illness and suffering in the world. Our ability to accurately assess these diseases in order to choose or measure the effects of treatment remains limited.

Hybrid positron emission tomography and computed tomography (PET/CT) is a scanning technique that allows doctors to look at the physical structures in the body at the same time as the underlying active biological processes. Two such processes of particular importance in aortic stenosis and atherosclerosis are inflammation and calcification (this is when tissues become hardened with limescale-like deposits).

The purpose of this research was to show how PET/CT is able to demonstrate calcification in the arteries and aortic valve and also to explore what the value of doing so might be to a patient. This use of scanning for calcification was then compared to scanning for inflammation which is the traditional method.

Using a variety of techniques, I have demonstrated that PET/CT is able to demonstrate the process of on-going calcification in the aortic valve. It does so by specifically highlighting the very earliest and tiniest deposits of calcium. Showing such "active calcification" in the aortic valve appears to predict whether or not a patient's illness is going to get worse or not. In the arteries, demonstrating "active calcification" with PET/CT highlighted areas of disease that were particularly prone to causing heart attacks or strokes. Compared to using PET/CT to measure inflammation, the calcification method performed better.

These findings show that using PET/CT to measure calcification may permit doctors to choose treatments for their patients more effectively. The method may also allow researchers to better test new treatments by proving a way of measuring the activity of disease in more detail**.**

Table of Contents

Abstract **3**

Lay Summary **4**

Acknowledgements **10**

Author's Statement **12**

Abbreviations **13**

Figures Index **15**

Tables Index **17**

Chapter 1 – Introduction ***18***

1.1 Overview **19**

1.2 Calcific Aortic Valve Disease **20**

1.2.1 Epidemiology 20

1.2.2 Normal Aortic Valve Anatomy and Function 20

1.2.3 Pathogenesis 22

1.2.4 Current Imaging Strategies And The Need For A New Paradigm 29

1.3 Atherosclerosis **30**

1.3.1 Epidemiology 30

1.3.2 Pathogenesis 30

1.3.3 In Search of The Vulnerable Plaque 38

1.4 Hybrid Positron Emission Tomography and Computed Tomography **40**

1.4.1 Positron Emission Tomography 40

1.4.2 PET/CT In Cardiovascular Disease 44

1.5 Summary **59**

1.6 Aims **60**

1.7 Hypotheses **61**

Chapter 2 – Methods ***63***

2.1 Patient Populations **64**

2.1.1 Aortic Stenosis Studies 64

2.1.2 Carotid Atherosclerosis 64

2.1.3 Coronary Atherosclerosis 64

2.2 Ethical Considerations **65**

2.3 Positron Emission Tomography / Computed Tomography **66**

2.3.1 Isotope generation 66

2.3.2 Injection for Static PET Acquisitions 67

2.3.3 Image Reconstruction and Motion Correction/Compensation 74

2.4 Ex Vivo & In Vitro Techniques **75**

2.4.1 Tissue Sampling 75

2.4.2 Histology 76

2.4.3 Immunohistochemistry 77

2.4.4 Autoradiography 78

2.4.5 Ex Vivo PET/CT using Clinical Scanner 79

2.4.6 Micro PET/CT 81

2.4.7 In Vitro Pharmacology Studies 83

2.5 Image Analysis 85
2.5.1 Clinical PET 85
2.5.2 Clinical CT 88
2.5.3 Micro PET/CT 90
2.5.4 Immunostaining and Autoradiography 91

2.6 Statistics 92

Chapter 3 – 18F-Fluoride And 18F-FDG Hybrid Positron Emission Tomography And Computed Tomography In Calcific Aortic Valve Disease – Mechanisms Of Action; Histological And Clinical Imaging Based Validation 94

3.1 Publication in Context 95
3.1.1 Background 95
3.1.2 Aims of Further Study 96
3.1.3 Contributions 96

3.2 Abstract 97
3.2.1 Background 97
3.2.2 Methods 97
3.2.3 Results 97
3.2.4 Conclusion 98

3.3 Introduction 99

3.4 Methods 100
3.4.1 Patient Populations 100
3.4.2 Baseline Assessment 100
3.4.3 Quantification of Aortic Valve PET Activity 101
3.4.4 Distribution of 18F-fluoride in the Aortic Valve Relative to Calcium Scoring 102
3.4.5 Histological Assessment 102
3.4.6 Reproducibility Studies 103
3.4.7 Autoradiography 103
3.4.8 Statistical Methods 104

3.5 Results 105
3.5.1 Histology Cohort 105
3.5.2 Immunohistochemistry and Autoradiography 106
3.5.3 Reproducibility Of Immunohistochemistry 108
3.5.4 Correlation With Radiotracer Uptake 108
3.5.5 Imaging Defined Disease Progression 110

3.6 Discussion 113

3.7 Conclusions 116

Chapter 4 – 18F-Fluoride and 18F-FDG Hybrid Positron Emission Tomography and Computed Tomography in Calcific Aortic Valve Disease – Prospective Clinical Validation 117

4.1 Publication In Context 118
4.1.1 Background 118
4.1.2 Aims of Further Study 119
4.1.3 Contributions 119

4.2 Abstract 120
4.2.1 Background 120
4.2.2 Methods 120

4.2.3 Results....120
4.2.4 Conclusions....121

4.3 Introduction....122

4.4 Methods....124
4.4.1 Patient Population....124
4.4.2 Baseline Assessment....124
4.4.3 Image Analysis....125
4.4.4 Assessment of Disease Progression....126
4.4.5 Follow-up for Clinical Events....126
4.4.6 Statistical Methods....127

4.5 Results....128
4.5.1 Study Population....128
4.5.2 Image Analysis Reproducibility Studies....130
4.5.3 Patient Follow-up....134
4.5.4 Prediction of Disease Progression....138
4.5.5 Prediction of Clinical Outcome....143

4.6 Discussion....146
4.6.1 18F-Fluoride In Aortic Stenosis....146
4.6.2 Computed Tomography in Aortic Stenosis....147
4.6.3 The Application Of 18F-Fluoride PET....147
4.6.4 18F-FDG In Aortic Stenosis....148
4.6.5 Study Limitations....149
4.6.6 Conclusions....149

Chapter 5 – 18F-Fluoride and 18F-Fluorodeoxyglucose Hybrid Positron Emission Tomography and Computed Tomography In Atherosclerosis – A Pilot Study With Imaging And Histological Validation....150

5.1 Publication In Context....151
5.1.1 Background....151
5.1.2 Aims of Further Study....152
5.1.3 Contributions....153

5.2 Abstract....154
5.2.1 Background....154
5.2.2 Methods....154
5.2.3 Results....154
5.2.4 Conclusion....155

5.3 Introduction....156

5.4 Methods....157
5.4.1 Patients....157
5.4.2 Procedures....160
5.4.3 Carotid Experiments....164
5.4.4 Statistical analysis....166

5.5 Results....167
5.5.1 Patients Characteristics And Protocol Details....167
5.5.2 Unstable Coronary Cohort....170
5.5.3 Carotid Cohort....173
5.5.4 Stable Angina Cohort....176
5.5.5 Percutaneous Coronary Intervention With Stent Implantation....180
5.5.6 Comparison Of 18F-Fluoride Uptake In Stable Angina And Myocardial Infarction....180
5.5.7 Repeatability Of Image Analysis....181

5.6 Discussion....182

5.6.1 Limitations 185

Chapter 6 – Delving Deeper Into The Mechanisms Of 18F-Fluoride Uptake In Cardiovascular Tissue 186

6.1 Publication In Perspective 187
6.1.1 Background 187
6.1.2 Aims of Further Study 189
6.1.3 Contributions 189

6.2 Abstract 190

6.3 Introduction 191

6.4 Methods 194
6.4.1 Human Tissues 194
6.4.2 Electron Microscopy 194
6.4.3 18F-Fluoride Binding To Cryostat Cut Carotid Artery Sections 196
6.4.4 18F-Fluoride Binding In Whole-Carotid Arteries 197
6.4.5 Tissue Staining 198
6.4.6 Micro PET/CT Imaging Of Carotid Plaques 199
6.4.7 2D Image Processing And Analysis 199
6.4.8 3D Image Processing And Analysis 201
6.4.9 Clinical PET/CT Acquisition And Dynamic Analysis 202

6.5 Results 206
6.5.1 Electron Microscopy Analysis 206
6.5.2 Pharmacodynamic And Pharmacokinetic Analyses 209
6.5.3 Immunohistochemical Analysis 216
6.5.4 Penetration By Autoradiography/Histology And Micro PET/CT 218

6.6 Discussion 223

6.7 Conclusion 229

Chapter 7 – 18F-Fluoride And 18F-FDG Hybrid Positron Emission Tomography And Computed Tomography In Carotid Artery Atherosclerosis 230

7.1 Publication in Context 231
7.1.1 Background 231
7.1.2 Aims of Further Study 231
7.1.3 Contributions 232

7.2 Abstract 233
7.2.1 Background 233
7.2.2 Methods 233
7.2.3 Results 233
7.2.4 Conclusion 234

7.3 Introduction 235

7.4 Methods 236
7.4.1 Patient Population 236
7.4.2 Exclusion Criteria 236
7.4.3 Ethical Matters 236
7.4.4 Baseline Assessment 237
7.4.5 PET/CT Protocol 237
7.4.6 Tissue Collection 238
7.4.7 Micro PET/CT 238
7.4.8 Autoradiography And Histology 239

7.4.9 Image Analysis 239
7.4.10 Statistical Analysis 240

7.5 Results 242
7.5.1 Study Population 242
7.5.2 Micro PET/CT and Histology 246
7.5.3 Imaging: Validation with Dynamic Imaging & Intra-, Inter-Rater Reproducibility 248
7.5.4 Assessment of Uptake: Culprit Compared With Contralateral and Controls 250
7.5.5 Uptake Compared With Plaque Features And Baseline Characteristics 254

7.6 Discussion 256
7.6.1 Limitations 259

7.7 Conclusions 260

Chapter 8 – Conclusions 261

8.1 Summary of Key Findings 262
8.1.1 Mechanism of Action of 18F-fluoride Uptake in Cardiovascular Tissue 262
8.1.2 Prediction Of Disease Progression And Clinical Events In CAVD 263
8.1.3 Identification of Culprit and High-Risk Plaque in the Carotid and Coronary Arteries 264

8.2 Recent Literature 266

8.3 Limitations 268

8.3 Future Directions 271
8.3.1 Mutability Of 18F-Fluoride Uptake In CAVD 271
8.3.2 Predicting Events In Atherosclerosis 271
8.3.3 Randomising Patients to an Investigational Strategy to Prove Worth 272
8.3.4 Utility of Combining PET and MR to Assess Cardiac Disease and Atherosclerosis 273
8.3.5 Other Pathologies 274

8.4 Final Conclusions 275

References 276

Appendices 298
Awards arising from this thesis 298
Selected Research Grants Arising From This Thesis And Related Work 299
Bibliography 300

Acknowledgements

I conducted this research under the supervision of Professor David Newby and Doctor Marc Dweck. They are inspirational mentors and my debt to them for their constant support, encouragement and guidance is inestimable. I had a wonderfully stimulating, challenging and enjoyable time working as part of their group. They are second to none as research leaders and supervisors.

I am also very grateful to my closest co-workers in Edinburgh. In particular Will Jenkins, Anoop Shah, Amanda Hunter, Nikhil Joshi, Michelle Williams, Tim Cartlidge, Alastair Moss, Rachael Forsythe and Christos Skouras all provided me with huge amounts of academic and personal support and I couldn't have achieved what I did without their help. In Edinburgh, I would also like to acknowledge the opportunities, guidance and support provided by Professor Nick Mills, Professor Martin Dennis, Professor William Whitely, Professor Rustam Al-Shahi, Roger Duffin, Mairi Brittan, Professor Donald Salter & Takeshi Fujisawa.

In Cambridge, I'm very grateful to my co-authors and collaborators Agnese Irkle, James Rudd and Anthony Davenport for our fruitful collaboration on 18F-fluoride mechanisms and other projects. I was made to feel very welcome on my visits to Cambridge and look forward to future collaborations.

I would like to acknowledge a debt of gratitude to the staff of the Clinical Research Imaging Facility who had to put up with some very difficult protocols as well as my anxiety and fussing. Without the help of Professor Van Beek, Christophe Lucatelli, Colin Young, Gemma Roberts, Martin Connell, Julian Sparrow, Callum Gray, Tim Clark, David Brien & his team as well as many others, my research would not have progressed. The dynamic PET was a particular challenge and its success was a testament to real team work.

I would also like to specifically thank Mike Miller and Melanie McMillan at the SuRF histology core for their infinite patience and kindness. The immunohistochemistry work was very difficult and without them, would have come to nothing. Mark Marsden from the Scottish Centre for Regenerative Medicine also made a very significant contribution to my lab work by helping me find my feet, open doors and negotiate the challenges of working with radioactive isotopes.

Professor Vicky MacRae and her group at the Roslin played a major part in my work as well through academic support, introductions and successful collaborations. I would particularly like to mention the late Neil MacKenzie who so kindly gave me his time and help with the microCT asking for nothing in return.

I'm very grateful to my Glasgow co-workers who were an immense help for the MA^{3}RS project and related endeavours. Without their support, it would have been impossible to deliver the Glasgow arm of this trial. Giles Roditi, Professor Andrew Baker, Margaret Ballantyne, Karine Pinel, Professor Colin Berry, Tracey Steedman, Rosie Woodward, Amani Brown, Laura Murdoch, Joanne Flynn, Lorraine McGregor, Sasha Radjenovich, Evonne McLennan, Pauline Barrientos-Hall and several others were all central to this effort.

The surgical, theatre nursing and vascular laboratory staff in the Edinburgh Vascular Unit were very helpful and I am indebted to them all. I single out Mr. Ray Dawson for particular, sadly posthumous, thanks; he has been an inspirational figure to me for my entire career and also happened to provide my best sample.

Finally, I acknowledge that my greatest debt of gratitude is to my long-suffering family. Hazel, Iris and Stella have lived this project as much as me. As well as peaks of research joy, there were many troughs of despair, and were it not for Hazel particularly, I would not have got through it.

Author's Statement

I declare that the work described in this thesis was carried out personally unless otherwise stated and has not been submitted in full or in part for consideration for any other degree or qualification.

Abbreviations

18F-FDG	18F-fluorodeoxyglucose
18F-fluoride	18F-sodium fluoride
ACE	Angiotensin converting enzyme
AS	Aortic stenosis
AU	Arbitrary units
AVR	Aortic Valve Replacement
BMI	Body mass index
CABG	Coronary artery bypass graft
CAC	Coronary artery calcium scoring
CAD	Coronary artery Disease
CAVD	Calcific Aortic Valve Disease
CEA	Carotid Endarterectomy
CHD	Coronary heart disease
CT	Computed tomography
CVD	Cardiovascular disease
DAMPS	Damage associated molecular signatures
EC	Endothelial cell
GMP	Good manufacturing practice
HDL	High density lipoprotein
HU	Hounsfield units
ICAM-1	Intercellular adhesion molecule 1
ICC	Intra-class correlation coefficient
IFG	Gamma interferon
IL	Interleukin
LDL	Low density lipoprotein
Lp(a)	Lipoprotein “little a”
MACE	Major adverse cardiovascular events
MCP-1	Monocyte chemoattractant protein 1
M-CSF	Macrophage colony stimulating factor
MMP	Matrix metalloproteinase
MI	Myocardial infarction
MRI	Magnetic Resonance Imaging
PCI	Percutaneous Coronary Intervention
PDGF	Platelet-derived growth factor
OPG	Osteoprotegerin
PBS	Phosphate buffered saline
PET	Positron emission tomography
RANK	Receptor activator of nuclear factor kappa B
Runx-2	Runt-related transcription factor 2
ROI	Region of interest
SD	Standard deviation
SEM	Standard error of the mean
SUV	Standardised uptake value
TAVI	Transcatheter aortic valve implantation
TIA	Transient ischemic attack

TBR	Tissue-(or Target-) to-background ratio
VEC	Valvular endothelial cell
VIC	Valvular interstitial cell
VCAM-1	vascular cell adhesion molecule 1
VSMC	Vascular smooth muscle cell
WNT	“Wingless/Integrated”

Figures Index

Figure 1.1 | Overview Of The Pathogenesis Of Calcific Aortic Valve Disease.....23
Figure 1.2 | Putative Mechanisms of Cardiovascular Calcification.....26
Figure 1.3 | The Principle Mechanisms Of Acute Plaque Events.....34
Figure 1.4 | Could Microcalcification Directly Cause Plaque Destabilisation Through Alteration Of Fibrous Cap Stresses?.....36
Figure 1.5 | Putative Mechanism for 18F-Fluoride Microcalcification Selectivity 47
Figure 1.6 | Valvular 18F-Fluorodeoxyglucose TBR_{max} Uptake According To Echocardiographic severity.....50
Figure 1.7 | Valvular 18F-fluoride TBR_{max} uptake according to echocardiographic severity.....53
Figure 2.1 | The Allogg ABSS.....71
Figure 2.2 | A Fully Dynamic 18F-fluoride PET Study.....73
Figure 2.3 | Example Of Excised Carotid Plaque.....75
Figure 2.4 | 18F-Fluoride Autoradiography.....78
Figure 2.5 | Ex Vivo Clinical PET/CT Scanning Of Carotid Plaque Specimens.....79
Figure 2.6 | NanoScan Preclinical micro PET/CT System.....81
Figure 2.7 | Derivation of Plaque Max, Mean Max and Mean SUV by MDS Method 86
Figure 2.8 | Screen Grab From CT Carotid Plaque Analysis.....89
Figure 3.1 | Histology And 18F-Fluoride Autoradiography Of Excised Aortic Valve Tissue From Patients With Aortic Stenosis.....107
Figure 3.2 | Correlations Between In Vivo Aortic Valve Positron Emission Tomography (PET) Activity And Histological Markers Of Calcification And Inflammation.....109
Figure 3.3 | Change In Aortic Valve Computed Tomography (CT) Calcium Score And 18F-Fluoride Positron Emission Tomography (PET) Activity After One Year 112
Figure 4.1 | Study Flow Chart.....128
Figure 4.2 | CT Calcium Scoring: Bland-Altman.....131
Figure 4.3 | Positron Emission Tomography, Aortic Valve Calcification And Imaging Defined Disease Severity.....137
Figure 4.4 | 18F-Fluoride Positron Emission Tomography and the Progression in Aortic Valve Calcification.....141
Figure 4.5 | 18F-Fluoride Uptake Indexed To Baseline CT Calcium Score.....142
Figure 4.6 | Prediction Of Clinical Outcome.....145
Figure 5.1 | Original Fused 18F-Fluoride PET/CT Showing Uptake In Culprit Coronary Plaque.....151
Figure 5.2 | Study Design.....159
Figure 5.3 | Focal 18F-Fluoride And 18F-Fluorodeoxyglucose Uptake In Patients With Myocardial Infarction And Stable Angina.....171
Figure 5.4 | 18F-Fluoride And 18F-Fluorodeoxyglucose Uptake In Patients With Myocardial Infarction.....172
Figure 5.5 | Histological Comparison Of 18F-Fluoride Positive And Negative Regions Of Carotid Endarterectomy Specimens.....174

Figure 5.6 | Carotid 18F-Fluoride Uptake And Carotid Plaque Rupture 175
Figure 5.7 | Lesions With And Without 18F-Fluoride Uptake, And Gray-Scale And Radiofrequency Intravascular Ultrasound In Patients With Stable Angina 178
Figure 6.1 | Putative Mechanism Of 18F-Fluoride Uptake In Unstable Atherosclerotic Plaque 188
Figure 6.2 | Fluoride Directly Co-Localizes With Calcium In A Concentration-Dependent Manner 208
Figure 6.3 | The Non-Specific Binding Of Fluoride Is Low 210
Figure 6.4 | Standardised Uptake Values And Target To Background Ratios For PET Positive Versus PET Negative Regions 213
Figure 6.5 | Dynamic Clinical PET Analysis 215
Figure 6.6 | 18F-Fluoride Pharmacokinetics 215
Figure 6.7 | 18F-Fluoride Uptake Correlates With Calcification But None Of The Histological Inflammatory Markers 217
Figure 6.8 | 18F-Fluoride Signal Detection Depends On The Sensitivity Of The Detection Modality 219
Figure 6.9 | High-Resolution Imaging Reveals Specificity Of 18F-Fluoride Binding To Vascular Calcification 221
Figure 6.10 | Model of 18F-Fluoride Binding To Vascular Calcification 227
Figure 7.1 | Study Flow Chart 242
Figure 7.2 | 18F-Fluoride And 18F-Fluorodeoxyglucose (FDG) Positron Emission Tomography Of Carotid Arteries 245
Figure 7.3 | 18F-Fluoride Micro Positron Emission Tomography (PET)/Computed Tomography (CT), Autoradiography, And Alizarin Red Staining 247
Figure 7.4 | Dynamic Positron Emission Tomography (PET) Acquisition And Examples Of 18F-Fluoride Uptake 249
Figure 7.5 | 18F-Fluoride And 18F-Fluorodeoxyglucose Positron Emission Tomography/Computed Tomography Uptake 253

Tables Index

Table 3.1- Baseline Clinical Data - Histology Cohort 105
Table 3.2 | Histology/Immunohistochemistry Data 106
Table 3.3 | Baseline Clinical Data – All Patients 110
Table 4.1 | Baseline Clinical Characteristics 129
Table 4.2 | Most Diseased Segment Versus Mean Whole Valve Technique for 18F-Fluorodeoxyglucose And 18F-Fluoride 131
Table 4.3 | Agreement Studies – Aortic Valve Calcium Quantification 131
Table 4.4 | Radiotracer Uptake Quantification Methods – Minimal Impact On Average Uptake Estimates 132
Table 4.5 | Radiotracer Uptake Quantification Methods – Minimal Impact On Correlations With Parameters Of Disease Progression 133
Table 4.6 | Disease Progression And Clinical Outcomes 136
Table 4.7 | Baseline Imaging And Prediction Of Disease Progression 140
Table 4.8 | Predicting Clinical Outcome 144
Table 5.1 | Baseline Characteristics Of Coronary Cohorts 168
Table 5.2 | Baseline Characteristics Of Carotid Cohort 169
Table 5.3 | Greyscale And Radiofrequency Intravascular Ultrasound Characteristics In 18F-Fluoride Positive And Negative Plaques Of Patients With Stable Angina 177
Table 5.4 | Plaque Characteristics On Invasive And Computed Tomography Coronary Angiography In Patients With Stable Angina 179
Table 6.1 | Electron Microscopy Analysis Of Hydroxyapatite Standards To Confirm Co-Localization With Fluoride 207
Table 6.2 - Standardised Uptake Values And Target To Background Ratios For PET Positive Versus PET Negative Regions 212
Table 6.3 - Patient Demographics And Basic Imaging Data 212
Table 6.4 | Dynamic PET Analysis (Patlak) 214
Table 7.1 | Baseline Clinical Characteristics 243
Table 7.2 | Baseline Scanning Protocol and Radiation Dose Data 244
Table 7.3 | Inter-Observer And Intra-Observer Reproducibility 248
Table 7.4 | Radiotracer Uptake: Comparative Data 251
Table 7.5 | Plaque Analysis By CT And PET 255
Table 7.6 | 18F-Fluoride Uptake In A Patient With A Large Anterior ST-Elevation Myocardial Infarction 257

Chapter 1 – Introduction

1.1 Overview

Calcific aortic valve disease and atherosclerosis are prevalent disorders with a large global impact because they associated with an enormous burden on patients and their families as well as healthcare providers and purchasers alike. Cardiovascular procedures are common but costly and potentially risky interventions. Although our knowledge of the natural history and treatment of these conditions has improved in the last four decades, much remains poorly understood and there is scope for improvement.

Many treatments are available for both CAVD and atherosclerosis but our ability to select optimally patients who will benefit the most frequently remains limited and is often based on outdated and basic clinical or anatomic markers of risk and disease activity. Improving risk stratification and patient selection has been highlighted as a key research priority by international expert groups. (1) Improving our ability to identify patients at particularly high or low risk will permit us to improve outcomes through more targeted intervention. This will in turn result in optimal resource allocation; a critical feature of modern medicine.

Clinical imaging with hybrid positron emission tomography and computed tomography (PET/CT) has shown promise in this respect in the domains of CAVD and atherosclerosis. The technique is able to resolve pathobiology at the molecular as well as the anatomic level. It is possible that such imaging may provide a way of better understanding and objectively measuring CAVD and atherosclerosis *in vivo.*

The aim of this thesis is therefore to investigate the potential of hybrid clinical PET/CT imaging in CAVD and atherosclerosis.

1.2 Calcific Aortic Valve Disease

1.2.1 Epidemiology

Calcific aortic valve disease (CAVD) is the most common cause of acquired aortic valve stenosis and the third leading cause of cardiovascular disease. (2) The prevalence (in a Western Population; Tromsø) is approximately 0.2% among adults between the ages of 50 and 59 years rising to nearly 10% in those between 80 and 90 years. (3) If symptomatic, untreated severe aortic stenosis is associated with a high risk of mortality (approximately 50-70% at 2 years) (4). It is the commonest cause of valve replacement in Europe and North America. (5-7) Indeed the number of aortic valve interventions, be they by open surgical replacement (AVR) or trans-catheter aortic valve implantation (TAVI), is high and rising. (6,7) CAVD is therefore associated with a significant disease burden and high healthcare costs in our ageing population.

1.2.2 Normal Aortic Valve Anatomy and Function

The normal aortic valve lies at the junction between the left ventricular outflow tract and the origin of the aorta. It has three extremely thin, semilunar diaphanous leaflets or cusps. These are attached to a coronet shaped "annulus" (a misnomer) made of a condensation of collagen fibres. The leaflets are comparatively sparsely populated by cells. The ventricular and aortic aspects are covered by a layer of valvular endothelial cells (VECs; whose normal orientation is perpendicular to blood flow, unlike that of vascular endothelial cells) interspersed with pericytes. Within the leaflets reside valvular interstitial cells (VICs). These remodel and maintain leaflet microarchitecture by either synthesising or degrading components of the extracellular matrix. (8,9) Normally, these cells remain quiescent although are capable of significant phenotypic plasticity in states of development and disease.

The valve leaflets are made of three discreet layers. The "innermost" (on the ventricular side) is called the *ventricularis* and is composed of radially arranged elastin fibres. The "outermost" is called the *fibrosa* and consists primarily of inelastic collagen fibres arranged concentrically (parallel to the aorta). A final component called the *spongiosa* is located at junction of the valve and annulus between the *ventricularis and fibrosa*. It is composed of loose connective tissue and possibly functions either like a hinge or a "lubricant" between the two other layers; this is speculative however and the precise function has not been shown with confidence. During systole, the leaflets "open" and flatten against the aortic intima permitting unobstructed laminar flow of blood into the aortic lumen. In diastole, the moment that aortic pressure exceeds that of the pressure in the relaxing ventricle, the leaflets snap shut and prevent regurgitation of blood into the ventricular cavity. Unlike the mitral valve, this is an entirely passive phenomenon with no requirement for energy expenditure. The leaflets distribute and resist this mechanical force evenly thanks to their macroscopic geometry as well the concentric alignment of inelastic collagen fibres within the *fibrosa*. The radially oriented elastin fibres within the *ventricularis* complement the collagen by stretching in the radial direction thus permitting increased leaflet coaptation and competence. Together the layers provide the necessary tensile strength to prevent prolapse and regurgitation and also to dampen the blood pressure impulse in concert with the elastic aorta. Another key function of two of the three leaflets is to direct blood flow into the coronary ostia during diastole. This exposes the aortic aspect of the leaflets to more oscillatory blood flow and varying shear stresses.

1.2.3 Pathogenesis

CAVD is characterized by the progressive thickening, stiffening and restriction of the aortic valve leaflets. This in turn results in progressive obstruction of the left ventricular outflow tract and secondary effects on the myocardium. The cardiomyocytes initially undergo an adaptive hypertrophic response to the chronically increased afterload but ultimately the ventricle begins to fail for a variety of reasons and the patient becomes symptomatic and at high risk of death. (8) The focus of this section and indeed this thesis, with be on the pathological processes that occur within the valve itself and not on the secondary myocardial effects.

A comprehensive causal sequence explaining the genesis of CAVD remains elusive. The disease shares many risk factors with atherosclerosis including male sex, increasing age, chronic kidney disease, tobacco smoking and the metabolic syndrome (hypertension, obesity, hypo-activity, type 2 diabetes mellitus, hyperlipidaemia). Other risk factors, such as a bicuspid aortic valve, are unique to CAVD. There are also genetic variants known to predispose to the disease. (10,11)

These risk factors can induce, or are associated with, biological phenomena such as increased systemic inflammation, increased oxidative stress or abnormal valvular stresses. These combine to produce chronic valvular endothelial injury and dysfunction that lead to the initiation of certain pathological processes within the valve itself: inflammation, angiogenesis, hypoxia, cell death, fibrosis and calcification. These then interact with each other in a positive feedback loop to further drive the process of increasing valve stiffness, increasing mechanical stress, increasing inflammation and increasing calcification and fibrosis (see Figure 1.1). CAVD is therefore often described as occurring in two phases: initiation and propagation.

Figure 1.1 | Overview Of The Pathogenesis Of Calcific Aortic Valve Disease

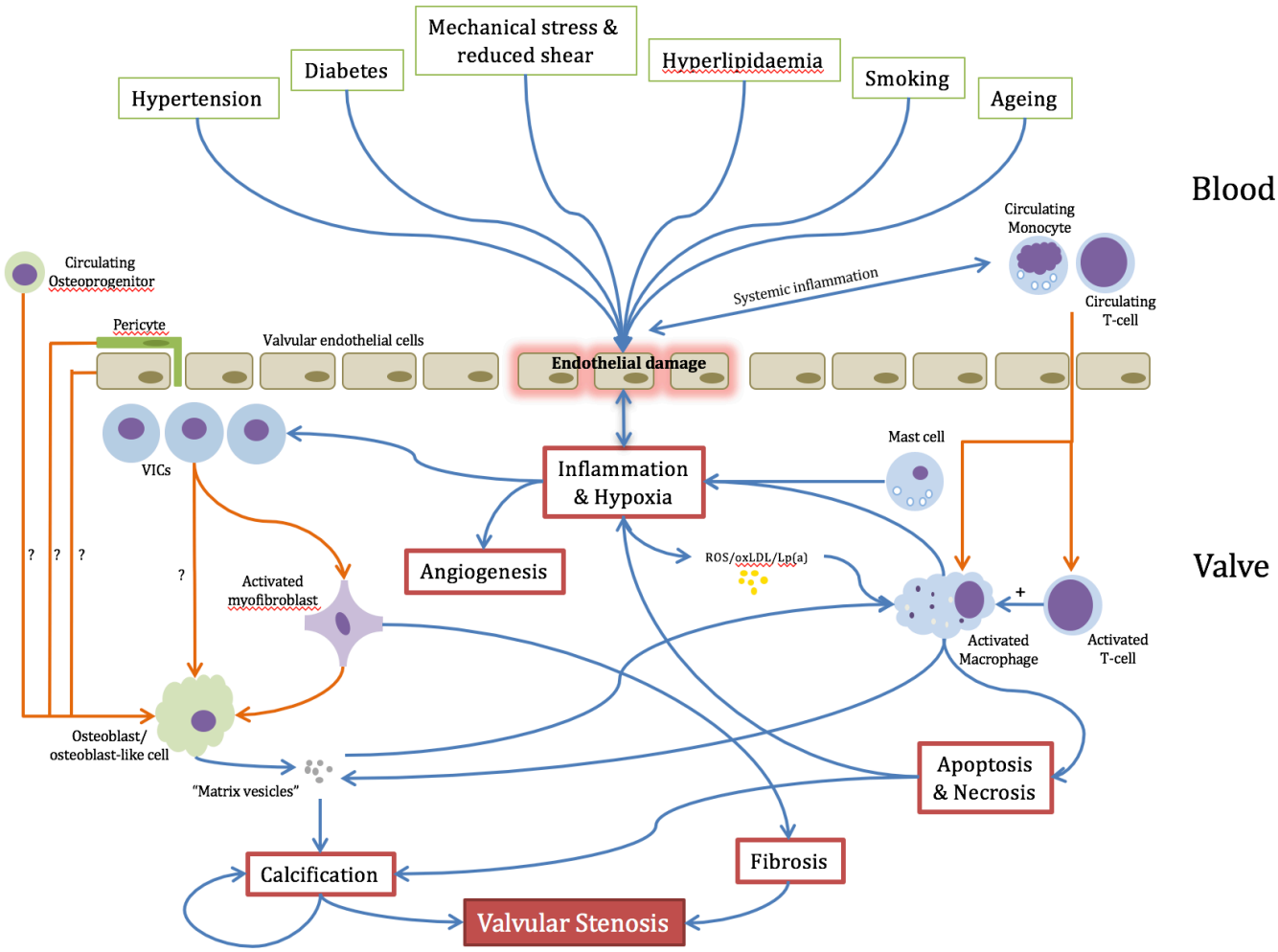

Processes and influences are represented by blue arrows. Cellular migration or phenotypic switching by orange arrows. Abbreviations: Lp(a), Lipoprotein little a; oxLDL, oxidised low-density lipoprotein; ROS, reactive oxygen species; VIC, valvular interstitial cells. Updated and adapted from Vesey et al(9)

1.2.3.1 Initiation

Endothelial Injury, Systemic Inflammation, Oxidative Stress and Lipid Infiltration

The likely primary event in the evolution of CAVD is endothelial injury. This is multifactorial. Direct mechanical stress plays a role demonstrated by the observation that bicuspid aortic valves (with abnormal and poorly distributed mechanical stresses) are universally affected by CAVD. (10,12) The fact that the non-coronary cusp (with little diastolic blood flow and therefore less shear stress) is the most severely cusp affected in CAVD supports the hypothesis that, as in atherosclerosis, low shear stress over the aortic aspect of the leaflet contribute to endothelial dysfunction and disease initiation.

Mediated though a variety of pathways, diabetes mellitus, the ageing process, hypertension and tobacco smoking increase systemic inflammation and heighten metabolic, osmotic and oxidative stress. This aggravates endothelial injury and further drives disease initiation. (11,13)

Once the integrity and health of the endothelium is compromised, oxidised low-density lipoprotein and lipoprotein(a) enter the subendothelial space on the aortic side of the valve triggering a localised inflammatory response. The endothelial injury itself and the oxidised lipid provide a strong signal for the recruitment and infiltration of macrophages (derived from circulating monocytes), T-lymphocytes and mast cells. This process is mediated by cell surface adhesion entities such as intercellular adhesion molecule 1 and vascular cell adhesion molecule 1. A vicious circle of increasing inflammation, increasing endothelial damage, increasing lipid infiltration and increasing cell death is then established.

1.2.3.2 Propagation

Calcification upon Calcification

Our understanding of the mechanisms underlying the induction and maintenance of valvular calcification is incomplete. It is certain that multiple complex mechanisms are at play. Historically, it was believed that valvular and indeed vascular calcification was an entirely passive and degenerative process and that all the relevant and *tractable* biology had already happened earlier in the disease process; the calcium and fibrosis was merely burnt out remains. Starting with the observation of intra-valvular mature chondral and osseous tissue at the microscopic level and moving to demonstrating the presence and activity of a host of chondrogenic and osteogenic genes, proteins and cells at the biomolecular level, it is now clear that cardiovascular calcification is a highly active and regulated process. (14,15)

As shown in Figure 1.2, there is a spectrum of putative mechanisms leading to cardiovascular calcium deposition. Truly dystrophic calcification is believed to arise from the simple precipitation of amorphous calcium phosphate deposits from the high concentrations of calcium and phosphate salts released during the process of cell death, particularly uncontrolled cell death; oncosis (leading to tissue necrosis). There is little to no biochemical regulation of this process. The trigger is cellular oncosis or caspase-dependent apoptosis which in turn is caused by the endothelial damage, lipid infiltration, oxidative stress and consequent inflammatory response that has already been discussed.

At the other end of the spectrum, true skeletal osteogenesis may be recapitulated within cardiovascular tissue. This leads to the formation of organised bony and cartilaginous tissue which may even be host to myeloid tissue. This has been shown histologically and also by the demonstration of activation of well-defined osteogenic genetic programs and the presence of related proteins within the valve. (11) This process, in contrast to dystrophic calcification, is highly regulated. Indeed, as in the skeleton, bone is laid down by

osteoblasts and then absorbed by osteoclasts – such remodelling is subject to modulation by a variety of systems, notably the receptor activator of nuclear factor kappa B (RANK)/ receptor activator of nuclear factor kappa B ligand (RANKL)/osteoprotegerin (OPG) axis – an important putative pharmacological target in treating CAVD. So-called non-classical extra-skeletal osteogenesis (or "pseudo-skeletal") has also been implicated. This process is characterised by the presence and activity of *some* osteogenic and chrondrogenic gene/protein pathways. The cells involved are not canonical osteoblasts, osteoclasts and related entities, but rather other transdifferentiated cells that express certain osteogenic/blastic/clastic markers (e.g. Runx2/Cbfa1). There are several potential candidate originator cells (see figure 1.1), but the exact pathways remain under investigation. The process of osteoblastic trans-differentiation is driven by a variety of inflammatory signalling moieties and also potentially by the RANK ligand.

Figure 1.2 | Putative Mechanisms of Cardiovascular Calcification

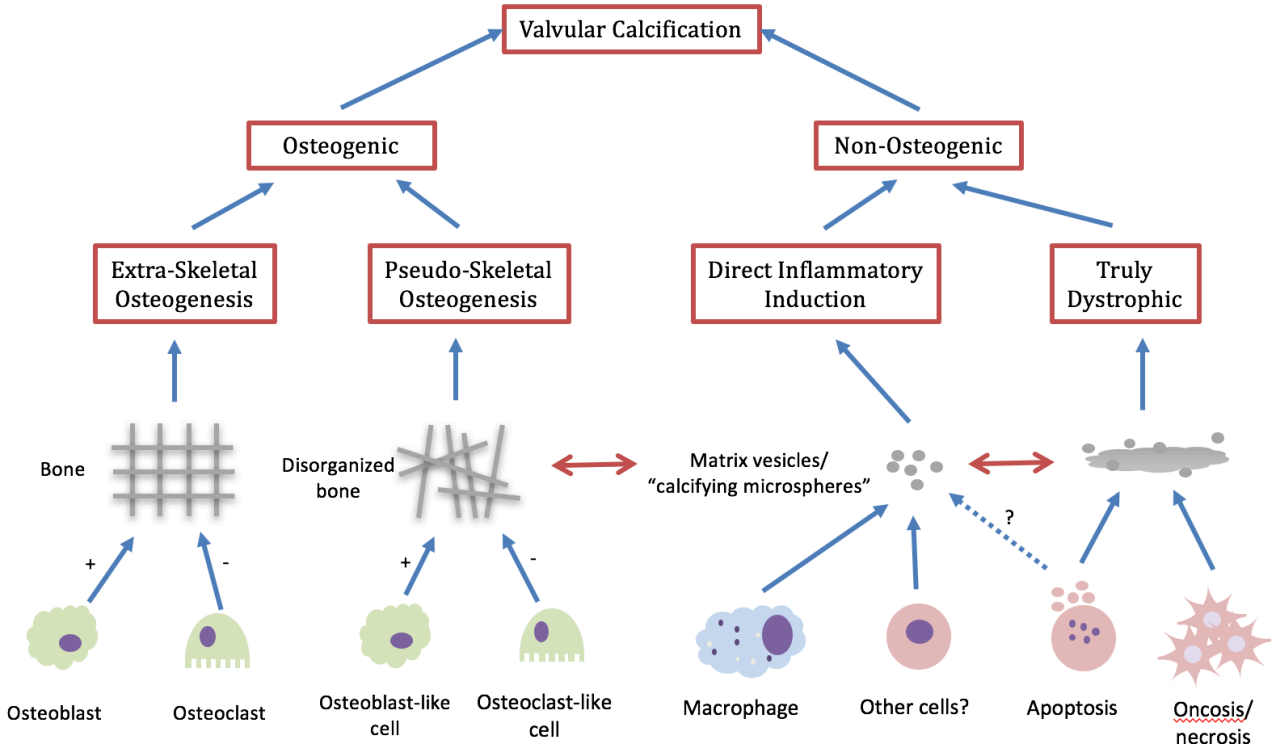

The final pathway is the most recently demonstrated. Work by Aikawa and co-workers(16) has demonstrated (in the mouse and human) that macrophages themselves (and potentially other cells e.g. vascular smooth muscle cells) may be able to directly calcify matrix through the release of microcalcification-generating matrix vesicles.

What all these pathways share in common is similar triggers: pro-inflammatory signalling, the presence of oxidised lipid and Lp(a), the increased presence of reactive oxygen species and cell death signalling. A wide variety of molecular techniques has demonstrated the central role of the macrophage(17) and a variety of proinflammatory cytokines (interleukin [IL]-1b, IL-6, IL-8, [TNF]-α, insulin-like growth factor-1, and transforming growth factor [TGF]-β. (18) An array of linked calcific pathways including the Notch, (19) Wnt/β-catenin, (20) and RANK/RANKL/OPG are also implicated. (21) This process of "inflammo-calcific" coupling occurs very early in the genesis of aortic stenosis. (20-22)

Alongside progressive calcification, valvular tissue also undergoes fibrosis leading to further exacerbation of stenosis and haemodynamic stress. Angiogenesis is also stimulated by the hypoxic and inflammatory milieu of the thickened valve leaflet leading to the formation of fragile neovessels highly prone to rupture and haemorrhage. These processes together all lead to further pro-inflammatory and pro-calcific signalling and a positive feedback loop of ever-increasing calcification, fibrosis and valve stenosis (Figure 1.1).

Why Is Calcification Perhaps The Most Important Process In CAVD?

Given that lipid infiltration and inflammation are key initiating processes in CAVD and that HMG-CoA reductase inhibitors (statins) have a proven track record in atherosclerosis (which shares many pathological features with CAVD), there was interest in using statins as disease modifying agents in CAVD. Three randomised studies of HMG-CoA reductase inhibition in CAVD have been published; SALTIRE(23), ASTRONOMER(24) and SEAS(25). The results were

concordant and disappointing; no effect on disease progression was demonstrated. The failure of statins in these trials led to the reappraisal of the role of inflammation in CAVD and the idea that it might only be an initiating insult. It is possible that the subsequent vicious circle of progressive calcification and fibrosis is a more tractable entity to target. A new focus of therapeutics has therefore been on pharmacological agents targeted at arresting calcification; agents of particular interest are the bisphosphonates or denosumab (a monoclonal osteoprotegerin analogue; see Pawade *et al*. (26) for a detailed description of their putative mechanisms of action in CAVD).

1.2.4 Current Imaging Strategies And The Need For A New Paradigm

At present, the management of CAVD is based on surveillance of a variety of cardiac haemodynamic parameters using echocardiography and more recently CT calcium scoring. (27,28) The key echocardiographic parameters are inferred from the velocity of the transvalvular jet of blood assessed by Doppler ultrasound. Once the degree of valvular obstruction becomes severe, intervention, be it by surgical valve replacement or transcatheter implantation, is indicated when symptoms become apparent. This approach is well established but has limitations. Symptoms are fickle in the context of the older and multi-morbid population of the current era. It is also increasingly recognised that echocardiographic parameters of ventricular function can be unreliable in the context of severe CAVD and multi-morbidity. (29) Fundamentally, echocardiography and symptoms-based management is focussed on the end stage of disease and provides no information on the biology within the valve itself. There is also increasing evidence that ventricular fibrosis can occur prior to symptoms developing and that such fibrosis is not necessarily reversible with valve replacement. (30)

Given the limitations of the current paradigm, a new approach to disease assessment and monitoring that is able to resolve disease activity within the valve tissue itself is likely to prove valuable not only in terms of clinical decision making but also in terms of assessing response to novel medical therapies. The cost of clinical trials in aortic stenosis can be very high and as we have seen from the statin studies, disappointing. The ability to assess the effect of a new treatment *in vivo* with a reliable imaging derived surrogate outcome and prove biological plausibility could potentially reduce costs, prevent many false starts and bring disease modifying agents more rapidly to the market.

1.3 Atherosclerosis

1.3.1 Epidemiology

Atherosclerosis is a disorder of global significance. (31) Myocardial infarction is the leading cause of death in the Western World and stroke is the leading global cause of disability and dependency. Atherosclerosis is responsible for countless deaths as well as an enormous burden of morbidity and disability as well as vast healthcare expenditure. Although significant advances have been made in understanding this disorder and reducing its toll, much remains unknown about how best to prevent and treat it.

1.3.2 Pathogenesis

1.3.2.1 The Central Role of Inflammation

It is now well recognised that atherosclerosis is fundamentally an inflammatory disease as opposed to a simple disorder of lipoprotein trafficking. Peter Libby, a US researcher and leader in the field has written the key reviews. (32-34)

A variety of biological entities (such as increased systemic inflammation, oxidative stress, elevated angiotensin 2 levels, etc.) associated with the classic atherosclerotic risk factors (obesity, diabetes, hypertension, hyperlipidaemia, tobacco use, etc) act as irritant stimuli on endothelial (EC) and vascular smooth muscle cells (VSMC).

Under normal circumstance, ECs resist adhesion of circulating cells, but when stimulated by cytokines, they and VSMCs, are induced to express adhesions molecules (e.g. vascular cell adhesion molecule (VCAM)-1, intercellular adhesion molecule1 (ICAM-1), etc. (35)) which cause circulating monocytes and lymphocytes to adhere to the endothelium and begin the process of ingress into the sub-intima where the crucial interaction with oxidised sub-intimal lipoprotein deposits will occur.

1.3.2.2 Chicken or Egg?

It remains an open question as to whether lipid ingress or an inflammatory process is the first event in atherogenesis. Tabas(36) has strongly argued in favour of the "lipid first" hypothesis yet describes lipid ingress occurring in areas of "susceptible intimal thickening" where the endothelium is relatively permeable and certain "pro-retentive" sub-intimal proteins are to be found. This begs the questions; what leads to the initial intimal thickening? There are clear and strong mechanistic/causative links with circulating low-density lipoprotein (LDL); Libby even describes LDL satisfying Koch's postulates. (37) The huge success of the statin trials(38) supports this view but the disappointing results of newer highly potent lipid modifying agents such a CETP inhibitors(39) in reducing cardiovascular events perhaps points to a more complicated picture that evades simple explanation. In any case, there is certainly a parallel process of increased endothelial permeability facilitating the ingress of both inflammatory cells and lipoprotein.

1.3.2.3 A Question of Balance

The monocyte is a key player. Once adhered to the endothelium, this cell then migrates into the sub-intimal space under the influence of cytokines such as monocyte chemoattractant protein-1 (MCP-1). There, it transdifferentiates into the macrophage and expresses scavenger receptors (Toll-like receptors(40)) for modified lipoproteins (and other damage associated molecular signatures (DAMPS) such as the heat shock proteins) under the influence of macrophage colony stimulating factor(M-CSF).(41-43) The macrophage then begins to phagocytose oxidised low density lipoprotein and begin the process of becoming a foam cell. This whole process represents a complex interplay between resident vascular cells (ECs and VSMCs), which release pro-inflammatory cytokines, and foreign inflammatory cells. The T-lymphocyte, although present in plaque in far fewer number than the macrophage is believed to act as a co-ordinating entity. T-cells are recruited into the plaque by IL-1 (interleukin 1) & IL-6 themselves induced by gamma interferon (IFG). (44)

The exact way in which T-cells, and other members of the adaptive immune system, influence atherogenesis remains under investigation but it seems likely that the T_H1 sub-population is important; releasing pro inflammatory interleukin-1β (IL-1β), IFG and tumour-necrosis factor (TNF). (34) Regulatory T-cells (TREGS) may play a counter-balancing role to the pro-inflammatory influence of T_H1 cells. (45) Mast cells, under the influence of IL-6 and IFG, eosinophils and B-cells have also been implicated. (46)

Whether a plaque progresses or regresses is a question of balance between pro- and anti-inflammatory processes. Not unlike the T-cell, the macrophage demonstrates polarity; the notion of proinflammatory M1 and anti-inflammatory M2 macrophage is now well established. (34,47) When pro-inflammatory processes dominate (presumably in the continuing presence of "irritants" – continued tobacco ingestion, untreated hypertension, etc.), the plaque milieu degenerates into an "unstable" state. Macrophages release reactive oxygen species and interstitial collagenases such as matrix metalloproteinase-1, 8 and 13 (MMP) promoting weakening of the fibrous cap. (48) They and VSMCs also express pro-coagulant tissue factor which is of critical importance in the event of plaque rupture.

In atherogenesis, the concept of the "necrobiome" is also of great importance; in a state of uncontrolled inflammation, the normally controlled processes of cell death and clearance of cellular debris and apoptotic bodies (efferocytosis) are overwhelmed. (34,47) Death signalling is increased and greater oncosis results in further inflammatory activation, further lipid oxidation and a positive feedback loop of increasing inflammation and increasing cell death. This leads to an inflamed intra-plaque necrotic core and a greater probability of plaque rupture.

In contrast, when pro-atherogenic stimuli are reduced, the influence of M2 macrophages and TREGS dominates. Pro-inflammatory signalling is reduced, VSMCs assume a different phenotype and migrate to the cap (under the

influence of platelet derived growth factor (PDGF)) where they multiply and secrete collagen and other matrix proteins generating a thicker, more stable fibrous cap. At the same time, the "necrobiome" becomes more controlled, with apoptosis dominating and the balance of efferocytosis resulting in an efficient clearance of cell debris and apoptotic bodies. A virtuous circle of reduced inflammation and controlled cell death and efferocytosis ensues and the plaque stabilises.

1.3.2.4 Towards A Greater Understanding Of Intimal Atherosclerotic Calcification

As has already been discussed in the introductory section on the pathophysiology of CAVD, our appreciation of the role that tissue calcification plays in atherosclerosis has radically changed. Far from being a passive and "degenerative" process, vessel mineralization appears to be a controlled response to a variety of insults, particularly oxidized inflammatory lipid. (49,50) This process has many similarities to the organising calcific response to tuberculosis infection where lipid-rich bacterial cell walls become oxidized through leukocyte activity. The chronic caseating necrotic inflammation associated with tuberculosis cannot be resolved, so is effectively "walled off" or replaced by calcium. It is therefore perhaps no surprise that direct links between atherosclerotic macrophage driven inflammation and the induction of pro-calcific pathways have been identified by Aikawa and co-workers. (13,16,51) Indeed, they have shown that macrophages themselves release matrix vesicles capable of inducing calcification. (50)The presence of cellular necrosis and increasing numbers of apoptotic bodies secondary to impaired efferocytosis are also likely to potentiate this relationship further. Hydroxyapatite nanocrystals themselves may also further drive the inflammatory cycle by setting up a positive feedback loop of increasing calcification, increasing inflammation, and increasing cell death.

1.3.2.5 From Evolving Plaque to Clinical Event

Atherosclerosis may lead to clinical syndromes in several ways. The cycle of inflammation and subsequent healing and scarring may cause stenosis that, despite collateralisation, leads to a supply/demand mismatch in the downstream tissues. The clinical manifestations depend on the tissues involved: angina with the coronary arteries, intermittent claudication with the peripheral arteries and mesenteric angina with the visceral arteries. The brain, which has a very high and unchanging resting metabolic demand isn't commonly affected by supply/demand mismatch. These are stable phenomena and can be dealt with in a controlled and elective setting. The more challenging acute clinical presentation of atherosclerosis (myocardial infarction, stroke, acute mesenteric ischaemia and acute limb ischaemia) relate to acute plaque events. Plaque causes acute clinical events most commonly in one of three ways; plaque rupture, plaque erosion and intra-luminal calcified nodule(48,52,53) (see figure 1.3).

Figure 1.3 | The Principle Mechanisms Of Acute Plaque Events

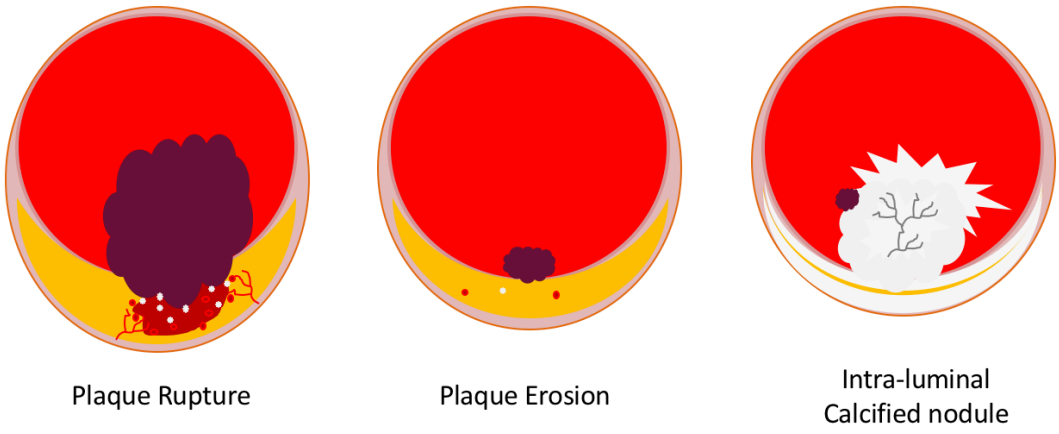

The white dots are micronodules of calcium, the red dots are inflammatory cells. The yellow crescent is the lipid pool. The red area within the plaque is the necrotic core. The red lines are fragile neo-vessels. The purple areas are thrombus. The larger white regions are macrocalcific deposits.

In plaque erosion, the endothelium overlying the plaque (which is usually of small volume with a thick cap and minimal inflammation) is denuded and platelets then aggregate on the exposed proteoglycans and smooth muscle cells. The thrombus may then embolise and cause distal ischaemia and infarction. Plaque erosion is more commonly seen in young female smokers. (52) In highly calcified, even ossified arteries, a coralline nodule may project into the lumen. This nodule has no anti-thrombotic endothelial covering and may lead to platelet aggregation and embolism.

Plaque rupture is the most important mechanism. Usually, a large inflamed and necrotic lipid core bursts through a thin fibrous cap. The highly thrombogenic contents of the necrotic core are then exposed. The atheromatous debris may then embolise causing atheroembolism, or a thrombus may form on the exposed material. The thrombus may cause occlusion of the vessel at the plaque (a typical mechanism in a ST elevation myocardial infarction) or fragments of thrombus may embolise and occlude smaller downstream vessels (a typical mechanism in ischaemic stroke).

The reason that the plaque core bursts is not fully understood. One putative mechanism is that much like in a pointing abscess, proteases and other lytic enzymes released by inflammatory cells increase the number of small molecules thus increasing oncotic pressure within the core causing more water to diffuse into it. This in turn leads to a higher hydrostatic pressure and then rupture. Clearly a thinner fibrous cap or a greater degree of inflammation and an unfavourable necrobiome will be associated with a higher risk of rupture.

Intra-plaque haemorrhage may also play a role. (54) The ischaemic necrotic core of the plaque stimulates the ingress of tiny blood vessels from the *vaso vasorum* in a process called angioneogenesis. These neo-vessels are very fragile and prone to haemorrhage. The haemorrhage may stimulate further inflammation, cell death and plaque rupture.

Another more recently proposed mechanism concerns microcalcific deposits. As I have already discussed, inflammation and cell death appear to lead directly to the nucleation of nano- and eventually micro-scale deposits of calcium apatite. When located deep within the plaque they are probably of little deterministic significance to the integrity of the cap. However a group has hypothesized and demonstrated(55-57), through the use of finite element analysis of coronary plaque microCT data, that microcalcific deposits in the fibrous cap may lead to interfacial debonding at the calcium-soft tissue interface and focally increased tissue stress in the thin fibrous cap. This could lead to a focal point for plaque rupture (see figure 1.4).

Figure 1.4 | Could Microcalcification Directly Cause Plaque Destabilisation Through Alteration Of Fibrous Cap Stresses?

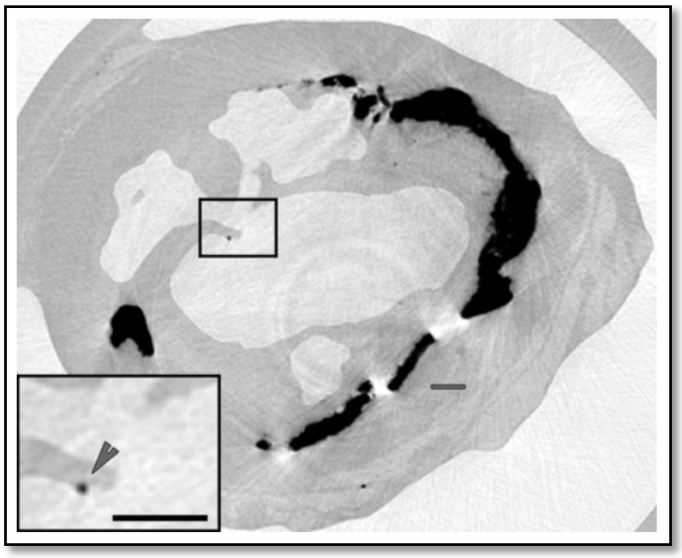

Finite element analysis of ex vivo coronary plaques has suggested microcalcifications located in the fibrous cap may destabilise the plaque by increasing focal tissue stress. Image from Maldonado *et al* 2012(56).

The hypothesis of microcalcification has some further support from clinical studies using CT coronary angiography. Motoyama *et al*(58) showed that "spotty calcification" (as opposed to large macrocalcific deposits) are frequently seen on CTCA in culprit lesions in acute coronary syndrome patients.

It remains of course difficult to infer causality between microcalcification and plaque rupture; the relationship may be epiphenomenal. As has previously been discussed, inflamed necrotic plaques are likely to microcalcify. They may rupture independently of small calcium deposits simply by virtue of inflammation and the other processes that have been discussed. Nevertheless, it is reasonable to conclude that microcalcification is a high-risk histopathological feature of plaque and its clinical identification may provide an interesting and potentially useful biomarker of plaque vulnerability.

1.3.3 In Search of The Vulnerable Plaque

When making clinical decisions about when to intervene in the context of both stable and unstable atherosclerotic syndromes in the carotid or coronary circulations, it is the case that luminal stenosis remains the dominant biomarker. Stenosis is simple in principle, reproducibly measured non-invasively whether by angiography or Doppler ultrasound and has a proven track record of providing prognostic information and helping direct therapeutic decisions. Yet it is nevertheless a fickle surrogate marker of plaque behaviour. Plaques that rupture or erode and cause events are not necessarily stenotic due to the process of positive remodelling, indeed severely stenotic but fibrocalcific lesions may be stable. (59)

In acute symptomatic situations (acute myocardial infarction, stroke, etc.) the benefits of intervention on a stenotic artery (carotid endarterectomy(60) or percutaneous coronary intervention(61)) are not in doubt but there is often uncertainty about whether or not there has been an acute plaque event *per se* and if so, which plaque has been the culprit. This is particularly the case in ischaemic stroke where approximately 26% of events are deemed cryptogenic; (62) a significant fraction of these unexplained strokes are believed to arise from non-occlusive plaque. It is also not infrequent to excise an entirely stable looking plaque at carotid endarterectomy performed for a neuroischaemic episode. The ability to detect the presence or absence of a culprit or vulnerable plaque confidently would make a huge difference to how atherosclerosis is treated.

In stable atherosclerosis the situation is more complex and controversial. When assessing the coronary circulation for potential pathology, there is an array of potentially useful diagnostic modalities. Some, such as angiography (invasive or non-invasive) are aimed at establishing coronary anatomy and sometimes plaque morphology, others, whether any putative occlusive disease is associated with inducible myocardial ischaemia. A vast sum of money is spent

in the US on assessing parameters of myocardial perfusion. Many argue that this "ischaemia" based strategy is irrational given that we know non-obstructive plaques can rupture and cause major adverse cardiovascular events. (59) It has also been difficult to prove that intervention in the context of stable angina does in fact reduce the risk of myocardial infarction or cardiovascular death. This is perhaps best illustrated by the ongoing major controversies over the DECREASE trial(63) and the continuing debate about carotid intervention in asymptomatic disease. (64-66) As such, a more nuanced plaque-based approach to treatment allocation, as opposed to one based purely on stenosis or inducible ischaemia, might be more rational. The ability to identify a "vulnerable" or high risk (and not necessarily obstructive) plaque by demonstrating inflammation or active microcalcification, as previously described in this introduction, may also provide a powerful way of monitoring the response to novel pharmacological interventions.

1.4 Hybrid Positron Emission Tomography and Computed Tomography

1.4.1 Positron Emission Tomography

1.4.1.1 Fundamentals

Positron Emission Tomography (PET) is a non-invasive molecular imaging technology that is able to resolve and quantitate *in vivo* a theoretically limitless number of biological processes by radiolabelling tuneable biomolecules and then detecting them at picomolar concentrations using a scanning platform.

The modality takes advantage of the fact that it is now reasonably straightforward to generate "proton heavy" isotopes, usually by bombarding suitable targets with protons in a cyclotron. The most commonly used isotopes in PET imaging are 11C, 13N, 15O and 18F, others that are less commonly used include 64Cu, 76Br, 82Rb, 68Ga and 124I. 18F is the most popular as its half-life of 110 minutes is a good compromise of factors (long enough to permit easier handling, delivery and therefore off-site commercial manufacture, but short enough to make the isotope less of a concern in terms of radiation dose and safety). Using a hot cell (an automated, miniaturised and radiation shielded chemistry laboratory), these reporters can then be chemically incorporated into a biomolecule, drug or peptide of interest before being administered to a patient as a radiotracer. One of the major challenges and expenses in PET science is the reliable, standardised and efficient production of bespoke complex radiotracers.

Once administered, the radiotracer localizes to and interacts with the biological process of interest. At a given moment, the unstable reporter isotope will undergo β+ decay; an excess proton is converted into a neutron thus restoring the optimal balance of protons and neutrons in the nucleus. This conversion also entails the generation of an electron neutrino and a positron. The emitted positron (with an energy of a few MeV) then travels for a distance in the tissue (the positron range) before thermalising and combining with an electron to form a positronium. The positronium then decays by annihilation and generates

two 511 keV photons emitted at nearly 180 degrees to each other (acollinearly). The photons go onto to be detected by scintillators, coupled to photomultiplier tubes, arranged into a ring detector. They are then 'electronically collimated' in time by co-incidence (i.e. only photons that strike the scintillator crystals within a 3-12 nanosecond time window are counted as a true co-incidences). It therefore becomes possible to localise the annihilation event along a line of co-incidence (line of response). With enough events, the data acquired during scanning can be reconstructed using statistical software into an interpretable image. Although data on many millions of events is collected, this is still significantly less than CT, and as such, random co-incidences, detector dead-time, photon attenuation, photon scatter and other factors that increase the noise in PET significantly require correction by statistical algorithms. The spatial resolution of PET is also fundamentally limited by the positron distance (0.5 mm with 18F) and acollinearity. As such, the resolution for most clinical PET systems is approximately 4-5 mm. This improves to approximately 700 μm with a pre-clinical microPET platform.

In order to aid image analysis, the PET scanner is usually employed as a hybrid system incorporating a CT scanner that allows for attenuation correction and for an anatomically detailed CT dataset to be accurately registered with the functionally detailed PET dataset as the subject does not need to move. The CT dataset may be augmented with the use of varying CT protocols (ECG gating for example) and the use of iodinated contrast with the patient in the same position.

1.4.1.2 Static Positron Emission Tomography

Most clinical PET scans are obtained with the scanner in static 3D mode. This is analogous to representing the PET data as a photograph (as opposed to a movie). Usually, the tracer is injected into the patient outside the scanning room. A period of time is then allowed to pass (uptake time) whilst the tracer makes its way around the body, distributes, is taken up in the tissues and

pharmacological steady state is achieved (the uptake time will vary according to the tracer pharmacology and the pathology under investigation). The patient is then moved through to the scanner. The body can be then be scanned, or "photographed", in approximately 22 cm thick axial slabs or "beds". All the co-incident events in one bed are counted and placed in a single time "bin". The time of acquisition for a single bed can be varied but is usually set at about 15 minutes (more time = more co-incident events = less noise OR a lower dose of tracer). The main limitation is time on the scanner (expensive and discomfort for the patient (who needs to stay still)) and also the amount of coverage required (more beds = more time). The data from each slice can then be decay corrected and the whole data set integrated into one volume and fused with a CT volume of choice (usually the attenuation correction dataset). Static PET acquisitions are not strictly quantitative but have the advantages of offering coverage of multiple beds (i.e. the whole body may be scanned) and of being clinically more user friendly to analyse than the alternative method (see "Dynamic Positron Emission Tomography" below).

Semi-Quantitative Uptake Measurement

In order to quantify radiotracer uptake in the tissues, static PET image data are analysed on commercially available software packages and regions or volumes of interest (ROI/VOI) are drawn on the CT images and then translated to the PET images. Radiotracer uptake is normally quantified as tissue radioactivity normalised to the injected dose and body surface area by the following equation:

$$SUV(t) = \frac{c(t)}{a \div w}$$

where SUV is the Standardised Uptake Value, t is the time of measurement, c is the radioactivity of the tissue within the region of interest, a is the decay corrected injected activity and w is either body weight, lean body weight or body surface area. All voxels in the volume of interest have a separate SUV and

most software packages will quote their mean, minimum, maximum and standard deviation. It has also become conventional to normalise tissue SUV to image-derived blood pool activity (normally from caval or atrial lumens) to generate a Tissue (or Target) to Background Ratio:

$$TBR = \frac{Tissue\ VOI\ SUV(t)}{Blood\ pool\ SUV\ (t)}$$

This is of particular use in cardiovascular PET when the tissues of interest are often affected by overspill from the blood pool.

1.4.1.3 Dynamic Positron Emission Tomography

In contrast to static PET imaging ("photography"), dynamic PET scanning may be regarded as more akin to filming a movie. This method is the gold standard for truly quantitative PET and can facilitate a huge variety of *in vivo* biological and pharmacological experiments. In brief, the scanner is used in "list" mode and scanning started at the moment of injection of radiotracer. The co-incidence data are then recorded as they vary with time. It is usually only possible to scan a single bed (i.e. a focussed area of anatomy) in list mode. The patient must remain still in the scanner for usually at least an hour (depending the isotope and PET experiment being performed). The technique is also usually supplemented by arterial blood sampling; initially continuously, then intermittently. This permits a precise estimate of the plasma concentration of isotope as it varies with time. The blood concentration or blood/plasma activity curve derived from this data will serve as the "input function" used to "drive" the mathematical modelling that can be subsequently performed to explore the pharmacodynamic and kinetic properties of the tracer under investigation. For complex PET radiotracers blood sampling is mandatory as it permits analysis of the metabolised products of the radiotracer using high-performance liquid chromatography.

1.4.2 PET/CT In Cardiovascular Disease

1.4.2.1 18F-Fluorodeoxyglucose

18F-Fluorodeoxyglucose, or more properly 2-deoxy-2-(18F)fluoro-D-glucose (18F-FDG) was first administered to humans in 1976(67) with the aim of demonstrating cerebral and total body glucose utilisation. Cells with high metabolic demand express large quantities of various GLUT transporter sub-types and metabolise glucose quickly thus generating a gradient across the cell membrane that causes a continuous large influx of glucose. 18F-FDG directly competes with glucose for transportation by GLUT and then undergoes phosphorylation to 18F-FDG-6-phosphate by hexokinase. Owing to the strict specificity of phosphoglucose isomerase for glucose-6-phosphate, 18F-FDG-phosphate is not altered and is unable to progress down the glycolytic pathway. It thus becomes trapped within the cell and its continuing accumulation allows detection by the PET. 18F-FDG is thus able to identify clusters of cells with very high rates of glucose uptake. Consequently, 18F-FDG is not specific to one cell type but will accumulate in any cell with increased metabolic demand e.g. neurons, active muscle cells, neoplastic cells and activated inflammatory cells.

As a result of its ubiquity, 18F-FDG remains the only putative PET marker of inflammation to have been investigated in clinical studies of CAVD. In PET imaging of atherosclerosis, pioneered by Rudd(68), Fayad(69) and Tawakol(70,71), it was hypothesized that macrophages, the key players in the inflammatory milieu of the high-risk plaque, were responsible for the observed signal. This was evidenced in Rudd's original paper using tritiated deoxyglucose autoradiography. Others have demonstrated a correlation between plaque SUV and CD68 macrophage immunohistochemical staining in humans(70). These data complement observations that macrophages have high baseline levels of glycolysis that increase dramatically when the cell becomes activated. (72,73) This may be particularly germane in the hypoxic environment of the plaque where glycolysis may be the only pathway available for the generation of ATP. (74,75) Indeed, pre-clinical and clinical data have suggested that hypoxia may

be the most important factor governing the uptake of 18F-FDG by macrophages. (76) Whether it is inflammation, hypoxia or a combination of both driving increased GLUT expression by macrophages, a growing body of clinical studies indicate that 18F-FDG highlights a pathological, hypermetabolic state in the arterial wall that appears to improve with statin therapy. (77) Although there have been no data published at the time of study exploring the mechanisms of 18F-FDG uptake in the aortic valve, it seems highly likely that similar mechanisms should also govern uptake.

1.4.2.2 18F-Fluoride

18F-fluoride (delivered as a solution of sodium fluoride; 18F-fluoride) was first mooted as a bone tracer in the seminal paper by Blau in 1972. (78) It has since established a track record in PET imaging of bone metabolism and disease with an excellent safety record. (79-98) It has been used in humans to assess disease activity(80,83) and indeed response to treatment in osteoporosis(86) and Paget's disease. (91) By virtue of its rapid elimination, high target specificity and availability for binding, it has pharmacokinetic and pharmacodynamics properties that are ideally suited to imaging, resulting in a high target to background ratio. (79,88)

It is often argued that 18F-fluoride is a marker of bone deposition(93) or osteoblastic activity but the reality is more complex. (78,95,96) Bone crystal is predominantly composed of calcium orthophosphate crystal that approaches mineral calcium hydroxylapatite. In purely physicochemical terms, the fluoride ion is incorporated onto the apatite surface by chemisorption and substituted for a hydroxyl group. In physiological conditions, this not a simple process; the original 4-step description by Blau still stands today. fluoride must first be delivered to the bone by blood (1) and then leave the plasma to enter the extracellular fluid (ECF) (2). The fluoride will then enter the shell of bound water enveloping the crystal (3) before eventually undergoing full incorporation (4). Steps one and two are predominantly determined by blood flow. Steps three and four are however critically dependent upon the surface area of apatite available for incorporation. In bone, this relates to increased osteoblast and osteoclast activity. Osteoblasts generate matrix vesicles, and the propagation of new regions of tiny nano-crystalline apatite particles, whilst osteoclasts promote the dissolution of solid blocks of established mineral. As a consequence, 18F-fluoride uptake reflects a combination of increased osteoblastic and osteoclastic activity, thus acting predominantly as a marker of bone turnover. Indeed, this hypothesis is now firmly supported by a large and expanding body of experimental and clinical PET data.(81,84,85,88,89,95)

1.4.4.3 Proposed Mechanism Of 18F-Fluoride Uptake In Cardiovascular Tissue

18F-fluoride uptake in the aorta and carotid arteries was first published by Derlin. (97,99) He made the key observation that some heavily calcified lesions did not demonstrate increased PET uptake, and indeed that CT calcium scores in the aorta did not correlate well with 18F-fluoride uptake. Subsequent studies have confirmed the disconnect between 18F-fluoride PET and CT calcium scoring, which similar to bone, probably relates to calcification activity and the effects of surface area on 18F-fluoride binding.

Figure 1.5 | Putative Mechanism for 18F-Fluoride Microcalcification Selectivity

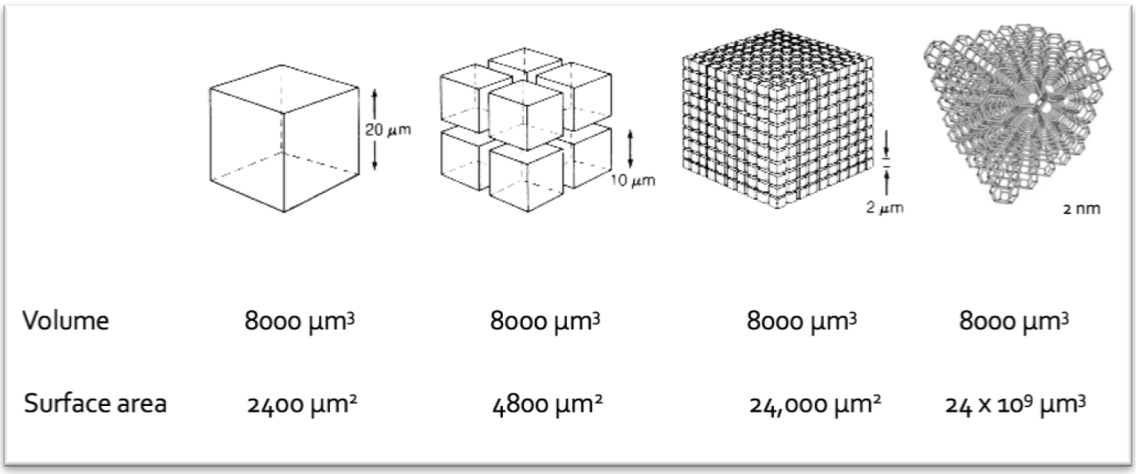

The total volumes of material in each example of this diagram do not change, but as the unit of division becomes smaller, the surface area available for absorption massively increases. The "block" on the left is analogous to an established lump of field calcification in a stable atherosclerotic plaque (low surface area to volume ratio), the situation on the right is akin to the countless nucleating nanocrystals of calcium in a necrotic unstable plaque(56,57) (a very high surface area to volume ratio)

As I have already described in the introduction, in the early stages of CAVD and similarly within the milieu of the high-risk or indeed ruptured atherosclerotic plaque, microcalcification is likely to represent a complex and regulated healing response to the inflammation, hypoxia and cell death characteristic of these lesions. **My central hypothesis** is that it is likely that these foci of calcium nanocrystals provide an extremely high surface area to which 18F-fluoride can

absorb, resulting in increased uptake of this tracer in regions of newly developing and active micro-calcification.

By contrast, in a stable atherosclerotic plaque, where healing has occurred and the calcium has coalesced into a large but unitary volume or "field" of macro-calcification, most of the calcium is internalised and "hidden" from the isotope.

The situation in the latter stages of aortic stenosis is perhaps more nuanced. Here the valve is characterised by an extensive calcification process that is co-ordinated by osteoblasts in a manner more akin to skeletal bone formation, involving many of the same humoral factors. Indeed, lamellar bone, microfractures and haemopoetic tissue have all been observed in the end-stages of the disease. The mechanism of 18F-fluoride binding in these valves is therefore more likely to be similar to that of bone, reflecting the deposition of new micro-calcific deposits on the surface of the valve, the remodelling of existing calcium towards the end-stage bone phenotype and perhaps isotope delivery through angiogenesis.

In summary, 18F-fluoride is believed to act as a marker of new and evolving microcalcification and calcium turnover patients with atherosclerotic plaque and CAVD. Given its proven specificity and excellent kinetics in bone and metastatic disease patients and complete lack of myocardial spillover, the isotope holds major advantages over 18F-FDG as an imaging biomarker of disease activity and plaque risk in both CAVD and atherosclerotic plaque.

1.4.4.4 Clinical Studies of 18F-FDG in CAVD

To the date, only two published studies have examined the use of 18F-FDG in the imaging of valvular glycolytic activity. (100,101) The first published report of 18F-FDG uptake in the aortic valve was produced by Marincheva-Savcheva and colleagues in 2011. (100) This was a retrospective study of patients having whole body 18F-FDG PET CT for oncological staging. The group identified a cohort of 42 patients with a diagnosis of CAVD and age-matched these patients to a second cohort of 42 cancer patients without CAVD. Patients with CAVD were stratified in to echocardiographically mild, moderate and severe groups. A semi-quantitative assessment of CT valvular calcification was made. PET scans were manually registered with CT scans and ROIs were drawn in the centre of the aortic valves (to minimise overspill from myocardial uptake). Tissue-to-background ratios were computed by normalising valvular SUVs to blood pool uptake in the right atrium. Intra- and inter-observer reproducibility studies were undertaken and, in a subgroup, the authors addressed the ability of 18F-FDG to predict disease progression.

To date, Dweck has performed the largest prospective study of PET CT 18F-FDG imaging in patients with CAVD. (101) A total of 121 patients were recruited and were representative of the full spectrum of CAVD severity including 20 subjects with aortic valve sclerosis and 20 age- and sex-matched controls with normal aortic valves. Baseline echocardiography was performed along with dedicated 18F-FDG and 18F-fluoride PET CT imaging and CT calcium scoring of the aortic valve. (102) Patients were also asked to adhere to a carbohydrate-free diet prior to their 18F-FDG scan in order to minimise myocardial uptake by encouraging the heart to switch from glucose to free fatty acid metabolism. PET CT analysis was undertaken using dedicated PET CT analysis software (OsiriX version 3.5.1 64-bit; OsiriX Imaging Software, Geneva, Switzerland).

Relationship Between FDG Uptake And Aortic Stenosis Lesion Severity

The key finding from Marincheva-Savcheva's study was that aortic valve 18F-FDG uptake was significantly higher in CAVD patients compared to controls (median TBR 1.53 [IQR: 1.42-1.76] *versus* 1.34 [1.20-1.55]; $p < 0.001$). There was also an apparent increase in 18F-FDG uptake upon moving from mild to moderate aortic stenosis (1.50 [1.36 to 1.75] *versus* 1.70 [1.52 to 1.94]). However 18F-FDG uptake reduced in those with severe disease (1.51 [1.38 to 1.54]), leading the authors to conclude that CAVD occurs in two distinct stages: an early principally inflammatory stage followed by a second stage, decoupled from inflammation, and dominated by a process of active calcification reminiscent of osteogenesis. (18) Dweck's findings largely reproduced those of Marincheva-Savcheva, in that he observed a steady although modest positive correlation between 18F-FDG uptake by all measures and aortic stenosis severity but did not see the fall in 18F-FDG uptake in patients with the most severe lesions. This discrepancy may be attributable to survival bias in the severe patients (they are more likely to progress to surgery and thus drop out of analysis), the small numbers of patients in the first study, the problems with reproducibility in one study or unaccounted differences in the different study population. The summary findings of both studies are shown in Figure 1.6. It should be noted that in both trials, large overlaps in TBR ranges between groups were observed, indicating that although statistical differences were present, the ability of 18F-FDG to distinguish between categories with confidence is limited.

Figure 1.6 | Valvular 18F-Fluorodeoxyglucose TBR_{max} Uptake According To Echocardiographic severity

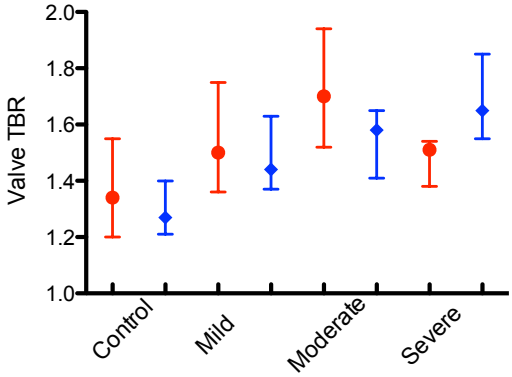

Marincheva-Savcheva (red) and Dweck (blue). Dots/diamonds are median, whiskers are interquartile range

Predicting Clinical Outcome and Disease Progression In CAVD

In a sub-group of patients with serial echocardiographic data available (n = 19), Marincheva-Savcheva showed that subjects with a valvular TBR greater than the median had a higher chance of progression: 5 of 6 patients with above median TBR progressed compared to 2 of 9 patients with below median values. This result only just reached statistical significance (p = 0.04) and the binary definition of progression was loose (any increase in severity class in any of the echocardiographic criteria).

Reproducibility, Methodological Strengths and Weaknesses

The Marincheva-Savcheva study was important in terms of proof-of-principle but was limited by several factors. The study was necessarily retrospective and the patients were not primarily selected on the basis of their cardiac disease. Moreover, the PET/CT protocols were neither standardised nor optimised for demonstrating valvular inflammation. The analysis was also limited by poor intra-observer reliability, with an intra-class correlation coefficient of 0.55 (95% CI: 0.27 - 0.73), although curiously, the inter-observer reliability was much better: intra-class correlation coefficient (ICC) = 0.97 (95% CI: 0.96 to 0.98). Therefore, the results need to be interpreted with caution. Dweck's group benefited from pre-specified and consistent PET/CT acquisition protocols, a prospectively recruited cohort and a standardised follow-up schedule. He explored multiple methods of analysing valvular 18F-FDG uptake, and concluded, like Marincheva-Savcheva, that the "centre-valve" approach produced the best intra- and inter-observer reliability with narrow limits of agreement(101). In keeping with Marincheva-Savcheva findings, the group also found that analysis was significantly hampered by overspill of signal from myocardial tissue near the aortic annulus. This occurred despite dietary modification and may have contaminated the valvular signal. Furthermore, as with any PET image analysis of relatively small volumes, the absolute measured activities may have been reduced by partial voluming artefact.

1.4.4.5 Clinical Studies of 18F-Fluoride in CAVD

At the time of writing, only two clinical studies have been published exploring the role of 18F-fluoride PET CT imaging in CAVD(101,103). Hyafil and colleagues employed a retrospective design looking at a small cohort (n = 5) of oncological and rheumatological patients who happened to have a diagnosis of CAVD. A control cohort of 10 patients without CAVD was randomly selected from the population who had undergone PET/CT. SUV_{max} and TBR_{max} values were obtained by drawing ROI around the aortic valve and within the right atrial lumen. Studies of intra- and inter-observer reliability were also undertaken. In Dweck's study, as described above, a cohort of 121 patients underwent 18F-fluoride PET CT along with 18F-FDG PET CT and CT calcium scoring of the aortic valve.

Relationship Between 18F-fluoride And Lesion Severity

Both studies demonstrated that stenotic aortic valves showed considerably higher 18F-fluoride uptake than normal valves (see figure 1.7). Hyafil compared normal with severe: valvular TBR_{max} 1.5 (IQR 1.5 to 1.7) *versus* 2.2 (IQR 2.0 to 2.7) respectively. Dweck recruited from across the CAVD severity spectrum, again demonstrating increased activity *versus* controls and a strong positive correlation (much stronger than 18F-FDG) between stenosis severity and all measures of 18F-fluoride uptake. This clear relationship remained if severity was assessed by other echo parameters (time-velocity integral: r^2=0.546, P<0.001; aortic valve area: r^2=0.387, P<0.001; dimensionless index: r^2=0.527, P<0.001) or indeed by the aortic valve calcium score (r^2=0.641, P<0.001).

Figure 1.7 | Valvular 18F-fluoride TBR_{max} uptake according to echocardiographic severity

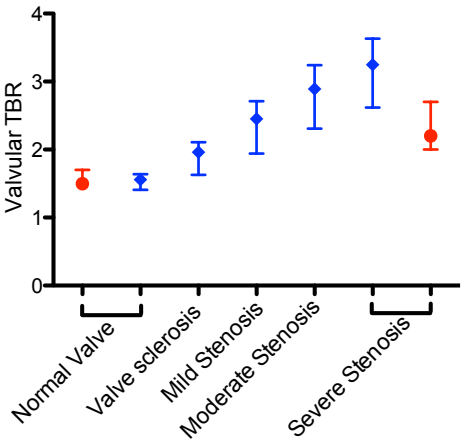

Valvular 18F-fluoride maximum tissue-to-background ratios from Hyafil (red) and Dweck (blue). Dots/diamonds are median, whiskers are interquartile range

However as described by Derlin(97) in the aorta, 18F-fluoride activity appeared to provide distinct and complementary information to CT calcium scoring, with regions of 18F-fluoride uptake frequently observed in the absence of underling calcium on CT and *vice versa*.

Predicting Outcome and Disease Progression with 18F-Fluoride

At the time of study, no prospective data on 18F-fluoride and clinical outcomes or disease progression had been published. This will be a key area of study in proving the potential utility of this tracer in CAVD and forms a major part of this work.

Reproducibility, Methodological Strengths and Weaknesses

Hyafil's study reported on measurement reliability for both SUV_{max} and TBR_{max} and found these to be excellent. These results closely match Dweck's with all measures of 18F-fluoride uptake (SUV_{mean}, SUV_{max}, TBR_{mean} and TBR_{max}) demonstrating intra-class correlation coefficients for intra- and inter-observer reproducibility >0.95. Furthermore, Bland-Altman analysis showed no fixed or proportional biases, with the majority of data points falling within narrow limits of agreement. These results were significantly better than those for 18F-FDG,

the discrepancy being explained by the lack of myocardial 18F-fluoride uptake causing problems with spillover.

Studies to date do have limitations. Hyafil's study provided proof of principle but was small, retrospective and involved patients having scans for indications other than cardiovascular disease. Furthermore, as with Marincheva-Savcheva's paper, PET/CT acquisition protocols were neither standardised nor optimised for cardiovascular imaging.

1.4.4.6 Clinical Studies of 18F-Fluoride in Atherosclerosis

18F-fluoride PET/CT has only recently been explored in the context of cardiovascular disease. A summary of all papers published prior to the work presented in this thesis is summarised in table 1.1. The key papers are here described in more detail.

Thorsten Derlin and co-authors(97) provided the first written report in 2010 on the potential utility of 18F-fluoride in imaging pathological cardiovascular calcification. They retrospectively studied 75 patients who had undergone 18F-fluoride PET/CT for the detection of metastases. They assessed the vasculature for visible calcification on CT and also for radiotracer uptake. They made two key findings:

1. 18F-fluoride uptake was more reliably present when a patient had a history of cardiovascular events.
2. Although there was a relationship between CT and PET defined calcification, this was nuanced with many vessel segments being CT positive but PET negative whilst others were PET positive but CT negative.

They concluded that 18F-fluoride PET may provide complementary data on atherosclerotic plaque physiology to that provided by CT.

Derlin then followed up his first paper with two linked and highly novel reports. (98,99). The first paper(99) studied 18F-fluoride alone. Using similar methodology to his first paper he studied a larger cohort of oncologic patients (n=269) and this time focussed on the carotid artery and patient clinical features. His findings essentially confirmed that of the first study, namely that CT defined calcification was related to 18F-fluoride uptake and that patients with a higher burden of CV risk factors had higher uptake of 18F-fluoride.

Table 1.1 | Clinical Studies of 18F-Fluoride PET/CT in Atherosclerotic Cardiovascular Disease

	Population	Study Design	n	Radioisotope	Key findings
Derlin 2010(97)	Oncologic	Retrospective case series	75	18F-fluoride	Association between vascular 18F-fluoride uptake and CV events Different pattern of uptake to arterial calcium on CT
Beheshti(104)	Oncologic	Retrospective case series	51	18F-fluoride	Association between CV 18F-fluoride and age
Derlin 2011a(99)	Oncologic	Retrospective case series	269	18F-fluoride	Association between vascular and cardiac 18F-fluoride uptake and CV RF Different pattern of uptake to arterial calcium on CT Good inter- and intra-rater reproducibility
Derlin 2011b(98)	Oncologic	Retrospective case series	45	18F-fluoride & 18F-FDG	Association between vascular 18F-fluoride uptake and CV RF Association between vascular 18F-FDG and CV RF Differential uptake of 18F-fluoride and 18F-FDG in vasculature Good inter- and intra-rater reproducibility for both isotopes
Li 2012(105)	Oncologic	Retrospective case series	61	18F-fluoride	Association between coronary 18F-fluoride uptake and CV RF Different pattern of uptake to arterial calcium on CT
Dweck 2012(106)	Aortic stenosis	Prospective cohort	119	18F-fluoride & 18F-FDG	Coronary 18F-fluoride PET/CT feasible Coronary 18F-FDG PET/CT difficult (spillover) Good inter- and intra-rater reproducibility for coronary 18F-fluoride 18F-fluoride uptake higher in coronary plaque *versus* control 18F-FDG uptake same in coronary plaque *versus* control Different pattern of uptake to arterial calcium on CT Association between CV 18F-fluoride and CVRF Potential for 18F-fluoride to identify culprit/high-risk plaque
Quirce 2013(107)	Carotid atherosclerosis	Case-control	15	18F-fluoride	Potentially higher 18F-fluoride uptake in symptomatic *versus* asymptomatic plaque
Blomberg 2014(108)	Chest pain	Case-control	38	18F-fluoride	Association between whole heart 18F-fluoride and CV risk "Corrected" SUV potentially more reliable than TBR 18F-fluoride uptake higher in patient *versus* controls
Morbelli 2013(109)	Oncologic	Retrospective case series	80	18F-fluoride	Association between vascular 18F-fluoride and CV risk Different pattern of uptake to arterial calcium on CT

Abbreviations: CT, computed tomography; CV, cardiovascular; PET, positron emission tomography; RF, risk factors; SUV, standardised uptake value; TBR, target to background ratio

The authors also observed that in some instances, 18F-fluoride uptake appeared to be less than expected in patients with calcified plaque on statins and speculated that this might support the notion of 18F-fluoride as an *in vivo* marker of response to pharmacotherapy. The second paper(98), although smaller (n=45) compared 18F-fluoride to 18F-18F-FDG. Again, oncologic patient scans were studied retrospectively. Both tracers correlated with some CV risk factors. Uptake quantification was found to be reliable although interestingly, 18F-fluoride appeared to perform slightly better than 18F-FDG. The key finding was the relationship between 18F-FDG and 18F-fluoride uptake. True co-incidental uptake of both tracers was comparatively rare. The authors hypothesized that 18F-FDG and 18F-fluoride highlighted different stages of the atherosclerotic process – with 18F-FDG identifying an early predominantly inflammatory stage whilst 18F-fluoride highlighted the later stages where the plaque becomes complex and advanced and the calcific processes (occurring in response to necrosis and apoptosis) predominate.

Marc Dweck *et al*(106)(from our group) published an important 18F-fluoride paper in 2012. This report was based on a re-analysis of a prospective cohort study looking at the role of 18F-fluoride and 18F-FDG in CAVD (see above in "Clinical Studies of 18F-Fluoride in CAVD"). The group recruited 120 patients (100 with aortic stenosis 20 disease-free controls) all of whom were subjected to 18F-fluoride and 18F-FDG PET/CT. The scans were re-analysed with a focus on the uptake of isotope into the coronary circulation. Inter- and intra-observer repeatability studies were carried out. Tracer uptake was compared in those with and without coronary atheroma (as defined by the presence of coronary calcification) and uptake was also compared to Framingham cardiovascular risk scores. The key findings were that 18F-fluoride coronary PET/CT was feasible and quantification by SUV analysis was repeatable. For reasons of signal spillover from adjacent mycocardium, coronary 18F-FDG analysis was frequently impossible and indeed proved less repeatable. 18F-fluoride uptake was higher in atherosclerotic coronary arteries compared to disease-free arteries. No such observation was seen for 18F-FDG. As previous reports have

shown 18F-fluoride was associated with the presence of cardiovascular risk factors, established cardiovascular risk scores and prior major adverse cardiovascular events. Again, confirming the findings of Derlin and others, there were segments of coronary artery that were calcified but not 18F-fluoride avid and conversely others that were 18F-fluoride avid but not obviously calcified indicating that 18F-fluoride is more than an expensive variant of the CT calcium score. Finally, an interesting single observation was made. One patient was recruited shortly after suffering a non-ST elevation myocardial infarction. The confirmed culprit artery showed intense 18F-fluoride uptake raising the tantalising possibility that the isotope might have a role beyond mere global risk prediction and rather might give more specific information about individual plaque vulnerability. This paper has in large part led to much of the work in this thesis.

Quirce(107) and colleagues published the first prospective study of 18F-fluoride PET/CT in acute carotid atherosclerotic pathology. The paper is really only notable for being the first and is significantly limited by its size (n=15), very rudimentary analysis and lack of any form of validation, histological or otherwise. The results suggested that 18F-fluoride uptake might be increased in acute symptomatic carotid plaque compared to asymptomatic lesions though the results did not achieve statistical significance.

Blomberg *et al*(108), as part of the CAMONA trial, published an interesting sub-study addressing the question of whether delaying imaging (at three different time points: 45, 90 and 190 minutes) with 18F-fluoride might have a positive impact on arterial image quality and uptake quantification reliability by reducing the amount of blood pool signal and thus signal contamination of the arterial wall. Importantly, the authors found that the TBR varied with the delay time; as blood pool activity decreased, the TBR naturally increased. They speculated that despite TBR proving the most popular semi-quantitative measure in the literature, it might not in fact be the most reliable as subjects

can't necessarily be assumed to clear 18F-fluoride at the same rate. They found that the "corrected SUV" was less, if at all, vulnerable to this effect:

$$cSUV = SUV_{tissue} - SUV_{blood}$$

Where *cSUV* is the corrected SUV, SUV_{tissue} is the SUV within a region or volume of interest incorporating the vessel under study (including the blood within it) and SVU_{blood} is the SUV from the blood pool (taken in their study from a volume of interest within the right atrium). The authors also noted that for all time points (with the exception of TBR at 45 minutes) 18F-fluoride uptake correlated with CV risk.

1.5 Summary

All the data published at the time that the work described in this thesis was undertaken suggest that 18F-fluoride PET/CT might play an interesting role in assessing atherosclerosis in a variety of anatomical sites. Vascular 18F-fluoride PET imaging has been shown to be feasible and repeatable. The isotope appears to have highly favourable pharmacodynamic and pharmacokinetic properties for vascular imaging. A clear relationship with cardiovascular risk has been demonstrated and then reproduced across multiple studies and critically, there doesn't appear to be a simple linear relationship on a per-plaque basis between CT defined calcium and 18F-fluoride uptake.

1.6 Aims

My aims were to build on my group's previous work and deepen understanding of how the 18F-fluoride and 18F-FDG PET radiotracers report on aortic valve stenosis and atherosclerotic plaque:

Calcific Aortic Valve Disease

1. To provide a mechanistic explanation of 18F-FDG and 18F-fluoride uptake in the aortic valve.
2. To assess whether baseline 18F-FDG and 18F-fluoride are able to predict disease progression and clinical outcomes in patients with CAVD.
3. To compare such predictive capability to other established and evolving imaging methods.

Atherosclerosis

1. To provide a comprehensive mechanistic model of 18F-fluoride uptake in atherosclerotic plaque.
2. The provide a pharmacokinetic and pharmacodynamic model of 18F-fluoride uptake in patients with atherosclerosis.
3. To validate semi-quantitative static PET uptake assessment with quantitative dynamic PET.
4. To examine the reproducibility of 18F-fluoride uptake assessment in coronary and carotid atherosclerotic plaque and compare this to 18F-FDG.
5. To compare 18F-FDG and 18F-fluoride PET/CT of atherosclerotic plaque with other plaque imaging modalities as well as histological plaque assessment.
6. To assess whether 18F-fluoride PET/CT is able to identify "culprit" (acute plaque deemed to have cause an acute ischaemic syndrome) or "high-risk" atherosclerotic plaque.

1.7 Hypotheses

Calcific Aortic Valve Disease

1. 18F-FDG uptake will reflect valvular inflammation defined by increased macrophage infiltration.
    a. Chapter 3
2. 18F-fluoride uptake will reflect valvular calcium nanocrystal formation and calcium turnover by binding hydroxyapatite. Such binding will be dependent of the surface area of crystal available for chemisorption.
    a. Chapter 3
    b. Chapter 6
3. Baseline 18F-FDG PET uptake will predict future disease progression and clinical events.
    a. Chapter 3
    b. Chapter 4
4. Baseline 18F-Fluoride PET uptake will predict future disease progression and clinical events.
    a. Chapter 5
    b. Chapter 6

Atherosclerosis

1. 18F-fluoride will reflect the genesis of calcium nanocrystal formation (triggered itself by intra-plaque necrosis and inflammation) in atherosclerotic plaque by binding hydroxyapatite. Such binding will be dependent of the surface area of crystal available for chemisorption.
    a. Chapter 5
    b. Chapter 6
2. 18F-fluoride will demonstrate pharmacokinetic and pharmacodynamic characteristics suitable for plaque imaging
    a. Chapter 5
3. 18F-fluoride uptake will be increased in clinically adjudicated carotid and coronary "culprit" plaque compared to control lesions that have not caused a clinical event.
    a. Chapter 4
    b. Chapter 7
4. 18F-fluoride uptake will be increased in carotid and coronary plaque with imaging defined phenotypic markers of high-risk compared to plaque of stable phenotype.
    a. Chapter 4
    b. Chapter 7
5. Principally for reasons of target selectivity, 18F-fluoride will compare favourably in terms of hypotheses 3 and 4 when compared to the current gold-standard, 18F-FDG.
    a. Chapter 4
    b. Chapter 7

Chapter 2 – Methods

2.1 Patient Populations

2.1.1 Aortic Stenosis Studies

The patients recruited for the studies of CAVD were recruited from cardiology clinics with NHS Lothian. 5 cohorts in total were recruited: these comprised disease free controls, patients with aortic valve sclerosis and 3 cohorts with true aortic stenosis divided into mild moderate and severe categories. Further details can be found in Chapters 3 and 4.

2.1.2 Carotid Atherosclerosis

Two cohorts of "carotid" patients were recruited.

1. Subject cohort of recently neurologically symptomatic patients (transient ischaemic attack or stroke or amaurosis fugax) with a ≥50% stenosis by NASCET(110) criteria for men and >70% for women.
2. Control cohort of recently neurologically symptomatic patients (transient ischaemia attack or stroke) **not** attributed to carotid artery stenosis.

Patients were recruited from stroke/neurology clinics or directly from stroke wards in NHS Lothian. The full inclusion/exclusion criteria, study protocols, recruitment data etc. may be found in Chapters 5, 6 and 7.

2.1.3 Coronary Atherosclerosis

Two cohorts of coronary patients were recruited from cardiology clinics, in-patient cardiology wards and coronary care in NHS Lothian.

1. "Unstable" cohort: patients with acute ST-segment elevation or non- ST-segment elevation myocardial infarction
2. "Stable" cohort: patients with stable angina pectoris undergoing planned invasive coronary angiography

Full details of the inclusion/exclusion criteria, study protocol and recruitment can be found in Chapter 5.

2.2 Ethical Considerations

All studies described in this thesis were conducted with full institutional ethics committee board review and approval. Two committees were consulted: South East Scotland Research Ethics Committee and the West of Scotland Regional Ethics Committee. All patients freely gave their written and informed consent and the research was conducted in accordance with the Declaration of Helsinki of the World Medical Association.

The studies were registered with the relevant European Union body and also on www.clinicaltrials.gov.

2.3 Positron Emission Tomography / Computed Tomography

All patients were recruited and scanned on the Edinburgh Royal Infirmary site and specifically at the Clinical and Research Imaging Centre (CRIC) within the Queen Elizabeth University Building.

Patients were greeted and taken through to the designated clinical area. A brief, standardised medical assessment was undertaken. The patients' height and weight were measured. The scales used were regularly calibrated. For cardiac subjects (Chapters 3, 4 and 5), an ECG was undertaken. This was not the case for carotid patients. An 18 Gauge peripheral intra-venous catheter was then sited and blood drawn for a baseline set of standardised biochemical and haematological parameters (see relevant Chapters for more detail). As per protocol, additional blood was then taken in a cool box to a core laboratory for centrifugation, separating into aliquots and storage at -80°C for subsequent biomarker analysis. After confirming that consent was still present for scanning, subjects were taken through to a series of shielded rooms and prepared for isotope injection.

All scanning was done using the same device: a 64- multidetector Biograph mCT manufactured by Siemens Medical Systems (Erlangen, Germany). Device calibration and quality control was regularly carried out by trained PET physicists and radiographers.

2.3.1 Isotope generation

For the original CAVD studies (Chapters 3 and 4), both 18F-FDG and 18F-fluoride were manufactured by a commercial producer (Erigal Ltd, Keele). For subsequent coronary and carotid studies, the CRIC had had a cyclotron and functioning hot cells established and therefore isotopes were manufactured in house according to established GMP-compliant protocols. 18F-FDG and 18F-fluoride were quality controlled and filtered to remove micro-organisms by the accredited radiochemistry suite team.

2.3.2 Injection for Static PET Acquisitions

The isotope was drawn up into a syringe using a semi-automatic system in order to minimize radiation exposure to the operator in a dedicated room. The precise radioactivity of the tracer solution was then measured and the time of measurement recorded. The volume in the syringe was adjusted in order to ensure the target dose was achieved. The isotope was then carried through to the shielded uptake room and then injected in to the patient and flushed with 10mLs of saline. The time of injection was recorded. Patients then rested for the relevant time (see below). Prior to transfer into the scanner, patients were asked to micturate in order to minimise signal from the bladder and avoid discomfort whilst lying still on the scanning table.

2.3.2.1 18F-FDG Dosing and Uptake

In all studies, the target dose for 18F-FDG was 200 MBq and the uptake time was set at 90 minutes. For details of achieved target doses and uptake time as well as variability, please see relevant chapters. One patient in the main carotid study (Chapter 7) was accidentally given an oncologic dose of 350 MBq. This event was logged through the relevant research and clinical governance systems and a full explanation and apology offered to the patient.

2.3.2.2 18F-Fluoride Dosing and Uptake

In all aortic valve and coronary studies (Chapters 3, 4 and 5), the target dose for 18F-fluoride was 125 MBq and the uptake time was set at 60 minutes. For the carotid studies, I elected to use a target dose of 250 MBq. This was in order to reduce noise (which had occasionally been a problem in some of our work with the lower dose) and more importantly to give the same dose to that given in the published literature(88) for the dynamic studies (see below). For details of achieved target doses and uptake time as well as variability, see relevant chapters.

2.3.2.3 CAVD Studies - Scanning

18F-Fluoride

After uptake patients were transferred on to the PET scanning table. Patients were asked to lie supine with their upper limbs abducted above their head. They were connected to a 3-lead ECG monitor, permitting ECG gating of the CT calcium score. Patients were scanned feet first. An attenuation correction CT scan (non-enhanced low-dose 120 kV and 50 mAs, pitch 0.8, field of view 780mm, 5mm slice thickness, 3mm increment, B19f LowDose kernel, standard filtered back projection reconstruction algorithm) was performed. This was followed by a standard 3D static PET acquisition covering two 10-minute bed positions centred over the valve. An ECG-gated, breath-held CT scan (non-enhanced, 40 mAs/rot [CareDose], 100 kV, Pitch 0.24, field of view 210mm, 3mm slice thickness, 1.5mm increment, B35f kernel, standard filtered back projection reconstruction algorithm) was then performed in order to derive aortic valvular and coronary arterial calcium scores.

Patients were then discharged from the CRIC with standardised instructions aimed at minimising close physical contact with infants or pregnant people for 24 hours.

18F-FDG

Scans were conducted similarly with a few variances:

- Patients were asked to relax and move as little as possible in order to reduce skeletal muscle uptake of 18F-FDG.
- All patients were asked to adhere to a carbohydrate-free diet for 24 h prior to their scan in order to suppresses myocardial uptake.
- PET beds were acquired over 15 minutes each (as opposed to 10 minutes for 18F-fluoride)

2.3.2.4 Coronary Studies – Scanning

18F-Fluoride

These studies were conducted similarly to the 18F-fluoride aortic valve scans with the following differences:

- The PET acquisition was made over two 10-minute beds (covering the thoracic cavity) in list-mode. ECG and respiratory monitor data was collected synchronously. This permitted retrospective gating of PET data to minimise the effects of cardiac and respiratory motion ("motion correction").
- Coronary artery calcium assessment and CT coronary angiography were undertaken immediately after the PET acquisition. In brief:
    - Calcium Score: ECG-gated breath-held CT scan (non-contrast-enhanced, 40 mAs/rotation, 120 kV; CareDose, Siemens Medical Systems)
    - Coronary angiogram: 330 ms rotation time, 100 (body mass index [BMI] <25 kg m^{-2}) or 120 (body mass index >25 kg m^{-2}) kV tube voltage, 160-245 mAs tube current, 3.8 mm $rotation^{-1}$ table feed, prospective (heart rate regular and <60 min^{-1}), or retrospective (heart rate >60 min^{-1}) electrocardiogram-gated. Depending on the body mass index, a bolus of 80-100 mL of contrast (400 mgI/mL; Iomeron, Bracco, Milan, Italy) was injected intravenously at 5 mL s^{-1}, after determining the appropriate trigger delay using a test bolus.

18F-FDG

Coronary 18F-FDG PET/CT scans were undertaken as described for aortic valve scans with the addition of the gating strategies described in the immediately preceding section

2.3.2.5 Carotid Studies – Scanning (Static Acquisitions)

18F-Fluoride

After 60 minutes of uptake, patients were positioned on the PET scanner table "head-first" and with their arms by their sides. A rigid neck collar was fitted to reduce movement and standardise position. An attenuation-correction CT scan (non-enhanced, low dose 120 kV, 50 mAs) was performed followed by PET acquisition covering 2 bed positions with the first centred over the carotid bifurcation. Data were acquired in 3-dimensional mode for 20 minutes (10 minutes per bed). A CT carotid angiogram was then performed without moving the subject (Care Dose 4D, 120 kV, 145 mA, rotation time 0.5 seconds, pitch 0.8. Contrast: 50 mL Niopam 370).

18F-FDG

Patients were fasted for 6 hours before scanning. Scanning took place as above but with 15 minutes per bed position and no angiogram was obtained.

2.3.2.6 18F-fluoride Dynamic Acquisitions

A subset of patients (n=5) underwent fully dynamic PET acquisitions. Of these five, three had an arterial cannula sited in their right radial artery.

Patients had an intra-venous cannula sited and a right sided radial arterial catheter sited using an aseptic standard technique (Seldinger for arterial line). Baseline samples were drawn off from the venous cannula as above as well as a separate pre-injection sample from the radial line. The radial line was connected via a length of tubing to an Allogg ABBS device (see figure 2.1; Allogg AB, Mariefred, Sweden). This device (see figure) comprises a non-reversible peristaltic pump, shielded radiation detector (itself comprised of a scintillation crystal made of bismuth germanate, a photomultiplier and amplifier) and data logger (connected to an in-built PC). By drawing blood continuously (at 5 mL $s^{-}1$) through the detector, the device permits the measurement (at high temporal resolution) of the arterial blood radioactivity as it varies with time. This

(certainly for simple radiotracers such as 18F-fluoride that are not metabolised) gives an excellent assessment of the pharmacokinetics of the tracer and more importantly allows the investigator to derive an exact input function for driving models of radioisotope binding. It is the gold-standard for truly quantitative PET. The continuous sampling only occurs for the first 15 minutes as this is when the variation in blood radioactivity is at its highest (the pattern is of an immediate rise to peak activity and then an exponential decay – see Chapter 6) and also limits blood loss.

Figure 2.1 | The Allogg ABSS

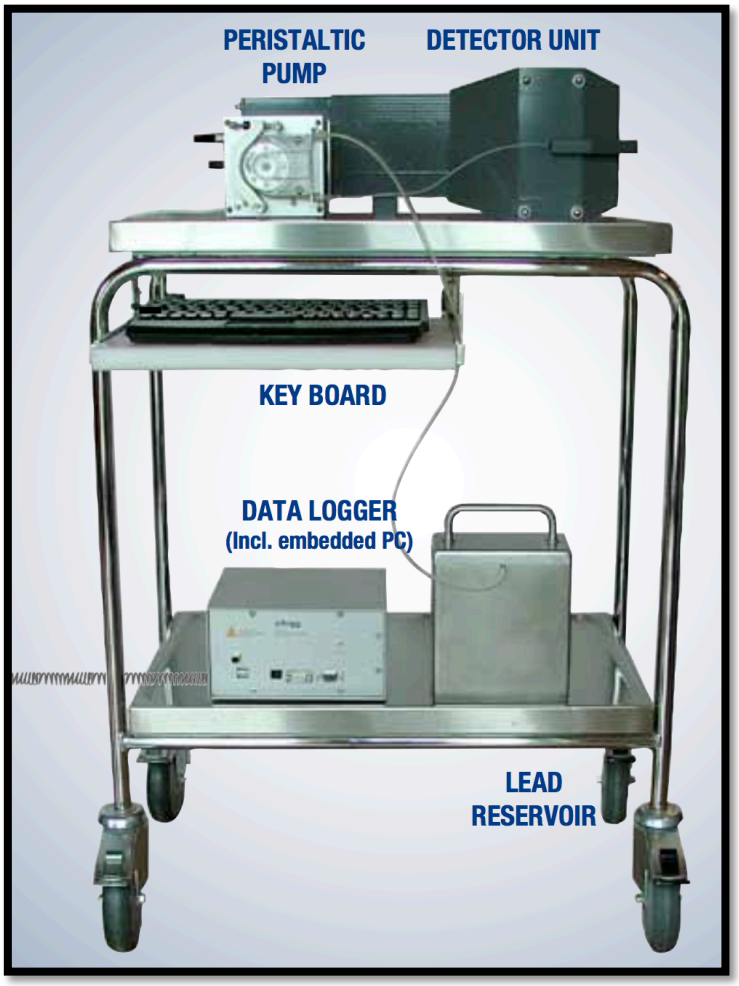

Image reproduced from manufacturer's brochure

The patient was then positioned supine with the head and neck immobilised with a rigid neck collar. An attenuation correction CT scan was obtained (as above). The Allogg device and PET acquisition was then commenced synchronously. PET acquisition was in list mode (with the single bed centred on the carotid bifurcation). A few seconds after the initiation of blood sampling and scanning the 18F-fluoride was injected into the patient. Scanning continued for 80 minutes. Arterial blood samples were taken at regular intervals. Figure 2.2 shows an example of an experiment in action. At the end of the scan, the patient was discharged as previously described. The baseline and multiple post-injection arterial samples were then taken to a separate lab in a shielded container. 1 mL Aliquots of whole blood were pipetted into dedicated sample tubes and placed in the Gamma counter cassette. The remaining blood was then centrifuged (10-15 mins at 2,000G) and matching plasma aliquots were pipetted into tubes and added to the cassette. The cassette was then loaded into the Gamma counter and the sample assayed. Great care was taken throughout the experiment to ensure the timings (PET, Allogg, samples) were documented and synchronised. The final radioactivity measurements were then decay corrected to the beginning of the scan (as the PET data are) and used to calibrate the initial 15 minutes of data from the Allogg device. Finally, a decay corrected truly arterial plasma input function curve was derived and used to perform the pharmacological analyses described in Chapter 5.

Figure 2.2 | A Fully Dynamic 18F-fluoride PET Study

Arterial blood sampling in progress. A typical curve can be seen on the monitor.

2.3.3 Image Reconstruction and Motion Correction/Compensation

2.3.1 CAVD

Static PET scans were reconstructed using the Siemens Ultra-HD algorithm. This algorithm incorporates time-of-flight data. No motion correction or compensation was undertaken in this early study.

2.3.2 Coronary

When imaging very small structures, such as coronary arteries, the presence of tissue motion can severely degrade visual image quality and quantitative data. The only practical method available at the time of study for PET motion correction/compensation was gating. This technique involves discarding PET data which is obtained during portions of the cardiac and/or respiratory cycles associated with excessive tissue movement. Therefore, only co-incidences sampled when the tissues are relatively static are used to develop the sinograms and reconstruct the PET images. Although the PET scans in the coronary cohort were acquired with the potential for correction of both respiratory and cardiac motion, including respiratory gating led to the loss of excessive amounts of co-incidence events and the statistical noise increased to unacceptable levels. Therefore, only electrocardiogram-gated cardiac motion correction was undertaken. The scans were reconstructed using data only from the diastolic phase (50–75% of the R-R interval). The Siemens Ultra-HD algorithm was used.

2.3.4 Carotid

Static and dynamic PET scans were reconstructed using the Siemens Ultra-HD algorithm. No motion correction or compensation was required beyond the use of a rigid neck collar. The co-incidence events in the dynamic data sets were parsed into time bins in the manner described by Frost and colleagues in their studies of 18F-fluoride uptake in bone.(88)

2.4 Ex Vivo & In Vitro Techniques

2.4.1 Tissue Sampling

Tissue specimens (aortic valve and carotid endarterectomy specimens) were retrieved at the moment of surgical excision in the operating room. They were handled in a sterile manner, carefully oriented and then photographed for gross morphological analysis (see figure 2.3 for example). They were then snap frozen in liquid nitrogen, placed in a sterile container and transferred to a -80°C fridge for subsequent batch processing and analysis.

Figure 2.3 | Example Of Excised Carotid Plaque

2.4.2 Histology

All specimens were processed and analysed in a core laboratory by a team of permanently employed expert technical staff (SuRF, Edinburgh University, Edinburgh). Specimens were retrieved from the -80°C fridge, thawed and then processed as required by the relevant experiment (see Results chapters for details). Gentle de-calcification was undertaken when necessary and appropriate (i.e. when no staining for calcium or phosphate was to be undertaken) using ethylenediaminetetraacetic acid (EDTA). This permitting specimen mounting in paraffin and standard microtome sectioning. When staining for mineral, specimens were not decalcified but rather embedded in OCT Compound (Optimal Cutting Temperature Compound) and then sectioned on a dedicated cryostat (details found in Chapters 3, 6 & 7). This naturally resulted in sub-optimal sectioning (given the variance in hardness between the hard and soft elements of the tissue samples) but was absolutely necessitated by the nature of the experiment. The use of methylmethacrylate embedding was considered but owing the cost, in terms of the potential negative effects of subsequent antibody binding, a decision was made to use cryostat sectioning.

Commonly used histological stains for general tissue structural analysis were:

- Haematoxylin and eosin
- Masson's Trichrome
- Movat's Pentachrome

Histological stains for calcification were:

- Alizarin Red (mineral calcium)
- Von Kossa (Phosphate)

All staining was executed following standardised protocols. For details please refer to the relevant results Chapters.

2.4.3 Immunohistochemistry

Specimens were prepared and sectioned as for histological analysis. For most immunohistochemical processing an automated system (BOND robot, Lecia Biossytems, Nussloch, Germany) was used (exception – data presented in Chapter 6; staining for these batches was done by hand). Secondary antibody reporting employed the horseradish peroxidase method.

A wide variety of antibody targets were employed. For details, please refer to the relevant Chapters. Examples with their "targets" include:

- Anti-CD68 – Macrophages
- Anti-smooth muscle actin – Arterial media
- Anti-CD31 – Endothelium
- Anti-tissue non-specific alkaline phosphatase – pro-mineralization enzyme
- Anti-cleaved caspase-3 – Apoptosis

Appropriate positive and negative controls were obtained in all cases and non-specific binding of the secondary antibody was always assessed by omitting the primary antibody in a set of parallel experiments.

2.4.4 Autoradiography

Autoradiography is a technique employed to assess the 2-dimensional spatial binding distribution of a radiolabelled agent (usually a tritiated biomolecule but in this body of work, the positron emitting isotope 18F-fluoride) within a sample of tissue at the histological to naked eye level of magnification. Briefly, the specimen of interest (which in this work was either a section or a whole specimen then subsequently sectioned) was incubated in a standardised solution of 18F-fluoride for a specified period of time (see Chapters 3, 5, 6 & 7 for details). The sample was then rinsed several times and placed on a freshly blanked phosphor screen. An overnight exposure was then undertaken (mainly to minimise operator dose). The screen was then read using a FujiFilm FLA-5100 Fluorescent Image Analyser (Raytek Scientific Limited, Sheffield, UK) in Edinburgh or a PerkinElmer's Cyclone Plus Phosphor Imager (Waltham, Massachusetts) in Cambridge. Images were then be registered to adjacent sections stained for a variety of epitopes/tissue structural components and comparisons drawn. An example from some calcified arterial tissue is shown in figure 2.4.

Figure 2.4 | 18F-Fluoride Autoradiography

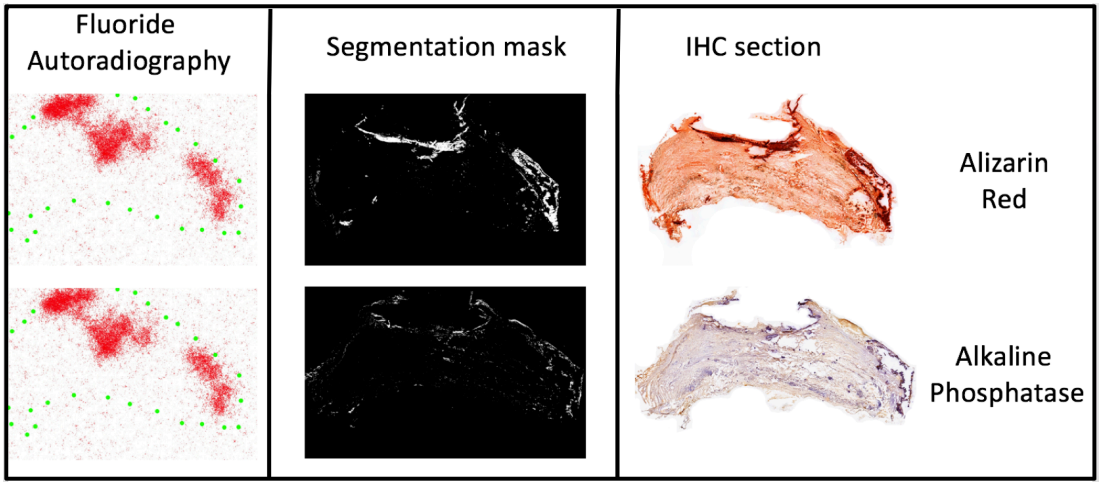

IHC, immunohistochemistry

2.4.5 Ex Vivo PET/CT using Clinical Scanner

For a set of experiments described in Chapter 5, a clinical hybrid PET/CT scanner (Biograph mCT, Siemens Medical Systems, Erlangen, Germany) was used to perform *ex vivo* 18F-fluoride PET/CT of carotid endarterectomy specimens. The aim of this experiment was to gain an appreciation for the 3-dimensional distribution of 18F-fluoride uptake within a carotid plaque thus permitting us to:

1. Assess the relation between CT visible calcium deposits and 18F-fluoride uptake
2. Parse the specimens into regions of relatively high and low 18F-fluoride uptake and analyse these regions histologically and immunohistochemically.

A clinical system was used because at the time we did not have a micro PET/CT system installed (see next section). Briefly, endarterectomy specimens were incubated in a clinically relevant concentration of 18F-fluoride for 60 minutes before being serially rinsed in PBS (see Chapter 5 for details). Specimens were photographed in situ on the scanning table (to confirm orientation and avoid confusion when looking at the PET images) and then scanned. Examples of PET/CT images and photographed specimens are shown in Figure 2.5.

Figure 2.5 | Ex Vivo Clinical PET/CT Scanning Of Carotid Plaque Specimens

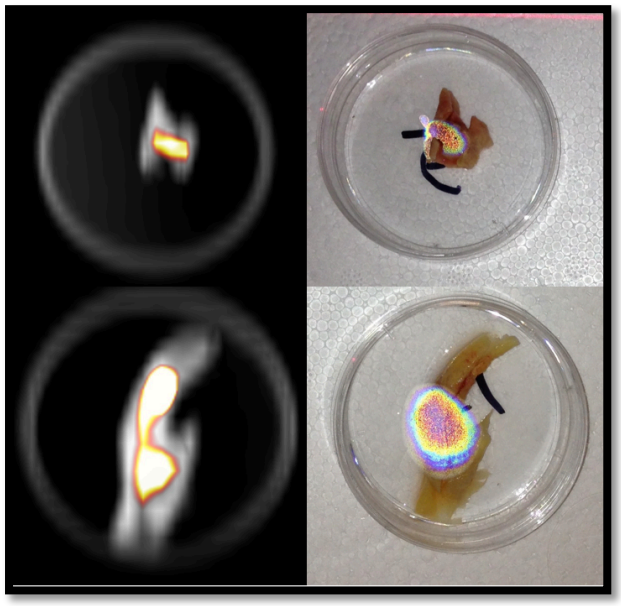

Specimens were then divided into segments that showed comparatively high or low 18F-fluoride uptake prior to being decalcified in EDTA (in this instance) and then processed as described in the histology section above and in Chapter 5 where more detail can be found.

2.4.6 Micro PET/CT

Although the *ex vivo* clinical PET/CT system experiments yielded interesting and useful results (Chapter 5), the experiments were limited by the fundamentally achievable resolution of clinical PET and CT systems. The natural next step was to use a higher resolution pre-clinical system (NanoScan PET/CT (Mediso, Budapest, Hungary). The resolution of the clinical PET system we used is estimated at 4 mm, the NanoScan has a quoted resolution of 0.5 mm; nearly an order of magnitude higher. This would permit me to explore in much greater detail the relationship between CT visible calcium and 18F-fluoride uptake as well as perform a higher resolution analysis of the spatial distribution of 18F-fluoride within a carotid plaque and the relationship with important molecular markers of plaque pathology (e.g. enzyme markers of calcification and inflammation).

Figure 2.6 | NanoScan Preclinical micro PET/CT System

From Mediso device brochure

The micro PET/CT experiments were very similar to those using the *ex vivo* clinical PET/CT. Scanning was carried out in separate experiments on the same system in Cambridge (Chapter 6) and Edinburgh (Chapter 7). In brief, after

incubation in 18F-fluoride and rinsing, specimens were placed in sealed plastic tubes and then loaded into the micro PET/CT scanner. PET data were acquired over 30 min in list mode. Data were reconstructed using a 3D ordered-subset expectation-maximization (OSEM) algorithm. The final images were isotropic with 300 μm voxels.

Two sets of micro CT were performed immediately after micro PET acquisition, using high and low zoom. Images were reconstructed using a modified cone beam filtered-back projection method. Micro PET and micro CT data were co-registered using previously established default shifts and then analysed. For more detail, please refer to Chapters 5 and 7.

2.4.7 In Vitro Pharmacology Studies

To study the pharmacological properties of 18F-fluoride, two principle sets of experiments were undertaken (these studies were conducted in Cambridge).

2.4.7.1 Electron Microscopy

In order to test the hypothesis that 18F-fluoride binds to specifically to calcium hydroxyapatite and not to other targets within plaque we used an electron probe micro analyser to directly measure the presence of fluoride (non-radioactive) within calcified and soft tissue areas of carotid endarterectomy specimens. As described above, undecalcified carotid plaque specimens were mounted in OCT compound and sectioned using a cryostat. Sections were placed on custom-made Melinex discs and allowed to dry. Sections were incubated with sodium fluoride (non-radioactive). Sections were then rinsed in distilled water and allowed to dry. The discs were stuck to scanning electron microscope stubs and coated with carbon in an Edwards Auto 306 evaporative carbon coater. Imaging was carried out using a Philips FEI XL-30 FEG scanning electron microscope. Spectra were collected using an Oxford Instruments SiLi atmospheric thin window detector running INCA software (ETAS Group, Stuttgart, Germany). Hydroxyapatite standards were also scanned as positive controls. Areas of soft and "hard' tissue were scanned within the specimen and fluoride quantity compared between areas of macro- (>50 μm diameter) and micro- (<50 μm diameter) calcification were compared. Details are found in Chapter 6.

2.4.7.2 Gamma Counter

In order to explore the pharmacodynamic and pharmacokinetic properties of 18F-fluoride three experiments were undertaken.

1. Concentration–response curves were derived by exposing carotid sections to increasing concentrations of 18F-fluoride prior to washing

and then assay in a gamma counter (Packard Cobra II E5003, GMI, Ramsey, Minnesota).

2. To derive association curves, whole carotid specimens were taken out of an incubating solution of 18F-fluoride at set time points. Specimens were then washed in PBS and assayed in the gamma counter. Mean decay-corrected activity was then plotted against time.

3. For dissociation, following incubation in 18F-fluoride, specimens were continuously washed in PBS and assayed at set time points using the gamma counter. Again, mean decay-corrected activity was plotted against time.

Exact details of these experiments are set out in Chapter 6.

2.5 Image Analysis

2.5.1 Clinical PET

2.5.1.1 Static PET

Analysis of static clinical PET data was undertaken in all studies using Osirix (OsiriX 64-bit; OsiriX Imaging Software, Geneva, Switzerland). PET data (18F-fluoride or 18F-FDG) were examined and then fused to relevant CT datasets. It the automated fusion was not adequate, manually adjustments were made. Regions of interest (ROI) were then drawn around the anatomy of interest on the CT dataset. ROI were then transferred to the PET data set and the voxel by voxel SUV data extracted and recorded.

The exact analysis method for the aortic valve has been published previously. (101) In brief, the PET and CT volumes were reoriented so that the valve could be assessed axially. ROI were then drawn around the perimeter of the valve or the centre of the valve (only for 18F-FDG to avoid myocardial spillover). In an update to the original analysis, we also limited the extent of ROI used in the *z*-axis to 3 slices (centred on the slice with the highest voxel of activity) to try and avoid "diluting" the signal from the valve as well as improve reproducibility. We called this technique "most diseased segment" or MDS and used it for the coronary and carotid analyses as well (see figure 2.7). Three main parameters were extracted:

1. Max SUV – The SUV from the voxel with the highest uptake in all three regions
2. Mean Max SUV – the average of the highest single voxel from **each** region
3. Mean SUV – the average from all voxels within all regions

These variables were (from valve/carotid/coronary) were then indexed to the blood pool SUV to calculate TBR as described in the introduction. Blood SUVs were derived from the superior vena cava in most circumstances. More detail for aortic valve analysis can be found in Chapter 3.

Carotid and coronary analysis was undertaken in a similar manner. ROI were drawn around the adventitial borders of the arterial segment or plaque of interest. Further detail on analysis methodology for the carotid and coronary analysis can be found in Chapters 5 and 7 respectively. An example of carotid analysis is shown below.

Figure 2.7 | Derivation of Plaque Max, Mean Max and Mean SUV by MDS Method

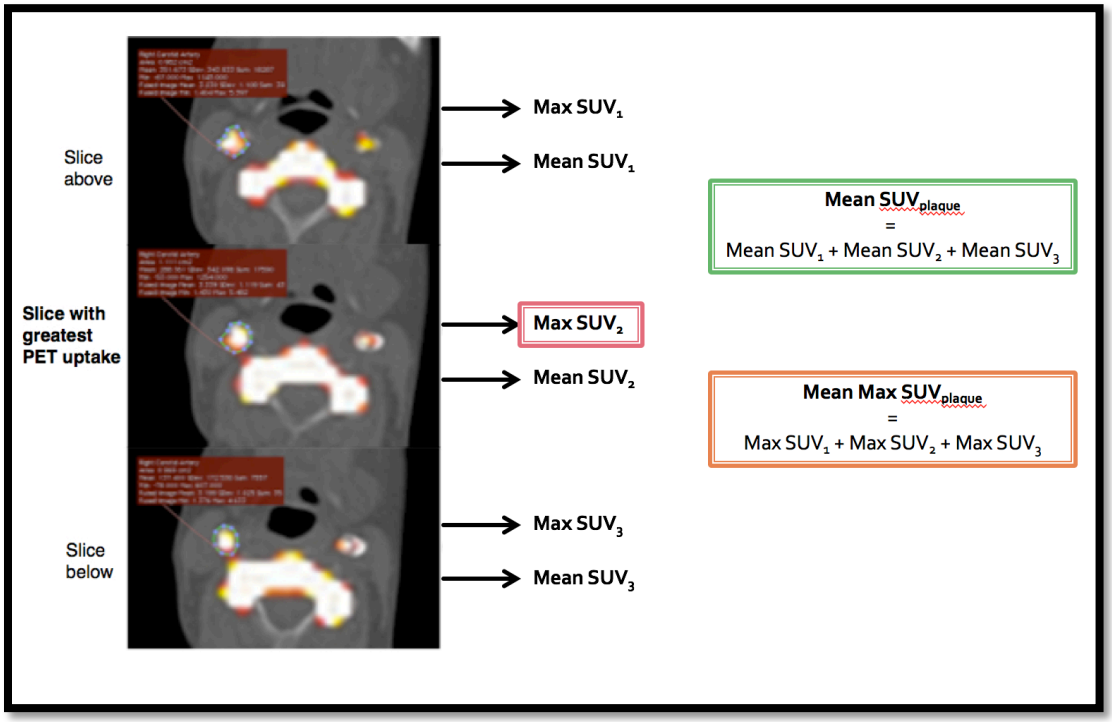

Three main variables were extracted per plaque – the single voxel of highest value (red box), the average of the highest voxels from each slice (mean max, orange box) and the average of all voxels with the three regions of interest (green box).

PET, positron emission tomography; SUV, standardised uptake variable

2.5.1.2 Dynamic PET

Dynamic analysis was undertaken using the industry and research standard software, PMOD (PMOD v3.408, PMOD Technologies LLC, Zürich, Switzerland). Dynamic PET datasets were time binned as per Frost and Hawkins (12 x 10 s, 4 x 30 s, 12 x 240 s) (79,88) and uploaded onto the PMOD workstation. When available, directly measured plasma activity curves (see 18F-fluoride Dynamic Acquisitions section) were formatted for compatibility with PMOD and also uploaded. Dynamic and CT datasets were then registered automatically (and nudged if required using obvious fiducial markers – cervical spine, mandible, calcified plaque). Volumes of interest were then drawn on the tissues of interest (plaque at the carotid bifurcation or a vertebral body) and tissue activity curves generated. For subjects where no blood sampling was available, plasma activity curves were estimated by using an image-derived input function. In order to generate these, volumes of interest were drawn within the lumen of the proximal common carotid artery.

For analysis, the image data were first reviewed for evidence of 18F-fluoride uptake, image quality and patient movement. The CT angiogram was scrutinized for plaque presence, location and characteristics. The PET data were then resliced as part of automated registration to the CT data. Volumes of interest were then generated by drawing regions of interest on sequential axial slices on the registered data sets. Volumes were drawn to separately incorporate internal carotid artery plaque (where present) and a vertebral body. Vertebral data were obtained as a comparator and also as a way of ensuring our data were commensurate with the work of others. Tissue activity curves were then generated and assessed and Patlak(111,112) analysis undertaken using the relevant software bolt-on. More detail is available in Chapter 6.

2.5.2 Clinical CT

2.5.1.1 Calcium Scores

Evaluation of the aortic valve, coronary and carotid calcium scores was performed using calcium score analysis software (Vitrea, Vital Images, Minnetonka, USA). Vessel specific and total Agatston calcium scores were derived. The Agatston score was calculated in Agatston units (AU) by multiplying the area of a region of interest by a weighting factor selected dependent on the peak signal within the region of interest. Vessel and total scores were obtained by adding the weighted scores.

2.5.1.2 Carotid Plaque Analysis

CT plaque analysis was also undertaken on a dedicated software platform (Vitrea, Vital Images, Minnetonka, USA) using the methodology specified by the manufacturer. Briefly, a vessel centre line was created semi-automatically and then adjusted manually. Separate circles were then generated and adjusted around the adventitial and lumen borders of the vessel. Plaques were then parsed into calcified, fibrofatty or necrotic segments using standardised Hounsfield unit ranges. The absolute volumes and percentage volumes of these segments were then calculated and recorded. Other parameters such as plaque burden, diameter stenosis and remodelling index were also calculated and recorded. An example is shown in Figure 2.8.

Figure 2.8 | Screen Grab From CT Carotid Plaque Analysis

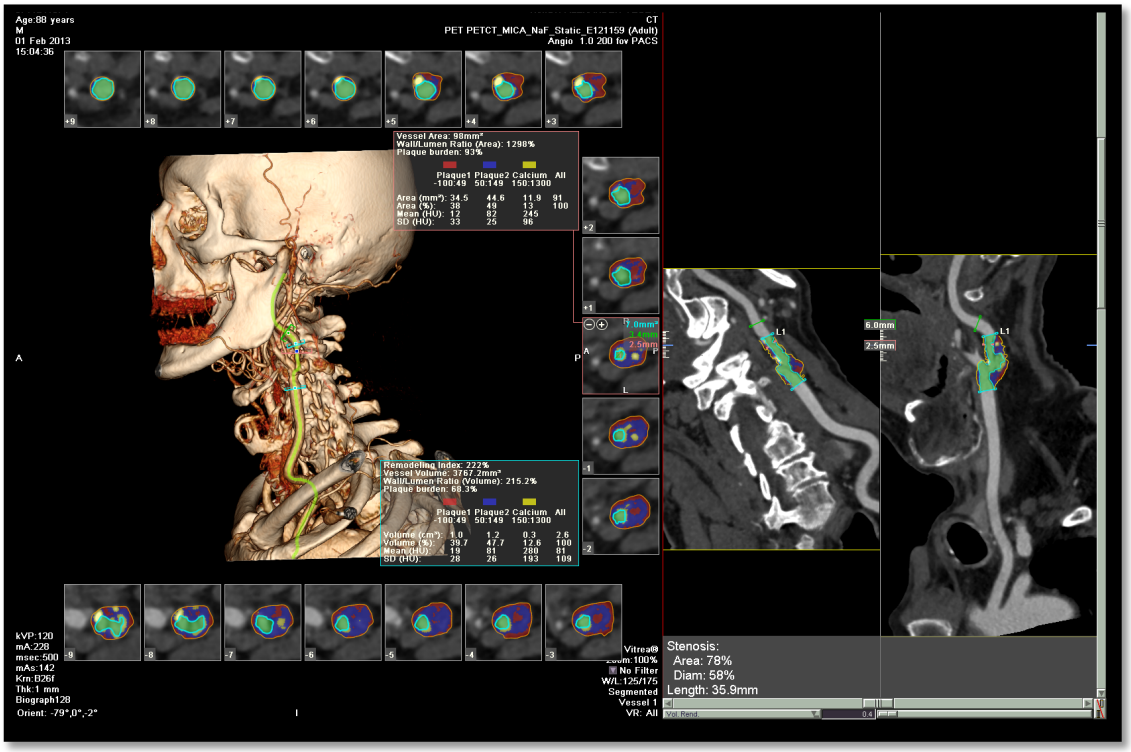

The curved planar reformat of the vessel of interest is shown on the right. On the left, the vessel is shown in three-dimensional context. The multiple cross-sectional images show the circles marking the boundary of the adventitia (red) and the lumen (blue/green). The data output is also seen in the boxes touching the three-dimensional image.

2.5.3 Micro PET/CT

3D images after data reconstruction were analysed using VivoQuant version 1.23, (InviCRO, Boston, Massachusetts) software. Files were cropped to reduce file size and remove experimental artifacts from matter outside the specimen. Once an image containing only the signals associated with the carotid was achieved, the colour intensities of both modalities were manually adjusted to match the histology and autoradiography signals as closely as possible. After that, the "Distance/Annotation" function was selected and 5–8-mm linear transects were made across slices in the transverse plane of carotids. The raw data were then downloaded and graphs showing micro CT densities and micro PET units along the transect lines were later reconstructed with Matlab (Mathworks, Natick, Massachusetts). To quantify PET+/CT-, PET+/CT- and PET-/CT+ regions in 3D, the "3D ROI Tool" function was selected. First, micro PET data were thresholded using the Otsu method to delineate the extent of PET+ signal. On the micro CT data we defined densities over 1000 Hounsfield Units (HU) as calcification. To detect PET+/CT+ signal, we selected PET+ delineated 3D areas and used Global thresholding for voxels ≥1,000 HU of the micro CT data in this area. To detect PET-/CT+ areas, we selected all remaining micro CT data and applied the ≥1,000 HU Global threshold. The data were downloaded and analysed with Microsoft Office Excel (Microsoft, Redmond, Washington).

2.5.4 Immunostaining and Autoradiography

For aortic valve and carotid analyses presented in Chapters 3, 4 and 5, immunohistochemical images were taken on a Zeiss Axioskop2 fitted with an Axiocam MRc digital camera using Axiovision software. Total vessel and plaque cross-sectional area was calculated using Image Pro Plus 5 (Rockville, MD, USA). Staining was quantified by a using a colour combination that only detected the brown DAB stain. This was set as a manual threshold value, irrespective of intensity. Immunohistochemical markers were expressed as number of cells per mm^2 or percentage staining of total cross-sectional area.

For the data in Chapter 6, two-dimensional histological, immunohistochemical and autoradiography image analysis was performed using ImageJ/Fiji (NIH, Bethesda, Maryland) and various relevant plug-ins (TurboReg33, JACoP34, Analyze Particles, etc.). Correlation between histology (Alizarin Red) sections and autoradiography images was achieved by using thresholded binary images of the different signals. These thresholded images were also filtered with Gaussian blur and thresholded again, to create segmentation masks that overcome the issue of inherent resolution differences between histology and autoradiography.

DAB-stained immunohistology (i.e. CD68, CD31 etc.) sections were analysed in a manner similar the that described for the aortic valve analyses. Autoradiography images were resized to match the size of the immunohistology images.

All two-dimensional histology images were subjected to background subtraction and histogram equalization.

More details are documented in Chapters 3, 4, 5, 6 and 7.

2.6 Statistics

Throughout this thesis, continuous variables are expressed as either mean ± standard deviation for normally distributed data and median (interquartile range; IQR) for skewed distributions. 95% confidence intervals are quoted when relevant. Normality was visually assessed using a frequency histogram and confirmed or refuted with the D'Agostino-Pearson omnibus test. Where possible non-parametric datasets have been log-transformed to achieve normality and permit the use of parametric tests.

Comparison of two continuous datasets was undertaken with either a paired or unpaired t-test for parametric data or the Wilcoxon matched pairs or Mann-Whitney U test for non-parametric data. Correlation between two continuous datasets was undertaken with either Pearson's *r* or Spearman's Rho again subject to the normality of the variables tested.

Categorical data are presented as n (%) and were compared when appropriate using a contingency table and Fisher's exact test or the χ^2 test.

To assess inter and intra-observer reproducibility the intra-class correlation coefficient (ICC) was calculated and Bland-Altman analysis undertaken. For repeatability of categorical/ordinal datasets Cohen's kappa coefficient was calculated

Adjusted and unadjusted Cox regression models were employed in one analysis to explore the relationship between PET uptake and clinical end points.

Statistical analyses were performed with the use of Graph Pad Prism version 6.0 (GraphPad Software Inc, California, USA), SPSS version 18 (SPSS Inc, Chicago, IL) and RStudio version 0.98.501 (2013).

Statistical significance was taken as two-sided $P < 0.05$. Advice was sought when required from a statistician. More details are nested within relevant sections of the data chapters.

Chapter 3 – 18F-Fluoride And 18F-FDG Hybrid Positron Emission Tomography And Computed Tomography In Calcific Aortic Valve Disease – Mechanisms Of Action; Histological And Clinical Imaging Based Validation

3.1 Publication in Context

3.1.1 Background

Dr Marc Dweck's original doctoral work was centred on the "Ring of Fire Study"(8,113). This was a prospective observational controlled cohort study carried out at Edinburgh University and the Royal Infirmary of Edinburgh. The study experimental participants were patients with aortic stenosis (of varying degrees of severity) already enrolled in a clinical surveillance program. The control patients were age and sex matched individuals without aortic stenosis. Subjects were scanned using clinical PET/CT with 18F-FDG and 18F-fluoride.

The three aims of the original study were as follows:

1. To test the feasibility of using 18F-FDG and 18F-fluoride PET/CT to assess CAVD.
2. To establish technique repeatability.
3. To undertake an *in vivo* pathobiological assessment of the relative importance of inflammation and calcification at different stages of the CAVD.

The results of this work, specifically focused on the aortic valve, have been published(8) and described in the introduction to this thesis. In brief, the study showed that aortic valvular PET/CT was feasible, repeatable and that radiotracer uptake correlated with traditional imaging biomarkers of disease severity. 18F-fluoride appeared to perform better than 18F-FDG.

3.1.2 Aims of Further Study

Dr. William Jenkins and I undertook to perform a follow-up study exploring the potential mechanisms of valvular 18F-FDG and 18F-fluoride uptake and how they might explain the findings of the original report. We aimed to use histological and immunohistochemical experiments to validate the radiotracers as well as *in vivo* follow-up scans to address this question. We also asked: would 18F-FDG or 18F-fluoride uptake predict imaging defined disease progression?

3.1.3 Contributions

The work described in this paper was undertaken as a joint effort between Dr Dweck, Dr Jenkins and I. Dr Dweck provided the baseline data from his original work and supervised Dr Jenkins and I in the subsequent work. Dr Jenkins and I both collected the follow-up data for the patients, devised and executed the histological, immunohistochemical and autoradiography experiments and the subsequent analyses. We carried out the statistical analysis and drafted the paper.

Published as: Dweck MR, Jenkins WSA, **Vesey AT**, Pringle MAH, Chin CWL, Malley TS, et al. 18F-Sodium fluoride Uptake Is a Marker of Active Calcification and Disease Progression in Patients With Aortic Stenosis. *Circulation: Cardiovascular Imaging* 2014 Mar 18;7(2):371–8.

3.2 Abstract

3.2.1 Background

18F-Sodium fluoride (18F-fluoride) and 18F-Fluorodeoxyglucose (18F-FDG) are promising novel biomarkers of disease activity in aortic stenosis. We compared 18F-fluoride and 18F-FDG uptake with histological characterization of the aortic valve and assessed whether they predicted disease progression.

3.2.2 Methods

Thirty patients with aortic stenosis underwent combined positron emission and computed tomography using 18F-fluoride and 18F-FDG radiotracers. In 12 patients undergoing aortic valve replacement surgery (10 for each tracer), radiotracer uptake (mean tissue/background ratio) was compared with CD68 (inflammation), alkaline phosphatase, and osteocalcin (calcification) immunohistochemistry of the excised valve.

3.2.3 Results

In 18 patients (6 aortic sclerosis, 5 mild, and 7 moderate), aortic valve computed tomography calcium scoring was performed at baseline and after 1 year. Aortic valve 18F-fluoride uptake correlated with both alkaline phosphatase (r=0.65; P=0.04) and osteocalcin (r=0.68; P=0.03) immunohistochemistry. There was no significant correlation between 18F-FDG uptake and CD68 staining (r=−0.43; P=0.22). After 1 year, aortic valve calcification increased from 314 (193–540) to 365 (207–934) AU (P<0.01). Baseline 18F-fluoride uptake correlated closely with the change in calcium score (r=0.66; P<0.01), and this improved further (r=0.75; P<0.01) when 18F-fluoride uptake overlying computed tomography–defined macrocalcification was excluded. No significant correlation was noted between valvular 18F-FDG uptake and change in calcium score (r=−0.11; P=0.66).

3.2.4 Conclusion

18F-fluoride uptake identifies active tissue calcification and predicts disease progression in patients with calcific aortic stenosis.

3.3 Introduction

The mechanisms underlying aortic stenosis (AS) remain incompletely understood, and the accurate prediction of disease progression remains a challenge. (114) Calcification and inflammation are thought to play key pathophysiological roles. Indeed, the amount of established calcium in the valve correlates with disease severity and predicts future adverse cardiovascular events. (115,116) Although computed tomography (CT) and echocardiography can provide measures of established valvular calcification, they cannot directly assess ongoing calcification activity, which is considered to be the main driver of disease progression.

Recent reports have investigated two positron emission tomography (PET) radiotracers, 18F-sodium fluoride (18F-fluoride) and 18F- fluorodeoxyglucose (18F-FDG), as measures of calcification activity and inflammation, respectively, in the aortic valve, (101) coronary arteries, (106,117) and major vessels. (98) 18F-FDG PET has become a widely used tool for the assessment of inflammation in the aorta and carotid arteries, with uptake correlating with macrophage burden. (70) Several studies have investigated its uptake in AS, although histological validation is lacking. (100,101) 18F-fluoride has been used as a bone tracer for >40 years, displaying increased activity in conditions associated with increased bone metabolism such as Paget's disease. In bone, it is thought to bind and then incorporate into exposed hydroxyapatite crystals via an exchange mechanism with hydroxyl groups to form fluorapatite. Given that hydroxyapatite is also a key structural component of calcification in the aortic valve and vascular atheroma, it is presumed that similar mechanisms explain its accumulation in these tissues. However, this remains hypothetical. The principal aims of the present study were, therefore, to validate the use of 18F-fluoride and 18F-FDG in AS by comparing *in vivo* radiotracer uptake with immunohistochemistry of calcification and inflammation in excised valvular tissue and to investigate whether either of these agents predicts disease progression at 1 year.

3.4 Methods

3.4.1 Patient Populations

Two cohorts of patients with AS were recruited into this study

1. 12 patients undergoing valve replacement surgery, and
2. 18 patients with asymptomatic disease under surveillance at the Edinburgh Heart Centre. The latter cohort was randomly selected for repeat scanning from a larger, previously described population who underwent baseline PET imaging. (101,106,118)

All patients were >50 years of age, and exclusion criteria included a normal aortic valve, insulin-dependent diabetes mellitus, end-stage renal failure, life expectancy of <2 years, and metastatic malignancy. Patients with severe AS were excluded from the cohort of patients under surveillance because of the potential for disease progression and symptom development before the follow-up 1-year scan. The study was performed in accordance with the Declaration of Helsinki and after local research ethics committee approval. All patients provided written informed consent before participating.

3.4.2 Baseline Assessment

All patients underwent full clinical assessment at baseline, and AS severity was assessed using Doppler and 2-dimensional echocardiography by means of the peak transvalvular velocity, mean gradient, and aortic valve area according to American Heart Association/American College of Cardiology guidelines. (119) Aortic sclerosis was defined as thickening of the aortic valve cusps in the absence of accelerated flow (<2 m/s) through the valve. Combined PET and CT scans of the aortic valve were performed using a hybrid scanner (Biograph mCT; Siemens Medical Systems, Erlangen, Germany) 60 minutes after administration of 125 MBq of 18F-fluoride. Subsequently, a second PET/CT scan was performed using the same hybrid scanner 90 minutes after administration of 200 MBq of 18F-FDG. Glucose is a major energy source of the myocardium, so that intense 18F-FDG uptake frequently occurs, spilling over and contaminating

the signal in the valve. We attempted to reduce myocardial uptake by asking patients to avoid carbohydrates for 24 hours before their 18F-FDG scan, thereby switching the myocardium from glucose to free fatty-acid metabolism. Myocardial 18F-FDG uptake was assessed within regions of interest (ROIs) placed in the basal septum of the left ventricle and classified as being adequately suppressed if mean standard uptake values were <5.0. (120) An ECG-gated breath-hold CT scan (non-contrast enhanced, 40 mA/rot [CareDose]; 100 kV) was performed for calculation of the aortic valve calcium score using dedicated analysis software (VScore; Vital Images, Minnetonka, MN) on axial scans. (23) Particular care was taken to differentiate valvular calcium from that in the aortic root and mitral valve annulus. (117) At 1-year follow-up, patients in the surveillance cohort underwent repeat clinical asessment and CT calcium scoring using the same protocol.

3.4.3 Quantification of Aortic Valve PET Activity

18F-fluoride and 18F-FDG uptake in the aortic valve was quantified using an OsiriX workstation (OsiriX version 3.5.1 64-bit; OsiriX imaging Software, Geneva, Switzerland) as reported previously. (120,121) Briefly, fused PET-CT images were reoriented into the plane of the valve and circular ROIs drawn on adjacent 3-mm slices until the entire valve had been examined. For 18F-fluoride, ROIs were placed around the perimeter of the valve while excluding the aortic root (whole-valve technique). To reduce the potential for myocardial 18F-FDG activity contaminating the aortic valve signal, ROIs for this tracer were drawn in the centre of the valve as previously described (centre-valve technique). (100,120) Within these ROIs, mean standard uptake values were calculated for each slice, averaged, and corrected for blood pool activity to provide mean tissue/background ratios. Mean tissue/background ratios were selected prospectively for subsequent comparisons with histology and disease progression because this measure was felt to best represent tracer uptake across the valve as a whole.

3.4.4 Distribution of 18F-fluoride in the Aortic Valve Relative to Calcium Scoring

We undertook a voxel-by-voxel analysis comparing the distribution of calcium on CT with 18F-fluoride uptake. ROIs were drawn around the valve, and each voxel was assessed for the presence of calcium (>130 HU) and increased 18F-fluoride uptake (tissue/background ratio max >1.97 based on the highest uptake in the control cohort of our previous study) (120) using dedicated software MATLAB (Mathworks Inc., Natick, MA). We hypothesized that regions of completely novel calcium development might have an even more important effect on disease progression, and therefore we calculated the percentage of the valve with increased radiotracer uptake in the absence of underlying calcium on CT (% of PET-positive but CT-negative voxels).

3.4.5 Histological Assessment

In the patients undergoing aortic valve replacement, the aortic valve was removed at the time of operation, with care taken to preserve the integrity of the valve architecture. Samples were then fixed in 4% paraformaldehyde for 24 hours. Plaques were decalcified in EDTA for 10 days and embedded in paraffin, and 5-μm sections were prepared. Immunohistochemical staining for osteocalcin (antihuman mouse mAb ab13418; Abcam), CD68 (antihuman mouse clone PG-M1 m0876, DAKO), and tissue nonspecific alkaline phosphatase (TNAP; antihuman rabbit pAb CAT#LF PA50004; Abfrontier) was then undertaken after heat-induced epitope retrieval using a Citrate Buffer pH 6 (Novocastra Leica microsystems) in a decloaking chamber. Osteocalcin staining required no heat-induced epitope retrieval. Sections were stained using a Leica Vision Biosystems Bond-X immunostaining robot. After blocking in peroxide for 10 minutes, sections were incubated with the specific antihuman antibodies for 2 hours at room temperature at the following dilutions: osteocalcin 1:200, TNAP 1:100, and CD68 1:100. All incubation steps were followed by washing in TBS/Tween. Sections for osteocalcin and CD68 were incubated for 15 minutes with pre-polymer/post-primary followed by 15 minutes with polymer (HRP)

for all antibodies before 3,3′-diaminobenzidine visualization and haematoxylin counterstain. Sections were dehydrated in graded ethanol and cleared in xylene before cover slipping in Pertex.

Images were taken on a Zeiss Axioskop2 fitted with an Axiocam MRc digital camera using Axiovision software. Tissue cross-sectional area on each section was manually delineated using Image Pro Plus 5 (Rockville, MD). Immunohistochemical staining for osteocalcin and TNAP was identified by visual assessment and quantified using automated colour-based segmentation by a trained observer blinded to the PET data. Staining was expressed as a percentage of the total valve area. Macrophage infiltration using CD68 was assessed using a similar approach but with an object size set threshold applied at 20×10 pixels to limit counting to cell-sized objects. The density of cell staining in the valve tissue was expressed as cells per square millimetre. This technique was also used to identify cellular staining for TNAP and osteocalcin.

3.4.6 Reproducibility Studies

Inter-observer reproducibility of the immunohistochemical data was investigated. Tissue staining with alkaline phosphatase, CD68, and osteocalcin was quantified in 5 valves independently by 2 trained observers.

3.4.7 Autoradiography

Clinical PET systems have limited resolution. To gain further information about the precise localization of the 18F-fluoride signal in aortic valve tissue, we undertook autoradiography. Non-decalcified valvular tissue was rapidly cooled in dry ice and then sectioned at 7-μm thickness using a cryostat (CM1520; Wetzlar, Germany). Sections for autoradiography were mounted on Superfrost slides (Gerhard Menzel, Braunschweig, Germany) before treatment with spray fixative. Sections were bathed in a solution of 18F-fluoride at a concentration close to in vivo imaging concentrations (1 kBq/mL) for 60 minutes and then rinsed with PBS. A freshly blanked phosphor screen was then placed over the slides and an overnight exposure undertaken. The screen was then read using a

FujiFilm FLA-5100 Fluorescent Image Analyser (Raytek Scientific Limited, Sheffield, UK). Sections adjacent to those used for autoradiography were stained for elemental phosphate (i.e. calcium orthophosphate) using Von Kossa stain, and after surface decalcification *in situ* with Von Ebner solution, for TNAP and osteocalcin. Sections were then manually registered and examined for co-localization with 18F-fluoride signal.

3.4.8 Statistical Methods

Continuous variables were assessed for normality both visually and using the D'Agostino-Pearson test. Variables were expressed as either mean±SD or median with interquartile ranges (IQRs) subject to whether they approximated a normal distribution. Categorical data were presented as n (%). The 95% normal range for differences between sets of immunohistochemical measurements (the limits of agreement) were estimated using Bland–Altman analysis by multiplying the SD of the mean difference by 1.96. (122) Intra-class correlation coefficients with 95% confidence intervals were calculated for inter-observer variation. Baseline and follow-up calcium scores approximated a normal distribution and were compared using a paired t test. However, despite attempts at data transformation, the changes in calcium scores were not normally distributed, and correlations with CT progression data were assessed using Spearman correlation and linear regression analysis. The limitations in using linear regression in the context of a non-normal distribution are acknowledged. A 2-sided $P<0.05$ was regarded as statistically significant. Statistical analysis was performed with the use of Graph Pad Prism version 6.0(GraphPad Software Inc, San Diego, CA).

3.5 Results

3.5.1 Histology Cohort

Twelve patients with symptomatic AS were recruited into the histology cohort (8 men; 76±6 years of age; peak aortic valve velocity, 4.6±0.9 m/s). Patients underwent PET scanning a median of 92 days before surgical aortic valve replacement. Eight patients received both 18F-fluoride and 18F-FDG PET scans. In addition, 2 had a single 18F-fluoride scan, whereas 2 more had a single 18F-FDG scan. Thus, 10 valves were available for the histological validation of each tracer. No patient had a significant perioperative complication (Table 3.1). Effective myocardial suppression of 18F-FDG activity was achieved in 40% (median myocardial standard uptake value, 5.4; IQR, 1.9–10.4).

Table 3.1- Baseline Clinical Data - Histology Cohort

Baseline characteristics	
No.	12
Age, y	76±6
Men	9 (75)
Hypertension	8 (66)
Hyperlipidemia	5 (42)
Ischemic heart disease	4 (33)
Cigarette smoking	1 (8)
Diabetes mellitus	0 (0)
Serum creatinine, μmol/L	87±26
Peak aortic valve velocity (m/s)	4.6±0.9
Aortic valve area, cm^2	0.70 (0.53–0.97)
Mean gradient, mm Hg	48 (44–65)
Aortic valve calcium score, AU	5343 (3114–6292)
Aortic sclerosis	0 (0%)
Mild aortic stenosis	0 (0%)
Moderate aortic stenosis	3 (25%)
Severe aortic stenosis	9 (75%)
Time between 18F-NaF scan and AVR, d	92 (24–345)
Time between 18F-FDG scan and AVR, d	96 (23–331)
18F-FDG dose injected, MBq	200 (193–209)
18F-NaF dose injected, MBq	129 (119–132)
In vivo aortic valve PET data	
18F-NaF uptake (mean TBR)	2.15 (1.98–2.48)
18F-FDG uptake (mean TBR)	1.40 (1.31–1.76)

Categorical data are displayed as n (%). Normally distributed data are displayed as mean±SD. Non-normally distributed data are distributed as median (interquartile range). AVR indicates aortic valve replacement; FDG, fluorodeoxyglucose; 18F-NaF, 18F-Fluoride; PET, positron emission tomography; and TBR, tissue/background ratio.

3.5.2 Immunohistochemistry and Autoradiography

All valve samples displayed positive cellular staining for TNAP (225 cells/mm^2 valve tissue; IQR, 143–328), osteocalcin (130 cells/mm^2 valve tissue; IQR, 85–274), and CD68 (172 cells/mm^2 valve tissue; IQR, 73–271; Figure 3.1; Table 3.2). Extensive TNAP and osteocalcin staining was also observed in the extracellular matrix, occupying approximately a sixth of the valve area sampled (17±5% and 17±7%, respectively; Figure 3.1; Table 3.2).

On autoradiography, 18F-fluoride uptake was observed to co-localise closely with staining for structural calcium phosphate, TNAP, and osteocalcin (Figure 3.1). However, signal was also clearly apparent in areas free of macroscopically visible calcium, thus highlighting the sensitivity of 18F-fluoride in the detection of newly evolving calcification

Table 3.2 | Histology/Immunohistochemistry Data

Histology	Osteocalcin	TNAP	CD68
No.	10	10	10
Mean valve area analyzed, mm^2	234±152	253±116	190±86
% staining of the valve	17±7	17±5	n/a
Positive cellular staining, cells/mm^2	130 (85–274)	225 (143–328)	172 (73–271)
Interobserver reproducibility			
Mean difference	–2.1%	–1.5%	0.8%
Limits of agreement	–13.4% to 9.3%	–8.0% to 5.0%	–7.9% to 9.6%
ICC	0.88 (0.60–0.97)	0.90 (0.35–0.99)	0.99 (0.99–1.00)

Categorical data are displayed as n (%). Normally distributed data are displayed as mean±SD. Non-normally distributed data are distributed as median (interquartile range). ICC as value (95% confidence interval). ICC indicates intra-class correlation coefficient; n/a, not applicable; and TNAP, tissue non-specific alkaline phosphatase.

Figure 3.1 | Histology And 18F-Fluoride Autoradiography Of Excised Aortic Valve Tissue From Patients With Aortic Stenosis.

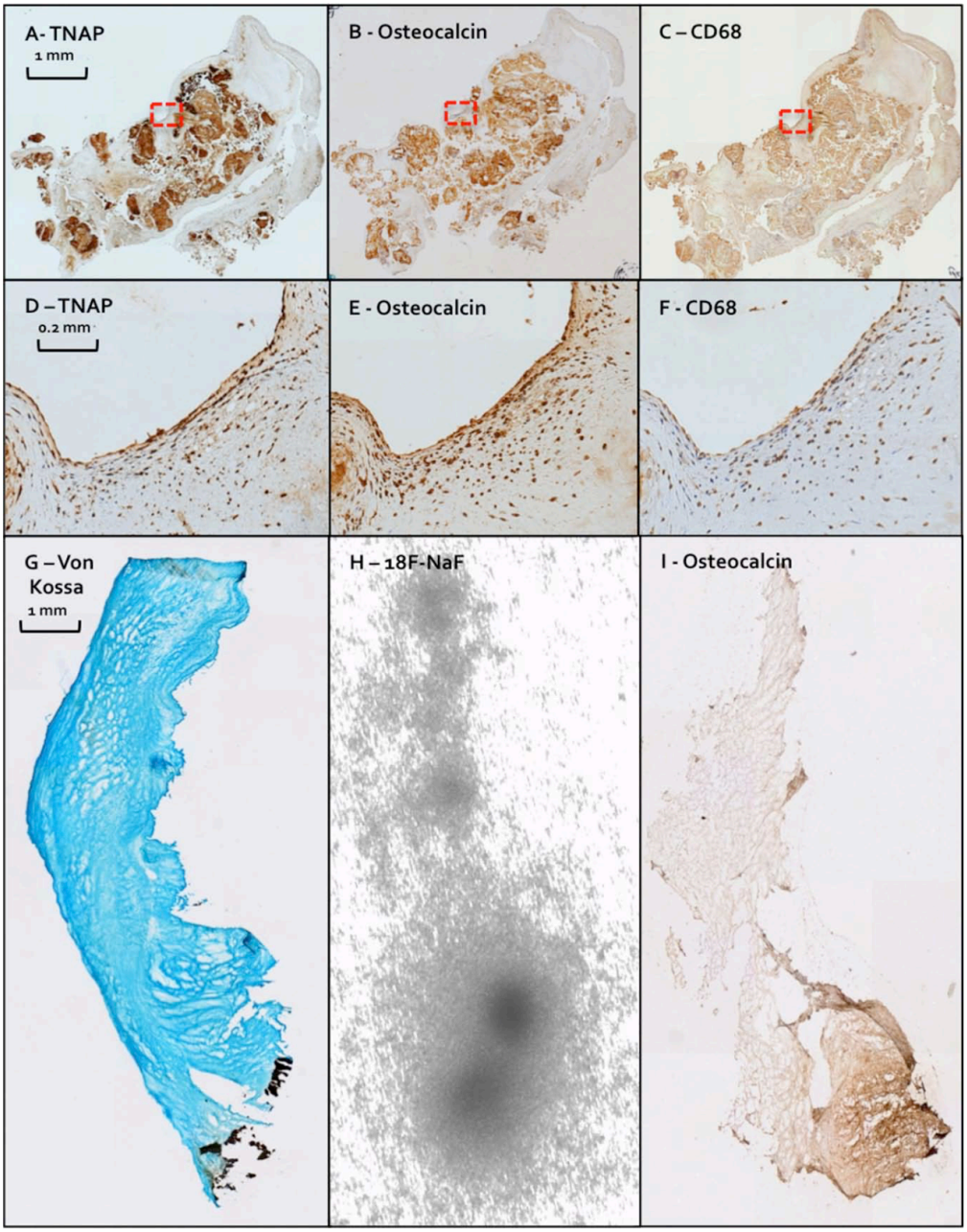

A–F, Fixed, decalcified, and paraffin-embedded aortic valve tissue after exposure to tissue nonspecific alkaline phosphatase (TNAP), osteocalcin, and CD68 antibodies. **A–C**, Widespread positive staining for TNAP, osteocalcin, and CD68 (magnification ×4) in the extra-cellular matrix, which is also observed on an individual cellular level (**D–F**, magnification ×20), respectively. **G-I**, three adjacent and consecutive aortic valve leaflet sections displaying positive immunohistochemical staining for osteocalcin (**I**, magnification ×4) that co-localises to areas of maximal 18F-fluoride (18F-NaF) uptake on autoradiography (**H**). These likely represent areas of ongoing calcification activity, which extend beyond the areas of established calcium identified in black by Von Kossa stain (**G**, magnification ×4).

3.5.3 Reproducibility Of Immunohistochemistry

Inter-observer reproducibility was good for the quantification of osteocalcin and TNAP staining, as well as CD68 cell counting. All observations were characterized by an absence of fixed or proportional biases, narrow limits of agreement (−13.4% to 9.3%, −8.0% to 5.0%, and −7.9% to 9.6%, respectively), and interclass correlation coefficient values of 0.90 (0.35–0.99), 0.88 (0.60–0.97), and 0.99 (0.99–1.00), respectively (Table 3.2).

3.5.4 Correlation With Radiotracer Uptake

There was a good correlation between *in vivo* valvular 18F-fluoride uptake and both alkaline phosphatase (r=0.65 [95% confidence interval, 0.03–0.90]; P=0.04) and osteocalcin (r=0.68 [0.10– 0.91]; P=0.03; Figure 3.2) staining of the excised tissue. In comparison, there was no association between 18F-FDG uptake and CD68 staining in the valve (r=−0.43; P=0.22).

Figure 3.2 | Correlations Between In Vivo Aortic Valve Positron Emission Tomography (PET) Activity And Histological Markers Of Calcification And Inflammation

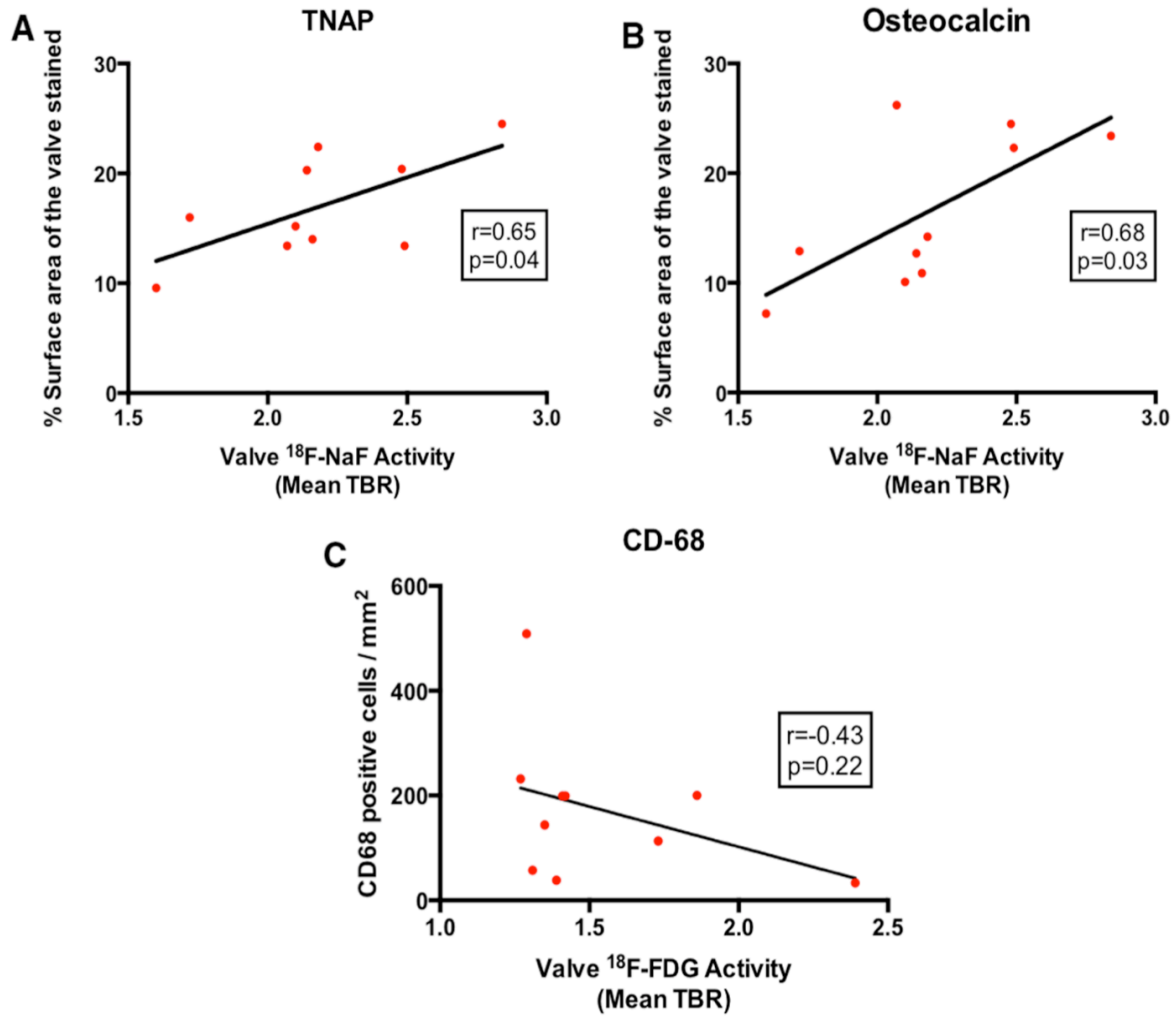

A, 18F-fluoride (18F-NaF) *versus* tissue nonspecific alkaline phosphatase (TNAP). A correlation was observed between the percentage aortic valve tissue staining for TNAP and the valvular 18F-fluoride uptake (mean tissue to background ratio [TBR]); r=0.65, P=0.04.

B, 18F-fluoride *versus* osteocalcin. A correlation was observed between the percentage surface area of the valve stained with osteocalcin and the aortic valve 18F-fluoride PET activity (mean TBR); r=0.68, P=0.03.

C, 18F-Fluorodeoxyglucose (FDG) *versus* CD68. No correlation was observed between CD68 staining on immunohistochemistry and 18F-FDG PET activity in the aortic valve (mean TBR); r=−0.43, P=0.22.

3.5.5 Imaging Defined Disease Progression

Of the 18 patients (75±6 years of age; 17 men; peak aortic-jet velocity, 2.6±0.9 m s^{-1}) reassessed at a median interval of 386 days (Table 3.4), 6 had aortic sclerosis, 7 had mild AS, and 5 had moderate AS. Effective myocardial suppression of 18F-FDG uptake was achieved in 66% (median myocardial standard uptake value, 3.6; IQR [2.0–5.4]). A correlation was observed between baseline aortic valve calcium scores on CT and 18F-fluoride activity on PET (r=0.74 [0.42–0.90]; P≤0.001). However, as described previously, the pattern of 18F-fluoride uptake was distinct from the distribution of established calcium. (121,123,124) Indeed 18F-fluoride uptake in the absence of underlying calcium occupied a median of 8.3% (IQR 1.6–23.4) of the total valve area, emphasizing that 18F-fluoride provides distinct and complementary information to CT calcium scoring (Figure 3.1).

Table 3.3 | Baseline Clinical Data – All Patients

	Total	Aortic Sclerosis	Mild Aortic Stenosis	Moderate Aortic Stenosis
No.	18	6 (33)	7 (39)	5 (28)
Age, y	75 (71–79)	74 (70–78)	74 (69–80)	79 (70–83)
Men	15 (83)	4 (66)	7 (100)	4 (80)
Hypertension	13 (72)	3 (50)	5 (71)	5 (100)
Hyperlipidemia	12 (67)	4 (66)	5 (71)	3 (60)
Diabetes mellitus	5 (28)	1 (16)	4 (57)	0 (0)
Ischemic heart disease	13 (72)	4 (66)	6 (86)	3 (60)
Serum creatinine, μmol/L	92±29	85 (72–92)	91 (67–125)	84 (69–133)
Cigarette smoking	0 (0)	0 (0)	0 (0)	0 (0)
Peak aortic valve velocity, m/s	2.6 (1.8–3.1)	1.7 (1.6–1.8)	2.4 (2.1–2.6)	3.4 (3.2–3.6)
Aortic valve area, cm^2	1.68 (1.26–2.28)	1.92 (1.8–2.1)	1.63 (1.42–1.87)	1.03 (0.78–1.18)
Mean gradient, mm Hg	10.8 (7.0–16.5)	6.2 (4.8–7.0)	11.0 (9.3–14.0)	22.0 (18.8–27.2)
Aortic valve calcium score, AU	314 (193–540)	106 (13–204)	355 (211–536)	1167 (436–1472)
Time between CT scans, d	386 (377–409)	390 (375–408)	394 (376–426)	183 (360–399)
18F-FDG dose injected, MBq	193 (188–196)	193 (185–205)	191(185–194)	194 (190–206)
18F-NaF dose injected, MBq	123 (120–126)	124 (117–127)	123 (117–128)	123 (120–126)

Categorical displayed as total number (%). Median (interquartile range). CT indicates computed tomography; 18F-FDG, 18F-fluorodeoxyglucose; and 18F-NaF, 18F-sodium fluoride

At 1 year, aortic valve calcium scores increased from 314 (193–540) to 365 (207–934) AU (P<0.01). Interestingly, these regions of novel calcium developed in much the same distribution as the observed baseline 18F-fluoride uptake (Figure 3.3 A & B). Indeed, we observed a correlation between baseline valvular 18F-fluoride PET uptake and the change in calcium score after 1 year (*r*=0.66 [0.27–0.86]; *P*=0.003; Figure 3.3 C). This was similar to that observed for the current gold standard method of prediction: the baseline calcium score (*r*=0.58 [0.15–0.82]; *P*=0.01; Figure 3.3 D). This association improved further when only increased 18F-fluoride uptake in the absence of underlying CT macrocalcification was considered (*r*=0.75 [0.42–0.90]; *P*=0.01). No statistically significant correlation was observed between 18F-FDG uptake and the subsequent change in CT calcium score (*r*=−0.11 [−0.56 to 0.39]; *P*=0.66; Figure 3.3 E).

Figure 3.3 | Change In Aortic Valve Computed Tomography (CT) Calcium Score And 18F-Fluoride Positron Emission Tomography (PET) Activity After One Year

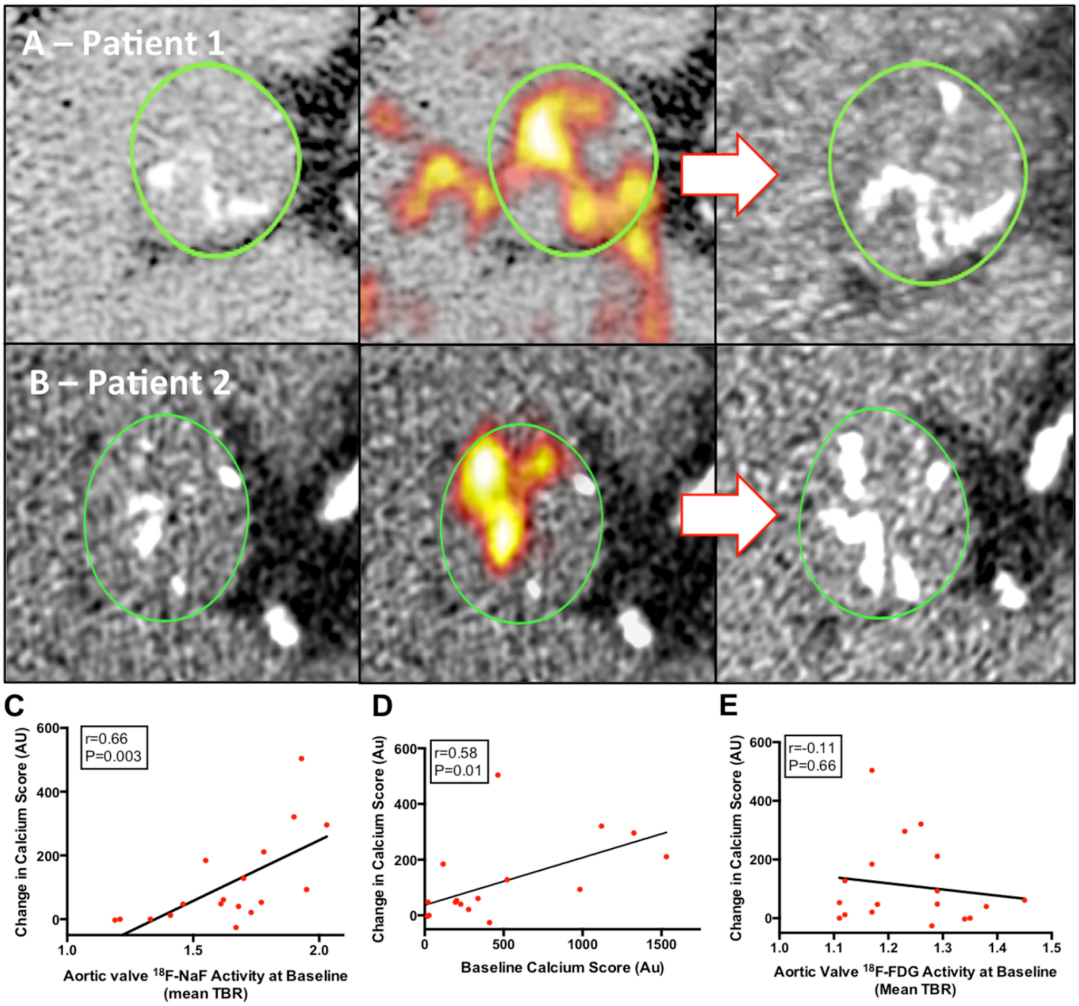

A and **B**, Coaxial short axis views of the aortic valve from 2 patients with mild aortic stenosis (top and bottom). On baseline CT scans (left) established regions of macrocalcification appear white. Baseline fused 18F-fluoride PET and CT scans (middle) show intense 18F-fluoride uptake (red, yellow regions) both overlying and adjacent to existing calcium deposits on the CT. One-year follow-up CT scans (right) demonstrate increased calcium accumulation in much the same distribution as the baseline PET activity.

C–**E**, Predictors of progression in aortic valve calcium score. An excellent correlation was observed between baseline 18F-fluoride (18F-NaF) activity in the aortic valve and the subsequent change in calcium score at 1 year r=0.66, P<0.01 (**C**). This matched the current gold standard predictor of disease progression, the baseline calcium score r=0.58, P=0.01 (**D**). By contrast, there was no correlation with 18F-Fluorodeoxyglucose (FDG) activity in the valve r=−0.11, P=0.66 (**E**).

3.6 Discussion

We provide the first preliminary evidence that valvular 18F-fluoride uptake acts as a marker of calcification activity in patients with AS. Not only did uptake values demonstrate a correlation with histological markers of active calcification (TNAP and osteocalcin), but they were also a good predictor of the subsequent progression in aortic valve CT calcium scores at 1 year. In contrast, 18F-FDG uptake did not correlate with CD68 staining on histology or the progression in calcium scores. Our data indicate that 18F-fluoride holds promise as a biomarker of disease activity in patients with AS.

The pathophysiology of AS is incompletely understood, delaying the development of biomarkers and effective medical therapies. Calcification and inflammation are thought to play a key pathological role(114) so that non-invasive markers of their activity are of interest in better understanding the cause of this condition and in predicting disease progression.

Recent studies have investigated 18F-fluoride PET as a marker of vascular calcification in AS(8) and atherosclerosis affecting the aorta, (125) coronary, (117,121) and carotid arteries. (126) However, this is the first study to provide histological validation of 18F-fluoride uptake in vascular tissue. In bone, 18F-fluoride is thought to incorporate onto the surface of hydroxyapatite crystal. (126) Given that hydroxyapatite is also a key component of vascular calcification, it too has been the presumed radiotracer target in AS and atherosclerosis. This hypothesis is supported by our autoradiography and immunohistochemical data, demonstrating a good correlation between 18F-fluoride activity and osteocalcin staining: a well-recognized osteogenic protein that itself binds to hydroxyapatite.

Given that 18F-fluoride binds to a structural component of vascular calcification, why then does it not simply label all regions of macrocalcification identified by CT? Indeed, it is common for regions of dense calcium on CT to

show no 18F-fluoride uptake. This phenomenon is probably related to the available surface area of exposed hydroxyapatite crystal to which the 18F-fluoride ion can adsorb and the biological inactivity of established areas of field calcification. 18F-fluoride uptake is much greater at sites of evolving "powdery" microcalcification than established regions of field calcification in which the core of hydroxyapatite is internalized and therefore hidden from the 18F-fluoride tracer. Thus, 18F-fluoride binds more readily to regions of developing calcium and acts as a marker of calcification activity, providing distinct information to calcium scoring. In contrast, the latter quantifies regions of established macroscopic calcium in the valve but cannot inform whether the process of calcification is quiescent or active. Again, this hypothesis is supported by our data. We have demonstrated a strong correlation between in vivo 18F-fluoride uptake and staining for one of the key enzymes regulating mineralisation: TNAP. This enzyme is expressed in the early stages of new calcium formation and is known to work by breaking down pyrophosphate: a potent inhibitor of mineralization. (127) Furthermore, as one would expect from a measure of activity, baseline 18F-fluoride uptake closely correlated with the subsequent change in calcium score at 1 year. Indeed, 18F-fluoride uptake performed as well as the current gold standard method of prediction, the degree of established calcium in the valve at baseline. (115,128) However, larger studies are now required to compare these two techniques, whereas calcium scoring may be easier to obtain; changes in the 18F-fluoride PET signal are likely to occur more quickly, making it a more attractive technique with which to assess the early and more immediate effects of novel treatment strategies.

Interestingly, the pattern of 18F-fluoride uptake may be important, with 18F-fluoride uptake remote from established macrocalcification on CT offering the best prediction of calcium score progression in our cohort. The spatial resolution of PET/CT is ~4 mm, and we acknowledge that the voxel-by-voxel analysis used to establish this observation is at the limit of resolution for PET imaging. Nevertheless, the strong correlation with progression is of interest and

indicates that further investigation of the spatial distribution of 18F-fluoride uptake is warranted.

The results of valvular 18F-FDG imaging were somewhat disappointing and surprising given previous data suggesting an important role for inflammation in AS. (129) Although correlations between 18F-FDG uptake and macrophage burden have previously been demonstrated in regions of aortic and carotid atheroma, (130) we were unable to replicate this with respect to the valve. There are several explanations for this discrepancy. The first is the close proximity of the valve to the myocardium. As discussed, avid uptake of 18F-FDG by the left ventricular myocardium can spill over into the aortic valve contaminating its signal. Unfortunately, despite the stringent dietary restrictions and centre-valve analysis technique, it remains possible that myocardial contamination occurred, confounding the correlation with CD68 immunohistochemistry. Poor myocardial suppression was achieved in the histology group, perhaps reflecting their advanced disease and symptomatic status. Alternative methods have been used to reduce further this myocardial uptake, including administration of heparin(131) and a high-fat drink before scanning. (132) However, these make the practicalities of scanning more difficult and have yet to show a clear advantage over dietary restrictions. An alternative explanation for the poor correlation with histology is that the aortic valve 18F-FDG signal relates to uptake by non-macrophage cell types within the valve, such as osteoblasts, or is governed by external factors, such as hypoxia. (76) In this scenario, one might still expect 18F-FDG to predict disease progression, but once again this was not evident in our cohort. It would therefore seem that 18F-FDG holds less potential as a predictor of disease progression than 18F-fluoride does, although it remains possible that longer periods of follow-up are required to detect such an association. Indeed, on occasion, we also observed 18F-fluoride activity that did not translate into a detectable change in calcium score at 1 year. AS is a slowly developing condition, so it is likely to take time for relatively low levels of 18F-fluoride or 18F-FDG uptake to translate into new areas of macrocalcification detectable on

CT imaging. Larger studies with longer follow-up are, therefore, required to address this issue, confirm our preliminary data, and assess whether 18F-fluoride PET can predict disease progression with respect to echocardiographic parameters of valvular stenosis.

3.7 Conclusions

We provide the first preliminary data to support 18F-fluoride as a marker of valve calcification activity in AS and as a potential method for predicting disease progression.

Chapter 4 – 18F-Fluoride and 18F-FDG Hybrid Positron Emission Tomography and Computed Tomography in Calcific Aortic Valve Disease – Prospective Clinical Validation

4.1 Publication In Context

4.1.1 Background

In the last chapter, I showed how we built on the original data and analyses arising from the Ring of Fire Study. (120) We showed that 18F-fluoride PET/CT highlights areas of nascent and biologically active calcification by demonstrating that tracer uptake into the valve correlated with immunohistochemical markers of calcification. The observation that 18F-fluoride uptake frequently identified regions of future aortic valve calcification on follow-up CT provided further *in vivo* validation of our histological findings. However, the prospective imaging-based data were limited (18 patients). We felt that we couldn't yet draw firm conclusions on the predictive capability of 18F-fluoride with such small numbers and with purely imaging defined disease progression.

We were also somewhat surprised to find that 18F-FDG didn't behave as we had originally hypothesised. 18F-FDG failed to correlate with the relevant inflammation parameter (CD68 staining) and didn't predict imaging defined disease progression. We felt it was possible that the follow-up hadn't been long enough or that the numbers weren't large enough to detect an association. Of course, conversely it was also possible that such an association (between cardiovascular 18F-FDG uptake and macrophage infiltration) might not be as strong as had originally been suspected – others have made this observation. (76,133)

In this project, we set out to complete the follow-up of the full original Ring of Fire cohort with the aim of seeing whether either 18F-FDG or 18F-fluoride could predict disease progression or clinical events in a larger cohort.

4.1.2 Aims of Further Study

We aimed to answer the following questions:

1. Does 18F-FDG uptake predict aortic stenosis disease progression as defined by standard imaging-based parameters?
2. Does 18F-fluoride uptake predict aortic stenosis disease progression as defined by standard imaging-based parameters?
3. Can either tracer predict relevant clinical events?
4. Does either 18F-FGD or 18F-fluoride add further predictive information to existing validated variables?

4.1.3 Contributions

Dr Jenkins and I led this work, supervised by Dr Dweck. We both analysed the data and drafted the paper together. For the purposes of this thesis monograph, the original manuscript has been converted to a traditional monograph format for narrative clarity.

Published as: **Vesey AT***, Jenkins WSA*, Shah ASV, Pawade TA, Chin CWL, White AC, et al. Valvular 18F-fluoride and 18F-Fluorodeoxyglucose Uptake Predict Disease Progression and Clinical Outcome in Patients With Aortic Stenosis. *Journal of the American College of Cardiology*. 2015 Sep 8;66(10):1200–1.

*equal contribution

4.2 Abstract

4.2.1 Background.

18F-fluoride and 18F-fluorodeoxyglucose (18F-FDG) are positron emission tomography (PET) radiotracers of calcification and inflammation activity respectively. We sought to assess their ability to predict disease progression and clinical outcome in patients with aortic stenosis.

4.2.2 Methods

PET and computed tomography (CT) were performed in 121 volunteers (72±8 years, 68% men) with and without aortic valve disease (20 controls; 20 aortic sclerosis; 25 mild, 33 moderate, and 23 severe aortic stenosis) using 18F-fluoride (125 MBq) and 18F-FDG (200 MBq). Disease progression was assessed at 1- and 2-years using CT aortic valve calcium score and echocardiography. The primary clinical outcome endpoint was a composite of cardiovascular death and aortic valve replacement (AVR).

4.2.3 Results

Aortic valve calcium score increased by 61 (5–226) AU yr^{-1} and aortic valve mean gradient increased by 0.7 (-0.2–2.9) mmHg yr^{-1}. Baseline valvular 18F-fluoride uptake correlated strongly with the rate of progression in aortic valve calcium score (r=0.80, $P<0.001$), matching that observed for the baseline aortic valve CT calcium score (r=0.88, $P<0.001$) and outperforming that observed for 18F-FDG ($r=0.43$, $P=0.001$). Modest correlations were observed between 18F-fluoride and 18F-FDG valvular uptake, aortic valve CT calcium score, and the echocardiographic measures of disease progression (mean aortic valve gradient; $r=0.36$, $P<0.001$; $r=0.32$, $P=0.001$ and r=0.26, $P=0.001$ respectively). After a median of 1,232 (IQR 1148-1322) days, 23 patients had undergone AVR whilst 5 had died from a cardiovascular cause. After age and sex-adjustment, aortic valve CT calcium score, valvular 18F-fluoride and 18F-FDG uptake were independent predictors of clinical outcome (HR 32.0 (8.0-130.4), $P<0.001$, 1.46 (1.24-1.71), $P<0.001$, and 1.59 (1.21-2.09), $P=0.002$ respectively).

4.2.4 Conclusions

Valvular 18F-fluoride uptake matches the aortic valve CT calcium score and outperforms 18F-FDG in predicting the progression of aortic valve calcification and stenosis. Each of these novel imaging methods are independently associated with an adverse clinical outcome.

4.3 Introduction

Aortic stenosis is the commonest form of valvular heart disease in the developed world and a major cause of morbidity and mortality, affecting 0.5% of the adult population and rising to 12% of those aged over 75 years. This translates to 2.7 million elderly patients in North America and 4.9 million patients in Europe alone.(134) Furthermore, with a progressively increasing life-expectancy, the health burden attributable to this condition is only set to increase.(2) However, despite its prevalence, we lack biomarkers of disease activity, accurate clinical methods of predicting disease progression, and medical therapies capable of halting the disease process.

Our understanding of the pathogenesis of aortic stenosis has evolved over recent years. What was considered a passive and degenerative process is now appreciated to be a complex and highly regulated response to injurious stimuli with inflammation and calcification playing key roles. (101) In particular, calcification appears to be of increasing importance since it may determine disease progression, drive progressive leaflet thickening, and narrow the valve orifice. (11,101)

Our group and others have investigated combined positron emission tomography (PET) and computed tomography (CT) as a means of measuring inflammation and calcification activity in aortic stenosis and other cardiovascular diseases. (100,120,135,136) 18F-Fluorodeoxyglucose (18F-FDG) is a PET radiotracer and glucose analogue taken up by metabolically active cells. In the vasculature, its uptake localizes to sites of macrophage infiltration and activity. On this basis 18F-FDG has become widely used as a marker of vascular inflammation, and for testing the safety and efficacy of novel therapies. (130,136) 18F-fluoride is an alternative radiotracer that binds hydroxyapatite, the key structural component of cardiovascular calcification. This process is critically dependent upon the surface area of apatite available for incorporation and is increased when either new calcium is being laid down in nanocrystalline

form, or when established areas of field calcification are being remodelled by osteoclasts. 18F-fluoride thus highlights *in vivo* calcification activity, and holds promise as a biomarker of disease activity in aortic stenosis. Indeed, in our recent pilot study of 18 patients, valvular 18F-fluoride PET uptake correlated closely with histological markers of valvular calcification activity and with the progression of aortic valve CT calcium scores after 1 year. (136)

The aim of the current study was to assess the ability of these two tracers to predict longer-term disease progression and adverse clinical outcomes in a larger prospective cohort of patients with calcific aortic valve disease.

4.4 Methods

4.4.1 Patient Population

Patients aged >50 years with aortic sclerosis and mild, moderate or severe aortic stenosis attending the outpatient department of the Edinburgh Heart Centre were approached for recruitment in this prospective cohort study alongside age- and sex-matched control subjects, as described previously. (118,120,121) Exclusion criteria were insulin-dependent diabetes mellitus, end-stage renal failure, life expectancy of <2 years, and metastatic malignancy. The study was performed with the written informed consent of all participants, with research ethics committee approval, and in accordance with the Declaration of Helsinki.

4.4.2 Baseline Assessment

All participants underwent full clinical assessment at baseline and aortic stenosis severity was assessed using Doppler and two-dimensional echocardiography by means of the peak transvalvular velocity, mean gradient, peak gradient and aortic valve area (calculated using the continuity equation) according to American Heart Association/American College of Cardiology guidelines. (137) Multiple acoustic windows with the S51 and D2cwc probes (Philips Medical Systems, the Netherlands) were assessed. Aortic sclerosis was defined as thickening of the aortic valve cusps in the absence of accelerated flow (<2 ms^{-1}) through the valve. (137) We also assigned the valve a semi-quantitative echocardiographic calcium score (ECS) as described by Rosenhek *at al*. (128) Finally, aortic stenosis disease severity was assessed using an ECG-gated breath-hold CT scan (non-contrast enhanced, 40 mA/rot [CareDose], 100 kV) that was used to measure the aortic valve CT calcium score. (120)

PET/CT scans of the aortic valve were performed as described previously(120) using a hybrid scanner (Biograph mCT, Siemens Medical Systems, Erlangen, Germany) 60 min after administration of 125 MBq of 18F-fluoride. On a separate occasion, a second PET/CT scan was performed using the same hybrid

scanner 90 min following administration of 200 MBq of 18F-FDG. (120) In an attempt to minimise cardiomyocyte uptake of 18F-FDG, patients were asked to avoid carbohydrate for 24 h prior to their 18F-FDG scan. (132)

4.4.3 Image Analysis

Calcium score analysis was performed on axial scans by an experienced investigator (WJ) blinded to clinical data using dedicated analysis software (Vitrea Advanced, Vital Images, Minnetonka, USA). Care was taken to differentiate valvular calcium from that in the aortic root and mitral valve annulus.

Valvular 18F-fluoride and 18F-FDG uptake quantification was performed using an OsiriX workstation (OsiriX version 3.5.1 64-bit; OsiriX Imaging Software, Geneva, Switzerland) as reported previously. (120,138) Briefly, fused PET/CT images were re-orientated to the short-axis plane of the aortic valve and circular regions of interest (ROI) drawn on adjacent 3 mm slices until the entire valve apparatus had been examined. For 18F-fluoride, ROIs were placed around the perimeter of the valve excluding the aortic root (whole-valve technique). For 18F-FDG, ROIs were drawn in the centre of the valve to reduce the impact of myocardial spill over, as described previously (centre-valve technique). (100,120) From these regions, standard uptake values (SUV) were used to calculate tissue-to-background ratios (TBR) in the valve, after correcting for blood pool activity measured within the lumen of the superior vena cava. We have previously noted difficulty in defining the limits of the valve in the z-axis. As well as introducing potential for bias and variability, this problem frequently results in signal dilution if more slices than necessary are assessed. In keeping with an image analysis technique established in the aorta, (69) we therefore also calculated a modified "most diseased segment" SUV (SUV_{MDS}) in the aortic valve. This was based upon the average of the SUV_{mean} values derived from the 2 adjacent slices within the valve that had the highest signal. This value was then

used to calculate the most diseased segment TBR after blood-pool correction (TBR_{MDS}).

In order to assess the reproducibility of our methods for measuring the CT-calcium score, the echocardiographic calcium score and the valvular PET uptake, the scans from 25 study subjects with a range of aortic valve disease were selected at random and analysed independently by two observers.

4.4.4 Assessment of Disease Progression

Subjects who had survived and had not undergone AVR were invited to return for repeat clinical assessment and echocardiography at both 1 and 2 years after enrolment. A single experienced echocardiographer performed each echocardiogram under standardised conditions. Annualized rates of echocardiographic progression for aortic stenosis were calculated over three time-points: baseline, 1 year and 2 years.

A subgroup of patients underwent repeat CT-calcium scoring after 1 year. (136) To limit their exposure to ionizing radiation, these subjects did not undergo further calcium scoring. In the remaining eligible patients, repeat CT scoring of the valve was performed after 2 years. The annualized change in CT calcium score was calculated for all subjects. For both echocardiography and CT, the same scanner and imaging protocol was used for all the baseline and follow up scans.

4.4.5 Follow-up for Clinical Events

The primary outcome measure was a composite of cardiovascular mortality or aortic valve replacement (AVR). (138) All deaths were captured from the General Register of Scotland. Cardiovascular death was defined as death due to myocardial infarction, sudden cardiac death, heart failure, stroke, death related to cardiovascular procedures, and death due to other cardiovascular causes. Each death was classified as cardiac or non-cardiac by two independent

investigators blinded to the imaging data, with any discrepancy resolved by consensus. All events, including AVR (either surgical or transcatheter), were confirmed by independent review of each patient's healthcare record. All patients were managed in our tertiary cardiac centre, and reviewed at a multi-disciplinary meeting prior to undergoing aortic valve replacement. Only patients with established indications according to contemporary guidelines were referred for AVR. (139)

4.4.6 Statistical Methods

Continuous variables were expressed as either mean ± standard deviation for normally distributed data and median (interquartile range; IQR) for skewed distributions. Non-parametric datasets were log-transformed in an attempt to achieve normality. Parametric (unpaired Student's t-test) and non-parametric (Mann-Whitney U) tests were used for normally distributed and skewed data respectively. Categorical data were presented as n (%) and compared when appropriate using a contingency table and Fisher's or Chi-squared tests. Correlation was undertaken with either Pearson's r or Spearman's Rho subject to the normality of the variables tested.

To assess inter and intra-observer repeatability of the two PET analysis techniques and the aortic valve CT-calcium scoring, the intra-class correlation coefficient (ICC) was calculated and Bland-Altman analysis undertaken. Due to its categorical nature, repeatability studies of the echocardiographic calcium score were assessed using Cohen's kappa coefficient.

Adjusted and unadjusted Cox regression models were used to assess whether 18F-fluoride and 18F-FDG were associated with aortic valve replacement or cardiovascular mortality. Statistical analyses were performed with the use of Graph Pad Prism version 6.0 (GraphPad Software Inc, California, USA), SPSS version 18 (SPSS Inc, Chicago, IL) and RStudio version 0.98.501 (2013). Statistical significance was taken as two-sided $P < 0.05$.

4.5 Results

4.5.1 Study Population

A total of 121 patients were recruited (aged 72±8 years; 69% male) and underwent both 18F-fluoride (66±7 min after 124±10 MBq) and 18F-FDG (94±7 min after 197±14 MBq) PET/CT imaging of their aortic valve. The study cohort comprised 20 control subjects, 20 patients with aortic sclerosis, and 25 patients with mild, 33 with moderate, and 23 with severe aortic stenosis as described previously. Subjects were well matched for age, sex, and comorbidity (Figure 4.1, Table 4.1).

Figure 4.1 | Study Flow Chart

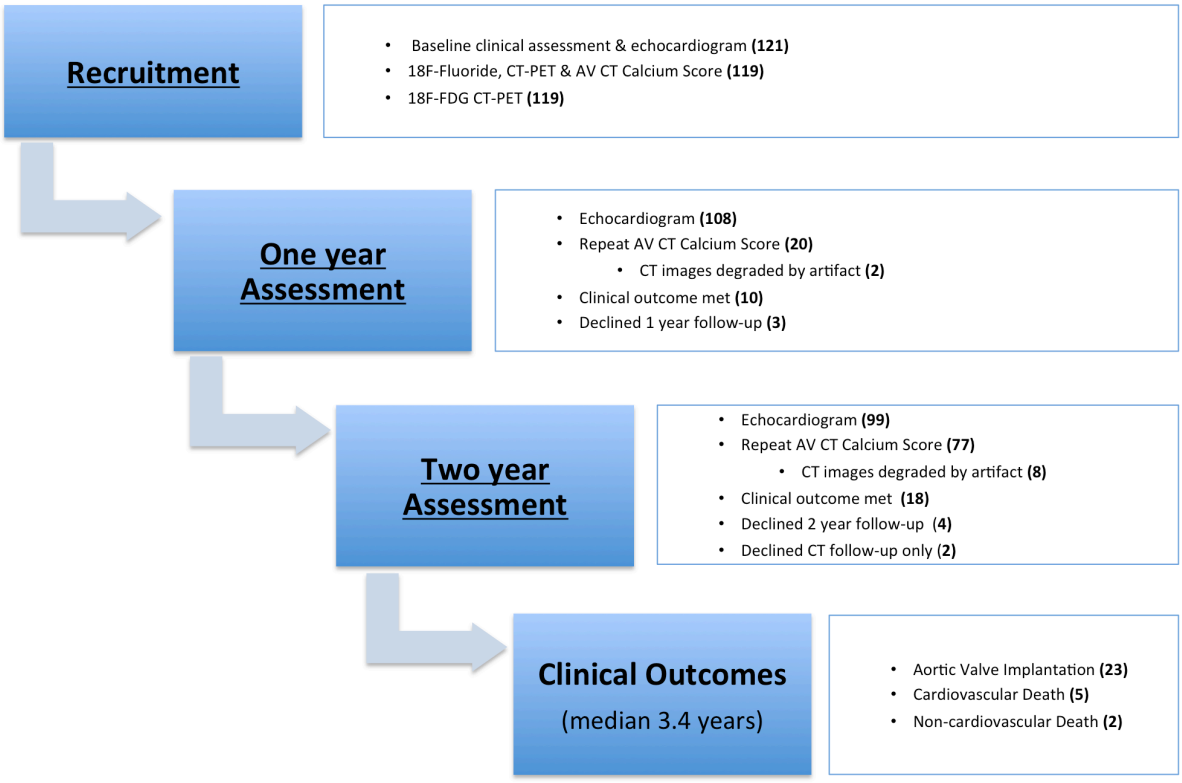

AV, aortic valve; CT, computed tomography; FDG, fluorodeoxyglucose; PET, positron emission tomography

	All Patients	Echocardiography Follow-up Cohort	Calcium Score Follow-up Cohort	Patients who had a Clinical Outcome (AVR/CV Death)
n	121	99	87	28
Age	72±8	72±8.5	72±8	70±7
Male	83 (69)	66 (65)	45 (51)	19 (68)
Body Mass Index	27±4	28±4	28±6	28±4
Systolic Blood Pressure (mmHg)	142±18	143±19	144±19	144±17
Co-morbidity				
Diabetes Mellitus	18 (15)	13 (13)	12 (14)	3 (11)
Hypertension	73 (60)	59 (60)	53 (61)	16 (53)
Documented CAD	43 (35)	36 (36)	38 (44)	8 (28)
Current smoker	14 (12)	11 (11)	7 (8)	4 (14)
Creatinine ($\mu mol\ L^{-1}$)	89.3±25.6	90.2±28.3	88.4±24.8	86.6±25.6
Medications				
ACE inhibitors	47 (39)	36 (36)	36 (41)	12 (43)
AIIRB	13 (11)	11 (11)	10 (11)	3 (11)
Beta Blockers	48 (40)	41 (41)	40 (46)	10 (33)
Statins	65 (54)	54 (54)	54 (62)	16 (57)
Echocardiography				
AV jet vel. ($m\ s^{-1}$)	2.8 (1.7-3.7)	2.6 (1.7-3.6)	2.6 (1.7-3.6)	3.3 (2.4-4.0)
AV peak gradient (mmHg)	31 (11-53)	28 (11-51)	28 (12-51)	43 (24-63)
AV mean gradient (mmHg)	16 (6-29)	14 (6-27)	14 (6-27)	23 (12-34)
AV area (cm^2)	1.34 (0.98-2.09)	1.37 (1.06-2.12)	1.33 (1.06-1.99)	1.15 (0.84-1.64)
Calcium Score	1.6±0.9	1.5±0.9	1.5±0.9	2.0±0.9
ECG Findings				
LVH	28 (23)	19 (19)	17 (20)	7 (25)
LV Strain	13 (11)	9 (9)	8 (9)	5 (17)
PET/CT				
AV Calcium Score (AU)	554 (19-1762)	530 (13-1515)	585 (46-1487)	1542 (314-3386)
Log_{10} AV Calcium Score	2.74 (1.27-3.25)	2.72 (1.11-3.18)	2.77 (1.66-3.17)	3.18 (2.50-3.53)
18F-FDG Dose (MBq)	196.6±13.9	197.0±13.8	197.0±12.0	196.6±14.7
18F-fluoride Dose (MBq)	123.8±9.5	123.6±9.0	124.0±7.8	128.2±9.6
18F-FDG Valve uptake (TBR_{MDS})	1.38±0.19	1.35±0.15	1.46±0.21	1.45±0.23
18F-fluoride Valve uptake (TBR_{MDS})	1.80±0.47	1.73±0.45	1.64±0.45	2.20±0.45
Time in study (days)	742±38	743±38	739±32	443 (325-796)

Table 4.1 | Baseline Clinical Characteristics

Parametric data are presented as mean±SD. Non-parametric data are presented as median(IQR). Categorical data are presented as number (percentage). ACE, angiotensin converting enzyme; AIIRB, angiotensin 2 receptor antagonists; AS, aortic stenosis; AV, aortic valve; CAD, coronary artery disease; FDG, Fluorodeoxyglucose; TBR, tissue to background ratio; AU, arbitrary unit; LV, left ventricle; LVH, left ventricular hypertrophy

4.5.2 Image Analysis Reproducibility Studies

The novel TBR_{MDS} method demonstrated superior inter-observer reproducibility compared to the established TBR_{mean} approach for the quantification of valvular 18F-FDG uptake. The two techniques performed equally well with respect to 18F-fluoride (see Table 4.2)

Baseline uptake of the two radiotracers across the cohort using the TBR_{mean} technique have been reported previously. (120) The TBR_{MDS} technique resulted in no major differences compared to the original observations (Table 4.4), with valvular radiotracer uptake increasing in line with the extent of valvular calcification (Figure 4.3A). Moreover, the choice of uptake analysis technique had no impact on the strength of the correlations observed between baseline PET uptake and disease progression (Table 4.5). Given the improved inter-observer reliability for 18F-FDG, TBR_{MDS} was used for all subsequent analyses.

The intra- and inter-observer repeatability of aortic valve CT calcium scoring (Agatston technique(102)) was excellent (Table 4.3, Figure 4.2) with echocardiographic calcium score performing more modestly (Table 4.3).

Table 4.2 | Most Diseased Segment Versus Mean Whole Valve Technique for 18F-Fluorodeoxyglucose And 18F-Fluoride

	TBR_{mean}		TBR_{MDS}	
	Mean absolute difference[a]	Intra-class coefficient[b]	Mean absolute difference[a]	Intra-class coefficient[b]
18F-fluoride	0.07 (-0.13-0.27)	0.98 (0.96-0.99)	-0.08 (-0.31-0.15)	0.99 (0.97-0.99)
18F-FDG	0.06 (-0.22-0.34)	0.76 (0.52-0.89)	<0.001 (-0.11-0.11)	0.97 (0.94-0.99)

[a] Mean difference between tissue to background ratio (TBR) measurements (95% limits of agreement)
[b] intra-class coefficient (ICC) values (95% confidence intervals)

Table 4.3 | Agreement Studies – Aortic Valve Calcium Quantification

	Inter-observer		Intra-observer	
	Bias (95% limits of agreement)[a]	ICC (95% CI)[b]	Bias (95% limits of agreement) [a]	ICC (95% CI) [b]
CT Calcium Score (AU)	22 (-35 – 79)	1 (1.0-1.0)	10 (-67 - 88)	1 (1.0-1.0)

	Inter-observer κ (SE)[c]	Intra-observer κ (SE)[c]
Echo Calcium Score	0.447 (0.138)	0.501 (0.132)

[a] mean difference
[b] Intra-class correlation co-efficient. 2-way mixed effects for absolute agreement.
[c] Kappa statistic
AU, Arbitrary units

Figure 4.2 | CT Calcium Scoring: Bland-Altman

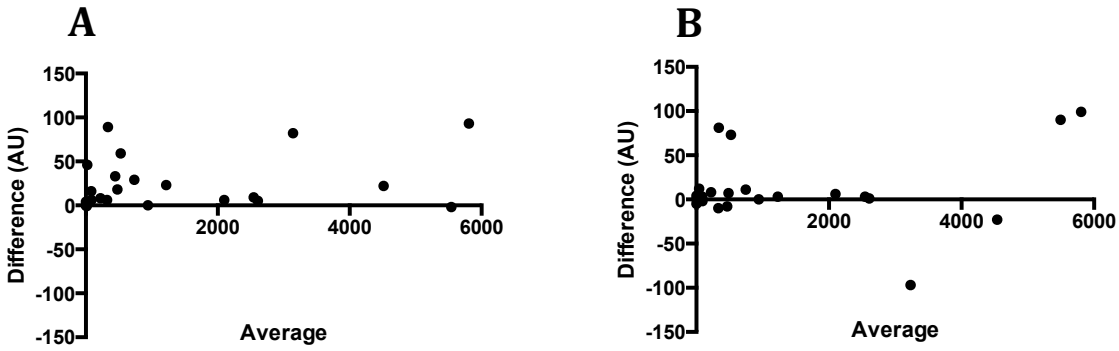

Mean difference plotted against average CT calcium score for intra-observer (**A**) and inter-observer (**B**) agreement.

Table 4.4 | Radiotracer Uptake Quantification Methods – Minimal Impact On Average Uptake Estimates

	All Patients	Echocardiography Follow-up Cohort	Calcium Score Follow-up Cohort	Patients who had a Clinical Outcome (AVR/CV Death)
n	121	98	87	28
18F-FDG ($mean_{CV}$TBR)	1.34±0.17	1.32±0.14	1.33±0.18	1.42±0.15
18F-FDG ($mean_{MDS}$TBR)	1.38±0.19	1.35±0.15	1.46±0.21	1.45±0.23
18F-fluoride ($mean_{WV}$TBR)	1.75±0.42	1.69±0.41	1.66±0.41	2.08±0.38
18F-fluoride ($mean_{MDS}$TBR)	1.80±0.47	1.73±0.45	1.64±0.45	2.20±0.45

AVR, aortic valve replacement; CV, cardiovascular, $mean_{CV}$, centre valve technique; FDG, fluorodeoxyglucose; $mean_{MDS,}$most diseased segment technique; $mean_{WV}$, whole valve technique; SUV, standardised uptake value; TBR, tissue to background ratio

Table 4.5 | Radiotracer Uptake Quantification Methods – Minimal Impact On Correlations With Parameters Of Disease Progression

Baseline Imaging Assessment	Rate of Change in AV Calcium Score (AU yr^{-1})	Rate of change in aortic jet velocity (m sec^{-1} yr^{-1})	Rate of change in mean gradient (mmHg yr^{-1})	Rate of change in peak gradient (mmHg yr^{-1})	Rate of change in Aortic Valve Area (cm^2 yr^{-1})
18F-fluoride $mean_{MWV}$TBR	*r*=0.79 (0.69-0.86) P<0.001	*r*=0.20 (0.00-0.39) P=0.04	*r*=0.29 (0.10-0.47) P=0.003	*r*=0.29 (0.09-0.47) P=0.004	*r*=0.13 (-0.08-0.33) P=0.20
18F-fluoride $mean_{MDS}$TBR	*r*=0.80 (0.60-0.86) P<0.001	*r*=0.23 (0.03-0.41) P=0.001	*r*=0.32 (0.13-0.50) P=0.001	*r*=0.32 (0.12-0.49) P=0.001	*r*=0.11 (-0.10-0.31) P=0.29
18F-FDG $mean_{CV}$TBR	*r*=0.47 (0.28-0.62) P<0.001	*r*=0.23 (0.03-0.42) P=0.02	*r*=0.26 (0.06-0.44) P=0.01	*r*=0.33 (0.14-0.50) P<0.001	*r*=-0.12 (-0.32-0.08) P=0.23
18F-FDG $mean_{MDS}$TBR	*r*=0.43 (0.23-0.59) P<0.001	*r*=0.28 (0.08-0.46) P=0.005	*r*=0.30 (0.10-0.47) P=0.002	*r*=0.36 (0.17-0.53) P<0.001	*r*=-0.14 (-0.33-0.07) P=0.18
18F-fluoride $mean_{MWV}$SUV	*r*=0.64 (0.49-0.75) P<0.001	*r*=0.28 (0.08-0.46) P=0.006	*r*=0.36 (0.16-0.52) P<0.001	*r*=0.34 (0.14-0.51) P<0.001	*r*=0.10 (-0.12-0.29) P=0.34
18F-fluoride $mean_{MDS}$SUV	*r*=0.67 (0.53-0.77) P<0.001	*r*=0.23 (0.03-0.41)) P=0.02	*r*=0.32 (0.13-0.49) P=0.001	*r*=0.34 (0.15-0.51) P<0.001	*r*=0.15 (-0.06-0.34) P=0.02
18F-FDG $mean_{CV}$SUV	*r*=0.41 (0.21-0.57) P<0.001	*r*=0.26 (0.07-0.45) P=0.004	*r*=0.25 (0.05-0.44) P=0.01	*r*=0.29 (0.09-0.47) P=0.004	*r*=0.01 (-0.20-0.20) P=0.98
18F-FDG $mean_{MDS}$SUV	*r*=0.42 (0.23-0.59)) P<0.001	*r*=0.29 (0.09-0.46) P=0.004	*r*=0.31 (0.11-0.48) P=0.002	*r*=0.31 (0.11-0.48) P=0.002	*r*=0.27 (0.08-0.45) P=0.008
AV Calcium Score(AU)	*r*=0.88 (0.82-0.92) P<0.001	*r*=0.36 (0.16-0.53) P<0.001	*r*=0.40 (0.21-0.56) P<0.001	*r*=0.46 (0.27-0.61) P<0.001	*r*=0.060 (-0.15-0.27) P=0.54
Aortic Jet Velocity (m sec^{-1})	*r*=0.79 (0.70-0.86) P<0.001	*r*=0.28 (0.08-0.45) P=0.006	*r*=0.40 (0.22-0.56) P<0.001	*r*=0.39 (0.21-0.55) P<0.001	*r*=0.08 (-0.13-0.27) P=0.45

$Mean_{CV}$, centre valve technique; FDG, fluorodeoxyglucose; $mean_{MDS,}$most diseased segment technique; $mean_{WV}$, whole valve technique, fluoride, Sodium fluoride; SUV, standardised uptake value; TBR, tissue to background ratio. Values in parentheses are 95% confidence intervals

4.5.3 Patient Follow-up

One year after enrolment, 107 subjects returned for clinical follow-up and echocardiography. As part of a pilot study, 20 subjects had received a repeat ECG-gated cardiac CT at one year and did not undergo further CT at two years. (136)

Ninety-nine subjects (81%) returned for repeat clinical assessment and echocardiography at the 2-year time point (median 736 [722–760] days from enrolment). Seventy-seven of these subjects received repeat CT calcium scoring. Including the patients scanned at 1 year, a total of 97 (78%) subjects underwent a repeat ECG-gated cardiac CT during the 2-year follow up period. CT scans were not interpretable in 10 subjects (including 2 at the 1-year time point) due to motion artifact and were excluded from subsequent analysis. In the remaining patients (n = 87), the annualized change in the aortic valve CT calcium score was calculated and used for future analysis (Figure 4.1).

Across all disease cohorts, modest progression of each echocardiographic measure of aortic stenosis severity was observed (Table 4.6). Peak aortic jet velocity increased by 0.08 (-0.02–0.18) m s^{-1} yr^{-1}, the mean transvalvular gradient by 0.7 (-0.2 – 2.9) mmHg yr^{-1} and the peak gradient by 1.3 (-0.3 – 4.0) mmHg yr^{-1}. The aortic valve area fell by -0.06 (-0.14 – 0.02) cm^2 yr^{-1}. By contrast, relatively large annualized changes in the CT valvular calcium scores were observed (61 [5 –2 26] AU/year, P <0.001), especially amongst patients with moderate (289 [106 - 443] AU yr^{-1}) and severe disease (342 [163 - 583] AU yr^{-1}; Table 4.6 and Figure 4.3).

Clinical outcomes were assessed at a median of 1,232 (1,148 - 1,322) days after enrolment. At this point, 23 (19%) patients had undergone either aortic valve replacement (AVR; n=22) or transcatheter aortic valve implantation (n=1). There were 7 (6%) deaths in total: five subjects died of a cardiovascular cause

and two of sepsis. Overall, 28/121 (23%) subjects were adjudicated to have reached the primary end-point (Table 4.6).

Table 4.6 | Disease Progression And Clinical Outcomes

Variable	All patients	Control Subjects	Aortic Sclerosis	Mild Aortic Stenosis	Moderate Aortic Stenosis	Severe Aortic Stenosis
Baseline Echocardiography						
No. of patients	121	20	20	25	33	23
Baseline aortic-jet velocity (m s^{-1})	2.8±1.2	1.3±0.2	1.7±0.2	2.5±0.2	3.4±0.3	4.6 ±0.6
Baseline mean gradient (mmHg)	16.2 (5.9-29.2)	3.6±1.0	5.9±1.4	13.2±2.7	25.2±4.1	48.6±15.4
Baseline peak gradient (mmHg)	31.1 (11.0-53.0)	7.1±2.1	11.1±2.6	25.8±5.0	46.5±7.5	84.2±24.8
Baseline aortic-valve area (cm^2)	1.34 (0.98-2.09)	2.54±0.49	2.27±0.41	1.42±0.30	1.13±0.27	0.76±0.21
Follow-Up Echocardiography						
No. of patients	99	20	17	24	26	12
Change in aortic jet velocity (m s^{-1} yr^{-1})	0.08 (-0.02-0.18) P<0.001	0.05 (-0.03-0.09)	0.03 (-0.08-0.08)	0.08 (-0.01-0.18)	0.17 (0.07-0.30)	0.10 (-0.11-0.19)
Change in mean gradient (mmHg yr^{-1})	0.7 (-0.2-2.9) P<0.001	0.1 (-0.5-0.3)	0.0 (-0.7-0.6)	1.0 (-0.3-2.2)	3.2 (0.7-5.0)	2.6 (-0.1-5.3)
Change in peak gradient (mmHg yr^{-1})	1.3 (-0.3-4.0) P<0.001	0.4 (-0.3-0.7)	0.3 (-0.9-1.1)	1.4 (-0.2-3.1)	4.1 (1.6-9.0)	3.2 (-3.7-6.8)
Change in aortic-valve area (cm^2 yr^{-1})	-0.05 (-0.14-0.02) P<0.001	-0.10 (-0.25--0.01)	-0.04 (-0.12-0.07)	-0.09 (-0.16--0.02)	-0.05 (-0.13--0.03)	-0.04 (-0.08--0.02)
Baseline Computed Tomography						
No. of patients	112	20	20	23	30	19
Baseline AV Calcium score	554 (19-1762)	0 (0-3)	46 (2-224)	489 (281-693)	1427 (777-2215)	3386 (1770-6211)
Log_{10} Baseline AV Calcium Score	1.79 (0.70-2.35)	0.30 (0.0-0.91)	1.28 (0.0-1.71)	1.81 (1.68-2.13)	2.46 (2.02-2.65)	2.53 (2.21-2.75)
Follow-Up Computed Tomography						
No. of patients	87	18	18	21	24	6
Change in AV calcium score (AU / year)	61 (5-226)	2 (0-8)	19 (0-52)	64 (48-134)	289 (106-443)	342 (163-583)
Log_{10} change in AV Calcium score / year	0.96 (0.69-2.35)	0.30 (0.0-0.91)	1.2 (0.0-1.71)	1.81 (1.68-2.13)	2.46 (2.02-2.65)	2.53 (2.21-2.75)
Clinical Outcome						
Number of event-free days	1232 (1148-1322)	1227 (1155-1258)	1257 (1190-1349)	1272 (1214-1333)	1216 (784-1357)	727 (322-1323)
All-cause mortality	7	1	1	1	1	4
Cardiovascular mortality	5	0	1	1	0	3
Aortic-valve replacement	23	0	0	0	12	11
Composite outcome	28	0	1	1	12	14

AV: aortic valve; AU: arbitrary unit

Figure 4.3 | Positron Emission Tomography, Aortic Valve Calcification And Imaging Defined Disease Severity

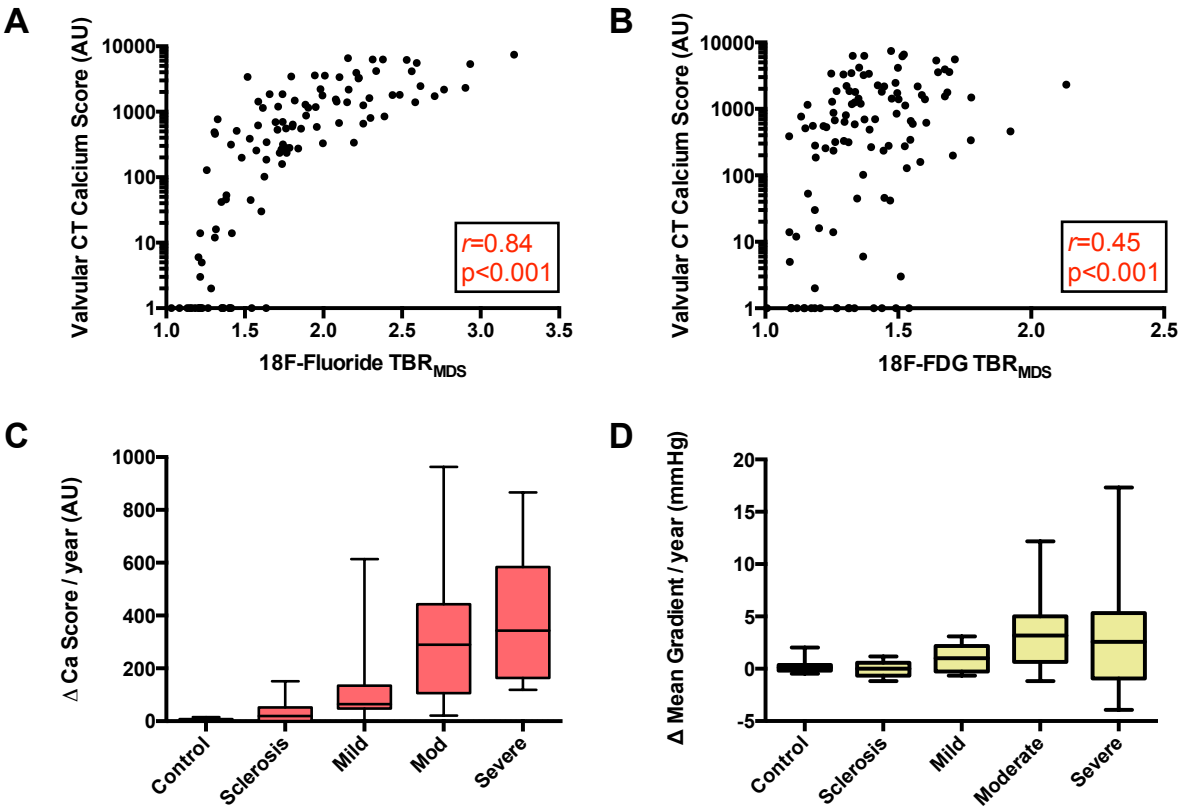

A & B: Scatterplots displaying the relationship between the baseline aortic valve computed tomography calcium score and baseline valvular 18F-fluoride and 18F-FDG uptake. To better demonstrate the lower calcium score data, a $\log_{10}$ scale has been used on the *y*-axis.

C & D: Box and whisker plots displaying the progression in aortic valve disease within each disease severity cohort, as assessed by the yearly change in aortic valve computed tomography calcium score and mean aortic valve gradient.

AV: aortic valve; FDG: fluorodeoxyglucose; MDS: Most Diseased Segment; TBR: tissue to background ratio

4.5.4 Prediction of Disease Progression

A strong correlation was observed between baseline 18F-fluoride uptake in the valve and the subsequent rate of progression in the aortic valve calcium score (r=0.80 [0.60–0.86], p<0.001; Table 4.7 and Figure 4.4). An alternative analysis of the relationship between 18F-fluoride uptake and disease progression as measure by the change in the valvular calcium score is shown in Figure 4.5. Here, we generated a regression line between 18F-fluoride uptake and baseline valvular calcium score. We defined data points above the regression line as subjects with a greater than expected 18F-fluoride uptake for a given contemporaneous calcium score and points below the line as less than expected. We then compared annualised progression in calcium score between these two cohorts, and found that patients with greater than expected 18F-fluoride uptake (for a given calcium score), showed a three-fold higher rate of progression that those with less than expected uptake. We did not observe the same phenomenon with 18F-FDG.

Moderate correlations were observed between valvular 18F-fluoride uptake and echocardiographic indices of disease progression, i.e. the rate of change in mean gradient (r=0.32 [0.13–0.50], p=0.001), peak aortic jet velocity (r=0.23 [0.03–0.41], p=0.001), and peak gradient (r=0.32 [0.12–0.49], p=0.002).

Moderate correlations were observed between baseline 18F-FDG valvular uptake and the rate of progression of the CT calcium score (r=0.43 [0.23–0.59], p<0.001), the mean gradient (r=0.26 [0.06–0.44], p=0.001), the peak velocity (r=0.24 [0.03–0.42], p=0.02), and peak gradient (r=0.33 [0.14–0.50], p=0.001).

There were strong associations between the baseline CT valvular calcium score and rate of change in calcium score (r=0.88 [0.82-0.92], p<0.001), similar to those observed for 18F-fluoride. Moderate associations were also observed between the baseline calcium score and the progression in echocardiographic measures of disease severity (change in mean gradient, r=0.40 [0.21–0.56], p < 0.001; change in peak velocity, r=0.36 [0.16–0.53], p < 0.001; and change in

peak gradient, r=0.46 [0.27–0.61], p<0.001). Finally, there was a moderate association noted between the rate of change in valvular calcium score and haemodynamic measures of progression (change in mean gradient, r=0.45 [0.26-0.61], p<0.001; and change in peak gradient, r=0.41 [0.22-0.58], p<0.001).

Table 4.7 | Baseline Imaging And Prediction Of Disease Progression

Baseline Imaging Assessment	**Rate of change in AV Calcium Score (AU yr^{-1})**	**Rate of change in aortic jet velocity (m s^{-1} yr^{-1})**	**Rate of change in mean gradient (mmHg yr^{-1})**	**Rate of change in peak gradient (mmHg yr^{-1})**	**Rate of change in Aortic Valve Area (cm^2 yr^{-1})**
PET Valvular Radiotracer Uptake					
18F-fluoride mean TBR_{MDS}	*r*=0.80 (0.60-0.86) P<0.001	*r*=0.23 (0.03-0.41) P=0.001	*r*=0.32 (0.13-0.50) P=0.001	*r*=0.32 (0.12-0.49) P=0.001	*r*=0.11 (-0.10-0.31) P=0.29
18F-FDG mean TBR_{MDS}	*r*=0.43 (0.23-0.59) P<0.001	*r*=0.28 (0.08-0.46) P=0.005	*r*=0.30 (0.10-0.47) P=0.002	*r*=0.36 (0.17-0.53) P<0.001	*r*=-0.14 (-0.33-0.07) P=0.18
CT Assessment					
AV Calcium Score (AU)	*r*=0.88 (0.82-0.92) P<0.001	*r*=0.36 (0.16-0.53) P<0.001	*r*=0.40 (0.21-0.56) P<0.001	*r*=0.46 (0.27-0.61) P<0.001	*r*=0.06 (-0.15-0.27) P=0.54
Echocardiographic Assessment					
Aortic jet velocity (m s^{-1})	*r*=0.79 (0.70-0.86) P<0.001	*r*=0.28 (0.08-0.45) P=0.006	*r*=0.40 (0.22-0.56) P<0.001	*r*=0.39 (0.21-0.55) P<0.001	*r*=0.08 (-0.13-0.27) P=0.45

AV, aortic valve; AU, arbitrary unit; CT, computed tomography; FDG, fluorodeoxyglucose; MDS, most diseased segment; PET, positron emission tomography; TBR, tissue to background ratio

Figure 4.4 | 18F-Fluoride Positron Emission Tomography and the Progression in Aortic Valve Calcification

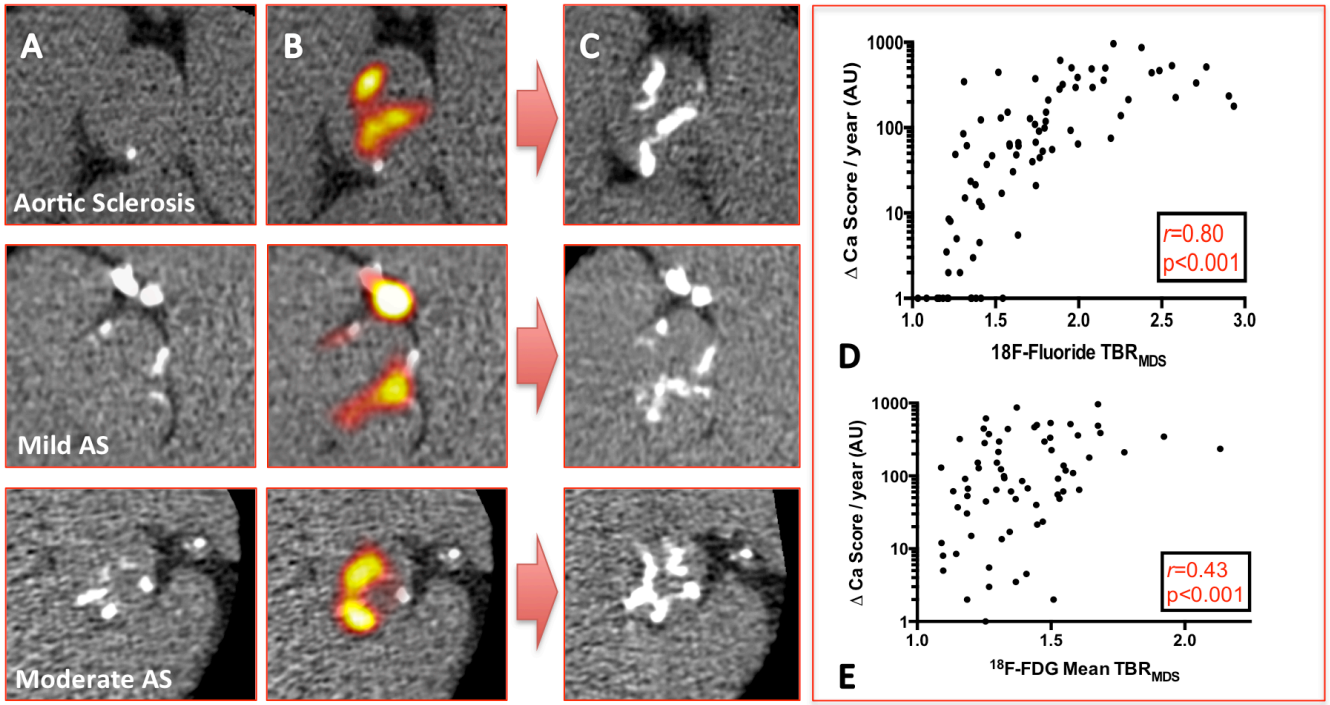

Co-axial short-axis views of the aortic valve in 3 separate study subjects and disease severity categories.

A Baseline CT calcium score scans with relatively little in the way of established calcium in the valve (white)

B Fused PET/CT images with increased 18F-fluoride valvular uptake (red and yellow regions) that does not well align with the established calcium on the CT. Also note the increased uptake in the proximal left anterior descending coronary artery

C Repeat CT calcium score at 2 years, demonstrating an increase in the amount of established macroscopic calcium in much the same distribution as the baseline PET uptake.

D-E Scatterplots demonstrating the close relationship between progression in the aortic valve computed tomography calcium score and baseline valvular 18F-fluoride (**D**) and 18F-FDG (**E**) uptake. To better demonstrate the lower calcium score data a $\log_{10}$ scale has been used on the y-axis.

AS, aortic stenosis; AU, arbitrary units; CT, computed tomography; FDG, fluorodeoxyglucose; MDS, Most Diseased Segment; PET, positron emission tomography; TBR, tissue to background ratio

Figure 4.5 | 18F-Fluoride Uptake Indexed To Baseline CT Calcium Score

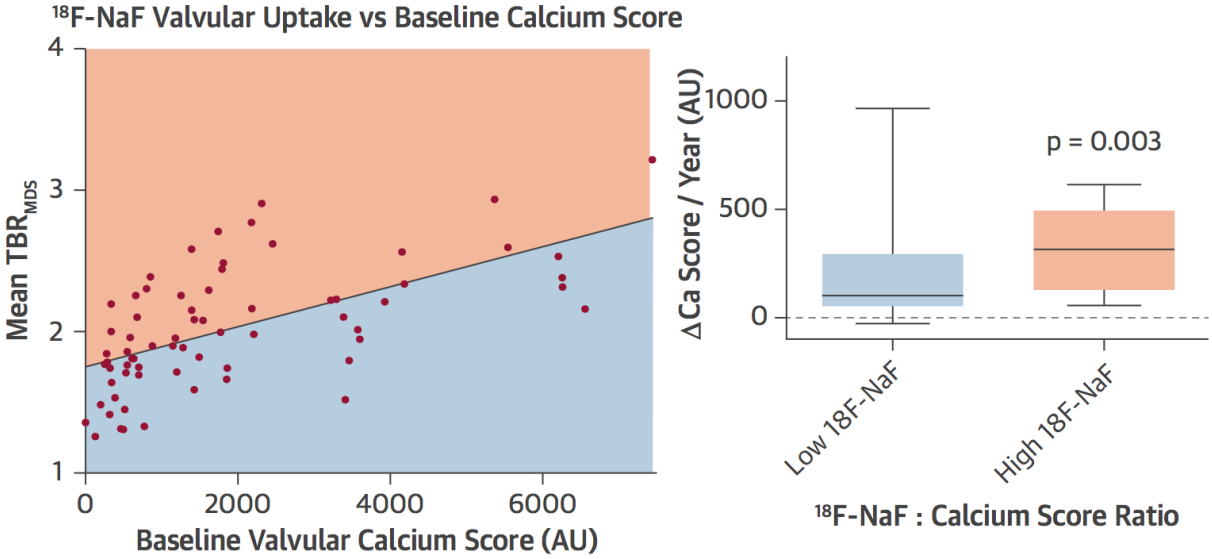

AS, aortic stenosis; TBR_{MDS}, most diseased segment tissue to background ratio; 18F-NaF, 18F-fluoride.

4.5.5 Prediction of Clinical Outcome

Using Cox regression analysis, valvular 18F-fluoride uptake emerged as a predictor of clinical outcome (cardiovascular mortality or AVR or all cause death) independent of age and sex (HR (hazard ratio): 1.46, 95% CI (confidence interval): 1.24 to 1.71; $p<0.0001$). The same was true of baseline 18F-FDG activity (HR: 1.59, 95% CI 1.21 to 2.09; $p=0.002$).

To facilitate comparison, the HR are expressed per decile of the full range of TBR_{MDS} values for each tracer. The baseline aortic valve CT calcium score also offered powerful prediction of clinical outcomes (HR per 10-fold change in calcium score: 32.02, 95% CI: 7.98-130.43; $p<0.0001$ after adjustment for age and sex). Finally, we assessed the echocardiographic calcium score. However, this performed poorly, with only a maximum score of 4 providing any risk prediction (Table 4 .8 and Figure 4.6).

Table 4.8 | Predicting Clinical Outcome

	Unadjusted HR (95% CI)	*P* Value	Age and Sex Adjusted HR (95% CI)	*P* Value
18F-Fluoride Valvular Uptake TBR_{MDS} (per 10th of range)	1.45 (1.24 - 1.69)	<0.001	1.46 (1.24 - 1.71)	<0.001
18F-FDG Valvular Uptake TBR_{MDS} (per 10th of range)	1.61 (1.23 – 2.11)	0.002	1.59 (1.21 – 2.09)	0.002

		Unadjusted HR (95% CI)	*P* Value	Age and Sex Adjusted (95% CI)	*P* Value
CT AV Calcium Score (per 10-fold increment)		17.6 (5.60 - 55.38)	<0.001	32 (7.98 - 130.43)	<0.001
Echocardiographic AV Calcium Score (ECS)	ECS				
	1	Reference	-	Reference	-
	2	0.58 (0.04 - 9.31)	0.702	0.53 (0.03 - 8.458)	0.650
	3	5.35 (0.71 - 40.41)	0.104	5.36 (0.71 - 40.68)	0.104
	4	16.9 (2.19 - 130.86)	0.007	17.0 (2.18 - 132.4)	0.007

AV, aortic valve; AU, Arbitrary Unit; CI, confidence interval; CT, computed tomography; ECS, echocardiographic calcium score; FDG, fluorodeoxyglucose; HR, hazard ratio; MDS, Most Diseased Segment; TBR, tissue to background ratio

Figure 4.6 | Prediction Of Clinical Outcome

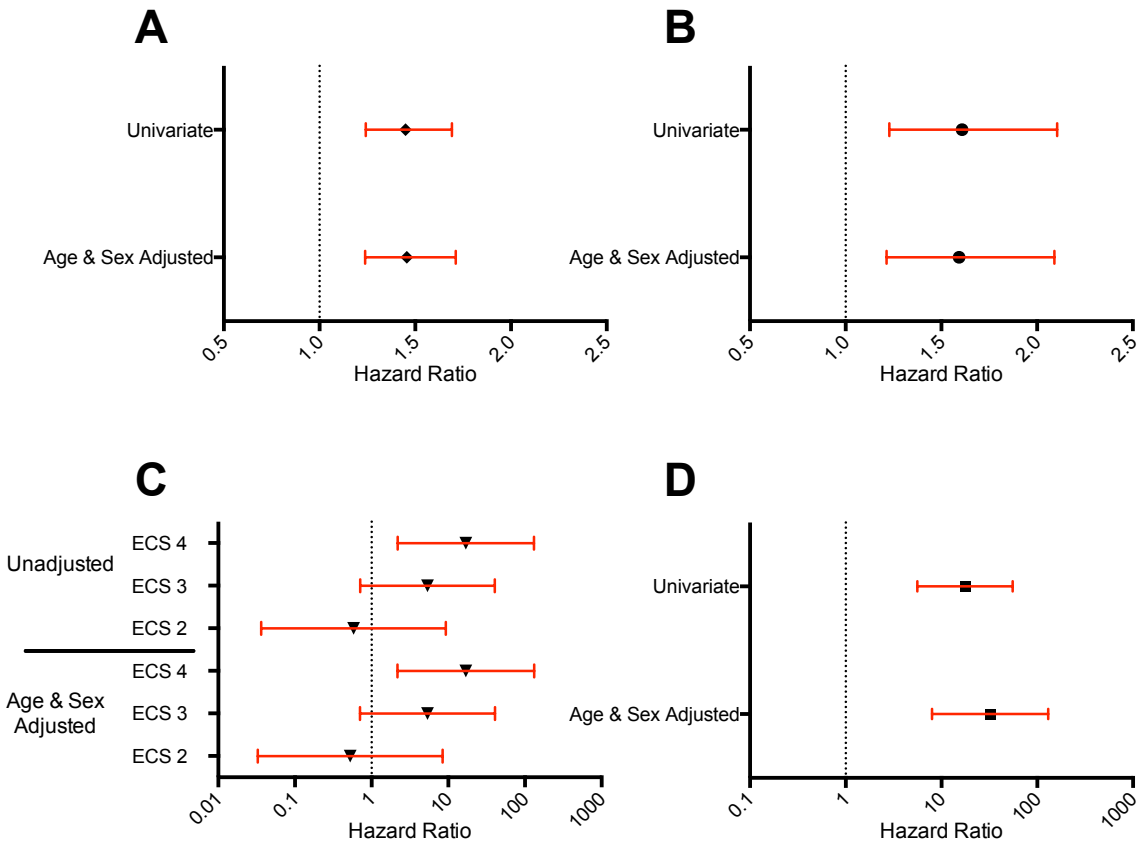

A 18F-Fluoride (HR are per 10th of range of mean TBR_{MDS} values)

B 18F-FDG (HR are per 10th of range of mean TBR_{MDS} values)

C Echocardiographic calcium score (with ECS score of 0 as reference)

D CT Calcium Score (HR – per 10-fold increase in AU)

Red bars are 95% confidence intervals

AU, arbitrary units; CT, computed tomography; ECS, echocardiographic calcium score; FDG, fluorodeoxyglucose; HR, hazard ratio

4.6 Discussion

We here report the first prospective longitudinal study to investigate the utility of 18F-fluoride and 18F-FDG PET/CT imaging in patients with aortic stenosis. We have demonstrated that both tracers offer a prediction of disease progression and adverse clinical outcome. 18F-fluoride appears to have a greater utility over 18F-FDG, providing an excellent prediction of the change in CT calcium score over a 2-year period and emerging as an independent predictor of cardiovascular death and AVR after adjustment for both age and sex. This would support calcification as the predominant pathological process in aortic stenosis and 18F-fluoride as a biomarker capable of quantifying its activity and predicting the natural history of this condition.

4.6.1 18F-Fluoride In Aortic Stenosis

An advantage that PET holds over other mainstream imaging modalities, such as CT, is that it goes beyond anatomy and is able to resolve valvular cellular pathophysiology. PET can provide immediate non-invasive quantification of on-going and potentially modifiable pathological processes within the body. This includes vascular calcification activity. Indeed, recent interest has surrounded 18F-fluoride as a marker of newly developing microcalcification in the coronary arteries that can be used to identify culprit and high-risk atheromatous plaque. (117) This tracer has also been investigated in aortic stenosis, with studies confirming that 18F-fluoride uptake correlates closely with histological markers of valvular calcification activity. (136) In a small interim analysis, we have previously reported that 18F-fluoride predicts the change in the aortic valve calcium score after 1 year. (136) We here extend these observations to a larger broader population with longer follow up. We have demonstrated that 18F-fluoride PET provides excellent prediction of disease progression as assessed by CT ($r=0.80$, $p<0.001$), and for the first time that it also predicts echocardiographic measures of hemodynamic progression. In addition, 18F-fluoride PET is an independent predictor of clinical outcome (cardiovascular death and AVR) even after adjustment for age and sex. In combination, these

data confirm 18F-fluoride PET as a non-invasive measure of disease activity in aortic stenosis, with the ability to predict its natural history.

4.6.2 Computed Tomography in Aortic Stenosis

Might 18F-fluoride PET be of use in the clinical setting as a tool for predicting disease progression and risk stratifying patients? The more widespread application of this technique is likely to be limited by cost, availability and radiation exposure. Furthermore, our results would suggest that simple CT calcium scoring is better suited to this role. (140) Whilst CT is unable to measure calcification activity in the valve directly, it is able to reliably and accurately quantify the progressive accumulation of macroscopic areas of established calcium within the valve. Indeed, our data would suggest that tracking disease progression with CT is perhaps easier than with traditional hemodynamic echocardiography measures given the relatively larger increases in the CT calcium score with time and its excellent reproducibility. Furthermore, because calcification activity increases proportionally with disease severity (Figure 4.3), baseline CT calcium scoring also provides a good surrogate marker of disease activity. This would explain the excellent prediction of disease progression and clinical outcomes provided by CT in this and other recent studies. (140,141) Therefore we believe that this simple and widely available technique is likely to assume a greater clinical role in the future, supported by its superior reproducibility to echocardiographic calcium scoring and incremental prognostic ability over and above the more traditional hemodynamic severity assessments. (28,140,142)

4.6.3 The Application Of 18F-Fluoride PET

We have previously hypothesized that calcification is the predominant driver of disease progression in aortic stenosis, and that anti-calcific interventions may slow or halt disease progression. (101) 18F-fluoride PET imaging would appear to be an excellent means of testing the efficacy of such novel potential therapeutic approaches. (18) The instant readout of valvular calcification

activity that 18F-fluoride PET provides has the potential to detect rapidly beneficial treatment effects without the need for protracted follow up. This contrasts favourably with more established imaging modalities such as CT calcium scoring and echocardiography that take many years to identify the anatomic and hemodynamic consequences of such alterations in disease activity. Ultimately 18F-fluoride PET has the potential to reduce the duration of clinical studies investigating the efficacy of novel treatments, and thereby to expedite their development.

4.6.4 18F-FDG In Aortic Stenosis

In this study, we applied a novel method of assessing valvular radiotracer uptake: Most Diseased Segment (MDS). This approach is simpler than previous methods and was highly reproducible, demonstrating a clear advantage to standard techniques with respect to 18F-FDG imaging. Cardiac 18F-FDG imaging has been hampered by myocardial uptake, making assessment of adjacent structures such as the aortic valve and coronary arteries challenging. In this study, we observed an association between baseline 18F-FDG uptake in the valve and disease progression at 2 years, albeit more modest than for either 18F-fluoride or calcium scoring. This result should, however, be interpreted with some caution as the exact mechanisms underlying 18F-FDG activity in the valve remain unclear. Previous studies have established a correlation between macrophage burden and 18F-FDG uptake in carotid atheroma. However, we have previously failed to demonstrate any such association in the aortic valve, (136) questioning whether 18F-FDG is truly acting as a marker of macrophage infiltration in aortic stenosis. Indeed 18F-FDG uptake is not limited to macrophages but instead can potentially reflect the metabolic requirements of a wide range of cells that utilize glucose. In aortic stenosis, 18F-FDG uptake might reflect uptake by valvular fibroblasts and osteoblasts as well as myocytes in the closely adjacent myocardium. (76) Further work is required to resolve this key issue and to better understand the information that 18F-FDG is providing in aortic stenosis.

4.6.5 Study Limitations

There are a number of limitations that we acknowledge. Firstly, due to the absolute number of clinical events in our cohort, we are unable to demonstrate the incremental value, if any, of valvular PET radiotracer uptake compared to CT calcium score. Secondly, the PET data were not motion corrected. This has limited our ability to investigate whether the spatial distribution of 18F-fluoride uptake within the valve is of importance and how this relates to the macroscopic calcium deposits seen on CT. We also need to establish whether modification of 18F-fluoride PET uptake can be achieved by potential therapeutic interventions, such as anti-calcific therapies, and whether any such reduction translates in to improved clinical outcomes. These are key priorities that need to be addressed in prospective studies using gated PET acquisitions.

4.6.6 Conclusions

This prospective cohort imaging study proves that 18F-fluoride PET is an excellent predictor of disease progression and adverse clinical outcomes in patients with aortic stenosis and matches the current best predictor; the CT aortic valve calcium score. The immediate readout of disease activity that it provides holds great promise in rapidly assessing the treatment effects of novel medical therapies for this important condition.

Chapter 5 – 18F-Fluoride and 18F-Fluorodeoxyglucose Hybrid Positron Emission Tomography and Computed Tomography In Atherosclerosis – A Pilot Study With Imaging And Histological Validation

5.1 Publication In Context

5.1.1 Background

During the analysis of aortic valve imaging data in the Ring of Fire Study(120), a key observation was made; significant coronary arterial uptake of 18F-fluoride was apparent and quantifiable. Coronary uptake was shown to correlate with Framingham and ASSIGN(143) risk scores indicating that the radioisotope may provide information on cardiovascular risk. These data were published by Dr Dweck. (121) However, a single particularly interesting finding was noted. One patient was recruited shortly after experiencing an acute coronary syndrome. The patient underwent invasive coronary angiography and the culprit lesion was found in the circumflex artery. The lesion was left untreated and the patient managed medically. At his PET scan, he was found to have intense uptake of 18F-fluoride at the site of the culprit lesion (highlighted with a white arrow in Figure 5.1).

Figure 5.1 | Original Fused 18F-Fluoride PET/CT Showing Uptake In Culprit Coronary Plaque

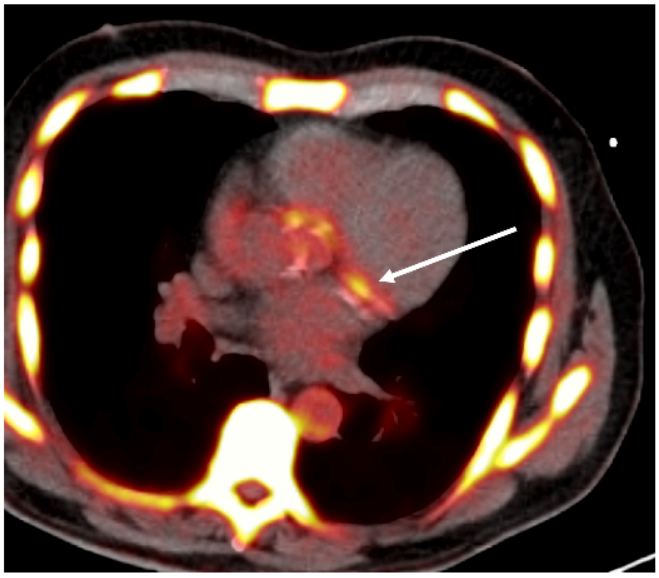

This finding suggested that 18F-fluoride uptake might identify recent plaque rupture; a very exciting and potentially practice changing possibility. This led us two apply successfully for two grants:

- Chief Scientist Office, Scotland (ETM/160)
- British Heart Foundation (PG/12/8/29371)

The first grant funded the work that is the basis of this chapter and the second funded the work that is presented in Chapters 6 and 7.

5.1.2 Aims of Further Study

Based on the unexpected but promising coronary findings in the aortic stenosis cohort, we undertook to conduct a pilot prospective observational cohort study specifically studying patients with coronary and carotid atherosclerosis aimed at answering the following questions:

1. Is 18F-fluoride and 18F-FDG PET/CT imaging of coronary atherosclerosis feasible?
2. Can either coronary 18F-fluoride or 18F-FDG PET/CT identify acute "culprit" plaque in a cohort of patients with acute coronary syndromes?
3. Can either coronary 18F-fluoride or 18F-FDG PET/CT identify high-risk plaque, defined using both *in vivo* intra-coronary ultrasound and CT coronary angiography, in a cohort of patient with stable coronary heart disease?
4. Is such imaging reproducible?
5. Using carotid plaque excised at the time of carotid endarterectomy (an operation offered to patients with an acute neurovascular syndrome analogous to an acute coronary syndrome), is it possible to provide:
    a. Histological validation of our *in vivo* coronary findings?
    b. A plausible mechanistic explanation for our findings?

5.1.3 Contributions

Dr Joshi and I led this work. He recruited and scanned the coronary cohorts. I recruited the carotid cohort and collected the endarterectomy specimens. I performed the *ex vivo* PET/CT of carotid plaque, *in vivo* patient PET/CT scans and the histological and immunohistochemical experiments. I also performed all the analyses for these experiments. We drafted the paper together. For the purposes of this thesis monograph, the supplementary appendices have been incorporated into the text for narrative clarity.

Published as: Joshi NV, **Vesey AT**, Williams MC, Shah ASV, Calvert PA, Craighead FHM, et al. 18F-fluoride positron emission tomography for identification of ruptured and high-risk coronary atherosclerotic plaques: a prospective clinical trial. *Lancet*. 2014 Feb 22;383(9918):705–13.

5.2 Abstract

5.2.1 Background

The use of non-invasive imaging to identify ruptured or high-risk coronary atherosclerotic plaques would represent a major clinical advance for prevention and treatment of coronary artery disease. We used combined PET and CT to identify ruptured and high-risk atherosclerotic plaques using the radioactive tracers 18F-sodium fluoride (18F-fluoride) and 18F-fluorodeoxyglucose (18F-FDG).

5.2.2 Methods

In this prospective clinical trial, patients with myocardial infarction (n=40) and stable angina (n=40) underwent 18F-fluoride and 18F-FDG PET-CT, and invasive coronary angiography. 18F-fluoride uptake was compared with histology in carotid endarterectomy specimens from patients with symptomatic carotid disease, and with intravascular ultrasound in patients with stable angina. The primary endpoint was the comparison of 18F-fluoride tissue-to-background ratios of culprit and non-culprit coronary plaques of patients with acute myocardial infarction.

5.2.3 Results

In 37 (93%) patients with myocardial infarction, the highest coronary 18F-fluoride uptake was seen in the culprit plaque (median maximum tissue-to-background ratio: culprit 1·66 [IQR 1·40–2·25] vs highest non-culprit 1·24 [1·06–1·38], p<0·0001). By contrast, coronary 18F-FDG uptake was commonly obscured by myocardial uptake and where discernible, there were no differences between culprit and non-culprit plaques (1·71 [1·40–2·13] vs 1·58 [1·28–2·01], p=0·34). Marked 18F-fluoride uptake occurred at the site of all carotid plaque ruptures and was associated with histological evidence of active calcification, macrophage infiltration, apoptosis, and necrosis. 18 (45%) patients with stable angina had plaques with focal 18F-fluoride uptake (maximum tissue-to-background ratio 1·90 [IQR 1·61–2·17]) that were associated with more high-risk features on intravascular ultrasound than those without uptake: positive remodelling (remodelling index 1·12 [1·09–1·19] vs

1·01 [0·94–1·06]; p=0·0004), microcalcification (73% vs 21%, p=0·002), and necrotic core (25% [21–29] vs 18% [14–22], p=0·001).

5.2.4 Conclusion

18F-fluoride PET-CT is the first non-invasive imaging method to identify and localise ruptured and high-risk coronary plaque. Future studies are needed to establish whether this method can improve the management and treatment of patients with coronary artery disease.

5.3 Introduction

Coronary atherosclerotic plaque rupture is the principal precipitant of acute myocardial infarction and an important cause of sudden cardiac death. Rupture is challenging to predict because most plaques are non-obstructive and are not identified by stress testing or coronary angiography. (144,145) Atherosclerotic lesions at risk of rupture have certain histopathological characteristics that include positive re-modelling, microcalcification, and a large necrotic core. (52,144,145) The development of modern molecular imaging techniques targeted at these features could lead to the identification of such high-risk plaques *in vivo* and guide the development of novel treatment strategies. (121,146-148)

Combined PET and CT is a non-invasive imaging technique that brings functional molecular imaging together with precise anatomical information. We have recently reported preliminary PET/CT data using the tracer 18F-sodium fluoride (18F-fluoride) as a marker of valvular and vascular calcification activity in patients with aortic stenosis. (118,120,121) Other studies have shown the usefulness of 18F-flurodeoxyglucose (18F-FDG) as a surrogate of vascular inflammation and macrophage burden. (130,146,149-151) We therefore investigated whether, compared with the current non-invasive gold standard of 18F-FDG, 18F-fluoride uptake could identify ruptured and high-risk atherosclerotic plaques in patients with symptomatic coronary and carotid artery disease.

5.4 Methods

5.4.1 Patients

Patients were recruited from the Royal Infirmary of Edinburgh between February, 2012, and January, 2013, in three cohorts (see figure 5.2):

1. 40 patients with acute ST-segment or non- ST-segment elevation myocardial infarction. Consecutive patients were approached and recruited if they fulfilled the criteria for type 1 myocardial infarction according to the Universal Definition of Myocardial Infarction. (152) ST segment elevation myocardial infarction was defined as new ST segment elevation at the J point in two contiguous leads with the cut-points: ≥0·1 mV in all leads except V2-V3 where the thresholds were ≥0·2 mV for men ≥40 years and ≥0·25 mV for women.
2. 40 patients with stable angina pectoris undergoing elective invasive coronary angiography. Consecutive patients with stable angina pectoris were recruited if they had typical symptoms of exertional anginal chest pain, previously documented coronary artery disease (>70% stenosis of at least one major epicardial coronary artery), and had been scheduled for invasive coronary angiography. Patients were excluded if they had suffered an acute coronary syndrome within the last 3 months.
3. 12 patients (nine evaluable) undergoing carotid enterectomy for symptomatic carotid artery disease. Patients with typical symptoms and signs of an acute transient ischemic attack, amaurosis fugax or stroke were recruited within 1-14 days of symptom onset. All patients underwent clinical evaluation and carotid Doppler assessment. Inclusion criteria were carotid stenosis >50% (North American Symptomatic Carotid Endarterectomy Trial [NASCET] criteria) (110) consistent with clinical presentation, and planned carotid endarterectomy.

Exclusion criteria were age younger than 50 years, insulin-dependent diabetes mellitus, women of child-bearing age not receiving contraception, severe renal failure (serum creatinine >250 μmol/L), known contrast allergy, and inability to provide informed consent. Only patients older than 50 years were recruited in the study to reduce any long-term risks associated with radiation exposure. Uncontrolled diabetes and high blood glucose concentrations (>11 mmol/L) interfere with the quality of 18F-FDG PET imaging because of the competition between glucose and 18F-FDG for cellular entry. The convention is therefore to exclude such patients from vascular 18F-FDG PET studies. (121,130,150,151) All patients underwent a comprehensive baseline clinical assessment including evaluation of their cardiovascular risk factor profile. Plasma troponin I concentrations were measured in patients with stable angina using the ARCHITECT STAT high-sensitivity troponin I assay (Abbott Laboratories, Abbott Park, IL, USA; lower limit of detection 1·2 ng/L; 99th percentile diagnostic threshold 26 ng/L). Studies were done with the approval of the local research ethics committee, in accordance with the Declaration of Helsinki, and with the written informed consent of each participant.

Figure 5.2 | Study Design

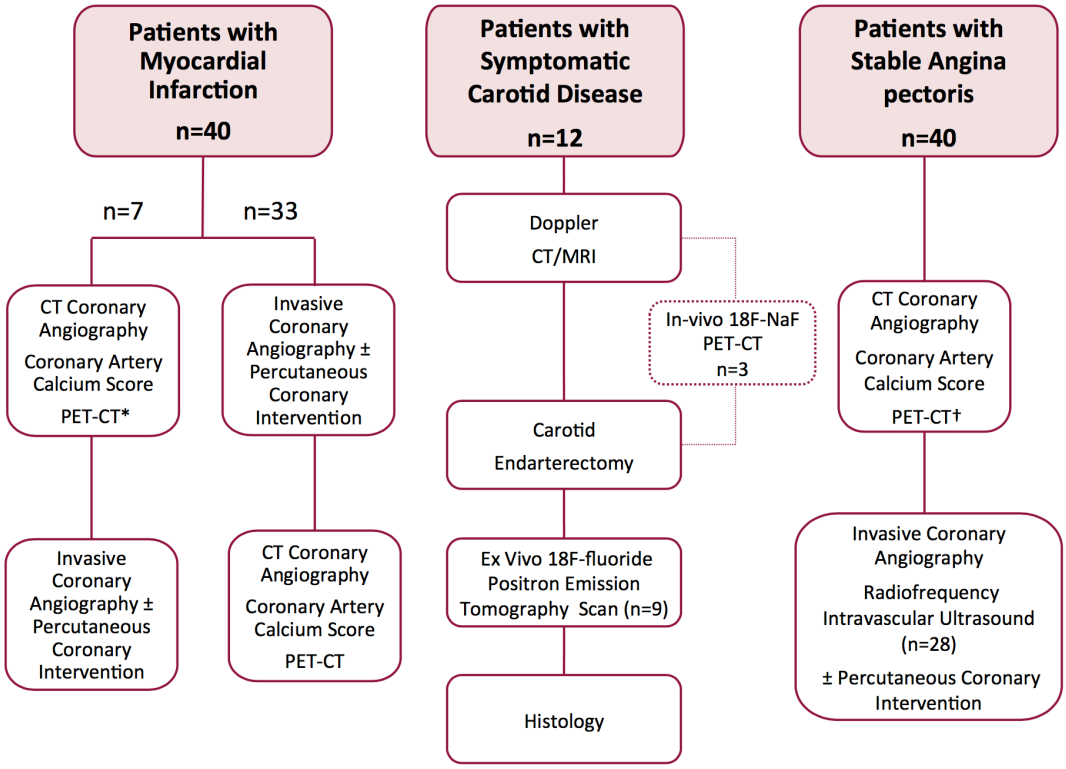

Patients were recruited in three cohorts: myocardial infarction, symptomatic carotid disease and stable angina. They underwent a series of investigations as shown in the flow diagram; PET-CT: 18F-fluoride and 18F-fluorodeoxyglucose positron emission tomography-computed tomography, MRI: Magnetic Resonance Imaging. *In seven patients with myocardial infarction, the 18F-fluorodeoxyglucose scans were undertaken after percutaneous coronary intervention. †In five patients with stable angina, the 18F-fluorodeoxyglucose scans were undertaken after their elective percutaneous coronary intervention.

5.4.2 Procedures

Patients with myocardial infarction and stable angina underwent 18F-fluoride and 18F-FDG PET-CT, CT coronary angiography, and CT calcium scoring (see figure 5.1). (121)

Patients with a heart rate exceeding 65 beats min^{-1} received oral beta-blockade (50 or 100 mg metoprolol) 1 h before the computed tomography (CT) examination. All patients received sublingual glyceryl trinitrate (300 μg) just prior to the CT coronary angiography (CTCA). Patients were asked to refrain from alcohol and caffeine on the day of the scan.

5.4.2.1 Visit 1: 18F-Fluoride

All patients underwent dual cardiac and respiratory-gated positron emission tomography (PET)-CT imaging of the coronary arteries with a hybrid scanner (64- multidetector Biograph mCT, Siemens Medical Systems, Erlangen, Germany). Study subjects were administered a target dose of 125 MBq 18F-fluoride (18F-fluoride) intravenously and subsequently rested in a quiet environment for 60 min. An attenuation correction CT scan (non-enhanced 120 kV and 50 mA) was then performed, followed by PET imaging of the thorax in list-mode for 20 min. Coronary artery calcium and CTCA were undertaken in the same visit as the 18F-fluoride scan. With the patient lying still on the scanner after acquisition of the PET, an electrocardiogram-gated breath-hold CT scan (non-contrast-enhanced, 40 mAs/rotation, 120 kV; CareDose, Siemens Medical Systems) of the coronary arteries was performed. CTCA was performed using the following settings: 330 ms rotation time, 100 (body mass index [BMI] <25 kg/m2) or 120 (body mass index >25 kg/m2) kV tube voltage, 160-245 mAs tube current, 3·8 mm/rotation table feed, prospective (heart rate regular and <60/min), or retrospective (heart rate >60 /min) electrocardiogram-gated. Depending on the BMI, a bolus of 80-100 mL of contrast (400 mgI/mL; Iomeron, Bracco, Milan, Italy) was injected intravenously at 5 mL/s, after determining the appropriate trigger delay with a test bolus of 20 mL contrast material.

Although the PET scans were acquired with the potential for dual motion correction, inclusion of respiratory gating led to significant loss of signal with increased noise. Therefore, only electrocardiogram-gated cardiac motion correction was undertaken. The PET scans were reconstructed in multiple phases of the cardiac cycle, with the diastolic phase (50–75% of the R-R interval) using the Siemens Ultra-HD algorithm. The CTCA scans were reconstructed at 0·75 x 0·7 mm and 0·6 x 0·3 mm for retrospective and prospective acquisitions respectively at 60%, 65% and 70% of the cardiac cycle. Additional reconstructions were undertaken if necessary.

5.4.2.2 Visit 2: 18F-Fluorodeoxyglucose

Intense uptake of 18F-fluorodeoxyglucose (18F-FDG) by the left ventricle leads to difficulties in discriminating between activity in the coronary arteries and the myocardium. All patients in our cohort were asked to observe a low-carbohydrate, high-protein and high-fat diet for 24 hours before their 18F-FDG scan because this suppresses myocardial uptake as the heart switches from glucose to free fatty acid metabolism. (121,130,150,151,153) Patients were provided with a list of food and drink to avoid and reminded of these restrictions the day before their scan. Dietary diaries were recorded for all patients.

Subjects were administered a target dose of 200 MBq 18F-FDG intravenously and subsequently rested in a quiet environment for 90 min. Combined PET-CT imaging was then performed as described for the 18F-fluoride scan.

5.4.2.3 Image Analysis

Electrocardiograph-gated PET images were fused with the CT coronary angiogram, and analysed by experienced observers blinded to the clinical diagnosis using an OsiriX workstation (OsiriX version 5·5·1 64-bit; OsiriX Imaging Software, Geneva, Switzerland). Two- dimensional regions of interest

were drawn around all major (diameter>2mm) epicardial vessels on 3mm axial slices just beyond the discernible adventitial border. The maximum standard uptake value (the decay corrected tissue concentration of the tracer divided by the injected dose per bodyweight) was measured and corrected for blood pool activity in the superior vena cava to provide tissue-to-background ratio (TBRs) measurements. Using this method, we have previously shown excellent reproducibility for 18F-fluoride TBR measurements in the coronary arteries with an intraclass correlation coefficient of 0·99. (121)

We used a previously established 95% lower reference limit to categorise coronary plaques into 18F-fluoride positive lesions (focal uptake with a TBR more than 25% higher than a proximal reference lesion) and negative plaques if these criteria were not achieved. This limit was based on our previous study, where plaques with high 18F-fluoride uptake had maximum TBRs that were 44% (95% CI 26–62) higher than a proximal quiescent reference lesion. (121) In patients with acute myocardial infarction, 18F-fluoride uptake in the culprit plaque was compared with the highest value in any of the non-culprit vessels.

Quantification of 18F-FDG uptake was performed as for 18F-fluoride uptake but restricted to the proximal and mid- portions of the coronary arteries, and to regions where myocardial uptake and spillover could be confidently excluded. (121) Again, 18F-FDG positive plaques were defined using the 25% threshold as described for 18F-fluoride. Effective myocardial suppression of 18F-FDG was predefined as a standard uptake value of 5·0 or less in the basal ventricular septum as per published data. (150)

In patients with stable angina, PET-CT imaging was prospectively used to direct greyscale and radio-frequency intravascular ultrasound (20 MHz Eagle Eye Platinum Catheters [Volcano Corp, San Diego, CA, USA], motorised pull-back 0·5 mm/s) to 18F-fluoride positive and negative plaques. The interventional cardiologist acquiring the intravascular ultrasound data was blinded to the PET-CT status of the plaque.

Intravascular ultrasound analysis was done as described previously(154) using dedicated VIAS software (Volcano Image Analysis Software version 3.0) by operators blinded to the PET data. Regions of interest were drawn around the external elastic membrane and luminal borders, and plaque area and composition (dense calcium, necrotic core, fibro-fatty tissue, and fibrous tissue) calculated. (154-156)The presence of microcalcification (spotty calcification in the absence of acoustic shadowing on three or more consecutive frames) and the maximum frame necrotic core (the highest percentage of necrotic core on a single frame) were recorded. (157) The remodelling index was defined as the ratio between the external elastic membrane cross-sectional area of the lesion and a proximal reference region in the same vessel. (158) Plaques were classified as thin-cap fibroatheroma, thick-cap fibro- atheroma, pathological intimal thickening, or fibrocalcific plaque as defined previously. (156,159)

CT analysis was done on a dedicated cardiovascular workstation (Vital Images, Minnetonka, MN, USA). Vessel-specific and total Agatston calcium scores were calculated as described previously. (121) An independent experienced and blinded observer determined the stenosis severity, plaque composition (calcified, non- calcified, mixed plaque), and presence of high-risk CT features (positive remodelling, microcalcification, necrotic core) according to standard definitions in plaques with and without increased 18F-fluoride activity. (160)

5.4.2.4 Image Analysis Reproducibility

Thirty patients were selected randomly to test the repeatability of image analysis in between two trained readers. Fifteen patients from each of the 18F-FDG and 18F-fluoride cohorts were selected and each reader repeated the analysis of these patients independently in random order to avoid recall bias.

5.4.3 Carotid Experiments

5.4.3.1 Summary

Intact atherosclerotic plaques were retrieved at the time of carotid endarterectomy and scanned using *ex-vivo* PET-CT to allow precise anatomical co-localisation of 18F-fluoride activity with pathological evidence of plaque rupture. Plaques were divided into 18F-fluoride positive and negative areas, and histological sections were assessed using Movat's pentachrome and immunohistochemistry to investigate calcification activity (tissue non-specific alkaline phosphatase and osteocalcin), macrophage infiltration (CD68), and cell death (apoptosis, cleaved caspase 3; microscopic presence of necrotic core).

5.4.3.2 Ex Vivo 18F-Fluoride Positron Emission Tomography

At the moment of retrieval during surgery, plaques were photographed before being wrapped in foil and snap frozen in liquid nitrogen. Subsequently, they were thawed in a batch and immersed in 18F-fluoride solution diluted with phosphate buffered saline (PBS) to a total activity of 10 MBq/mL. After 60 min, plaques were rinsed 3 times in PBS before being oriented and placed in a clinical PET-CT hybrid scanner (64-multidetector Biograph mCT, Siemens Medical Systems, Erlangen, Germany). After an attenuation correction CT scan, PET imaging was undertaken over a single bed for 15 min.

5.4.3.3 Histology and Immunohistochemistry

Immediately following *ex vivo* scanning, plaques were fixed in 4% paraformaldehyde for 24 hours before transfer to 70% ethanol. Plaques were decalcified in ethylenediaminetetraacetic acid before being divided into

segments with or without 18F-fluoride uptake. These segments were paraffin-embedded, and 5-μm sections were prepared and stained with Movat's pentachrome. Immunohistochemical staining for CD68 expression (mouse anti-human CD68 mAb, M087601-2, Dako), cleaved caspase 3 (anti-human rabbit mAb #9664, Cell Signalling Technology) and tissue non-specific alkaline phosphatase (anti-human rabbit pAb CAT#LF PA50004, Abfrontier) was then undertaken following heat induced epitope retrieval (HIER) using 0·01 M citrate buffer at pH 6·0 in a decloaking chamber. Osteocalcin staining (anti-human mouse mAb ab13418, Abcam) required no HIER. Sections were stained using a Leica Vision Biosystems Bond-x immunostaining robot. Optimization of antibody dilution was undertaken by determining positive and negative controls. Positive controls for CD68 were generated using human kidney, cleaved caspase 3 using sections of normal human tonsil and spleen, and for tissue non-specific alkaline phosphatase and osteocalcin using decalcified human bone to determine optimal antibody dilutions. Negative controls were generated by omitting the primary antibody. After blocking in peroxide for 10 min, sections were incubated with the specific anti-human antibodies for 2 hours at room temperature at the following dilutions: CD68 1:100, osteocalcin 1:200, cleaved caspase 3 1:150, and tissue non-specific alkaline phosphatase 1:100. All incubation steps were followed by washing in TBS/Tween. Sections for osteocalcin were incubated for 15 min with pre-polymer/post primary followed by 15 min with polymer (HRP) for all antibodies prior to DAB (3,3'-Diaminobenzidine) visualization and haematoxylin counterstaining. Sections were dehydrated in graded ethanol, cleared in xylene before cover slipping in Pertex.

Images were taken on a Zeiss Axioskop2 fitted with an Axiocam MRc digital camera using Axiovision software. Total vessel and plaque cross-sectional area was calculated using Image Pro Plus 5 (Rockville, MD, USA). Staining was quantified by semi-automated colour-coded segmentation. Immunohistochemical markers were expressed as number of positive cells per mm^2 or percentage staining of total cross-sectional area.

5.4.4 Statistical analysis

The primary endpoint of the study was the comparison of 18F-fluoride tissue-to-background ratios of culprit and non- culprit coronary plaques of patients with acute myocardial infarction. The main secondary endpoints were comparative imaging and histological characterisation of 18F-fluoride positive and negative atherosclerotic plaques in patients with coronary and carotid artery disease. Based on our previous data, (121) we required 36 patients with myocardial infarction to detect a difference of 0·23 in the tissue-to-background ratio between culprit and non-culprit plaques at 90% power and two-sided p<0·05. We recruited 40 patients to account for incomplete data and recruited a similar sized (n=40) comparator group of patients with stable angina.

Continuous data were tested for normality with the D'Agostino-Pearson omnibus test. Continuous parametric variables were expressed as mean (SD) and compared using Student's t tests. Non-parametric data were presented as median (IQR) and compared using Mann-Whitney U test or Wilcoxon signed-rank test as appropriate. Fisher's exact test or chi-squared test was used for analysis of categorical variables. Statistical analysis was done with Graph Pad Prism version 5 (GraphPad Software, La Jolla, CA, USA). A two-sided p<0·05 was taken as statistically significant.

5.5 Results

5.5.1 Patients Characteristics And Protocol Details

Patients were predominantly middle-aged men and had multiple cardiovascular risk factors (tables 5.1 and 5.2). The coronary cohorts underwent both 18F-fluoride (60 [SD 9] min after 123 [SD 5] MBq) and 18F-FDG (90 [7] min after 192 [11] MBq) PET-CT scanning within a median of 6 (IQR 3–9) days. The median duration between PET-CT scanning and coronary angiography was 7 (IQR 1–12) days. The total effective radiation dose from study participation was 13·7 (SD 3·0) mSv (conversion factor of 0·014 mSv/mGy.cm): 18F-fluoride (3·8 [SD 0·3] mSv) and 18F-FDG (4·9 [0·5] mSv) PET-CT, CT coronary angiogram (3·7 [2·1] mSv), and calcium score (1·3 [0·5] mSv). The total time spent in the imaging centre for each patient was ~100 min for visit 1 (18F-fluoride PET-CT scans) and ~120 min for visit 2 (18F-FDG PET-CT scans).

Table 5.1 | Baseline Characteristics Of Coronary Cohorts

	Myocardial infarction			Stable angina All (n=40)
	All (n=40)	STEMI (n=26)	NSTEMI (n=14)	
Age in years, mean (SD)	62 (8)	63 (9)	60 (8)	67 (8)
Men, n (%)	37 (93%)	24 (92%)	13 (93%)	36 (90%)
Body-mass index (kg/m²), mean (SD)	28 (5)	27 (5)	30 (4)	30 (5)
Antecedent angina (active), n (%)	9 (23%)	5 (19%)	4 (29%)	40 (100%)
Heart rate (per min), mean (SD)*	56 (7)	56 (7)	56 (7)	59 (9)
Systolic blood pressure (mm Hg), mean (SD)	132 (21)	131 (20)	121 (21)	134 (14)
Diastolic blood pressure (mm Hg), mean (SD)	76 (9)	76 (9)	76 (8)	77 (10)
Cardiovascular history, n (%)				
Previous MI	5 (13%)	1 (4%)	4 (29%)	15 (38%)
Previous CVA/TIA	2 (5%)	1 (4%)	1 (7%)	4 (10%)
Previous PCI	5 (13%)	2 (8%)	3 (21%)	19 (48%)
Previous CABG	2 (5%)	2 (8%)	0	11 (28%)
Risk factors, n (%)				
Smoking habit (ex or current)	25 (63%)	19 (73%)	6 (43%)	24 (60%)
Non-insulin dependent diabetes	8 (20%)	7 (27%)	1 (7%)	13 (33%)
Hypertension	17 (43%)	11 (42%)	6 (43%)	36 (90%)
Hypercholesterolaemia	19 (48%)	11 (42%)	8 (57%)	39 (98%)
Medications, n (%)†				
Aspirin	40 (100%)	26 (100%)	14 (100%)	33 (83%)
Clopidogrel	39 (98%)	25 (96%)	14 (100%)	5 (13%)
Statin	39 (98%)	26 (100%)	13 (93%)	36 (90%)
β blocker	32 (80%)	20 (77%)	12 (86%)	28 (70%)
ACEI/ARB	35 (88%)	25 (96%)	10 (71%)	20 (50%)
Calcium channel blockers	2 (5%)	2 (8%)	0	16 (40%)
Other anti-hypertensive	3 (8%)	1 (4%)	2 (14%)	6 (15%)
Oral nitrates	1 (3%)	0	1 (7%)	15 (38%)
Serum biochemistry, mean (SD)				
Cholesterol (mmol/L)	4·7 (1·2)	4·7 (1·3)	4·8 (1·1)	3·9 (0·8)
HDL cholesterol (mmol/L)	1·1 (0·3)	1·1 (0·3)	1·0 (0·3)	1·1 (0·3)
LDL cholesterol (mmol/L)	2·9 (1·1)	2·8 (1·1)	3·1 (1·0)	2·1 (0·7)
Triglycerides (mmol/L)	1·6 (0·8)	1·7 (0·7)	1·5 (0·7)	1·6 (0·7)
Creatinine (μmol/L)	84 (27)	86 (29)	82 (24)	85 (23)
Coronary artery calcium score (Agatston units), median (IQR)	159 (42–456)	176 (45–474)	122 (26–442)	599 (60–1302)
Peak troponin concentration (ng/L), median (IQR)	32 300 (10 200–50 000)	11 200 (3300–50 000)	3800 (1000–9200)	

NSTEMI=non-ST elevation myocardial infarction. MI=myocardial infarction. CVA=cerebrovascular accident. TIA=transient ischaemic attack. PCI=percutaneous coronary intervention. ACEI=angiotensin converting enzyme inhibitor. ARB=angiotensin receptor blocker. CABG=coronary artery bypass graft. HDL=high-density lipoprotein. LDL=low-density lipoprotein. STEMI=ST-elevation myocardial infarction. *Heart rate at the time of CT coronary angiography. †Medications at the time of scan.

Table 5.2 | Baseline Characteristics Of Carotid Cohort

Demography	
Age (years)	70±10
Male sex	8 (67%)
BMI (kg/m^2)	27±3
Antecedent angina (active)	0 (0%)
Heart rate (per min)	67±13
Systolic blood pressure (mmHg)	141±25
Diastolic blood pressure (mmHg)	75±11
Clinical Presentation	
Ischaemic Stroke	6 (50%)
Transient Ischaemic Attack	3 (25%)
Amaurosis Fugax	3 (25%)
Cardiovascular History	
Previous MI	3 (25%)
Previous CVA/TIA	3 (25%)
Previous PCI	1 (8%)
Previous CABG	2 (16%)
Risk Factors	
Smoking Habit (ex or current)	9 (75%)
Diabetes mellitus	1 (8%)
Hypertension	8 (66%)
Hypercholesterolemia	7 (58%)
Medications	
Aspirin	3 (25%)
Clopidogrel	9 (75%)
Statin	12 (100%)
β-Blocker	1 (8%)
ACEI/ARB	5 (42%)
Calcium channel blockers	3 (25%)
Other Anti-hypertensive	5 (41%)
Oral Nitrates	0 (0%)
Serum Biochemistry†	
Cholesterol (mmol/L)	4·2±0·9
HDL-Cholesterol (mmol/L)	1·1±0·4
LDL-Cholesterol (mmol/L)	1·9±0·6
Triglycerides (mmol/L)	1·4±0.5
Creatinine (μmol/L)	80±17

BMI body mass index, MI myocardial infarction, CVA cerebrovascular accident, TIA transient ischemic attack, PCI percutaneous coronary intervention, ACEI angiotensin converting enzyme inhibitor, ARB angiotensin receptor blocker, CABG coronary artery bypass graft, HDL high- density lipoprotein, LDL low-density lipoprotein.

5.5.2 Unstable Coronary Cohort

5.5.2.1 18F-Fluoride

The culprit vessel was the left anterior descending artery in 17 (42%) patients, the left circumflex artery in seven (18%), and the right coronary artery in 16 (40%). Patients underwent 18F-fluoride scans 6 [IQR 3–10] days after hospitalisation for myocardial infarction (symptoms to 18F-fluoride scan, 8 [3–10] days). 18F-fluoride activity in the culprit plaque was 34% higher than the maximum activity recorded anywhere else in the coronary vasculature (maximum TBR 1·66 [1·40–2·25] vs 1·24 [1·06–1·38], p<0·0001; figures 5.3 and 5.4). In 37 of the 40 patients (93%), increased 18F-fluoride uptake was seen in the culprit plaque (figure 5.3). In the three patients without uptake, two were younger smokers (aged 50 and 52 years) and, in the third, the culprit lesion was adjudicated as the right coronary artery although focal increased activity was seen in the left circumflex artery. In five patients, increased 18F-fluoride activity was seen at multiple sites within the coronary circulation.

5.5.2.2 18F-FDG

Predefined myocardial suppression of 18F-FDG uptake was achieved in 28 (70%) patients (median myocardial standard uptake value 3·92 [IQR 2·71–5·55]). However, coronary 18F-FDG uptake could not be distinguished from patchy myocardial uptake in 22 patients affecting 52% of vessel territories. Increased uptake of 18F-FDG was observed in the culprit vessels of six (33%) of the remaining 18 patients. Overall, no significant differences could be shown between the maximum TBRs in the culprit plaques and those recorded elsewhere in the coronary vasculature (1·71 [IQR 1·40–2·13] vs 1·58 [1·28–2·01], p=0·34: figure 2) with a mean difference of 0·09 (95% CI −0·07 to 0·24).

Figure 5.3 | Focal 18F-Fluoride And 18F-Fluorodeoxyglucose Uptake In Patients With Myocardial Infarction And Stable Angina

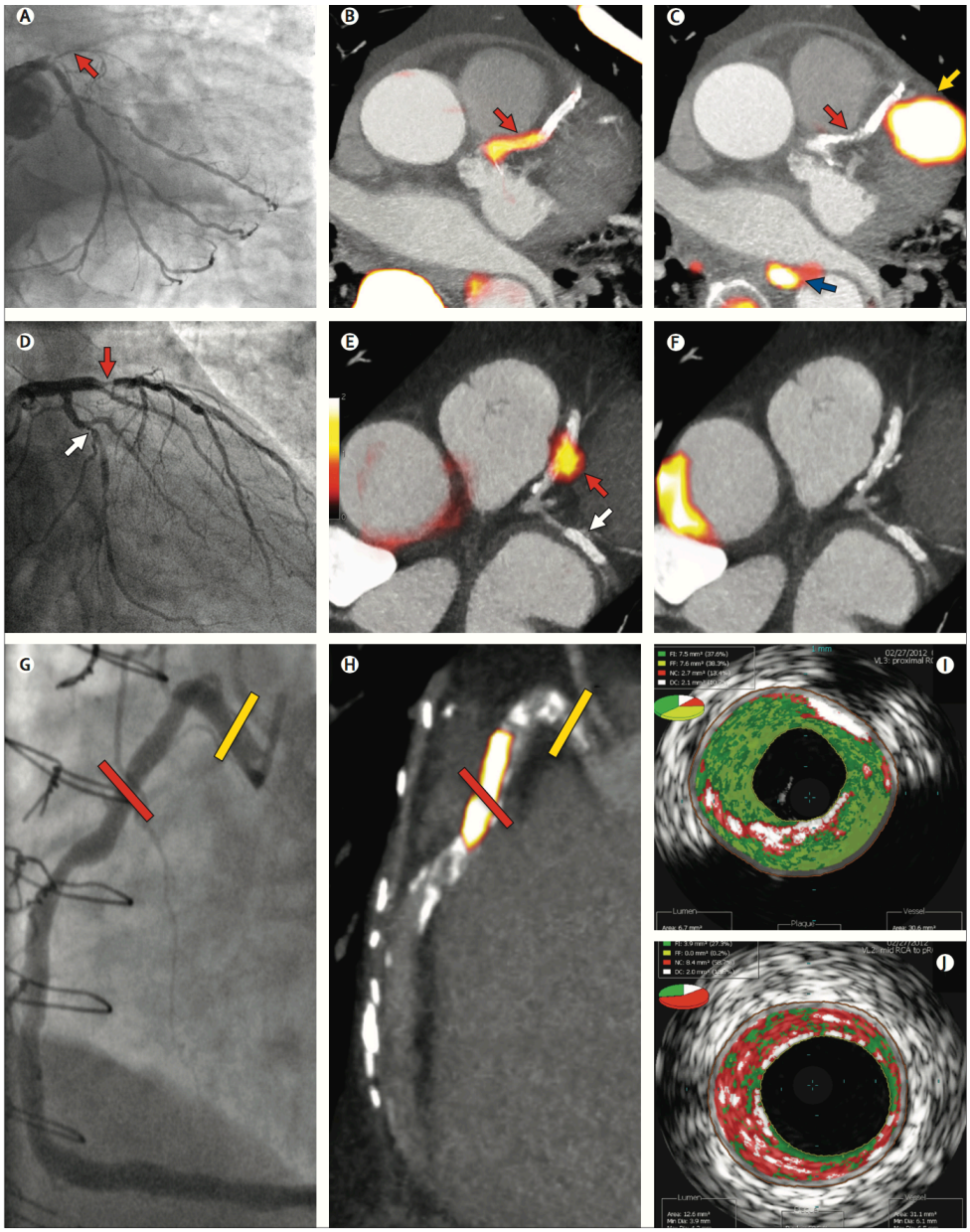

Patient with acute ST-segment elevation myocardial infarction with (**A**) proximal occlusion (red arrow) of the left anterior descending artery on invasive coronary angiography and (**B**) intense focal 18F-fluoride (18F-fluoride, tissue-to-background ratios, culprit 2·27 versus reference segment 1·09 [108% increase]) uptake (yellow-red) at the site of the culprit plaque (red arrow) on the combined positron emission and computed tomogram (PET-CT). Corresponding 18F-fluorodeoxyglucose PET-CT image (**C**) showing no uptake at the site of the culprit plaque (18F-FDG, tissue-to-background ratios, 1·63 versus reference segment 1·91 [15% decrease]). Note the significant myocardial uptake overlapping with the coronary artery (yellow arrow) and uptake within the oesophagus (blue arrow). Patient with anterior non-ST-segment elevation myocardial infarction with (**D**) culprit (red arrow; left anterior descending artery) and bystander non-culprit (white arrow; circumflex artery) lesions on invasive coronary angiography that were both stented during the index admission. Only the culprit lesion had increased 18F-fluoride uptake (18F-fluoride, tissue-to-background ratios, culprit 2·03 versus reference segment 1·08 [88% increase]) on PET-CT (**E**) after percutaneous coronary intervention. Corresponding 18F-fluorodeoxyglucose PET-CT showing no uptake either at the culprit (18F-FDG, tissue-to-background ratios, culprit 1·62 versus reference segment 1·49 [9% increase]) or the bystander stented lesion. Note intense uptake within the ascending aorta. In a patient with stable angina with previous coronary artery bypass grafting, invasive coronary angiography (**G**) showed non-obstructive disease in the right coronary artery. Corresponding PET-CT scan (**H**) showed a region of increased 18F-fluoride activity (positive lesion, red line) in the mid-right coronary artery (tissue-to-background ratio, 3·13) and a region without increased uptake in the proximal vessel (negative lesion, yellow line). Radiofrequency intravascular ultrasound shows that the 18F-fluoride negative plaque (**I**) is principally composed of fibrous and fibrofatty tissue (green) with confluent calcium (white with acoustic shadow) but little evidence of necrosis. On the contrary, the 18F-fluoride positive plaque (**J**) shows high-risk features such as a large necrotic core (red) and microcalcification (white)

Figure 5.4 | 18F-Fluoride And 18F-Fluorodeoxyglucose Uptake In Patients With Myocardial Infarction

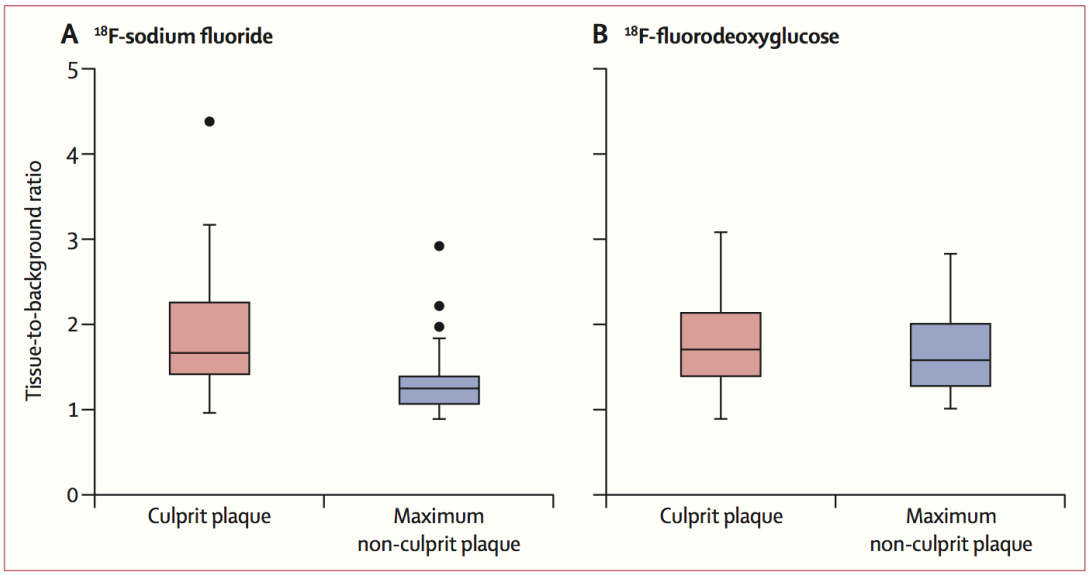

18F-Fluoride activity (maximum tissue-to-background ratio) was increased in the culprit plaque (red) compared with the maximum uptake in any of the non-culprit plaques (blue). By contrast, there was no difference in the activity of 18F-fluorodeoxyglucose between these regions.

5.5.3 Carotid Cohort

The median duration between clinical symptoms and carotid endarterectomy was 17 [IQR 10–27] days. Carotid endarterectomy specimens (figure 5.5 and 5.6) were obtained for 12 patients, although three specimens could not be excised intact and were discarded. Ex-vivo 18F-fluoride PET-CT was undertaken in nine specimens and uptake was localised to the site of macroscopic plaque rupture in all patients (figure 3). Compared with sections of tissue without uptake (n=15), those with increased 18F-fluoride uptake (n=24) had increased calcification activity (tissue non-specific alkaline phosphatase 4·07% [SD 3·42] *vs* 0·76% [0·51], p<0·0001; osteocalcin 1·88% [IQR 0·58–4·10] *vs* 0·25% [0·11–0·58], p<0·0001), macrophage infiltration (CD68, 350 [IQR 172–840] *vs* 145 [24–362] cells mm^{-2}, p=0·013), and cell death (apoptosis, cleaved-caspase-3, 1·23% [0·69–1·91] *vs* 0·09% [0·04–1·38], p=0·005; necrotic core, 22/24 *vs* 4/15; p<0·0001; Figures 5.5 and 5.6).

Figure 5.5 | Histological Comparison Of 18F-Fluoride Positive And Negative Regions Of Carotid Endarterectomy Specimens

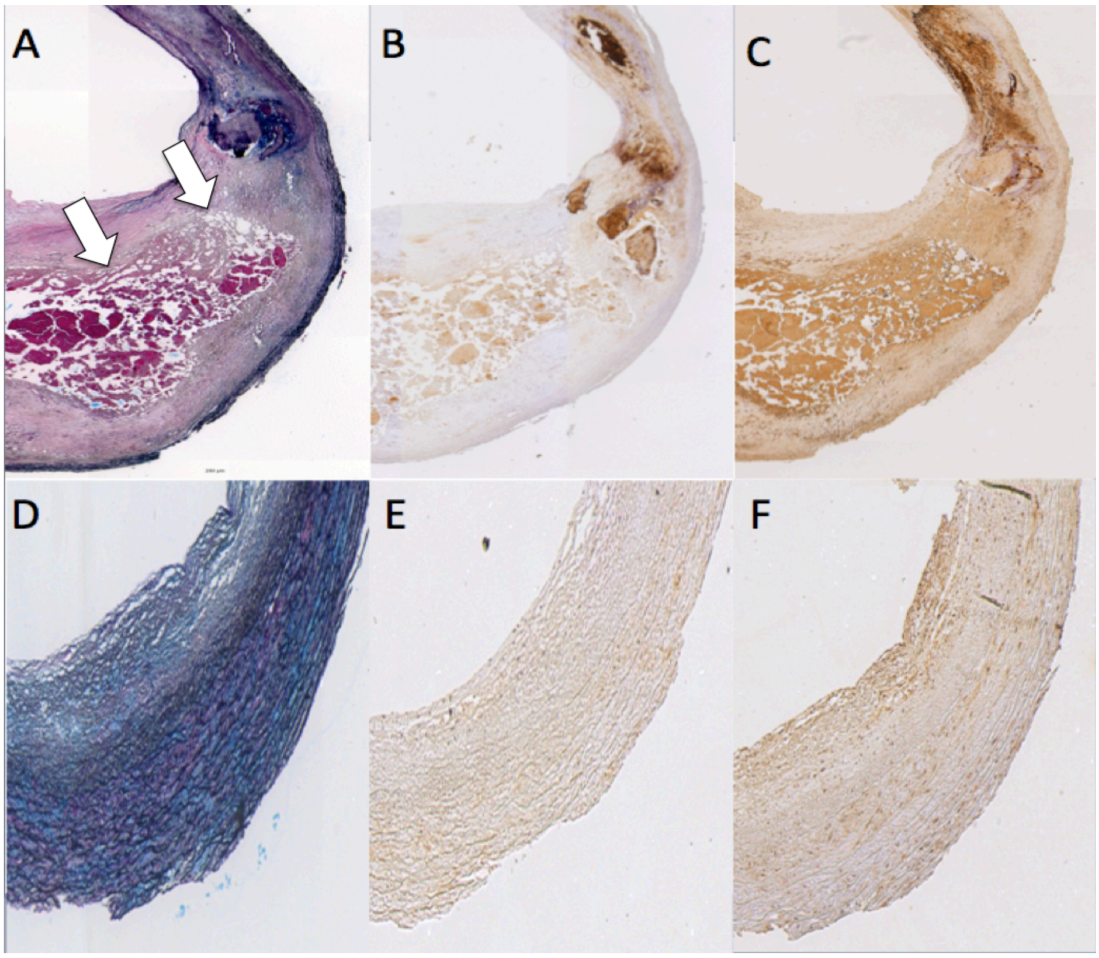

Histological sections of carotid endarterectomy specimens in regions with (**A**-**C**) and without (**D**-**F**) 18F-fluoride (18F-fluoride) uptake. Movat's pentachrome (**A** and **D**) showing a large necrotic core in a plaque with increased 18F-fluoride uptake (**A**; arrows). Calcification activity (non-specific alkaline phosphatase) and apoptosis (cleaved caspase-3) are increased in the necrotic core and its shoulder region of 18F-fluoride positive plaque (**B** and **C** respectively; brown staining) compared to the 18F-fluoride negative plaque (**E** and **F** respectively).

Figure 5.6 | Carotid 18F-Fluoride Uptake And Carotid Plaque Rupture

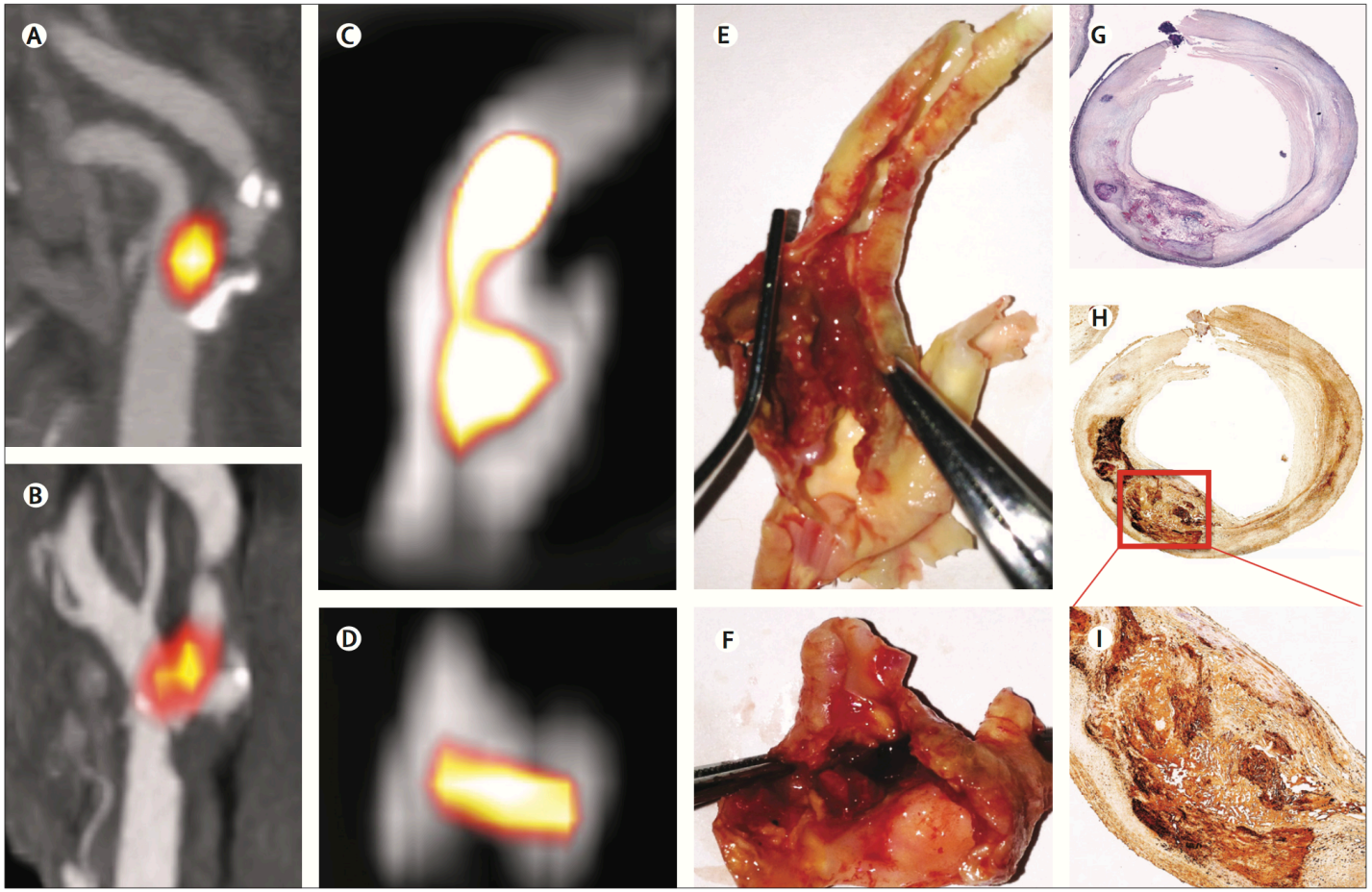

In-vivo (**A** and **B**) and *ex-vivo* (**C** and **D**) positron emission and computed tomograms showing co-localisation of 18F-fluoride (18F-fluoride) uptake (yellow-orange) to the site of plaque rupture with adherent thrombus on excised carotid endarterectomy tissue (**E** and **F**). Histology of the 18F-fluoride-positive region shows a large necrotic core (Movat's pentachrome, magnification 4×, **G**), within which increased staining for tissue non-specific alkaline phosphatase can be seen as a marker of calcification activity on immunohistochemistry (magnification 4×, **H**; magnification 10×, **I**).

5.5.4 Stable Angina Cohort

Patients with stable angina were older (67 [SD 8] *vs* 62 [8] years, p=0·006) and had more severe coronary artery disease (coronary artery calcium score 599 [IQR 60–1302] *vs* 159 [42–456] arbitrary Agatston units, p=0·006) than those with myocardial infarction (table 1). Focal 18F-fluoride uptake was noted in 18 patients (45%), which did not seem to be related to percutaneous coronary intervention and stent deployment (see section 5.5.5). The maximum TBR for 18F-fluoride positive plaques was 1·90 [IQR 1·61–2·17] and for 18F-fluoride negative plaques was 1·02 [0·82–1·17]. 18F-fluoride positive plaques were predominantly (72% of patients) non-obstructive (<70% luminal stenosis) on coronary angiography and showed multiple high-risk features on radiofrequency intravascular ultrasound (positive remodelling [remodelling index 1·12 [IQR 1·09–1·19] *versus* 1·01 [0·94–1·06]; p<0·001, microcalcification (73 vs 21%, p=0·002) and necrotic core (24·6% [20·5–28·8] vs 18·0% [14·0–22·4]), p=0·001), with similar observations for CT (figure 5.7, table 5.3 & table 5.4). Multivessel uptake was commonly seen: two-vessel uptake in six (15%) and three-vessel uptake in five (13%) patients. Patients with 18F-fluoride positive lesions had higher concentrations of plasma troponin at baseline (3·35 [IQR 2·35–10·20] *versus* 2·45 [1·85–4·02] ng/L; p=0·047), with one individual having a concentration (35 ng/L) above the 99th percentile diagnostic threshold.

Although predefined myocardial suppression of 18F-FDG uptake was achieved in 34 (85%) patients (median myocardial standard uptake value 2·60 [IQR 1·83–3·83]), coronary 18F-FDG uptake could not be confidently interpreted in 45% of vessel territories. Increased focal 18F-FDG uptake was noted in just four patients: three at the site of recent coronary stenting and one at the ostium of a saphenous vein graft.

Table 5.3 | Greyscale And Radiofrequency Intravascular Ultrasound Characteristics In 18F-Fluoride Positive And Negative Plaques Of Patients With Stable Angina

	^{18}F-fluoride positive plaques (n=15)	^{18}F-fluoride negative plaques (n=24)	p
Lumen			
Area (mm²)	9·0 (5·7–13·5)	6·7 (4·7–9·7)	0·078
Minimal diameter (mm)	2·6 (1·7–3·1)	1·9 (1·7–2·6)	0·165
Maximum diameter (mm)	4·9 (4·1–5·3)	3·6 (3·1–4·6)	0·006
Vessel			
Area (mm²)	24·1 (17·2–27·1)	14·5 (11·9–18·1)	0·002
Minimal diameter (mm)	4·4 (3·4–5·2)	3·6 (3·0–4·1)	0·057
Maximum diameter (mm)	6·5 (6·0–7·1)	5·2 (4·7–5·9)	0·0001
Plaque			
Length (mm)	14·2 (6·2–23·5)	15·2 (6·7–25·0)	0·941
Volume (mm³)	152·9 (99·6–289·7)	91·0 (45·8–158·2)	0·032
Burden (%)*	55·6 (48·6–64·4)	54·2 (46·3–57·3)	0·174
Remodelling index	1·12 (1·09–1·19)	1·01 (0·94–1·06)	0·0004
Plaque composition			
Fibrous tissue (%)	51·0 (46·3–56·6)	58·1 (51·6–65·5)	0·015
Fibro-fatty (%)	10·9 (6·0–13·8)	12·6 (9·3–17·8)	0·092
Necrotic core (%)	24·6 (20·5–28·8)	18·0 (14·0–22·4)	0·001
Maximum frame necrotic core (%)†	35·5 (34·2–40·5)	29·2 (23·9–42·1)	0·009
Dense calcium (%)	12·6 (9·1–18·1)	10·2 (4·0–14·9)	0·092
Microcalcification, n (%)	11 (73%)	5 (21%)	0·002
Plaque classification, n (%)			
Thin-cap fibroatheroma	7 (47%)	4 (16%)	0·068
Thick-cap fibroatheroma	5 (33%)	9 (38%)	1·0
Pathological intimal thickening	0	7 (29%)	0·003
Fibrocalcific plaque	3 (20%)	4 (16%)	1·0

Data are median (IQR) unless otherwise stated. *Plaque burden calculation = (average vessel area − average lumen area) /average vessel area. †Maximum necrotic core in any single frame in the plaque.

Figure 5.7 | Lesions With And Without 18F-Fluoride Uptake, And Gray-Scale And Radiofrequency Intravascular Ultrasound In Patients With Stable Angina

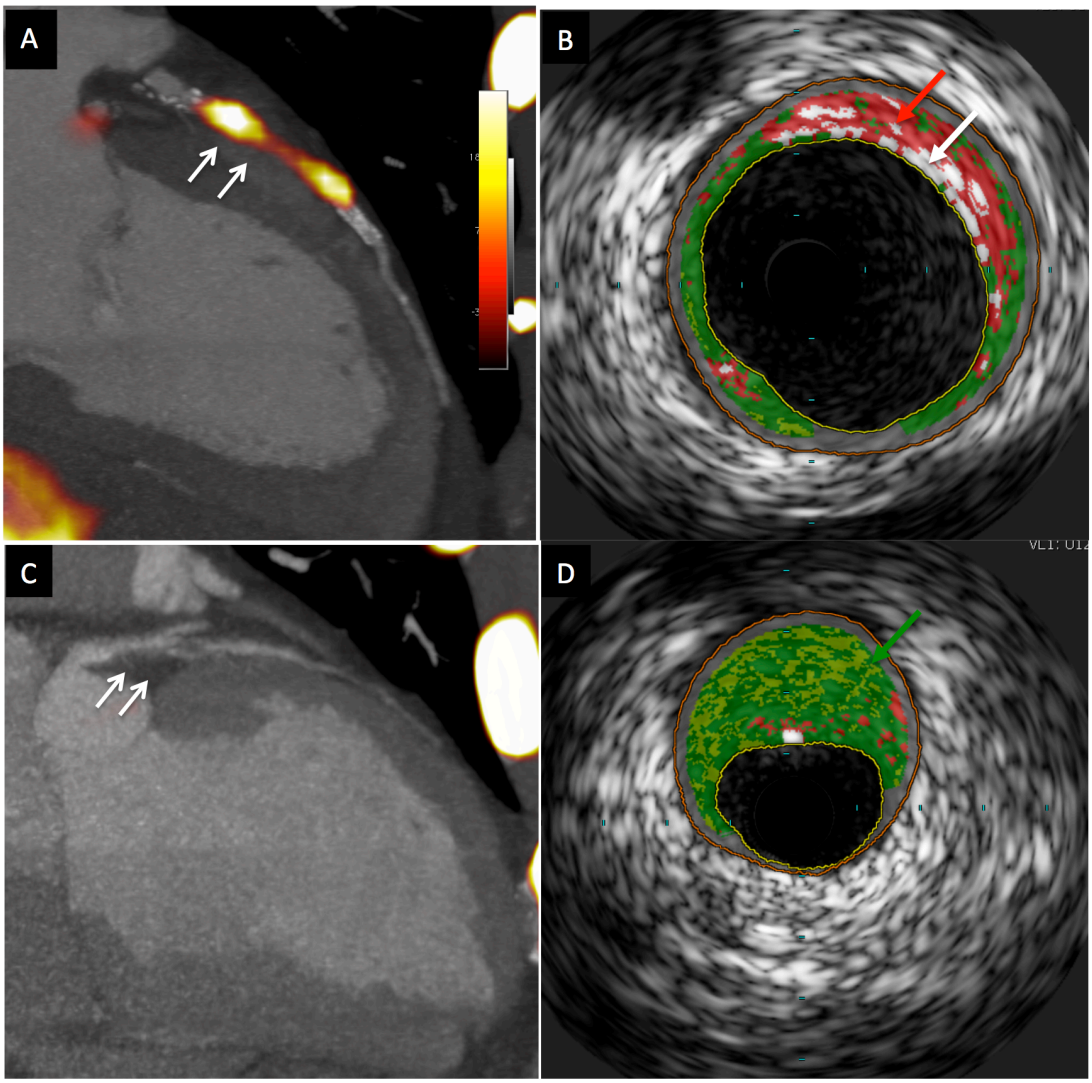

Panels **A** and **B**: Proximal left anterior descending artery lesion showing intense 18F-fluoride uptake (tissue-to-background ratio 2·81; arrows) on combined positron emission tomography and computed tomography images (**A**). The radiofrequency and grey-scale intravascular ultrasound of this lesion (**B**) shows significant necrotic core (red arrow) and microcalcification (white arrow).
Panels **C** and **D**: Proximal left anterior descending artery lesion with no 18F-fluoride uptake. The radiofrequency and grey-scale intravascular ultrasound show that this lesion is principally composed of fibrous and fibro-fatty tissue (green arrow) with minimal necrotic core.

Table 5.4 | Plaque Characteristics On Invasive And Computed Tomography Coronary Angiography In Patients With Stable Angina

	18F-NaF positive plaques (n=32)	18F-NaF negative plaques (n=53)	p value
Lesion stenosis*			
>70%	9 (28%)	8 (15%)	0·99
50% to 70%	11 (39%)	23 (43%)	0·67
10% to 50%	6 (19%)	10 (19%)	1·00
<10%	6 (19%)	12 (23%)	1·00
Type of Plaque†			
Non-calcified	2 (6 %)	11 (21%)	0·97
Mixed	23 (72%)	28 (53%)	0·98
Calcified	7 (22%)	14 (26%)	1·00
Plaque Analysis			
Positive remodeling‡	16 (50%)	30 (57%)	0·650
Necrotic core§	10 (31%)	9 (17%)	0·179
Microcalcification¶	20 (63%)	15 (28%)	<0·001
Dense calcification	21 (66%)	34 (64%)	1·000

*On invasive coronary angiogram.

†On CT Coronary Angiogram.

‡Positive Remodelling: diameter at the plaque site was at least 10% larger than the proximal reference segment.

§Necrotic core: Based on Hounsfield Units of less than 30 within the plaque.

¶Microcalcification: Defined <3 mm in size on curved multi-planar reformation images and occupying <180° on cross-sectional images.

18F-NaF, 18F-Fluoride

5.5.5 Percutaneous Coronary Intervention With Stent Implantation

Seven patients with myocardial infarction underwent 18F-fluoride scanning prior to percutaneous coronary intervention (PCI) with stent implantation (6 non-ST elevation myocardial infarction and 1 late presentation ST elevation myocardial infarction). Focal 18F-fluoride uptake was observed at the site of culprit plaque in all 7 patients (culprit lesion tissue to background ratios 1.74 [1.40-1.95] versus maximum non- culprit lesion 1.25 [1.07-1.29], p=0.007). Furthermore, at the time of their PCI, two patients with myocardial infarction underwent additional coronary stenting to a bystander non-culprit stenosis (Figure 5.3). Although intense 18F-fluoride uptake was observed at the site of culprit lesion, none was observed at the site of the bystander lesions. Amongst patients with stable angina, 5 patients underwent 18F-fluoride PET imaging shortly after elective coronary stenting (24 [12-29] days). There was no uptake noted at the site of the percutaneous coronary intervention in these patients (TBR stented lesion 1.07 [0.78-1.16] versus reference lesion 0.98 [0.81-0.98], p=0.92). Taken together, these data indicate that 18F-fluoride uptake does not appear to occur as a response to stent implantation.

5.5.6 Comparison Of 18F-Fluoride Uptake In Stable Angina And Myocardial Infarction

Patients with 18F-fluoride positive plaques in our stable angina cohort had higher 18F-fluoride activity when compared to those with myocardial infarction. What might explain this? When comparing the signal intensity of 18F-fluoride plaque uptake between the two groups of patients with coronary artery disease, it is important to recognize both the differences in these populations and the underlying disease processes. First, patients with stable angina pectoris were older (67±8 versus 62±8 years, p=0·006), had a more adverse cardiovascular risk factor profile and had more extensive coronary atherosclerotic plaque burden. Second, 18F-fluoride uptake occurs on the surface of hydroxyapatite nanocrystals that are laid down as part of the calcific

healing response to intense inflammation either within the necrotic core or that triggered by atherosclerotic plaque rupture. Following myocardial infarction, plaque rupture will disrupt plaque integrity and there will be some loss of plaque content(161) including hydroxyapatite, thereby reducing the surface area available to bind 18F- fluoride. In addition, we believe that the plaque rupture event itself will further stimulate hydroxyapatite deposition and 18F-fluoride uptake may take time to develop and may not have been at its peak when we performed the imaging relatively early (~6 days) after the incident myocardial infarction. We therefore believe it is perhaps not unexpected that the tissue-to-background ratios were on average higher in the 18F-fluoride positive plaques in the older patients with stable angina and more extensive coronary artery disease

5.5.7 Repeatability Of Image Analysis

The repeatability for measurements of coronary 18F-FDG and 18F-fluoride activity in the present study were excellent, with no fixed or proportional biases for measurements of the maximum tissue-to-background ratios for either tracer. The limits of agreement for maximum coronary 18F-FDG tissue to background ratios were 0·04±0·23 (mean bias±2SD) with intraclass correlation coefficient values of 0·97 after exclusion of uninterpretable segments [95% CI 0·90-0·99]. For 18F-fluoride limits of agreement were 0·01±0·11 with intraclass correlation coefficient values of 0·99 [95%CI 0·99-1·00].

5.6 Discussion

We have shown that intense 18F-fluoride uptake localises to recent plaque rupture in patients with acute myocardial infarction and in those with symptomatic carotid disease. Moreover, in patients with stable coronary artery disease, 18F-fluoride uptake seems to identify coronary plaques with high-risk features on intravascular ultrasound. This technique holds major promise as a means of identifying high-risk and ruptured plaque, and potentially informing the future management and treatment of patients with stable and unstable coronary artery disease.

Over 90% of our patients with myocardial infarction had increased 18F-fluoride uptake at the site of their culprit ruptured plaque, with TBR values that were a third higher than the maximum activity anywhere else in the coronary vasculature. These findings were not unique to the coronary circulation since we also noted increased focal 18F-fluoride uptake at the site of plaque rupture in all excised carotid endarterectomy specimens from patients with symptomatic carotid disease. However, it is acknowledged that this was not a universal finding. Of the three patients with myocardial infarction who had no uptake, two were younger smokers with only mild underlying irregularities on coronary angiography, implicating plaque erosion and thrombosis as the mechanism of their infarction rather than plaque rupture. (162) The third patient sustained an inferolateral non-ST segment elevation myocardial infarction and had a lesion stented in the right coronary artery. Increased 18F-fluoride activity was seen in the co-dominant circumflex artery that could have equally explained the clinical presentation, raising the intriguing possibility that 18F-fluoride might have a clinical role for patients in whom the culprit lesion is not readily apparent.

Focal regions of increased 18F-fluoride activity were seen in almost a half of our patients with stable coronary artery disease. To understand the mechanism of uptake in these patients, we sought to compare plaque characteristics of lesions

with and without increased 18F-fluoride uptake. Because histology of the coronary arteries in this population is not feasible, we undertook greyscale and radiofrequency intravascular ultrasound, a widely used and validated process that provides detailed characterisation of plaque composition. (159) This method showed that lesions with increased 18F-fluoride uptake were associated with greater positive remodelling, more microcalcification, and a larger necrotic core. These findings were corroborated by, and consistent with, the findings of plaque analysis done with CT coronary angiography. Plasma troponin concentrations measured by a novel high-sensitivity assay were also higher in those patients with 18F-fluoride positive plaques than in patients with 18F-fluoride negative plaques, perhaps implicating subclinical plaque rupture with embolisation and microinfarction.

Why does 18F-fluoride bind to ruptured or high-risk plaque? Similar to the caseating granulomata of tuberculosis, atherosclerotic vascular calcification is a controlled cellular response to an intense, necrotic, and chronic inflammatory stimulus. Indeed, direct links between inflammatory cells and osteoblastic metaplasia in the vasculature are well described. (13,163) Hydroxyapatite is the central structural component of vascular calcification and is laid down during the earliest and most active stages of mineralisation: (13) hydroxyapatite nano-crystals nucleate, propagate, and mineralise the extra-cellular matrix. fluoride ions are incorporated into the hydroxyapatite by ion exchange with hydroxyl groups at the crystal surface. This process is dependent on the crystal surface area that will be greatest in the earliest and most active nanocrystalline stages of mineralisation associated with plaque inflammation and necrosis. We believe that these processes are responsible for the observed 18F-fluoride uptake and is consistent with our data showing 18F-fluoride uptake in regions of necrosis, macrophage infiltration, apoptosis, microcalcification, and alkaline phosphatase and osteocalcin staining. Moreover, mathematical modelling indicates that micro-calcification at the surface of thin-capped atheroma (figure 5.3) can intensify and double incident stresses. (55) Microcalcification is therefore not only a marker of acute plaque rupture but is implicated in its precipitation.

Coronary arterial calcification is considered pathognomonic of atherosclerosis and is a powerful independent risk predictor for cardiovascular events that can be further refined by the rapidity of its progression. (164,165) Why then not rely on CT coronary calcium scoring alone as a biomarker? Microcalcification cannot be detected on CT and confluent coronary macrocalcification develops slowly, taking many months or years to become apparent on CT, and can become dormant once inflammation in the plaque has subsided. By identifying areas of nascent and ongoing calcification activity, 18F-fluoride uptake allows us to detect regions of metabolically active plaque, thus providing complementary information to CT. (104,105,123,166) Indeed, we noted large areas of coronary CT calcium in the absence of increased 18F-fluoride uptake (figure 5.3) whereas other regions with minimal or no CT calcium had intense 18F-fluoride uptake in keeping with previous observations in the aorta by Derlin and colleagues. (123,166) Moreover, given that 18F-fluoride seems more closely aligned with the process of necrotic inflammation and plaque metabolic activity, we believe that it potentially offers major improvements to the prediction of cardio- vascular risk compared with calcium scoring.

Our data have already established that 18F-fluoride identifies plaque with multiple high-risk features, but prospective studies are now needed in a broad range of patients to assess whether increased coronary 18F-fluoride activity will ultimately translate into future adverse events. If the results prove confirmatory then this technique has the potential to fundamentally alter the way we treat coronary artery disease: moving us away from the current framework based on lesion severity and ischaemia to one focused on plaque metabolism and inflammation. It could, for example, permit the identification of the vulnerable patient with single or multiple high-risk or silently ruptured plaques, providing an opportunity to treat and modify their risk to prevent future adverse cardiovascular events.

By contrast with 18F-fluoride, 18F-FDG imaging was hampered by problems related to tracer uptake in the myocardium. Our stringent dietary recommendations resulted in suppression of myocardial activity in 70–85% of patients: a rate that compares favourably with previous studies (57–84%).(146,150,151) However, this suppression resulted in a patchy distribution of myocardial uptake that frequently obscured activity in one or more coronary vessels. Increased 18F-FDG uptake might possibly occur in the culprit plaque and we failed to show this because of incomplete data or the delay in scanning. However, given its limitations, we believe that 18F-FDG is unlikely to become sufficiently robust to permit its clinical application to the coronary circulation. Nevertheless, 18F-FDG uptake remains an important measure of general vascular inflammation in the aorta and carotid arteries, providing complementary and distinct metabolic information to that of 18F-fluoride uptake.

5.6.1 Limitations

We acknowledge that there are limitations to our study that include a lack of respiratory gating, potential partial volume artefacts, and the use of surrogate measures for coronary histology. (159) However, we believe that the totality of our comprehensive evidence using multiple approaches and imaging modalities provides a robust and cogent argument to support our contention that 18F-fluoride uptake identifies vulnerable and high-risk plaques in patients with stable and unstable coronary heart disease. Further work is now needed to establish whether 18F-fluoride PET-CT will provide a clinically useful technique capable of improving risk stratification, monitoring disease progression, guiding therapeutic interventions, and assessing novel anti-atherosclerotic therapies.

Chapter 6 – Delving Deeper Into The Mechanisms Of 18F-Fluoride Uptake In Cardiovascular Tissue

6.1 Publication In Perspective

6.1.1 Background

My work on 18F-fluoride PET/CT imaging had so far demonstrated that the technique had promise in terms of identifying potentially "culprit" acute atherosclerotic plaque, (117) plaque with high risk features in stable coronary heart disease patients(117) and indeed aortic valves at higher risk of progressive calcification. (136) I had provided some mechanistic explanation for this phenomenon using tissue from excised aortic valves and carotid plaque and a variety of *ex vivo* techniques. This data was interesting and provided a basis upon which to proceed with our work but was essentially preliminary. I did not feel that it went far enough in explaining the underlying observation that 18F-fluoride appeared to identify volumes of "active" calcification or future calcification but didn't necessarily highlight volumes of older, so-called field calcification associated with a stable plaque phenotype.

I hypothesised that the observed phenomenon was due to a difference in the surface area to volume ratio of the different forms of vascular calcification; actively inflamed and necrotic plaque would be undergoing a calcification response(163) with innumerable numerous tiny nucleating crystals of apatite (with a relatively large surface area to volume ratio) and conversely, stable or stabilised plaque would have a large volume of discreet apatite most of which would be hidden within the nodule and not available for 18F-fluoride adsorption (see figure 6.1).

Figure 6.1 | Putative Mechanism Of 18F-Fluoride Uptake In Unstable Atherosclerotic Plaque

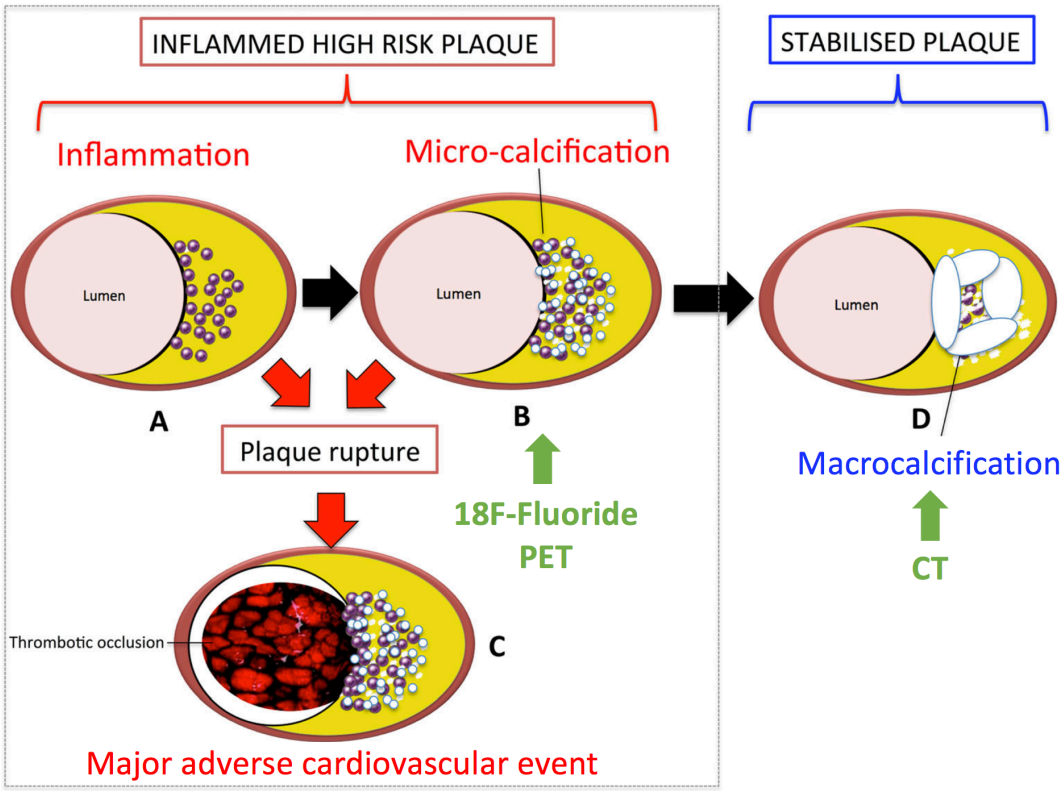

Image **A** shows an inflamed thin-capped fibroatheroma. The necrotic inflammation that is characteristic of this lesions may then initiate a microcalcific response(163) in an attempt at healing (**B**). The massively numerous nanoscale crystals of calcium apatite trigger by such inflammation then provide the large surface area for 18F-Fluroide to adsorb to. These microcalcifications thus provide the basis of imaging and may even themselves be implicated in progression to a plaque rupture (through alterations in biomechanical stress in the cap(55)) and a major adverse cardiovascular event such as a stroke or myocardial infarction (**C**). Conversely, a plaque that has stabilised will have a large but discreet nodule with a smaller surface area to volume ratio (**D**); these lesions are apparent on CT whereas the microcalcifications demonstrated in **B** are far beyond the resolution of CT. Image adapted with permission from Joshi NJ, Vesey AT et al. *Curr Cardiol Rep*. 2014. (167)

6.1.2 Aims of Further Study

Through a long-established collaboration with James Rudd and Anthony Davenport (both Cambridge University), I set out to answer the following questions:

1. What is the precise binding target of 18F-fluoride in vascular tissue?
2. Is the previously observed phenomenon of strong 18F-fluoride uptake in high-risk or stable plaque *versus* low uptake in stable plaque explained by a difference in available surface area of putative target (apatite)?
3. *Ex vivo*, what are the target/receptor binding characteristics of 18F-fluoride?
4. *In vivo,* what are the pharmacodynamic properties of 18F-fluoride with respect to atherosclerotic plaque?
5. *In vivo,* what are the pharmacokinetic properties of 18F-fluoride with respect to atherosclerotic plaque

6.1.3 Contributions

Dr Agnes Irkle and I led this work supervised by James Rudd, Anthony Davenport, Marc Dweck and Professor David Newby. We designed the experiments together. I recruited all the patients, performed all the *in vivo* scanning and analysis. I also collected the specimens (blood & tissue). I designed, executed and analysed the *in vivo* pharmacology experiments. Dr Irkle performed and analysed the *ex-vivo*/*in vitro* experiments. We drafted the paper together. For the purposes of this thesis monograph, the supplementary appendices have been incorporated into the text for narrative clarity. The style has also been changed from that demanded by *Nature Communications* into a traditional one.

Published as: Irkle A, **Vesey AT**, Lewis DY, Skepper JN, Bird JLE, Dweck MR, et al. Identifying active vascular microcalcification by 18F-sodium fluoride positron emission tomography. *Nature Communications*. 2015;6:7495.

6.2 Abstract

Vascular calcification is a complex biological process that is a hallmark of atherosclerosis. While macrocalcification confers plaque stability, microcalcification is a key feature of high-risk atheroma and is associated with increased morbidity and mortality. Positron emission tomography and X-ray computed tomography (PET/CT) imaging of atherosclerosis using 18F-sodium fluoride (18F-fluoride) has the potential to identify pathologically high-risk nascent microcalcification. However, the precise molecular mechanism of 18F-fluoride vascular uptake is still unknown. Here we use electron microscopy, autoradiography, histology and preclinical and clinical PET/CT to analyse 18F-fluoride binding. We show that 18F-fluoride adsorbs to calcified deposits within plaque with high affinity and is selective and specific. 18F-fluoride PET/CT imaging can distinguish between areas of macro- and microcalcification. This is the only currently available clinical imaging platform that can non-invasively detect microcalcification in active unstable atherosclerosis. The use of 18F-fluoride may foster new approaches to developing treatments for vascular calcification.

6.3 Introduction

Vascular calcification is a complex pathological process pathognomonic of atherosclerosis(14,168-170). Currently, the extent of macroscopic calcification can be determined by X-ray computed tomography (CT) imaging and this can be used clinically to predict cardiovascular morbidity and mortality. (171-173)

Vessel mineralization is first marked by the appearance of calcified micro nodules which grow and coalesce into much larger macroscopic deposits. (174) The genesis of these micro nodules is principally mediated by a coordinated cellular pathway that shares similarities to active skeletal osteogenesis but may also involve a more passive process where a combination of high local concentrations of phosphates and phosphatidylserines from necrotic cells and an absence of calcification inhibitors results in the precipitation of calcium phosphate particles. It is likely that much of the mineral present is made up of hydroxyapatite, a crystalline form of calcium orthophosphate. (175,176)

Although there is no universal size convention, emerging consensus categorizes micro- and macrocalcification based on nodules of <50 and >50μm, respectively. (177) This distinction is important because although macrocalcification imparts plaque stability, microcalcification heralds the onset of vessel mineralization triggered by cell death and inflammation(163,174) and may itself be implicated in the aetiology of plaque rupture and major adverse cardiovascular events. (57,178)

Detection of microcalcification is not possible with clinical CT systems that can only identify large areas of macrocalcification: ∼200–500 μm in diameter. (13,176,179,180) Furthermore, the rapid progression of existing vascular calcium is driven by on-going microcalcification, carries a poor prognosis and is not amenable to current medical therapies. As a consequence, the development of techniques to identify microcalcification is a major research goal with the potential for improving patient risk stratification and outcomes.

Positron emission tomography PET/CT imaging of atherosclerosis using 18F-sodium fluoride (18F-fluoride) has recently been reported and, for the first time, has the potential to non-invasively identify high-risk microcalcification. (117,121,165,166) In patients with stable coronary artery disease, 18F-fluoride uptake correlates with CT coronary calcium scores although nearly half of the patients with very high scores have no 18F-fluoride uptake and increased 18F-fluoride uptake is often seen in the absence of calcification on CT. 18F-fluoride would therefore appear to provide distinct information to CT with potentially important clinical implications. (121) Recently, we have shown that 18F-fluoride uptake identifies culprit ruptured coronary plaques after myocardial infarction and, in carotid plaque, correlates with markers of active calcification and cell death. (117) Moreover, 18F-fluoride appears to identify high-risk coronary lesions in stable patients indicating that it may have a role in identifying vulnerable plaques at risk of rupture and in predicting myocardial infarction. In bone imaging, 18F-fluoride uptake involves the exchange of fluoride ions with hydroxyl groups in hydroxyapatite; (78,123) however, the mechanism underlying 18F-fluoride uptake in the vasculature has not been established. This is a major limitation that must be addressed before the nascent field of vascular 18F-fluoride PET imaging can progress.

The goal of the study was to characterize the selectivity, specificity and pharmacodynamics of 18F-fluoride uptake in vascular tissue in the human carotid atherosclerotic plaque. First, we performed electron probe X-ray microanalysis to measure 18F-fluoride presence directly in the areas of calcification identified by electron microscopy. Second, we studied the pharmacodynamic properties of 18F-fluoride adsorption to vascular calcification to characterize its potential as a clinical imaging agent. We correlated the extent of 18F-fluoride adsorption to vascular calcification and to cell-specific markers of atherosclerosis to exclude the possibility of 18F-fluoride binding to markers of inflammation, neovascularization and smooth muscle cells as opposed to solely calcified deposits. We next compared the ability of

18F-fluoride to penetrate carotid micro- and macrocalcifications using high-resolution phosphor-imaging autoradiography and light microscopy to understand 18F-fluoride-binding properties to these different forms of vascular calcifications. Finally, we compared clinical 18F-fluoride PET/CT images with micro PET/CT images of excised carotid endarterectomy specimens to develop a translational model of 18F-fluoride vascular uptake from bedside to bench and back and understand 18F-fluoride adsorption to vascular calcification on all three levels studied.

We propose a comprehensive translational model of 18F-fluoride pharmacological characteristics to vascular calcification in pre- clinical and clinical imaging systems.

6.4 Methods

All chemicals were purchased form Sigma-Aldrich, Dorset, UK, unless stated otherwise.

6.4.1 Human Tissues

The atherosclerotic intimal layers of human carotid arteries (further in text: carotids) were obtained with ethical approval and informed consent after endarterectomy (National Health Service Local Research Ethics Committee approval in Cambridge: 97/084, National Health Service West of Scotland Research Ethics Committee approval in Edinburgh: 12/WS/0227). The mean patient age was 71±2 years and both male and female patient carotids were used. The tissue was collected immediately after the surgery and was fresh frozen at -80 °C. It was kept frozen until the start of the experimental procedures.

In clinical imaging, the concentration of the injected 18F-fluoride in plasma was calculated as approximately $1x10^{-11}$ M. Initial experiments were performed both on fresh carotids and carotids that had undergone a freeze-thaw cycle and no differences in 18F binding were observed in terms of radioactivity penetration into macrocalcifications.

6.4.2 Electron Microscopy

Frozen carotid tissue was placed in cryostat for 1 h to equilibrate to -20 °C temperature. It was then immersed in Optimal Cutting Temperature compound (OCT) Embedding Matrix (CellPath, Powys, UK) and 30-mm thick, serial sections were cut on a Bright (Huntingdon, UK) cryostat. Sections were placed on custom-made Melinex discs (diameter: 12 mm) and allowed to dry. Discs were then frozen at -80 °C until the day of experiment. During the experiment, tissue sections were allowed to thaw and then incubated with 120 mL 0.01 M non-radioactive fluoride for 2 h at room temperature. After incubation, sections were dipped in distilled H_2O three times and allowed to dry. The discs were

stuck to 12.5 mm Cambridge style scanning electron microscope stubs and coated with carbon in an Edwards Auto 306 evaporative carbon coater. They were imaged in an FEI XL30 FEGSEM operated at 20 kV with secondary and backscattered electron detectors. Calcification was detected predominantly in the regions of intimal thickening and was designated micro-(spherical or near spherical deposits <50 μm in diameter) or macrocalcification (where large regions between 50 μm and several mm in size were calcified). Both types of calcification were analysed by energy-dispersive X-ray micro- analysis in 10 arteries. Spectra were collected using an Oxford Instruments SiLi atmospheric thin window detector running INCA software (ETAS Group, Stuttgart, Germany).

Between 10 and 57 spectra were collected from both types of calcification (where present) for 100 s live time. As a control to assess nonspecific binding of fluoride, spectra were also collected from regions of the arterial media where no backscattered electron signal for hydroxyapatite was present. The spectra were deconvolved in the INCA software and to estimate F/Ca, only Ca and F spectra were input into the analysis. The quantitative data were expressed as atomic %. F/Ca was estimated by dividing the atomic % of F by the atomic % of Ca. Data are presented as means±s.e.m. and F/Ca between regions of micro- and macrocalcification was compared using an ANOVA and Tukey Kramer post hoc test.

Additional electron microscopy analysis was performed with commercial hydroxyapatite standards. Hydroxyapatite (2 mg) was incubated with 1 mL of 1% fluoride on a rotator for 8 h or 4 days. The standards were then rinsed 10 times for 20 min in distilled water and air dried onto coverslips. They were mounted onto 12.5 mm Cambridge scanning electron microscope stubs, carbon coated and analysed in the same way as the cryostat sections. Control samples of hydroxyapatite standards were treated similarly as described above but the fluoride incubation step was omitted. The hydroxyapatite analysed in the cryostat section is at least partially embedded/encapsulated in the tissue of the arteries and sections were coated in the same way with carbon to make them

electrically conductive. As the carbon was added it was excluded from the analysis. Concentrations of O, P and Ca in the control hydroxyapatite are expressed in atomic per cent.

In the fluoride-treated hydroxyapatite, no signal for Na was seen after extensive washes, and the concentrations of O, F, P and Ca were expressed as atomic per cent. Despite extensive washing, a clear signal for F was retained, indicating binding to the hydroxyapatite. In these control samples the interaction volume of the electron beam is expected to remain within hydroxyapatite alone whereas in the tissue sections a proportion of the interaction volume will also generate X-rays from the surrounding arterial tissue. Therefore, the ratio of F/Ca was used to measure differences in F concentration between areas of macro- and micro-calcification.

6.4.3 18F-Fluoride Binding To Cryostat Cut Carotid Artery Sections

For all experiments 18F-fluoride was synthesized by the Wolfson Brain Imaging Centre (WBIC) (Cambridge, UK). The typical activity was approximately 285 MBq.

Frozen whole carotids were placed in the cryostat for 1 h to equilibrate to 20 °C temperature. Tissue was then immersed in the OCT Embedding Matrix (CellPath, Powys, UK) and 20 mm thick, serial sections were cut on a Bright (Huntingdon, UK) cryostat. Sections were allowed to dry in room temperature and stored at -80 °C temperature until the start of the experiment.

The concentration of 18F-fluoride was detected using F^- electrode (Thermo Scientific, Loughborough, UK) and was then diluted to $1x10^{-11}$ M. For nonspecific binding detection, 20 mL of 0.1 M **non-radioactive** fluoride solution (Orion Ionplus F^- Standard, Thermo Scientific, Loughborough, UK) were added to an aliquot of the radioactive 1×10^{-11} M solution. Frozen tissue sections were allowed to thaw and washed with PBS for 10 min in room temperature. Adjacent sections were incubated either with 18F-fluoride or 18F-fluoride plus

non-radioactive fluoride solutions for 1 h at room temperature. They were then washed in PBS 3 x 5 min and dipped in distilled H_2O. After drying, tissues were placed on a charged phosphor screen (Perkin Elmer, Waltham, Massachusetts) and left overnight. The following day screens were read using PerkinElmer's Cyclone Plus Phosphor Imager (Waltham, Massachusetts) and data were analysed with OptiQuant software (Packard Instrument, Meriden, Connecticut). Areas of micro- and macrocalcification were identified visually based on the size of nodules of <50 and >50 μm to several mm, respectively, and manual measurements made.

For concentration–response curve, the same method was used, except stock 18F-fluoride solution was split into serial dilutions from 10^{-12} to 10^{-7} M. After washing in PBS and dipping in distilled H_2O, tissues were wiped off the slides with filter paper, which was put into radioimmunoassay tubes and measured in the gamma counter (Packard Cobra II E5003, GMI, Ramsey, Minnesota).

6.4.4 18F-Fluoride Binding In Whole-Carotid Arteries

Whole-carotid arteries were thawed in 5 mL PBS for 1 h, and then placed in 5 mL of 10^{-11}M 18F-fluoride solution for 1 h at room temperature. They were then washed in PBS 3 x 2 min, followed by a dip in distilled H_2O. Carotids were transferred to cryostat, immersed in OCT and allowed to freeze. Tissue was then cut into 20-mm serial sections, which were allowed to dry on microscopy slides. After drying, tissues were placed on a charged phosphor screen and left overnight.

For whole-carotid association and dissociation binding curves, the same method was used, except during association binding experiments, carotids were taken out from the 5 mL of 10^{-11} M 18F-fluoride tube at set time points — 0, 5, 15, 30, 60 min, washed and measured in the gamma counter. For the dissociation binding experiment, after the incubation in 5 mL of 10^{-11} M 18F-fluoride for 1 h, tissues were continuously washed in PBS for set amounts of time — 0, 5, 10, 15,

30, 45, 60, 90, 120 min. Instead of cryostat cutting, arteries were placed in radioimmunoassay tubes and measured in the gamma counter.

6.4.5 Tissue Staining

Tissue sections were cut on cryostat as described above.

6.4.5.1 Alizarin Red Staining

Alizarin Red staining (Alfa Aesar, Heysham, UK) was used for calcification detection in carotid arteries. In brief, cryosections were left to dry overnight. They were then fixed in acetone for 10 min at 4 °C and washed in PBS 2 x 5 min at room temperature. After washing, 300 mL Alizarin Red were applied to each section for 1 min. Tissue was then put in acetone for 1 min, followed by a wash in 50:50 acetone:xylene for 1 min and then left in xylene for at least 1 h.

6.4.5.2 Immunohistochemistry

Immunohistochemistry was used to detect multiple inflammatory tissue markers in cryosections. Tissue was left to dry overnight and the following day it was fixed in acetone at 4 °C for 10 min and washed in PBS 2 x 5 min at room temperature. Sections were blocked in 10% goat serum for 1 h and H_2O_2 for 5 min. Each blocking step was followed by washing in PBS for 2 x 5 min. Carotids specimens were then incubated in primary antibody for 30 min at room temperature. Antibodies included CD68 (1:500, clone PG-M1), CD31 (1:20, clone JC70A) and Smooth Muscle Actin (1:500, clone 1A4) (all from Dako UK, Ely, UK). Labelled polymer-HRP anti-rabbit application and visualization with 3,3′-diaminobenzidine (DAB) was done using EnVision þ System-HRP (DAB) kit (Dako UK, Ely, UK), following manufacturers specifications. Counterstain of 150 mL haemotoxylin was applied to each section and incubated for 1 min. Slide was then dipped six times in destain solution (1% HCl, 50% methanol, 49% distilled H2O) and washed in tap water for 2 min. Afterwards tissue was quickly dehydrated in 1 min intervals through graded alcohols (30 to 70% to 100% to absolute alcohol 1 to absolute alcohol 2) and cleared in xylene for at least 1 h.

6.4.5.3 Section Mounting

After staining, all tissues were mounted using DePeX mounting medium Gurr (VWR, Lutterworth, UK) and glass coverslips (Menzel-Gläser, Braunschweig, Germany). After hardening of the mounting solution, tissues were imaged using Wild Heerbrugg M3Z microscope (Leica, Heerbrugg, Switzerland).

6.4.6 Micro PET/CT Imaging Of Carotid Plaques

Whole-carotid plaques were removed from the -80 °C freezer and thawed in 5 mL PBS at room temperature for 1 h. After thawing, tissues were placed in 1 x 10^{-9} M 18F-fluoride solution and incubated for 1 h. Tissues were then washed in PBS 3 2 min and dipped in distilled water. They were then placed in sealed plastic tubes. Tissue radioactivity was read using dose calibrator and they were then placed into the micro PET/CT scanner. Images were acquired over 30 min in list mode using a NanoScan PET/CT (Mediso, Budapest, Hungary). Data were reconstructed using a 3D ordered-subset expectation-maximization (OSEM) algorithm with eight iterations and six subsets using corrections for decay, dead time, random events, attenuation and scatter, the resulting image was isotropic with 300 μm voxels. Two sets of micro CT were performed immediately after micro PET acquisition, using high and low zoom (67.1 mm and 219 mm between object and source, respectively). Images were obtained by helical acquisition using a voltage, current and exposure time of 65 kVp, 123 μA and 1,100 ms. Images were reconstructed using a modified cone beam filtered-back projection method using a Butterworth filter producing a 22 μm and a 213 μm isotropic data set. Micro PET and micro CT data were co-registered using previously established default shifts.

6.4.7 2D Image Processing And Analysis

Two-dimensional image analysis was performed using open-source software ImageJ/Fiji (http://fiji.sc) (NIH, Bethesda, Maryland). Correlation between histology sections and autoradiography images was achieved by using

thresholded binary images of the different signals. In addition, these thresholded images were filtered with Gaussian blur ($\sigma = 20$) and thresholded again, to create segmentation masks that overcome the issue of inherent resolution differences between histology and autoradiography signal detection processes. (181)

Alizarin Red-stained calcification detection was performed using histogram-based Otsu automated thresholding method(182) and after Gaussian filter, it was processed using Li thresholding. (183)

DAB-stained immunohistology sections were analysed using a colorimetric thresholding method. While calcification stains provided excellent signal-intensity to background ratio, this was not the case for immunohistochemistry. Therefore, a colour combination that only detected the brown DAB stain was set as the manual threshold value, irrespective of intensity. After Gaussian blurring, signal was detected using Li auto-thresholding method.

Autoradiography images were resized to match the size of the histology images. Then they were thresholded using Otsu method, Gaussian blurred and thresholded using Li method.

All two-dimensional histology images were subjected to background subtraction and histogram equalization.

Correlation between the various stained sections was accomplished using multiple ImageJ/Fiji plug-ins. The position of specimens between individual images was co-registered using TurboReg(184) plug-in. Although tissues had been exposed to acetone and alcohol fixation protocols, we did not observe prominent contraction or shrinkage that would affect our data analysis. Images were then thresholded and turned into binary data as described above. Pearson's correlation coefficient was calculated using JACoP(185) plug-in. Overlapping images of histological and autoradiography signals were acquired

using Co-localization Finder plug-in. The overlapped images were processed further to determine PET+/CT-, PET+/CT+ and PET-/CT+ regions in individual sections. Each colour corresponding to one of the three detection modalities was separated out and quantified using Analyze Particles command which counts the number of pixels in the binary segmented mask.

6.4.8 3D Image Processing And Analysis

3D images after data reconstruction were analysed using VivoQuant version 1.23, (InviCRO, Boston, Massachusetts) software. (186) For micro PET/CT, initially the files were cropped to reduce file size and remove experimental artefacts, such as the scanning panel and tube in which the carotid was placed. Once an image containing only the signals associated with the carotid was achieved, the colour intensities of both modalities were manually adjusted to match the histology/autoradiography signals as closely as possible. After that, the "Distance/Annotation" function was selected and 5–8 mm linear transects were made across slides in the transversal plane of carotids. The raw data were then downloaded and graphs showing micro CT densities and micro PET units along the transect lines were later reconstructed with Matlab (Mathworks, Natick, Massachusetts). To quantify PET+/CT-, PET+/CT+ and PET-/CT+ regions in 3D, the "3D ROI Tool" function was selected. First, micro PET data were thresholded using the Otsu method, to delineate the extent of PET+ signal. On the micro CT data, we defined densities over 1000 Hounsfield Units (HU) as calcification. To detect PET+/CT+ signal, we selected PET+ delineated 3D areas and again used global thresholding of the micro CT data set at ≥1,000 HU in this area. To detect PET-/CT+ areas, we selected all remaining micro PET data and applied the ≥1,000 HU Global threshold. The raw data containing information about the different modality regions was downloaded and analysed with Microsoft Office Excel (Microsoft, Redmond, Washington).

Clinical PET/CT data were analysed by initially manually co-registering the PET, CT and CT angiogram using bones as anatomical landmarks of the three

different modalities. Following this the images were zoomed in to the culprit plaque and was cropped around this area. The division into PET+/CT-, PET+/CT+ and PET-/CT+ regions was similar to as described for the micro PET/CT data.

6.4.9 Clinical PET/CT Acquisition And Dynamic Analysis

Recruitment and scanning for the *in vivo* aspect of this study took place following approval from the local research ethics committee (National Health Service West of Scotland Research Ethics Committee approval in Edinburgh: 12/WS/0227) and in accordance with the Declaration of Helsinki. Patients with symptomatic carotid artery stenosis (scheduled to undergo carotid endarterectomy) ≥50% by NASCET criteria(110) were recruited from stroke and vascular surgery clinics at the Royal Infirmary of Edinburgh between January 2013 and April 2014. Exclusion criteria included a modified Rankin score of ≥3, insulin-dependent diabetes mellitus, women of child-bearing age not receiving contraception, severe chronic kidney disease (estimated glomerular filtration rate of < 30 mL min^{-1} per 1.73 m^2), known iodine-based contrast allergy, prior ipsilateral carotid intervention, prior neck irradiation and inability to provide informed consent.

After giving their consent, patients underwent baseline clinical assessment before undergoing dynamic or static 18F-fluoride PET/CT and CT carotid angiography with the use of a hybrid scanner (Biograph mCT, Siemens Medical Systems, Erlangen, Germany).

For static 18F-fluoride PET/CT, a target dose of 250 MBq of 18F-fluoride was administered intravenously. Scanning took place 60 min after injection. An attenuation-correction CT scan (non-enhanced, low dose 120 kV, 50 mAs) was then performed followed by PET imaging covering two bed positions with the first upper bed centred over the carotid bifurcation in 3D mode for 15 min per bed. Analysis was undertaken as described above.

In five patients, 18F-fluoride PET imaging was undertaken as a dynamic acquisition with the PET scanner in list mode. Three of these subjects underwent arterial blood sampling to directly assay the plasma arterial input function for model creation and to assess 18F-fluoride pharmacokinetics. An image-derived input function was utilized for modelling in the two patients that did not undergo arterial cannulation and sampling. The image-derived input function was generated by drawing regions of interest in the proximal carotid artery lumen. After the fitting of a soft neck collar to minimize movement, subjects were placed in the PET/CT scanner with intravenous and radial arterial catheters sited. An attenuation-correction CT scan (non-enhanced, low dose 120 kV, 50 mAs) was performed followed by PET imaging with the single bed centred over the carotid bifurcation. A target dose of 250 MBq of 18F-fluoride was then administered intravenously at the same time as scanning and blood sampling were initiated. Scanning took place for 75 min. Real-time whole-blood radioactivity was assayed using a calibrated Allogg ABSS V3 system (Allogg Technology, Mariefred, Sweden). In brief, whole arterial blood was sampled through a narrow bore polytetrafluoroethylene tube using a roller pump at a rate of 5 mL min^{-1} before being drawn through a shielded scintillation-based detector. Counts were recorded using a data-logger. After 15 min, the pump was deactivated and 5 mL samples were drawn intermittently for the remaining 60 min. Decay corrected whole blood and plasma radioactivity was then assayed using a gamma counter. The fractional difference between whole blood and plasma radioactivity was then calculated to adjust the data for the first fifteen min from the Allogg device.

Following static and dynamic PET acquisitions, CT carotid angiograms were also undertaken (Care Dose 4D, 120 kV, 145 mA, rotation time 0.5 s, pitch 0.8). Dynamic imaging data were reconstructed using the Siemens Ultra-HD algorithm (time of flight + True X) with corrections applied for attenuation, dead time, scatter and random coincidences. Imaging data were then parsed into the following time bins as per Hawkins(79) and Frost(187) (12 x 10 s, 4 x

30 s, 12 x 240 s) and analysed on a PMOD workstation (PMOD v3.408, PMOD Technologies Ltd., Zurich, Switzerland).

For analysis, the image data were first reviewed for evidence of 18F-fluoride uptake, image quality and patient movement. The CT angiogram was scrutinized for plaque presence, location and characteristics. The PET data were then resliced as part of automated registration to the CT data. Volumes of interest were then generated by drawing regions of interest on sequential axial slices on the registered data sets. Volumes were drawn to separately incorporate internal carotid artery plaque (where present) and a vertebral body. Vertebral data were obtained as a comparator and also as a way of ensuring our data were commensurate with the work of others. Tissue activity curves were then generated and assessed.

Dynamic analysis of fluoride uptake in the bone has been well described. Since, our data and that of others shows that over the time course of a typical 18F-PET/CT scan fluoride dissociation from calcified tissue is undetectably slow, the Patlak technique(111,112) may be used to gain an estimate for the net flux of fluoride (Ki) into a region of interest. Patlak derived Ki is calculated as follows:

$$\frac{Ct(t)}{Cb(t)} = Ki\frac{\int_0^t Cb\,(t)dt}{Cb(t)} + V$$

Equation (1)

Ct(t) is the activity concentration of 18F-fluoride at time *t* within the volume of interest, *Cb(t)* is the blood activity concentration of 18F-fluoride at time *t* and *V* relates to the effective volume of distribution for 18F-fluoride. The Patlak plot is obtained by plotting plotting $\frac{Ct(t)}{Cb(t)}$ against $Ki\frac{\int_0^t Cb(t)dt}{Cb(t)}$ and calculating the slope of the regression line as given in equation (1).

This method has been extensively described and compared with multi-compartmental modelling with both techniques showing good agreement. To ensure equilibrium between the plasma and compartments had been achieved, we only plotted the data from 10 min onwards as described by Frost. (187) Patlak plots were generated for all carotid plaques and vertebra. We also plotted directly measured plasma activity curves for illustration of the pharmacokinetics of 18F-fluoride.

6.4.10 Data Analysis

Numerical data analysis was performed using Microsoft Office Excel (Microsoft, Redmond, Washington), Matlab (Mathworks, Natick, Massachusetts) and Prism (GraphPad, San Diego, California) software. Written text was produced using Microsoft Office Word (Microsoft, Redmond, Washington) and figures were made using Adobe Illustrator CS5 (Adobe Systems, San Jose, California).

6.5 Results

6.5.1 Electron Microscopy Analysis

We used an electron microprobe to measure directly the presence of non-radioactive fluoride within calcified and soft tissue areas of carotid endarterectomy specimens. We also used hydroxyapatite standards to confirm co-localization (see Table 6.1). When tissues were preincubated with fluoride, an energy-dispersive X-ray spectroscopic peak for fluoride was detectable and co-localized with regions of calcification (Figure 6.2a).

Microcalcifications showed greater levels of fluoride than macrocalcifications (F/Ca ratio: 0.59±0.23 (n = 10, individual plaques) *versus* 0.37±0.15 (n = 7, individual plaques), respectively, $P<0.02$, ANOVA (analysis of variance) and Tukey Kramer *post hoc* test, Figure 6.2b) and no tissue fluoride was observed in the absence of calcification (Figure 6.2c). Thus, at the resolution of electron microscopy, fluoride co-localized to arterial calcification, with increased levels in the regions of microcalcification.

Table 6.1 | Electron Microscopy Analysis Of Hydroxyapatite Standards To Confirm Co-Localization With Fluoride

Sigma hydroxyapatite (no NaF incubation - control)

	Oxygen	Phosphorous	Calcium	Fluorine
Mean ± SD	77.76 ± 7.21	9.26 ± 2.73	12.98 ± 4.74	n/a

Sigma hydroxyapatite (after incubation with 1% NaF for 8 hours)

	Oxygen	Phosphorous	Calcium	Fluorine
Mean ± SD	76.01 ± 2.58	5.30 ± 2.78	7.48 ± 0.79	11.21 ± 1.30
F/Ca Mean ± SD	0.70 ± 0.26			

Sigma hydroxyapatite (after incubation with 1% NaF for 4 days)

	Oxygen	Phosphorous	Calcium	Fluorine
Mean ± SD	73.44 ± 2.81	7.91 ± 2.87	7.37 ± 0.73	11.28 ± 1.20
F/Ca Mean ± SD	0.70 ± 0.26			

Element concentration in espressed as atomic % (n= 51). NaF, sodium fluoride; SD, standard deviation; F/Ca, ratio of fluorine/calcium

Figure 6.2 | Fluoride Directly Co-Localizes With Calcium In A Concentration-Dependent Manner

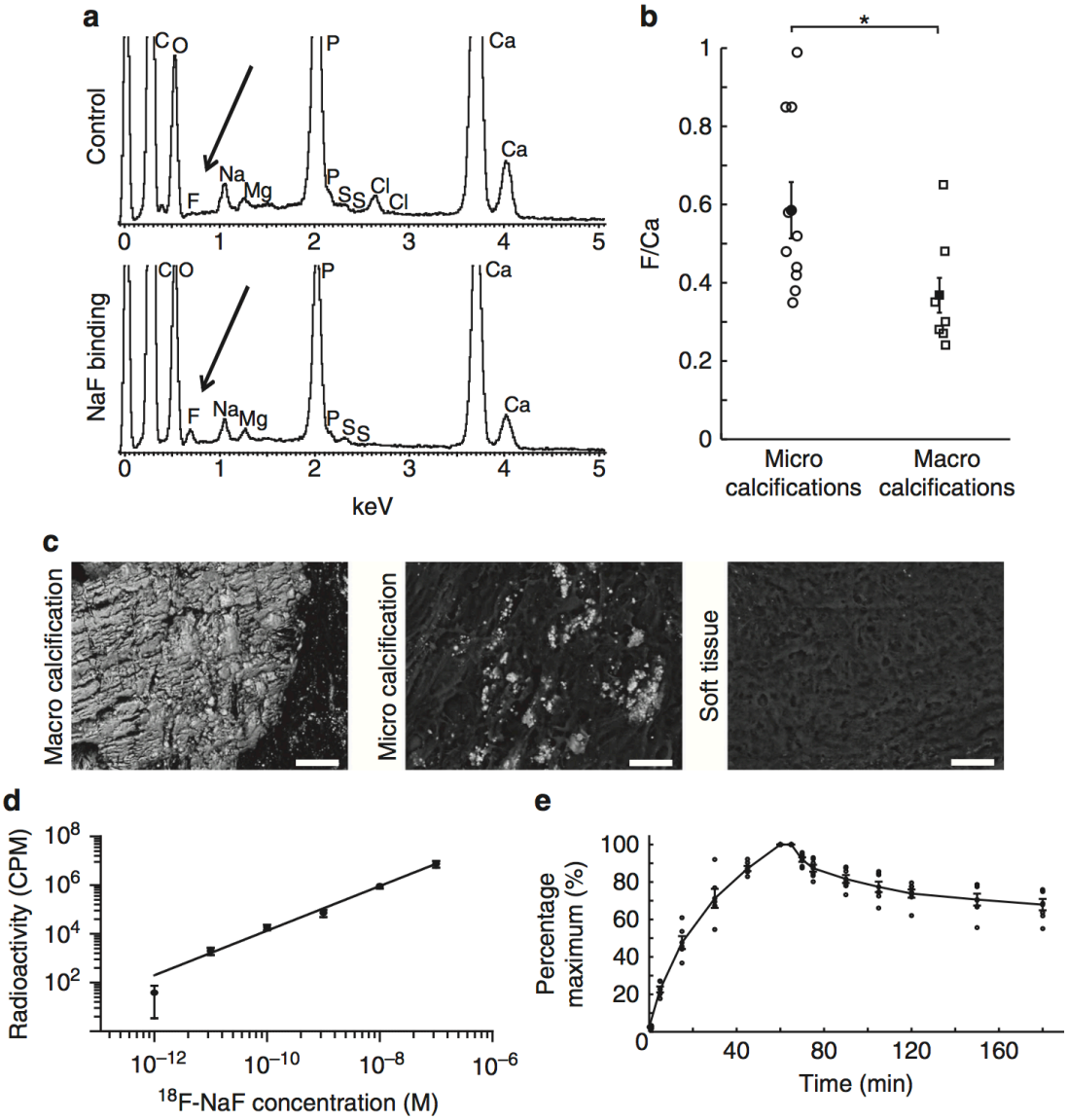

(**a**) Fluoride peak is detected only in the calcified regions of those carotids that have been exposed to fluoride. (**b**) The amount of fluoride adsorbed to microcalcifications (identified visually based on the size of nodules of <50 and manual measurements made) is significantly higher than macrocalcifications (>50 mm to several mm; F/Ca in microcalcifications 0.59±0.23, n = 10 (circles); in macrocalcifications 0.37±0.15, n = 7 (squares)); *P*<0.02. (**c**) Representative images of macro- and microcalcifications and soft tissue. F presence was detected only in the calcified regions. Scale bar, 50 μm. (**d**) 18F-fluoride binding to cryostat sections is linear over the clinically relevant concentration range from 1.0 x 10^{-12} to 1.0 x 10^{-7} ($y = 10^{(0.92*\log(x)+13)}$, n = 5). (**e**) There is a fast exponential association and slow exponential dissociation of 18F-fluoride to the whole carotids over time. In all figures filled shapes show mean, error bars denote standard error of the mean.

6.5.2 Pharmacodynamic And Pharmacokinetic Analyses

To confirm the specificity in pharmacological assays, we incubated carotid sections with a clinically relevant concentration (1 x 10^{-11} M) of 18F-fluoride for 1h. (117) As a control for non-specific binding, adjacent sections were incubated at the same concentration of 18F-fluoride, but with an excess (4 x 10^{-4} M) of **non-radioactive** fluoride. Phosphor-imaging autoradiography revealed a strong 18F-fluoride signal with negligible nonspecific binding and no 18F-fluoride binding in areas without calcification (Figure 6.3). Concentration–response curves were constructed by exposing carotid sections (n = 5) to increasing concentrations of 18F-fluoride (10^{-12} – 10^{-7} M) for 1 h. (121,123) There was a positive linear correlation between the radioactivity and concentration of 18F-fluoride (Fig. 6.2d). We then performed association and dissociation binding experiments at a clinically relevant concentration (1 x 10^{-11} M; n = 5). There was a rapid and time-dependent exponential association and, following washing, a slow exponential dissociation from the plaque (Fig. 6.2e). The data were fitted to a one-site model, with an association rate constant (k_1) of 4.5±0.6 x 10^{9} M^{-1} min^{-1} and a half-time for association of 14.3±1.9 min. Dissociation was slow but detectable with a dissociation rate constant of 0.0027±0.0005 min^{-1}, a half-time for dissociation of 254±43 min and an affinity constant (K_D) calculated from these kinetic data of 0.6pM. The affinity constant is a measure of the strength of binding of 18F-fluoride to areas of calcification. The very high affinity is consistent with the comparatively low concentrations of radiolabelled 18F-fluoride required *in vitro* and *in vivo* to detect calcifications in tissues and demonstrates the sensitivity of the tracer.

Figure 6.3 | The Non-Specific Binding Of Fluoride Is Low

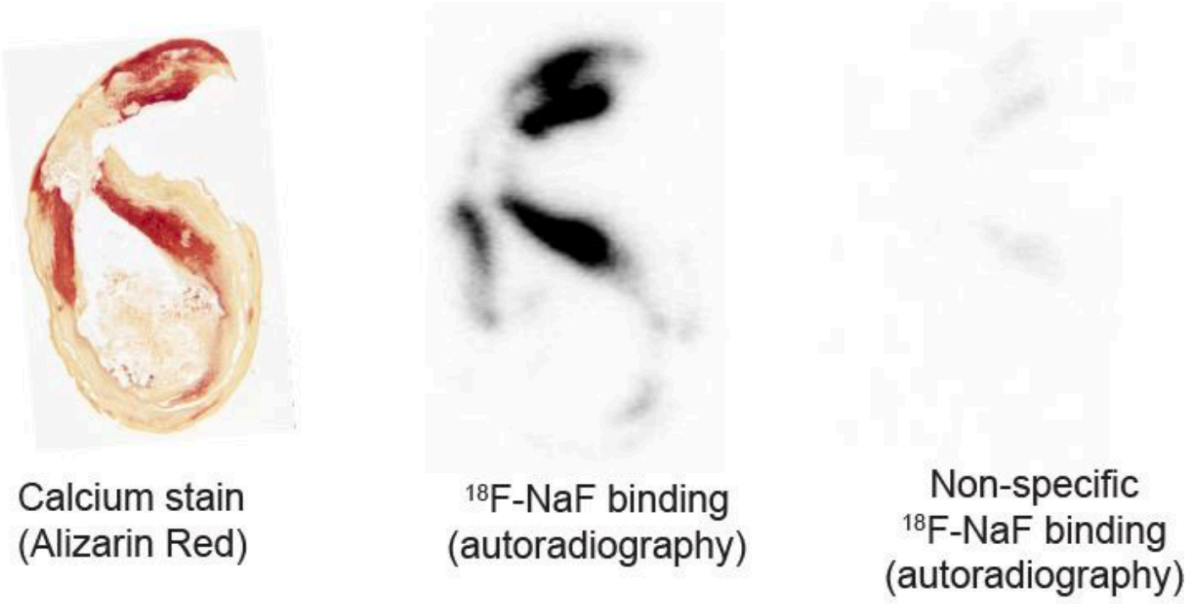

Abbreviation: 18F-NaF, 1F-fluoride

We undertook dynamic PET analysis to explore the *in vivo* pharmacodynamic and pharmacokinetic properties of 18F-fluoride in five patients scheduled to undergo carotid endarterectomy for symptomatic disease (patient demographics are given in Table 6.2). The standardised uptake value (SUV) and target to background ratio (TBR) values for areas of carotid artery deemed visually PET positive and PET negative (of static and dynamic scans (reanalysed as static acquisitions)) are demonstrated: Table 6.3 and Figure 6.4).

$$SUV = \frac{r}{(a'/w)}$$

Equation (2)

SUV is a standardised semi-quantitative method of measuring radioisotope uptake with a volume of interest. *r* is the radioactivity concentration [kBq/mL] within a region of interest (ROI), *a ′* is the decay-corrected injected dose in kBq, and *w* is the patient's mass (g)

$$TBR = \frac{SUV_{ROI}}{SUV_{BP}}$$

Equation (3)

TBR is utilised in cardiovascular static PET analysis to correct for "background" or blood pool activity. SUV_{ROI} is the SUV within a ROI and SUV_{BP} is the SUV within a standardised volume of blood.

Table 6.3 - Patient Demographics And Basic Imaging Data

Subject	Age	Sex	Neurovascular syndrome	Stenosis severity	Days between symptoms and PET scan	Static or Dynamic Scan	Used for Micro/Clinical Comparison
1	88	Male	Stroke	65	10	Static	Yes
2	73	Female	TIA	80	13	Static	Yes
3	76	Male	TIA	85	26	Dynamic	Yes
4	59	Male	TIA	85	14	Dynamic	Yes
5	47	Female	Stroke	65	9	Dynamic	No
6	63	Female	Asymptomatic	60	n/a	Dynamic	No
7	76	Male	Asymptomatic	40	n/a	Dynamic	No

TIA' transient ischaemic attack; stenosis severity is expressed as % according to NASCET method(110).

Table 6.2 - Standardised Uptake Values And Target To Background Ratios For PET Positive Versus PET Negative Regions

Subject Number	PET Positive				PET Negative			
	SUV		TBR		SUV		TBR	
	Mean Max	Mean Mean	Mean Max	Mean Mean	Mean Max	Mean Mean	Mean Max	Mean Mean
1	2.66	1.47	3.33	1.84	1.01	0.82	1.27	1.02
2	3.05	2.06	1.80	1.22	1.61	1.32	0.95	0.78
3	2.75	1.94	2.48	1.75	1.09	0.89	0.98	0.80
4	2.99	2.01	5.26	3.53	0.76	0.60	1.34	1.06
5	1.39	1.23	1.63	1.45	0.57	0.46	0.67	0.54
6	2.30	1.88	2.24	1.84	0.88	0.71	0.86	0.70
7	2.16	1.70	2.57	2.03	1.06	0.82	1.26	0.98

PET, positron emission tomography, SUV, standardised uptake value; TBR, target to background value; Mean Max, mean value of single voxel with highest SUV per PET slice within a region of interest, Mean Mean, mean value of all voxels within a region of interest.

Figure 6.4 | Standardised Uptake Values And Target To Background Ratios For PET Positive Versus PET Negative Regions

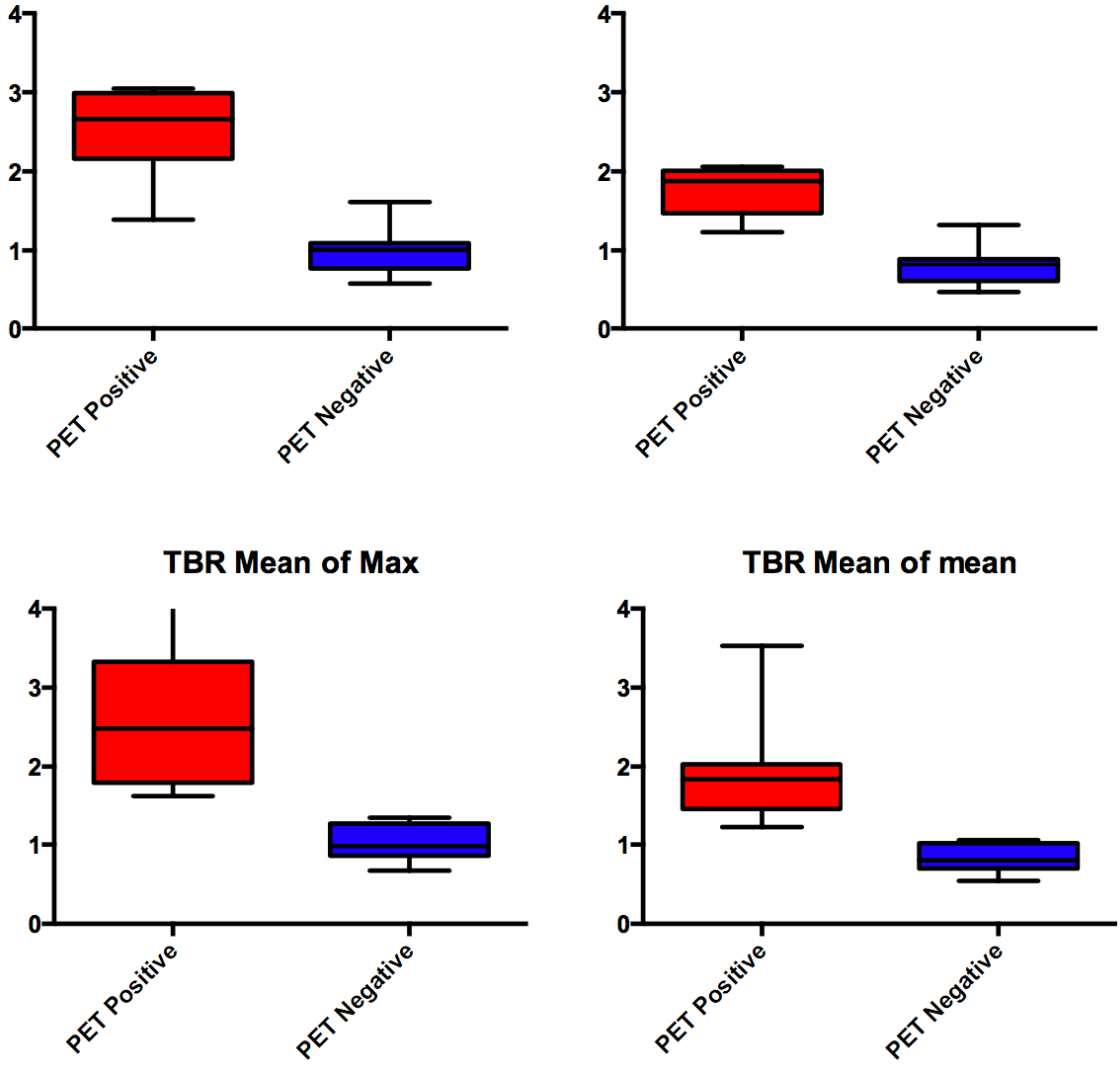

Box and whisker plots of Standardised Uptake Values (SUV) and Target to Background Ratios (TBR) for visually deemed PET positive regions (red) and PET negative regions (blue) (Boxes show interquartile range, whiskers show range).

There was clear visual carotid plaque uptake (see figure 6.9) and Patlak analysis showed a good model fit with 18F-fluoride influx varying from 0.0005 to 0.007 mL cm^{-3} min^{-1} as compared with 0.05 to 0.08 mL cm^{-3} min^{-1} in the vertebral bodies (Table 6.4 and Figure 6.5). No deviation of the data from the model was observed during the time course of these experiments although patients could only tolerate scanning for 75min following tracer injection. Although very slow dissociation can be detected *in vitro*, this was too slow to detect during our imaging window *in vivo* and therefore is unlikely to be an important factor to consider in clinical imaging. 18F-fluoride was rapidly eliminated from the plasma and showed a typical biexponential decay in keeping with immediate redistribution and then subsequent renal elimination (Figure 6.6) 60 min from injection, plasma activity was 4–8% of its peak activity and excellent contrast between vascular tissue and blood pool was observed.

Table 6.4 | Dynamic PET Analysis (Patlak)

		K_i [ml/cm^3/min]	SE [%]
Subject 1	Right Carotid	0.0063	12.7
	Left Carotid	0.0060	10.3
	Vertebra	0.0486	3.0
Subject 2	Right Carotid	0.0042	10.5
	Left Carotid	0.0028	7.1
	Vertebra	0.0459	1.8
Subject 3†	Right Carotid	0.0005	24.0
	Left Carotid	0.0009	34.1
	Vertebra	0.0431	2.8
Subject 4*	Left Carotid	0.0045	21.6
	Vertebra	0.0694	1.9
Subject 5*	Left Carotid	0.0068	28.2
	Vertebra	0.0649	3.4

K_i values for individual carotid plaques and vertebra. SE, standard error. Subjects 4 and 5 had no plaque in their right internal carotid arteries. The vertebral values are in agreement with previously published data. (187) † Subject 3 had very little carotid plaque uptake. * Subject 4 and 5 Ki were estimated using an image derived input function.

Figure 6.5 | Dynamic Clinical PET Analysis

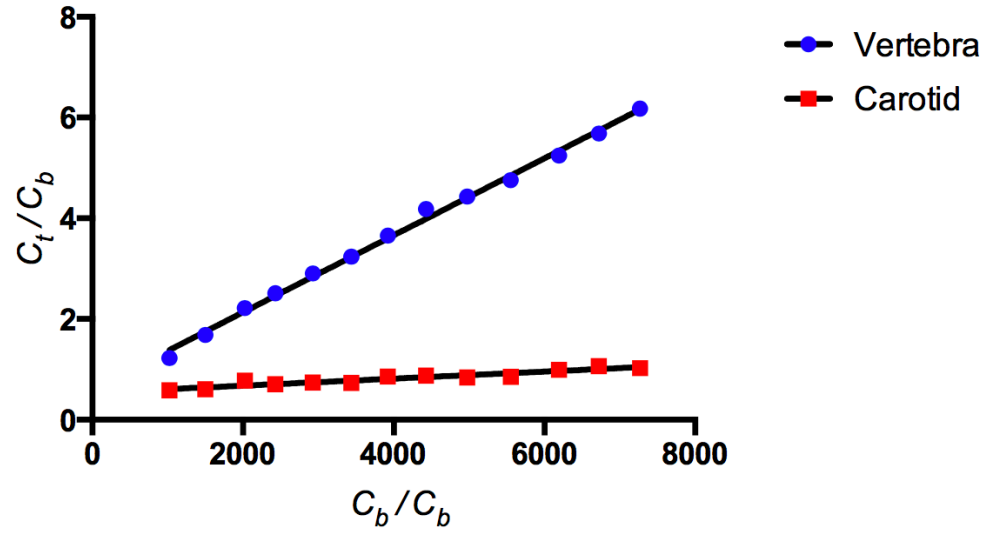

Representative Patlak plots from a single subject showing vertebral and carotid uptake where C_b = plasma counts & C_t = counts within the region of interest. PET, Positron Emission Tomography

Figure 6.6 | 18F-Fluoride Pharmacokinetics

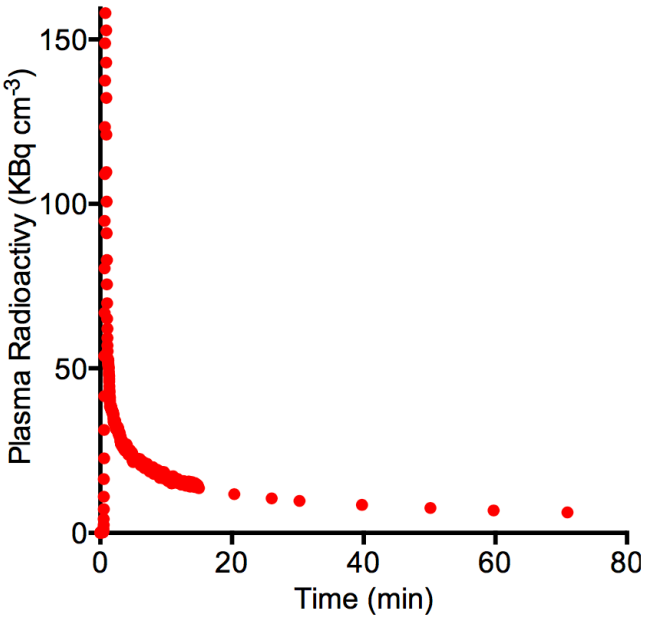

A typical arterial plasma activity curve (from a single patient) showing a very rapid redistribution and clearance of 18F-fluoride from the circulation. KBq, Kilo Becquerels

These complementary *ex vivo* and *in vivo* data demonstrate the favourable imaging properties of 18F-fluoride: an absence of metabolites, rapid ligand-binding site association with minimal dissociation and a rapid reduction in radiotracer background giving excellent tissue contrast resolution 1h following its administration.

6.5.3 Immunohistochemical Analysis

Vascular calcification is believed to occur in response to hypoxia, necrosis and chronic inflammation and has been linked with macrophage burden and neo-vascularization. (170) To test the cellular specificity of 18F-fluoride binding, we stained sequential sections with Alizarin Red (calcification marker) and antibodies for CD68 (macrophage marker), CD31 (endothelial cell marker of neovascularization) and smooth muscle actin (smooth muscle marker; n = 8 individual plaques for each stain). We then filtered and applied an auto-threshold to both the 18F-fluoride radioactivity signal and each of the histological stains, and overlaid them to correlate the two signals (Figure 6.7a). The only high correlation detected was between the 18F-fluoride signal and Alizarin Red calcification stain (r = 0.69±0.03, n = 8) indicating that 18F-fluoride specifically co- localizes to vascular calcification and not other upstream triggers to the calcific response (Figure 6.7b).

Figure 6.7 | 18F-Fluoride Uptake Correlates With Calcification But None Of The Histological Inflammatory Markers

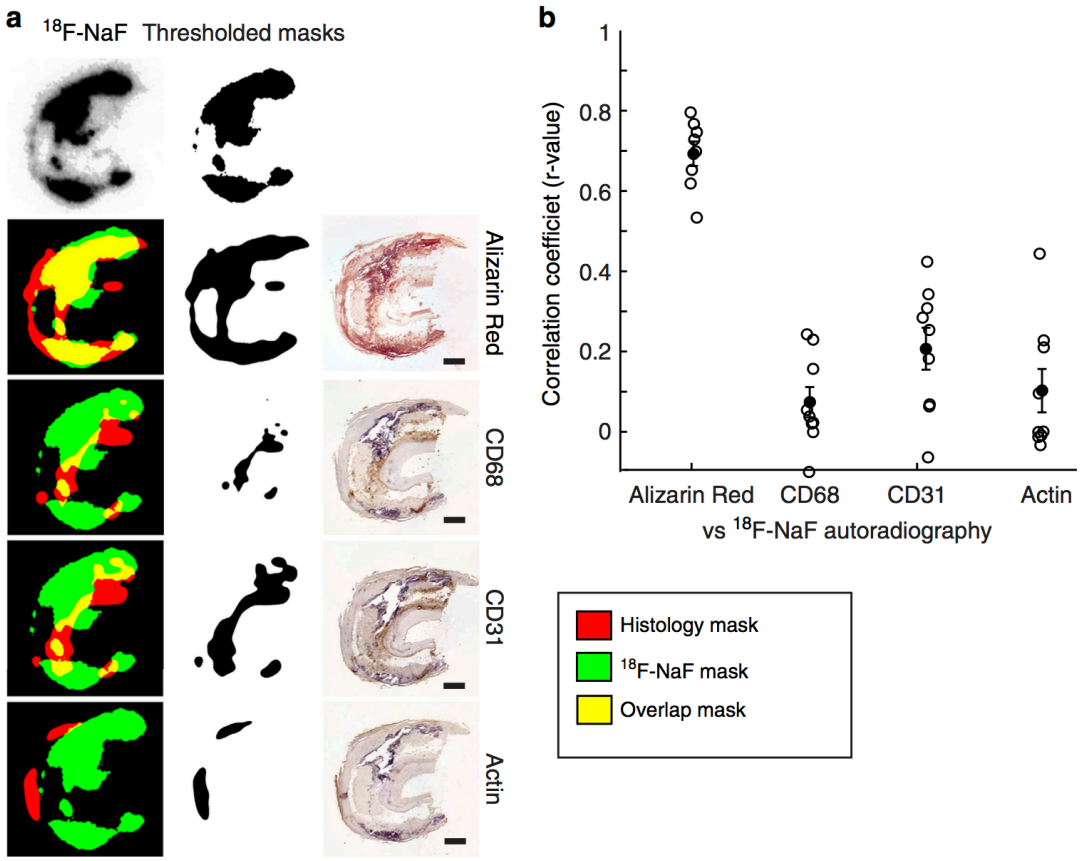

(**a**) Representative images of 18F-fluoride autoradiography signal overlap with immunohistochemistry (IHC)-stained sequential sections. Green: 18F-fluoride signal, red: histology signal, yellow: overlap. Scale bar, 1 mm. (**b**) High correlation is observed between 18F-fluoride and Alizarin Red calcification staining, while low correlation is seen between 18F-fluoride autoradiography and inflammatory and other IHC signals.

6.5.4 Penetration By Autoradiography/Histology And Micro PET/CT

We next compared areas of 18F-fluoride uptake with tissue micro- and macrocalcification. We first sectioned carotid plaques to remove barriers to penetration and incubated with 1 x 10^{-11} M 18F-fluoride for 1 h, followed by exposure to a phosphor-imaging screen. 18F-fluoride uptake correlated with calcification staining (Figure 6.8a, macrocalcifications: closed arrowheads, microcalcifications: open arrowheads) and was observed across all regions of the calcific deposits (Figure 6.8b). In contrast, if carotids were first incubated with 18F-fluoride and then sectioned, 18F-fluoride binding was only detected on the outer surface layer of macrocalcific deposits with the ligand unable to penetrate deeper (Figure 6.8c, d). Irrespective of presectioning of tissue, 18F-fluoride appeared to bind freely to regions of micro-calcification and co-localized with histological staining for calcification (Figure 6.8a–d). Using micro PET/CT, we saw similar results with 18F-fluoride binding only to the surface of macrocalcific deposits (Figure 6.8e, f), matching the limits of penetration demonstrated with autoradiography.

One of the main aims of this work was to explain the previously observed differences between the PET and CT signals in the clinical setting. We chose to investigate this using preclinical micro PET/CT because of the higher spatial resolution that it offers (microPET, 900 μm; microCT, 30 μm). We hypothesized that the use of higher-resolution micro PET/CT would allow detection of microcalcifications. While microcalcifications identified on histology (Figure 6.8g) were not detectable by micro CT (Figure 6.8i), they were identified by an increased 18F-fluoride micro PET signal (Figure 6.8j) that closely matched phosphor-imaging autoradiography (Figure 6.8h). Finally, we further investigated 18F-fluoride penetration by examining the intensity and density of the micro PET and micro CT signals (where calcification was defined as >1,000 Hounsfield units (HU)) along 5–8 mm linear transects of atherosclerotic tissue (Figure 6.8k–o). Once again there were clear differences in the signal produced by these two imaging techniques with increased 18F-fluoride activity on the

Figure 6.8 | 18F-Fluoride Signal Detection Depends On The Sensitivity Of The Detection Modality

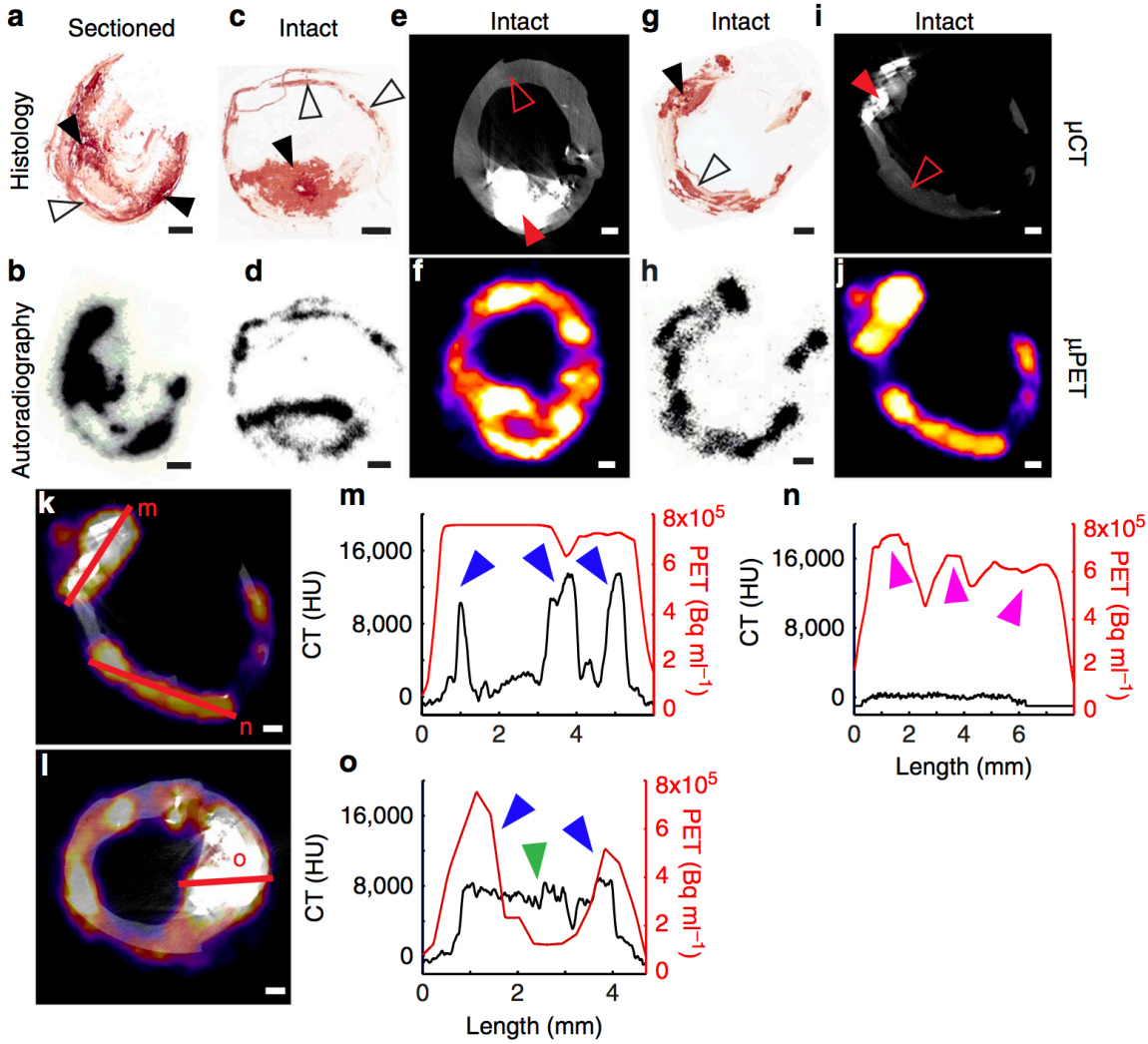

(**a,b**) If the carotid is sectioned first and incubated in 18F-fluoride second, binding occurs to all macro- (closed arrowheads) and microcalcification (open arrowheads) surfaces. (**c,d**) However, if the carotid is incubated in 18F-fluoride first and then sectioned, 18F-fluoride is able to bind only to the surface level of macrocalcifications (closed arrowheads), while binding occurs to all microcalcifications (open arrowheads). (**e,f**) 18F-fluoride binding solely to the surface level of macrocalcifications can also be observed in a micro PET/CT scan, if the macrocalcification size is larger than micro PET resolution. (**g,i**) Microcalcifications that are detected with Alizarin Red histology cannot be seen in a micro CT scan, due to insufficient sensitivity. (**h,j**) Yet, 18F-fluoride micro PET scan closely matches autoradiography signal and can detect microcalcifications. (**k,l**) micro PET/CT signal quantification by measuring the intensity of the 18F-fluoride micro PET signal and the micro CT density measure along the same transects. (**m**) 18F-fluoride binding can be observed throughout the three macrocalcification peaks due to macrocalcification size being smaller than micro PET resolution (PET+/CT+, blue arrowheads); (**n**) Microcalcifications detected with 18F-fluoride micro PET and autoradiography (see **h**) as well as Alizarin Red histology (see **g**) but not micro CT (PET+/CT-, magenta arrowheads); (**o**) If macrocalcifications are larger than μPET resolution, 18F-fluoride binding solely around the surface level of macrocalcifications can be observed, similarly as in autoradiography (center green arrowhead PET-/CT+, blue arrowheads PET+/CT+). Scale bar, 1 mm.

surface of macroscopic calcium deposits that by contrast was not observed within their core.

Comparing clinical *in vivo* PET/CT and *ex vivo* micro PET/CT. We applied a novel approach to compare the *in vivo* and *ex vivo* imaging of carotid atherosclerotic plaque using co-registered clinical PET with CT, micro PET with micro CT and autoradiography with histology. In particular, we focused on the mismatch between the 18F-fluoride PET signal and CT identifiable calcification (Figure 6.9). We recruited four patients who were scanned with 18F-fluoride PET/CT before carotid endarterectomy (Figure 6.9a). After surgery, we incubated the endarterectomy specimens with 18F-fluoride and imaged them with the micro PET/CT scanner (Figure 6.9h). Finally, we again incubated the carotid endarterectomy specimens with 18F-fluoride and cryosectioned them to obtain autoradiography images and light microscope histology to detect areas of calcium (Figure 6.9n). On the clinical PET/CT and micro PET/CT scans, we confirmed differences in the distribution of calcium on CT and 18F-fluoride uptake on PET (Figure 6.9c–g). Regions of 18F-fluoride uptake were most commonly observed in the absence of calcium on CT, representing areas of microcalcification (PET+/CT- ; Figure 6.9b,i). In addition, there were also large CT-detected areas of macrocalcification that did not demonstrate concomitant 18F-fluoride uptake (PET-/CT+ ; Figure 6.9b,g). These are likely to represent regions where nascent microcalcification is mild or absent.

The findings on micro PET/CT were similar to the clinical scans. Indeed, the distribution of calcium detected with micro CT closely matched that observed on the clinical CT although additional smaller areas of macrocalcification were also identified and resolved (Figure 6.9j–m). The distribution of the 18F-fluoride signal was also similar although again it was more refined on the micro PET compared with the clinical PET systems (Figure 6.9j–l).

Figure 6.9 | High-Resolution Imaging Reveals Specificity Of 18F-Fluoride Binding To Vascular Calcification

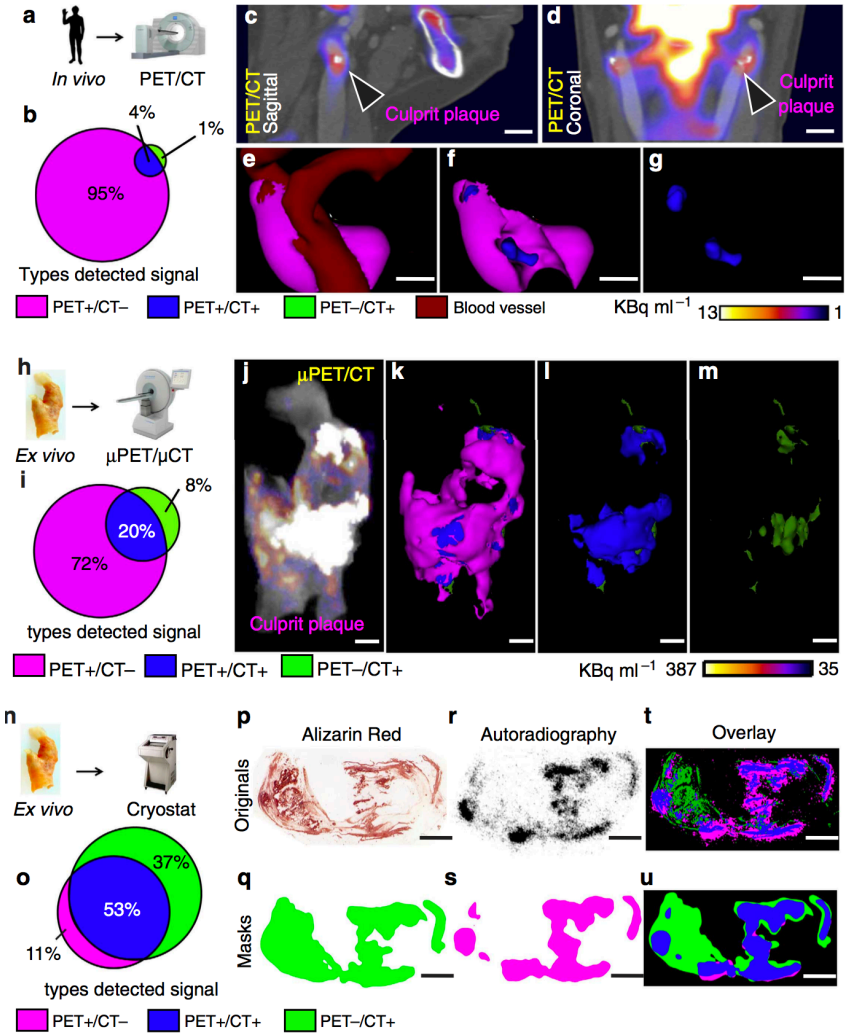

(**a**) Four symptomatic patients underwent clinical PET/CT imaging after injection of 18F-fluoride and before carotid endarterectomy.

(**b**) Comparison of PET and CT signals. Although clinical PET spatial resolution is much less than CT, PET detects a larger area than CT, demonstrating higher sensitivity. PET+/CT-: magenta, 95%, PET+/CT+: blue, 4%, PET-/CT+: green, 1%.

(**c,d**) Clinical PET/CT scan with the culprit atheroma (arrowheads). Scale bar, 11 mm (c) Sagittal view; (d) Coronal view.

(**e–g**) Analysis of the carotid in vivo, where PET signal (magenta) was detected using observer-independent Otsu histogram-based thresholding. PET signal is co-localized with CT vascular calcification (blue). CT angiogram defined lumen is dark red. Scale bar, 7 mm.

(**h**) After endarterectomy, carotids were recovered, incubated in 18F-fluoride and scanned in a micro PET/CT scanner. (**i**) Ratio of PET+/CT- area and CT+ signals is smaller than in **b**, due to the higher micro PET resolution, which results in more precise signal detection. PET+/CT-: magenta, 72%, PET+/CT+: blue, 20%, PET-/CT+: green, 8%.

(**j–m**) *Ex vivo* images of the carotid from the same patient as in **c–g**. (**j**) microPET/CT image without thresholding; (**k–m**) 3D thresholded micro PET/CT images. PET+/CT- (magenta), PET+/CT+ (blue), PET-/CT+ (green).

(**n**) After micro PET/CT scan, carotids were incubated in 18F-fluoride and sectioned on cryostat prior to Alizarin red staining and autoradiography (**o**) Ratio between Autoradiography ("PET") +/ Alizarin red ("CT") - and "CT" + regions indicate naturally higher resolution of Alizarin red for calcium compared to clinical CT or micro CT. "PET" +/"CT" - : magenta, 11%, "PET"+/"CT"+: blue, 53%, "PET" -/"CT"+: green, 37%. (**p**) Carotid from the same patient as in **c–g**, **j–m**. Alizarin Red detects both macro- and microcalcifications with the highest precision of all methods described here. (**q**) Alizarin Red image after Gaussian filter and Li thresholding, to match resolution to autoradiography image. (**r**) Autoradiography shows highly specific binding to all microcalcifications, but is not able to penetrate the deeper levels of macrocalcifications. (**s**) Autoradiography image after Gaussian filter and Li thresholding, to match resolution to the filtered Alizarin Red image. (**t**) Overlay of unfiltered histology and autoradiography images showing a high PET+/CT- signal, due to mismatch in resolution. (**u**) Overlay of filtered histology and autoradiography images shows matching signal resolution. Scale bar = 3 mm.

Finally, histology and 18F-fluoride autoradiography provided the most sensitive method for the detection of tissue calcification (Figure 6.9o–u). Histological staining with Alizarin Red confirmed that both micro CT and clinical CT only detect regions of macrocalcification with extensive regions of microcalcification left unresolved by these techniques (Figure 6.9p–u). By contrast, the 18F-fluoride signal detected by autoradiography was observed in a very similar distribution to that observed by the microPET (albeit providing better spatial resolution), with both able to resolve regions of microcalcification (Figure 6.9r–u).

6.6 Discussion

For the first time, we demonstrate the specificity and sensitivity of 18F-fluoride adsorption to calcium deposits in human atherosclerotic vascular tissue and demonstrate that it can non-invasively detect areas of microcalcification indicative of nascent calcification and active unstable atherosclerosis. This unique and characteristic signal has implications and ramifications for the non-invasive clinical imaging of human atherosclerosis—a condition that represents the leading cause of death worldwide.

In bone, the binding of fluoride to areas of calcification is mediated through a chemical reaction with hydroxyapatite, a crystalline structure that is also the main component of vascular mineralization. (117) Using electron microprobe analysis, we have shown for the first time that fluoride also closely co-localizes to pathological mineralization within vascular tissue. The precise target for fluoride binding in living vasculature has been uncertain, as fluoride ions were not expected to have the selectivity as seen between ligands and their cognate receptors, and fluoride could target molecules other than hydroxyapatite. Here we demonstrate that 18F-fluoride co-localizes to areas of nascent calcification and potentially provides a novel non-invasive biomarker of this high- risk pathology. Moreover, we observed that there is preferential adsorbing of fluoride to microcalcification, a clinically more significant manifestation of vascular mineralization. The extent of fluoride adsorption depends on the surface area of the mineral(188,189) and would be consistent with the proposal that the complex convex surface structure of microcalcifications allows more binding of fluoride than the relatively flat and smaller surface area of macrocalcification.

The association and dissociation of 18F-fluoride to carotid endarterectomy specimens showed an exponential rise and decay of signal, with excellent contrast between activity in vascular tissue and the blood pool observed as early as 60 min following injection. Studies in artificial chemical models have

shown that fluoride binding to hydroxyapatite also occurs in an exponential binding reaction(188,189) and can be explained both by physico- and chemisorption. (188) This also appears as the most likely mechanism in human carotids but it is important to emphasize that not all calcification observed can be generalized to consist of hydroxyapatite. Previous clinical radiology reports have described an initial fluoride-bound water shell entrapment and a slow ion exchange; (78) however, no mechanistic studies to prove these assumptions have been published, at least to our knowledge. Therefore, we propose that our observations match the findings in artificial systems and the fluoride adsorption to hydroxyapatite in whole-carotid sections can be explained by physico- and chemisorption and the dissociation is a result of a washout, similar to what has been described in artificial systems. (188)

The mechanism of early micronodular intimal atherosclerotic calcification is not yet clearly understood although its genesis has been linked to, amongst others factors, inflammatory macrophages, inflammatory lipids, apoptosis, neovascularization and phenotypically altered vascular smooth muscle cells. (170) We have demonstrated that 18F-fluoride binds specifically and sensitively to the final common pathway of precipitated micro nodules of pathological calcification (whether through active or passive mechanisms) and not directly to any of these putative earlier upstream triggers. This is in contrast to 18F-fluorodexoyglucose, which although linked to activated macrophages in the vasculature, may lack sensitivity and specificity for identifying inflammation specific activation(76) and does not have the highly favourable pharmacokinetics of 18F-fluoride. (71,76)

The main question we sought to answer was why does the 18F-fluoride clinical PET/CT imaging result in a signal mismatch between the two modalities? Specifically, why do some areas of macrocalcification show no uptake, while other areas without apparent calcification show high 18F-fluoride uptake? To address this, we used carotid endarterectomy sections and compared *ex vivo* and *in vivo* imaging approaches. Since vascular calcification consists

predominantly of mineral and only a small amount of soft tissue, the architecture of the calcification in the *in vivo* and *ex vivo* environments was very similar. Using autoradiography, we were able to show that if the *ex vivo* carotid was first incubated in 18F-fluoride and then cryosectioned, 18F-fluoride only bound to the outer surface of the macrocalcifications. In contrast, microcalcifications had a greater surface area and no barriers to penetration of the tissues resulting in high levels of 18F-fluoride adsorption. This suggests that 18F-fluoride cannot penetrate into the deeper layers of macrocalcification. Since macrocalcifications have a large volume but small surface area, the detected radioactivity signal is proportionally smaller than microcalcifications with a small volume and large surface area. Microcalcifications are also dispersed in large numbers per given area of the tissue, again resulting in a disproportionally high signal compared with macrocalcifications. Furthermore, when sectioned carotid endarterectomy specimens were directly exposed to 18F-fluoride, uptake was this time observed also in the centre of macroscopic deposits that had now been made accessible to the tracer. We therefore conclude that the adsorption of 18F-fluoride to areas of calcification in carotid endarterectomy tissue is a measure of the available surface area accessible to the isotope. This is consistent with findings in the bone and explains the observed greater adsorption of 18F-fluoride to microcalcifications (Figure 6.10a, b).

Micro PET/CT scans of *ex vivo* carotids and their comparison with autoradiography revealed that micro PET closely matches autoradiography. On the other hand, micro CT was only able to detect macrocalcifications (Figure 6.10c) and underestimated the extent of vascular microcalcification identified by Alizarin Red histology. Back-correlation of micro PET/CT *ex vivo* scans to clinical *in vivo* PET/CT scans showed similar results. Using clinical CT, it was possible to detect the larger macrocalcifications, and their shape closely matched the data acquired by micro CT. In contrast, the 18F-fluoride uptake detected by the clinical and micro PET co-localized with both underlying calcium deposits (PET+/CT+) and regions with no apparent calcification (PET+/CT-) as assessed on CT (Figure 6.10d). For the latter situation, our

histological studies showed that the PET signal was in fact binding to microcalcifications below the detection limit of clinical CT and micro CT. We therefore conclude that areas of 18F-fluoride uptake are reporting underlying microcalcifications, which are undetectable by CT. Conversely, large CT-detected macrocalcifications that do not co-localize with 18F-fluoride PET uptake (PET-/CT+) might be considered to represent dormant areas where on-going mineralization, as evidenced by the presence of microcalcification, has ceased and atherosclerotic disease is quiescent. Indeed, more heavily calcified plaques have been reported to be particularly prevalent in more stable disease and are much less vulnerable to rupture. (190,191)

Figure 6.10 | Model of 18F-Fluoride Binding To Vascular Calcification

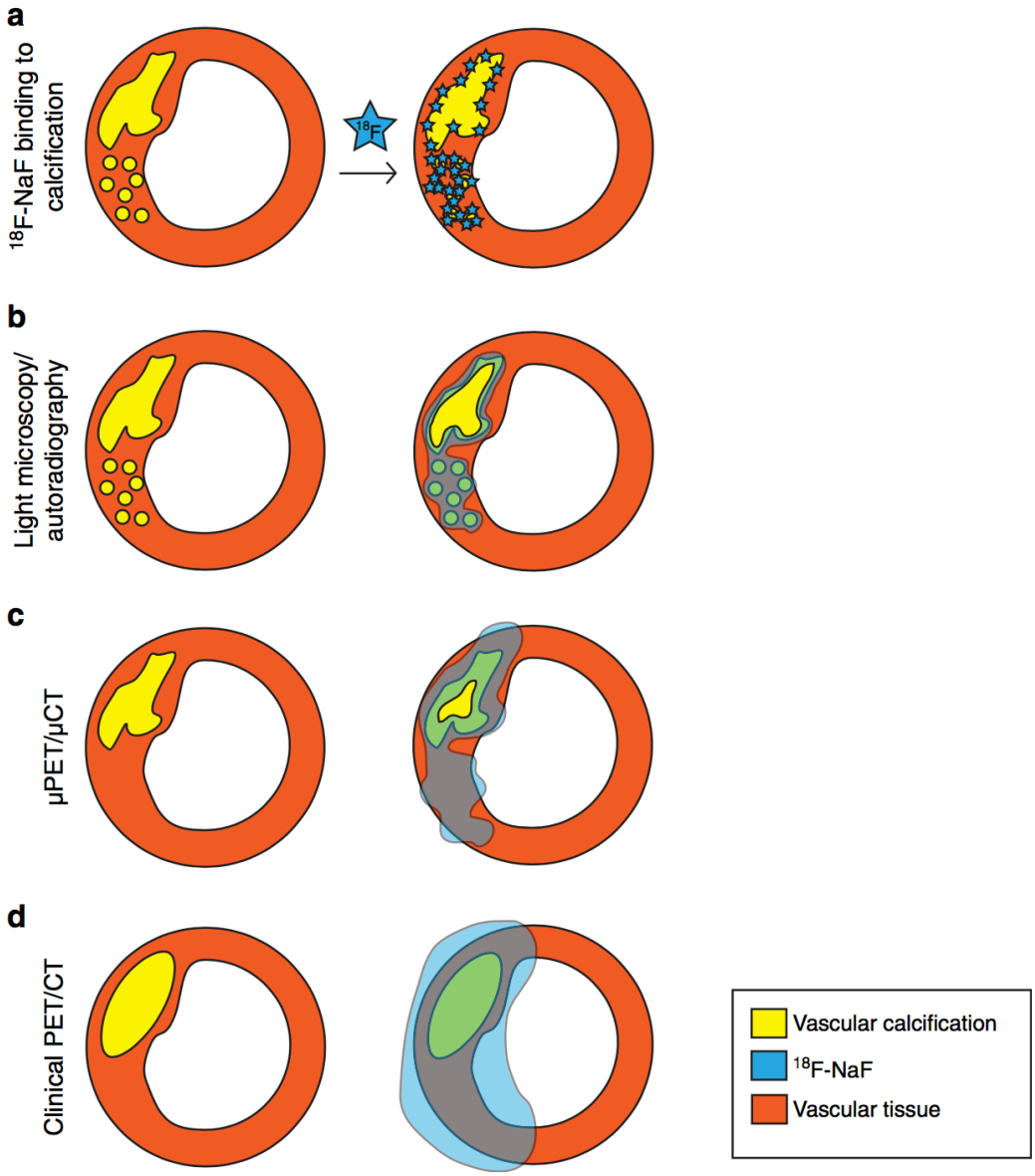

(a) 18F-Fluoride (18F-NaF) highly specifically binds to both micro- and macrocalcifications and the signal strength depends on the available surface area of these calcifications. **(b)** Schematic of histology/autoradiography vascular calcification detection. Alizarin Red histology results in the most definitive delineation of calcification, with the detection limit into the nanometre range. Phosphor screen autoradiography also has a much higher resolution compared with PET and micro PET, resulting in accurate detection of calcifications. **(c)** Schematic of preclinical micro PET/CT vascular calcification detection. Micro CT detects macrocalcifications and their finer architecture. Proportionally less signal is detected on micro CT than using histology, yet more than the clinical CT. Micro PET very precisely detects both macro and microcalcifications. In addition, if the macro- calcifications exceed micro PET resolution, it is possible to observe 18F-fluoride binding to the outer surface of macrocalcifications. There are less PET-/CT + regions observed than using autoradiography but more than clinical PET/CT. **(d)** Schematic of clinical PET/CT vascular calcification detection. Here CT is able to detect gross macrocalcifications and PET detects both CT+ and CT- calcifications. However, the signal is diffuse, resulting in much larger and therefore less precise PET+ detections, as compared with the *ex vivo* imaging modalities described here.

In summary, using electron microprobe analysis, we have demonstrated for the first time that fluoride directly adsorbs to calcified areas in mineralized vascular tissue. We have shown that binding is highly specific since 18F-fluoride radioactivity is confined solely to calcification, with no localization to other soft tissues. Furthermore, we observed that 18F-fluoride signal is highly dependent on the surface area of the calcification, being able to adsorb only to the outer layer of macrocalcifications without deeper penetration. We replicated these findings on three levels— autoradiography, light microscopy, *in vivo* clinical PET/CT and *ex vivo* micro PET/CT. These characteristics position 18F-fluoride as a highly specific ligand for the detection of pathologically high-risk microcalcification and early unstable atherosclerotic disease. 18F-Fluoride is an economical PET ligand that is easy to manufacture. If used clinically, 18F-fluoride uptake has the potential to identify microcalcification within high-risk plaques as well as determine the locations of plaque rupture. In addition, as a marker of nascent calcification, it could test the efficacy of pharmacological therapies targeting atherosclerosis or calcification in both the clinical and preclinical settings. Microcalcifications are also linked to other disease processes, such as breast cancer, prostate cancer and stroke. The main aim of this study was to understand the molecular mechanisms of 18F-fluoride uptake and not to define patients at risk. With data validating its co-localization with calcification, the potential now exists to evaluate these processes. Whether or not 18F-fluoride will be useful in stratifying risk of cardiovascular events remains to be demonstrated. Large-scale prospective investigations will be essential to determine the prognostic value for 18F-fluoride role in risk stratification. Nevertheless, 18F-fluoride PET/CT holds promise and may have wideranging applications and become a valuable clinical tool to study active calcification across many disease areas and disciplines.

6.7 Conclusion

We conclude that 18F-fluoride PET/CT is the only currently available non-invasive clinical imaging platform that can detect microcalcification in active unstable human atherosclerosis.

Chapter 7 – 18F-Fluoride And 18F-FDG Hybrid Positron Emission Tomography And Computed Tomography In Carotid Artery Atherosclerosis

7.1 Publication in Context

7.1.1 Background

My work so far has demonstrated the potential that 18F-fluoride PET/CT has in the field of plaque imaging. The data suggest that in the coronary circulation the isotope is able to selectively identify culprit and high-risk atherosclerotic plaque *in vivo* (see Chapter 5). My *in vitro* and preliminary *in* vivo experiments in the carotid circulation (see Chapter 6) suggest that this clinical phenomenon is explained by the fact that, compared to discrete volumes of stable field calcification, pathologically high-risk micro-calcification is preferentially highlighted by 18F-fluoride due to the presentation of a much larger surface-area for isotope adsorption. The clinical utility and feasibility of carotid 18F-fluoride PET/CT however remained undescribed.

7.1.2 Aims of Further Study

The goal of this final part of my work was to study the *in vivo* clinical utility and feasibility of 18F-fluoride PET/CT in the context of unstable carotid artery atherosclerosis and to compare it to the existing "gold-standard" PET tracer 18F-Fluorodeoxyglucose. The study aims were as follows

1. Is 18F-fluoride PET/CT of the carotid territory clinically feasible?
2. Is 18F-fluoride carotid uptake quantification reliable in terms of intra- and inter-rater differences? How does this compare to 18F-FDG?
3. Does 18F-fluoride selectively highlight clinically adjudicated culprit carotid plaque?
4. What is the relationship between 18F-fluoride and 18F-FDG carotid plaque uptake and traditional markers of plaque vulnerability?
5. What is the relationship between 18F-fluoride and 18F-FDG plaque uptake and clinical cardiovascular risk?

7.1.3 Contributions

I led this work supervised by Doctor Marc Dweck and Professor David Newby. I designed the experiments, gained all the relevant ethical and supervisory board approvals, recruited all the patients, performed all the scanning and analysis. I collected the specimens (blood & tissue). I drafted the manuscript.

Published as: **Vesey AT**, Jenkins WS, Irkle A *et al*. 18F-fluoride and 18F-Fluorodeoxyglucose Positron Emission Tomography After Transient Ischemic Attack or Minor Ischemic Stroke: Case-Control Study. *Circulation: Cardiovasc Imaging*. 2017;10:e004976.

7.2 Abstract

7.2.1 Background

Combined positron emission tomography (PET) and computed tomography (CT) can assess both anatomy and biology of carotid atherosclerosis. We sought to assess whether 18F-fluoride or 18F-Fluorodeoxyglucose can identify culprit and high-risk carotid plaque.

7.2.2 Methods

We performed 18F-fluoride and 18F-Fluorodeoxyglucose PET/CT in 26 patients after recent transient ischemic attack or minor ischaemic stroke: 18 patients with culprit carotid stenosis awaiting carotid endarterectomy and 8 controls without culprit carotid atheroma. We compared standardized uptake values in the clinically adjudicated culprit to the contralateral asymptomatic artery, and assessed the relationship between radiotracer uptake and plaque phenotype or predicted cardiovascular risk (ASSIGN score [Assessing Cardiovascular Risk Using SIGN Guidelines to Assign Preventive Treatment]). We also performed micro PET/CT and histological analysis of excised plaque.

7.2.3 Results

On histological and micro PET/CT analysis, 18F-fluoride selectively highlighted microcalcification. Carotid 18F-fluoride uptake was increased in clinically adjudicated culprit plaques compared with asymptomatic contralateral plaques ($\log^{10}$ standardized uptake value mean 0.29 ± 0.10 *versus* 0.23±0.11, $P = 0.001$) and compared with control patients ($\log_{10}$ standardized uptake value mean 0.29 ± 0.10 *versus* 0.12 ± 0.11, $P = 0.001$). 18F-fluoride uptake correlated with high-risk plaque features (remodelling index [r = 0.53, $P = 0.003$], plaque burden [r = 0.51, $P = 0.004$]), and predicted cardiovascular risk [r = 0.65, $P = 0.002$]). Carotid 18F-Fluorodeoxyglucose uptake appeared to be increased in 7 of 16 culprit plaques, but no overall differences in uptake were observed in culprit versus contralateral plaques or control patients. However, 18F-Fluorodeoxyglucose did correlate with predicted cardiovascular risk (r = 0.53, $P = 0.019$), but not with plaque phenotype.

7.2.4 Conclusion

18F-fluoride PET/CT highlights culprit and phenotypically high-risk carotid plaque. This has the potential to improve risk stratification and selection of patients who may benefit from intervention.

7.3 Introduction

Although carotid endarterectomy reduces risk of ipsilateral stroke in people with symptomatic carotid artery stenosis, the number needed to treat to prevent one stroke is large, (60) especially in asymptomatic stenosis. (192) Furthermore, the pathological event that leads to cerebral thromboembolism (atherosclerotic plaque rupture) is not necessarily correlated with luminal stenosis severity. (156) Other pathological features, such as inflammation, cell death, and microcalcification, are important in driving both plaque formation and instability. (48,178,193) New imaging biomarkers of these processes are therefore needed to improve risk stratification and clinical decision-making. Such biomarkers could also assess the response of plaque biology to novel pharmacological interventions and provide a way of identifying culprit lesions in patients with multiple plaques.

Hybrid positron emission tomography and computed tomography (PET/CT) is a molecular imaging modality that has high sensitivity for non-invasive *in vivo* detection of radiolabelled biomolecules tuned to a variety of pathophysiological processes. In carotid atherosclerosis imaging, the most widely used tracer has been 18F-Fluorodeoxyglucose (18F-FDG). (71,130,194-198) Recently, we have described another radiotracer, 18F-fluoride, in atherosclerosis imaging. (117,121) We(117,121,124,136) and others(104,105,107,135,199) have shown that this tracer has major potential in cardiovascular disease. 18F-Fluoride can highlight culprit plaque in patients after myocardial infarction and high-risk plaques in patients with apparently stable coronary heart disease. (117) We have shown that this is because 18F-fluoride can highlight areas of microcalcification indicative of necrotic atheroma. (200) The ability to identify high risk or culprit plaque in the cephalic circulation has the potential to improve risk stratification in patients at high risk of stroke with a view to more targeted interventions. Our study aims were to compare and contrast the identification of clinically adjudicated culprit and high- risk plaque at the carotid bifurcation using 18F-fluoride and 18F-FDG PET/CT.

7.4 Methods

7.4.1 Patient Population

Two cohorts of people with a recent transient ischemic attack (TIA) or minor ischemic stroke were recruited: a case cohort with a high-grade internal carotid artery stenosis (≥50% by North American Symptomatic Carotid Endarterectomy Trial(110) criteria for men, ≥70% for women) scheduled to undergo carotid endarterectomy and a control cohort in whom the cause of stroke was not attributed to carotid atheroma. Participants were recruited from outpatient clinics in National Health Service Lothian between January 2013 and June 2014.

7.4.2 Exclusion Criteria

These were as follows:

- A modified Rankin score >3 (due to the burden of participation in those with limited mobility)
- Insulin-dependent diabetes mellitus (due to the variability of 18F-FDG uptake)
- Women of child-bearing potential
- Severe chronic kidney disease (estimated glomerular filtration rate <30 mL min^{-1} 1.73 m^{-2})
- Known allergy to iodine-based contrast media
- Prior ipsilateral internal carotid artery intervention
- Prior neck irradiation
- Those unable to provide informed consent

7.4.3 Ethical Matters

Research ethics committee approval (National Health Service West of Scotland Research Ethics Committee: 12/WS/0227) and the written and informed consent of all participants were obtained.

7.4.4 Baseline Assessment

Participants underwent clinical assessment at baseline including standard hematologic and biochemical indices. Serum C-reactive protein concentration was measured using the MULTIGENT CRP Vario assay on the high-throughput ARCHITECT system (Abbott Laboratories, Abbott Park, IL). Predicted cardiovascular risk was estimated using the ASSIGN score: a validated Scottish cardiovascular risk score that is similar to the Framingham risk score but includes additional factors, such as social deprivation and family history. (143)

7.4.5 PET/CT Protocol

Static 18F-FDG PET/CT was acquired using a hybrid scanner (Biograph mCT, Siemens Medical Systems, Erlangen, Germany) 90 minutes after the intravenous administration of a target dose of 200 MBq. A rigid neck collar was fitted to minimize movement and standardise position. An attenuation-correction CT scan (non-enhanced, low dose 120 kV, 50 mAs) was then performed followed by PET acquisition covering 2 bed positions with the first upper bed centred over the carotid bifurcation in 3-dimensional mode for 20 minutes per bed. Patients were fasted for 6 hours before scanning.

18F-fluoride PET/CT was undertaken the subsequent day 60 minutes after administering 250 MBq 18F-fluoride. A neck collar was fitted and an attenuation-correction CT scan was performed. This was followed by PET acquisition covering 2 similar bed positions to the 18F-FDG scan allowing 15 minutes per bed. A subset of 5 patients underwent fully dynamic 18F-fluoride PET/CT with pharmacokinetic analysis as described previously (chapter 6(200)) Dynamic PET provides a quantitative assessment of uptake and these data were used to validate the semi-quantitative static imaging data.

After PET acquisition, a CT carotid angiogram was performed without moving the subject (Care Dose 4D, 120 kV, 145 mA, rotation time 0.5 seconds, pitch 0.8. Contrast: 50 mL Niopam 370).

Static PET data were reconstructed using the Siemens UltraHD algorithm: ordered subset expectation maximization + point spread function modelling + time-of-flight; 2 iterations and 21 subsets; matrix size 200×200; 5 mm full-width half-maximum Gaussian smoothing. Dynamic PET data were similarly reconstructed but only using coincident events from the 60- to 75-minute time-bin. Dynamic data were analysed as reported previously(200) and a K_i value was calculated using Patlak analysis. (111,112)

7.4.6 Tissue Collection

At the time of endarterectomy, plaques were collected immediately after excision, photographed, and snap frozen. A random selection (n=8) of specimens was analysed by micro PET/CT and histology to explore 18F-fluoride binding patterns.

7.4.7 Micro PET/CT

Carotid artery specimens were stored at -80 degree Celsius following removal during carotid endarterectomy. Thawed non-decalcified carotid artery specimens were incubated for 60 minutes in 18F-sodium fluoride 104.89 kBq/mL solution (10.5 MBq 18F-fluoride in 99.5 mLs 0.9% NaCl). Samples were twice washed in 100mLs 0.9% NaCl for 2 minutes to remove unbound 18F-fluoride. Carotid artery specimens were scanned using high-resolution micro-positron emission tomography and non-contrast computed tomography [50kVp tube voltage, 300msec exposure time] (Mediso nanoScan PET/CT, Mediso Medical Imaging Systems, Hungary). PET/CT images were analysed on an OsiriX workstation (OsiriX version 7.5.1, 64- bit, OsiriX Imaging Software, Geneva, Switzerland).

7.4.8 Autoradiography And Histology

To perform autoradiography, 18F-fluoride was diluted to 1 x 10^{-11} M. Whole carotid plaque specimens were thawed in 5 mL PBS for 1 h, and then placed in 5 mL of the diluted 18F-fluoride solution for 1 h at room temperature. They were then washed in PBS three time and dipped in distilled water. Specimens were then embedded in OCT Compound (CellPath, Powys, UK) and 20 μm thick, serial sections were cut on a Bright (Huntingdon, UK) cryostat and placed on Superfrost Plus slides (VWR, Lutterworth, UK). After drying, sections were placed on a charged phosphor screen (Perkin Elmer, Waltham, Massachusetts) and left overnight. The next day screens were read using PerkinElmer's Cyclone Plus Phosphor Imager (Waltham, Massachusetts) and data analysed with OptiQuantTM software (Packard Instrument, Meriden, Connecticut).

Alizarin Red (Alfa Aesar, Heysham, UK) was employed to stain calcium. Sections were fixed in acetone (4 °C) for ten minutes then washed in PBS at room temperature. After washing, 300 μL Alizarin Red was applied to each section for one minute. Samples were then transferred to acetone for 1 min, before being washed in acetone:xylene (50:50) for 1 min. Sections were then incubated in xylene for at least 1 h. Tissue was then mounted using DePeX mounting medium Gurr (VWR, Lutterworth, UK) and glass coverslips (Menzel-Gläser, Braunschweig, Germany) were applied. Slides were imaged using Wild Heerbrugg M3Z microscope (Leica, Heerbrugg, Switzerland).

7.4.9 Image Analysis

7.4.9.1 Positron Emission Tomography/Computed Tomography

Static analysis of 18F-FDG and 18F-fluoride uptake was performed on an OsiriX workstation (OsiriX version 3.5.1 64-bit; OsiriX Imaging Software, Geneva, Switzerland). PET/CT data were reviewed alongside the CT angiogram. Scans were qualitatively assessed for registration, image quality, patient movement, and visual evidence of radiotracer uptake. PET and CT data were individually and carefully manually co-registered by lining up fiducial markers apparent on

both modalities (e.g. cervical spine, mandible and hyoid on 18F-fluoride imaging; skin, spinal cord, and brain on 18F-FDG imaging). No formal inter-PET registration was performed. Three regions of interests (ROIs) were drawn on the carotid of interest on adjacent 3-mm axial slices. If a plaque was present, the ROIs were centred on the area of highest uptake. If there was no plaque, the uptake in the proximal 1 cm of internal carotid artery, just distal to the bifurcation was quantified. From these, standardized uptake values (SUVs; maximum, mean maximum, and mean) were recorded. Blood pool activity was determined from the average of 5 ROIs within the lumen of the superior vena cava to calculate target to background ratios.

Uptake in the proximal left common carotid artery was quantified to explore the relationships between arterial 18F-FDG and 18F-fluoride uptake in a site unaffected by an acute plaque event. Three ROIs were placed around this vessel and uptake was recorded.

Inter- and intra-observer reproducibility of 18F-fluoride uptake measurements were determined using a random selection of 12 patients (24 carotids) by 2 experienced observers who were blinded to the clinical data during analysis.

7.4.9.2 Computed Tomography

The CT angiogram was assessed for image quality, plaque presence, location, and characteristics. Analysis was undertaken on a cardio- vascular workstation (Vital Images, Minnetonka, MN). A blinded and experienced observer (AV) performed the semi-automated CT plaque analysis.

7.4.10 Statistical Analysis

Radiotracer uptake, expressed as mean and maximum SUV, was compared between the clinically adjudicated culprit carotid plaque and the contralateral side. Continuous variables are expressed as mean ± standard deviation for normally distributed data and median (interquartile range) for skewed

distributions. Skewed datasets underwent logarithmic transformation to normalize their distribution. Parametric (unpaired and paired t-tests) and nonparametric (Mann–Whitney U or Wilcoxon matched-pairs signed rank) tests were used for normally distributed and skewed data, respectively. Categorical data are presented as n (%) and were compared using Fisher's exact or Chi-squared tests. Correlation was undertaken with either Pearson's *r* or Spearman's ρ subject to the normality of the variables tested. To quantify inter- and intra-observer reproducibility of 18F-fluoride uptake measurement, the intraclass correlation coefficient was calculated and Bland-Altman analysis was undertaken.

Statistical analyses were performed with the use of SPSS version 18 (SPSS Inc, Chicago, IL) and Graph Pad Prism version 6.0 (GraphPad Software Inc, San Diego, CA). Statistical significance was defined as a 2-sided $P<0.05$.

7.5 Results

7.5.1 Study Population

We recruited 26 patients (see figure 7.1 for study flow chart):

- 18 in the carotid endarterectomy cohort
- 8 in the control cohort

Baseline characteristics (Table 7.1) were similar in both cohorts. Twenty patients completed all the imaging techniques (Figure 7.2). A minority did not receive all scans because of the technical and feasibility challenges of completing our multi- modality imaging protocol in the very short time frame before surgery. Actual doses and uptake times are specified in Table 7.2. There were no adverse events during the study. There were 3 withdrawals.

Figure 7.1 | Study Flow Chart

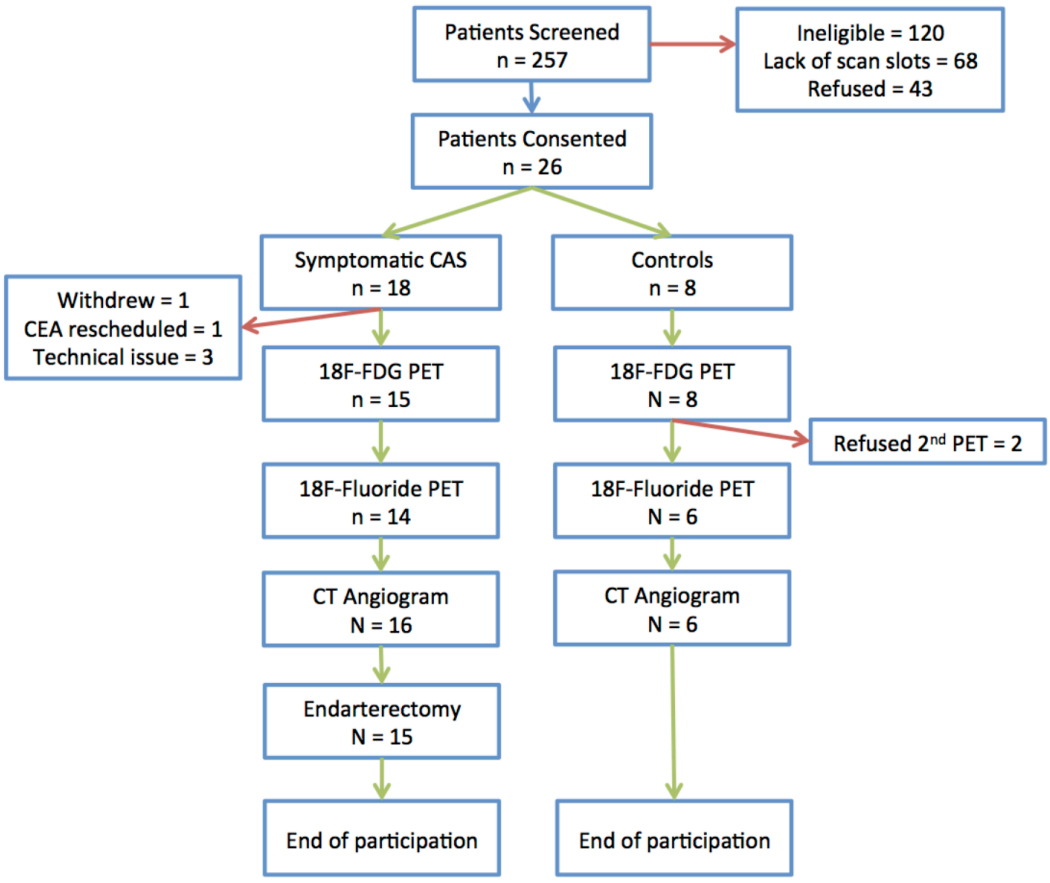

CAS, carotid artery stenosis, CEA, carotid endarterectomy; CT, computed tomography; FDG, fluorodeoxylucose; PET, positron emission tomography.

Table 7.1 | Baseline Clinical Characteristics

	Stenosis Symptomatic	No Stenosis Symptomatic	*P* Value
n	18	8	
Age, y	71.7±12.3	66.1±12.5	0.30
Men, n (%)	12 (66.7)	4 (50)	0.67
BMI, $kg \cdot m^{-2}$	26.2±5	27.3 (23.38–36)	0.40
Systolic blood pressure (mm Hg)	137±25	154±16	0.08
Diastolic blood pressure (mm Hg)	78±18	85±3.4	0.34
ASSIGN score	31±15.5	21.1±13.1	0.13
Presenting syndrome, n (%)			0.22
Stroke	8 (44)	6 (75)	
TIA/amaurosis fugax	10 (56)	2 (25)	
CEA side, right (%)	8 (44)		
Cardiovascular history, n (%)			
Coronary artery disease	10 (56)	2 (25)	0.22
Myocardial infarction	5 (28)	1 (13)	0.63
Risk factors, n (%)			
Hypertension	11 (61)	7 (88)	0.36
Diabetes	1 (6)	0	1
Hypercholesterolemia	13 (72)	5 (63)	0.67
Current smoker	6 (33)	2 (25)	0.67
Medication, n (%)			
Single antiplatelet therapy	14 (78)	6 (88)	1
Dual antiplatelet therapy	3 (17)	0	0.53
Anticoagulant	1 (6)	2 (25)	0.22
Statin	17 (94)	6 (75)	0.22
ACEi/AIIRB	7 (39)	2 (25)	0.20
Beta-antagonist	7 (39)	(131)	0.36
Calcium antagonist	7 (39)	2 (25)	0.67
Other antihypertensive	6 (39)	3 (38)	1
Hematology			
Hemoglobin, g/L	139.8±19	142.6±12.3	0.71
White cell count, $\times 10^9$/L	8±1.4	6.4 (3.8–7.9)	0.06
Platelet count, $\times 10^9$/L	259±64	273±63	0.60
Biochemistry			
Creatinine, mmol/L	88.5 (78–97.5)	76.8±13.5	0.07
Total cholesterol, mg/dL	117.9±34.8	181.7±54.1	0.81
C-reactive protein, mg/L*	3.1±2.6	2.4±3.5	0.66

Parametric data presented as mean±SD. Nonparametric data presented as median (IQR). Categorical data presented as number (%). ACEi, angiotensin converting enzyme inhibitor; AIIRB, angiotensin 2 receptor antagonist; BMI, body mass index; CAD, coronary artery disease; CEA, carotid endarterectomy; IQR, interquartile range; and transient ischemic attack.

*C-reactive protein values > 10 excluded as per AHA guidelines

Table 7.2 | Baseline Scanning Protocol and Radiation Dose Data

	All Patients
Target 18F-FDG Dose (MBq)	200
Actual 18F-FDG Dose (MBq)	199.8 (194.7-203.7)
Actual 18F-FDG Dose range	184-206
Target 18F-Fluoride Dose (MBq)	250
Actual 18F-Fluoride Dose (MBq)	244.5±12.66
Actual 18F-Fluoride Dose range	218 – 266
Target 18F-FDG Uptake Time (min)	90
Actual 18F-FDG Uptake Time	94.1±5.5
Actual 18F-FDG Uptake Time range	84.9-109.8
Target 18F-Fluoride Uptake Time (min)	60
Actual 18F-Fluoride Uptake Time (min)	64.6±5.6
Actual 18F-Fluoride Uptake Time range	56.0 -80.5
Interval between 18F-FDG and 18F-Fluoride (days)	1 (1-2)
Effective Radiation Dose	
Average CT dose (mSv)	4.1
Average dose from 18F-Fluoride (mSv)	5.8
Average dose from 18F-FDG (mSv)	4
Average total dose (mSv)	12.9

Parametric data are presented as mean±SD. Non-parametric data are presented as median(IQR). Categorical data are presented as number (percentage). Abbreviations: FDG, fluorodeoxyglucose; MBq, megabecquerels; MSv, millisieverts. *One patient was accidentally given an oncologic dose (368.9MBq) so the actual 18F-FDG dose data are skewed (this patient has been excluded from the range)

Figure 7.2 | 18F-Fluoride And 18F-Fluorodeoxyglucose (FDG) Positron Emission Tomography Of Carotid Arteries

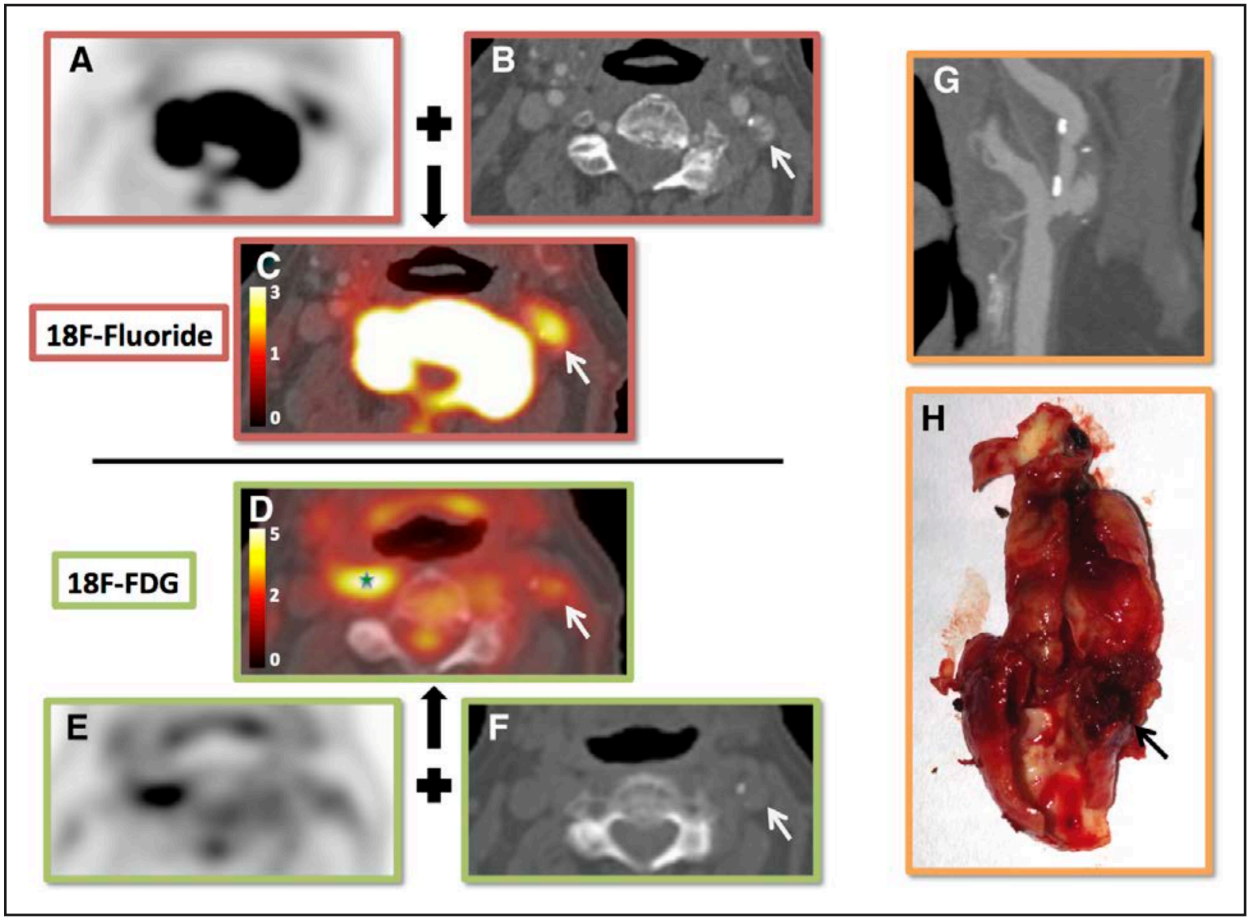

Example of 18F-fluoride (**A, B, C**) and 18F-FDG (**D, E, F**) positron emission tomography (PET)/computed tomography (CT) of one patient before surgery for symptomatic carotid stenosis. **A**, 18F-fluoride PET axial slice. **B**, Registered CT angiogram axial slice. **C**, Fused PET/CT image. White arrow, ruptured plaque showing 18F-fluoride uptake. **D–F**, Same slice but with 18F-FDG. Culprit shows uptake, but the contralateral side is obscured by uptake in the right longus colli (green star). An oblique computed tomography carotid angiogram reformat of the culprit (**G**). The operative specimen (**H**).

7.5.2 Micro PET/CT and Histology

18F-Fluoride was observed to selectively highlight areas of pathologically high-risk microcalcification (Figure 7.3). Both on autoradiography and micro PET/CT, 18F-fluoride was observed to bind avidly to areas of microcalcification but only to the surface of large volume stable macrocalcifications. Our previous study (Chapter 6(200)) would suggest that this was because of the inability of the fluoride ion to penetrate to the deeper layers of a large crystalline mass (with a low surface-area-to-volume ratio). In contradistinction, the powdery deposits of microcalcification (not visible on CT) provide a large area (high surface-area-to- volume ratio) for the fluoride ion to bind.

Figure 7.3 | 18F-Fluoride Micro Positron Emission Tomography (PET)/Computed Tomography (CT), Autoradiography, And Alizarin Red Staining

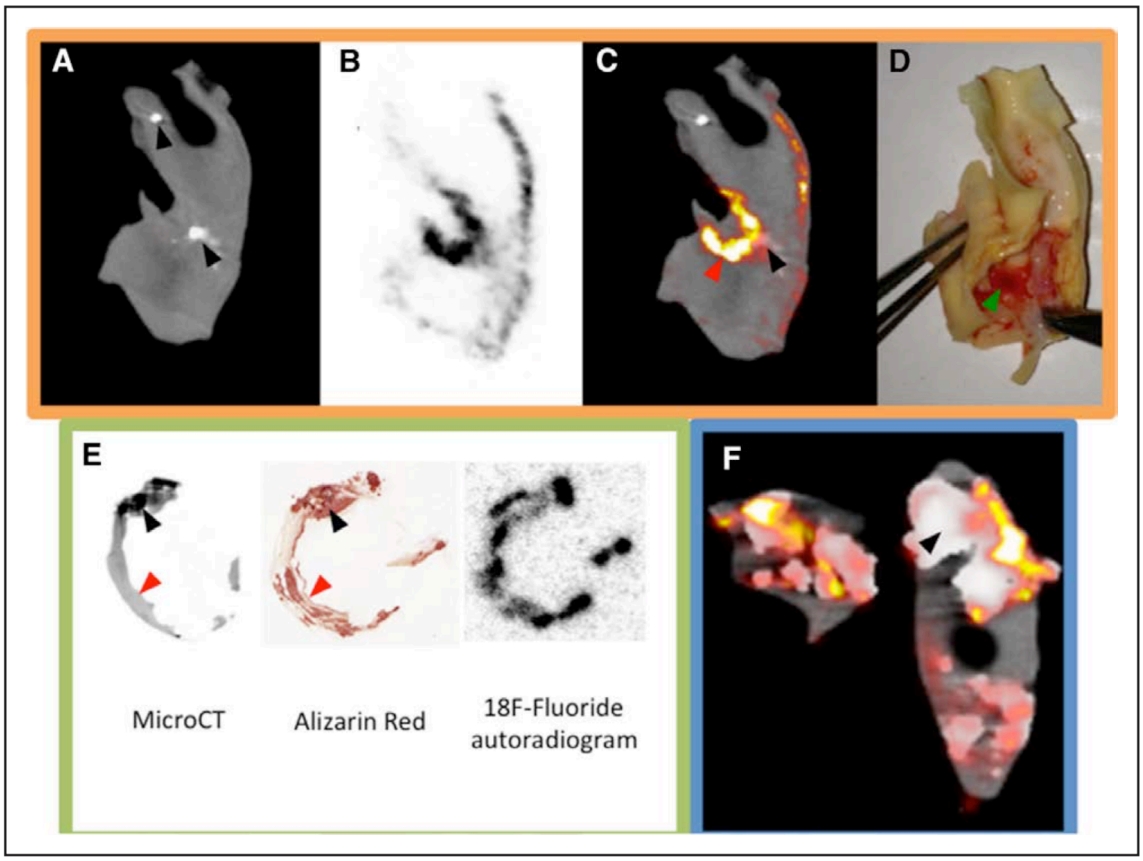

Two examples of *ex vivo* 18F-fluoride micro PET/CT are shown (**A–D, F**).

A, Coronal micro CT slice; **B**, corresponding micro PET; **C**, fused image; **D**, the plaque. Green arrow, Adherent thrombus over plaque rupture. Red arrow, Associated area of 18F-fluoride uptake (microcalcification). Black arrows, Areas of macrocalcification showing comparatively little uptake (**A, C, F**). These examples show that 18F-fluoride provides information of the presence of microcalcification and does not simply highlight all calcification.

E, An example of micro CT slice registered to an alizarin red-stained section and the corresponding autoradiogram from a specimen that had been incubated whole in 18F-fluoride. It can be seen that the tracer is unable to penetrate the deeper layers of macrocalcification (black arrow), but is able to highlight microcalcification beyond the resolution of even micro CT (red arrow), thus explaining the findings in the micro PET/CT images.

7.5.3 Imaging: Validation with Dynamic Imaging & Intra-, Inter-Rater Reproducibility

When comparing the 18F-fluoride uptake on static imaging with full, quantitative dynamic modelling, as would be expected, K_i was most strongly correlated with the SUV_{mean} (r = 0.93 [95% confidence interval 0.64 – 0.99], P = 0.001; Figure 7.4a). There were no fixed or proportional biases in the SUV measurements within and between observers (Table 7.3). These assessments also demonstrated high intra-class correlation coefficients (all >0.90).

Table 7.3 | Inter-Observer And Intra-Observer Reproducibility

Interobserver	Bias	SD of bias	95% LoA	ICC (95%CI)
ICA SUV_{max}	0.04	0.22	-0.39 – 0.47	0.98 (0.96 – 0.99, p<0.001)
ICA $SUV_{meanmax}$	0.04	0.28	-0.50 – 0.59	0.97 (0.93 – 0.99, p<0.001)
ICA SUV_{mean}	-0.002	0.26	-0.51 – 0.51	0.93 (0.84 – 0.97, p<0.001)
Blood pool SUV_{mean}	0.004	0.18	-0.35 – 0.36	0.85 (0.54 – 0.96, p = 0.001)

Intraobserver	Bias	SD of bias	95% LoA	ICC (95%CI)
ICA SUV_{max}	0.04	0.25	-0.44 – 0.53	0.97 (0.93 – 0.99, p<0.001
ICA $SUV_{meanmax}$	0.01	0.22	-0.41 – 0.44	0.97 (0.94 – 0.99, p<0.001
ICA SUV_{mean}	-0.10	0.15	-0.39 – 0.19	0.97 (0.92 – 0.99, p<0.001
Blood pool SUV_{mean}	0.04	0.12	-0.19 – 0.27	0.96 (0.86 – 0.99, p<0.001

ICC – intra-class correlation co-efficient (calculated used a 2-way random effects model to assess absolute agreement). ICA, internal carotid artery, SUV, standardised uptake value, SD, standard deviation; LoA, limits of agreement; CI, confidence interval

Figure 7.4 | Dynamic Positron Emission Tomography (PET) Acquisition And Examples Of 18F-Fluoride Uptake

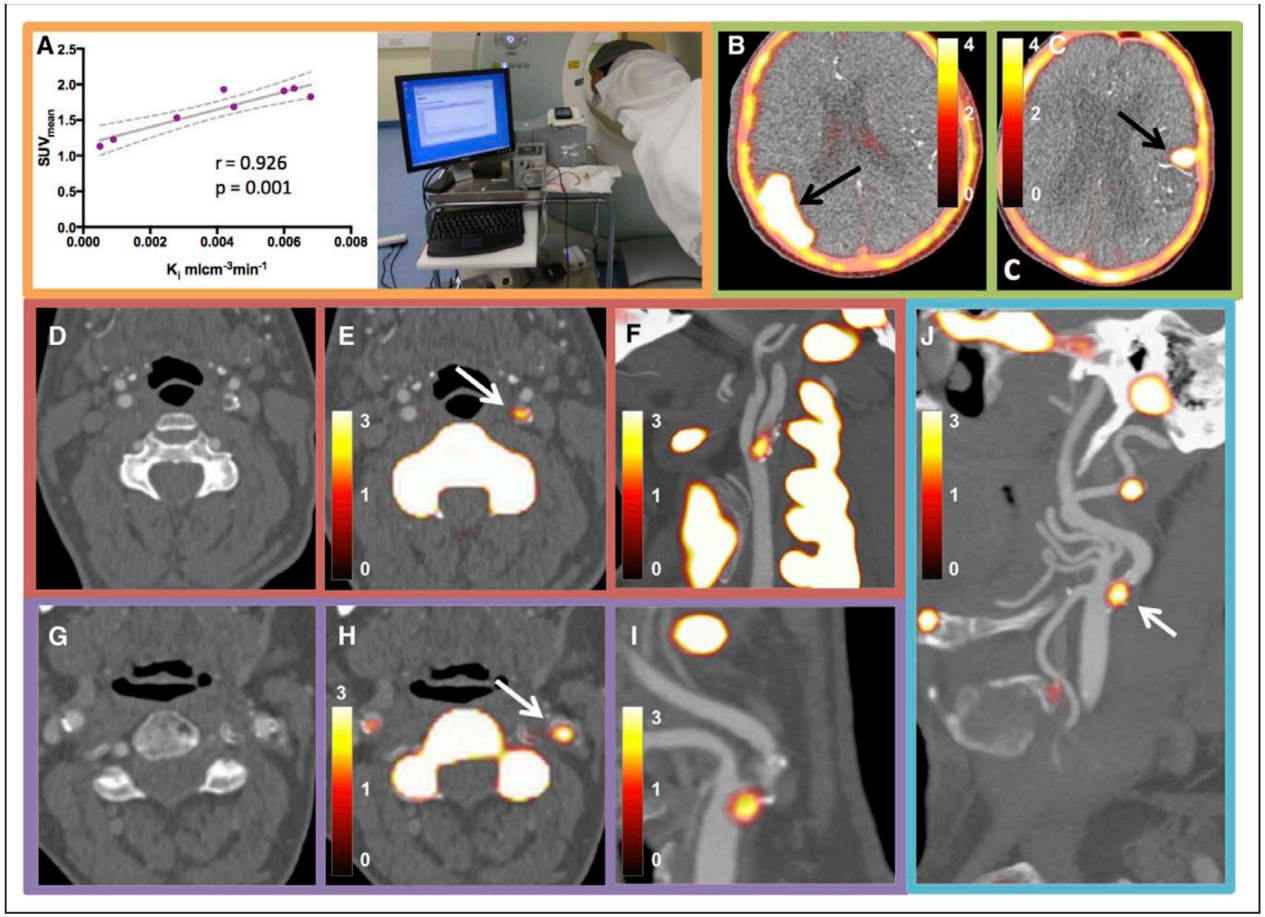

A, Correlation between statically derived standardized uptake value (SUV)mean and dynamically measured K_i (dotted line is 95% confidence interval). Photograph shows a dynamic PET study in process. **B, C,** 18F-fluoride uptake into areas of cerebral infarction. **D–F**, From on patient. **D**, Axial image from computed tomography carotid angiogram; **E**, Fused axial 18F-fluoride PET/computed tomography (CT; white arrow, culprit plaque); **F**, Oblique reconstruction. **G–I**, Similar reconstructions from a different patient. **J**, Obliquely reformatted PET/CT image from a patient who developed a fatal stroke (ipsilateral to the lesion marked by a white arrow) 2 weeks after this scan. The contralateral side, which had shown minimal uptake, had been deemed the culprit based on duplex and clinical assessment.

7.5.4 Assessment of Uptake: Culprit Compared With Contralateral and Controls

7.5.4.1 18F-Fluoride

18F-Fluoride uptake was variably present in most plaques, with all culprits showing uptake on visual assessment. In the large majority of patients undergoing carotid endarterectomy who were scanned (87%; 13/15), there was more visual uptake of 18F-fluoride in the culprit compared with the contralateral side. In the 2 patients without discriminatory uptake, there was heavy uptake bilaterally but more 18F-fluoride uptake on the contralateral side. One patient had grossly ossified carotids and the second, at the time of surgery, was found to have a fibrous stenosis (low signal side) and was subsequently admitted with a fatal ischemic stroke on the contralateral side (high signal side, Figure 7.4j).

18F-fluoride uptake was focal and readily identifiable with excellent signal to background discrimination. Spillover from the hyoid bone, thyroid cartilage and cervical vertebrae occasionally made drawing ROI difficult, but only 1 vessel was rendered uninterpretable. On SUV analysis, the clinically adjudicated culprit showed higher uptake than either the paired contralateral ($log_{10}SUV_{mean}$ 0.29±0.10 *versus* 0.23±0.11, P=0.001) or an unpaired control ($log_{10}SUV_{mean}$ 0.29±0.10 *versus* 0.12±0.11, P=0.001) irrespective of the method of quantification (Table 7.4 and Figures 7.4 and 7.5).

Of note, in patients with a stroke in whom the imaging extended to encompass the affected territory of the brain (n=3), intense 18F-fluoride uptake was noted in regions of cerebral infarction (SUV_{mean} 4.8±1.98 *versus* SUV_{mean} of 0.07±0.02 for contralateral noninfarcted brain, P<0.001; Figure 7.4 b and c).

Table 7.4 | Radiotracer Uptake: Comparative Data

	Culprit Vessel	Contralateral Vessel	*P* Value for Culprit vs Contralateral	Control	*P* Value for Culprit vs Control
^{18}F-Fluoride					
SUV_{max}	2.56 (2.35–3.54)	2.18 (1.94–3.01)	*	1.78 (1.55–2.22)	*
$SUV_{meanmax}$	2.42 (2.24–3.24)	1.97 (1.78–2.74)	*	1.67 (1.41–2.08)	*
SUV_{mean}	1.92 (1.71–2.46)	1.64 (1.39–1.98)	*	1.41 (1.10–1.53)	*
TBR_{max}	2.75 (2.39–3.21)	2.42 (2.02–2.82)	*	2.44 (1.715–2.48)	*
$TBR_{meanmax}$	2.61 (2.24–2.90)	2.32 (1.74–2.58)	*	2.29 (1.61–2.37)	*
TBR_{mean}	1.96 (1.62–2.22)	1.71 (1.38–1.86)	*	1.67 (1.28–1.95)	*
$Log_{10}SUV_{max}$	0.44±0.14	0.38±0.16	0.013	0.25±0.09	<0.001
$Log_{10}SUV_{meanmax}$	0.42±0.13	0.34±0.15	0.005	0.22±0.10	<0.001
$Log_{10}SUV_{mean}$	0.29±0.10	0.23±0.11	0.001	0.12±0.11	<0.001
$Log_{10}TBR_{max}$	0.45±0.13	0.39±0.13	0.014	0.31±0.15	0.016
$Log_{10}TBR_{meanmax}$	0.43±0.13	0.35±0.12	0.005	0.28±0.15	0.014
$Log_{10}TBR_{mean}$	0.30±0.12	0.24±0.11	0.001	0.18±0.13	0.029
^{18}F-FDG					
SUV_{max}	2.32±0.78	2.32±0.77	0.675	2.61±0.53	0.375
$SUV_{meanmax}$	2.21±0.72	2.24±0.74	0.755	2.51±0.46	0.317
SUV_{mean}	1.83±0.55	1.81±0.46	0.346	2.08±0.33	0.269
TBR_{max}	1.88±0.31	1.81±0.31	0.496	1.86±0.27	0.848
$TBR_{meanmax}$	1.80±0.29	1.74±0.29	0.554	1.79±0.20	0.925
TBR_{mean}	1.49±0.19	1.44±0.19	0.358	1.48±0.10	0.922

Parametric data presented as mean±SD. Nonparametric data presented as median (IQR). FDG, fluorodeoxyglucose; SUV, standardized uptake value; TBR, target to background ratio; IQR, interquartile range. *Statistical testing performed on the normalized log_{10} transformed data.

7.5.4.2 18F-Fluorodeoxyglucose

Seven of the 16 culprit carotid plaques demonstrated clear and discernible increased 18F-FDG uptake. However, this uptake was generally more diffuse than 18F-fluoride and analysis was more frequently hampered by spillover from sternocleidomastoid, longus colli, tonsillar tissue, and the submandibular salivary glands (Figure 7.2). This rendered 5 vessels uninterpretable. In the remaining 4 culprit vessels, no increase in 18F-FDG uptake could be observed. Overall on semi-quantitative analysis, 18F-FDG uptake was not higher in the clinically adjudicated culprit compared with either the paired contralateral (SUV_{mean} 1.83±0.55 *versus* 1.81±0.46, *P*=0.269) or control vessels (SUV_{mean} 1.83±0.55 *versus* 2.08±0.33, *P*=0.269) irrespective of the method of quantification (Table 7.4 and Figure 7.5).

Figure 7.5 | 18F-Fluoride And 18F-Fluorodeoxyglucose Positron Emission Tomography/Computed Tomography Uptake

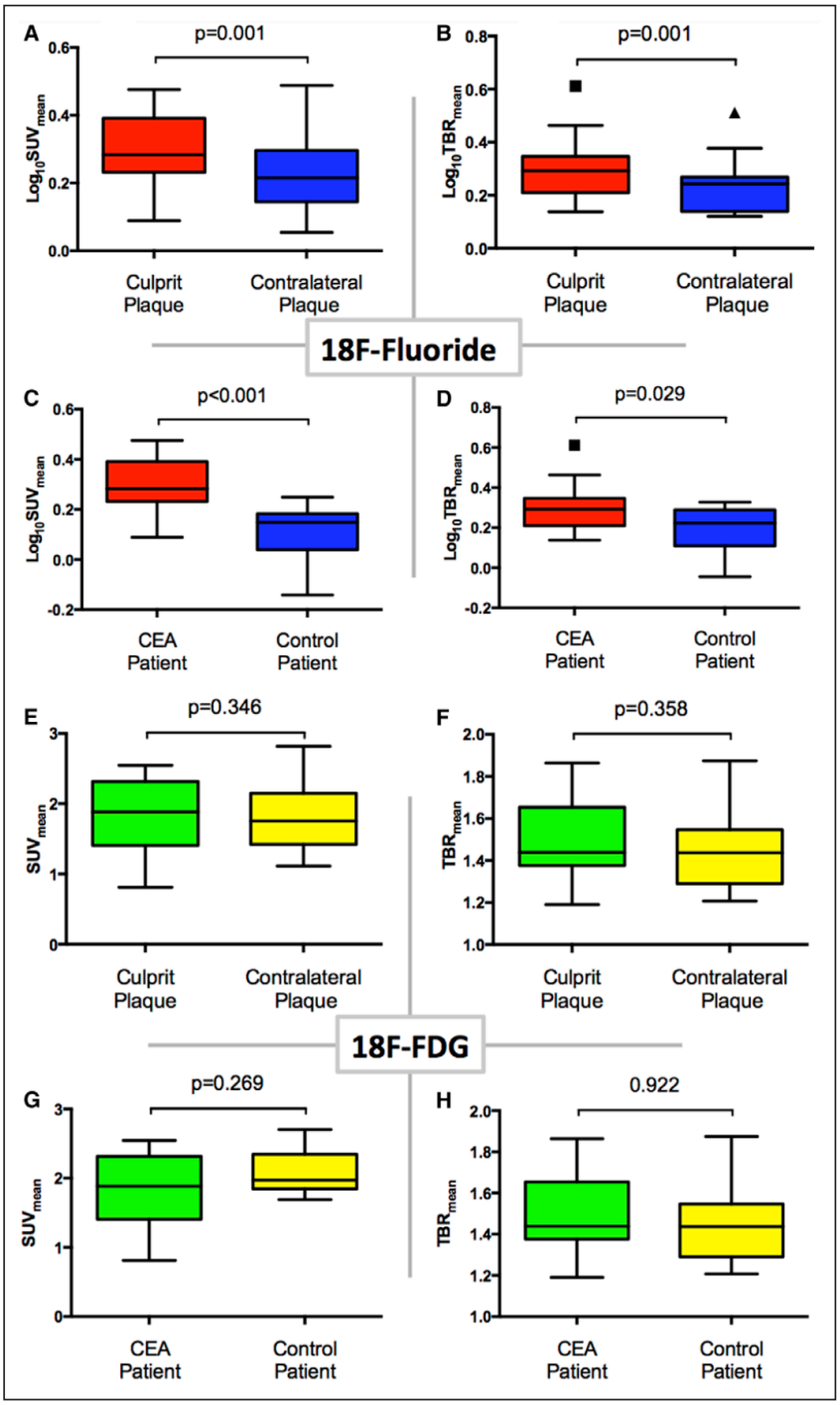

Uptake in clinically adjudicated culprit *versus* contralateral and *versus* controls. Tukey box and whisker plots. **A, B**, 18F-fluoride uptake into culprit (red) and contralateral (blue) plaque using the standardized uptake value (SUV) mean and target to back-ground ratio (TBR) mean measurements, respectively. **C, D**, Each demonstrate comparison in 18F-fluoride uptake between carotid endarterectomy (CEA) patients (red) and controls (blue); uptake is reported by SUV_{mean} in **C** and TBR_{mean} in **D. E–H**, The same comparisons but using 18F-FDG.

7.5.5 Uptake Compared With Plaque Features And Baseline Characteristics

18F-Fluoride uptake was correlated with several plaque characteristics on CT plaque analysis (Table 7.5). The strongest correlation was with the Agatston score (SUV_{mean} r=0.72, P<0.001), although there were also strong correlations with high-risk features such as plaque burden (SUV_{mean} r=0.51, P=0.003) and positive remodelling (wall-distal internal carotid artery lumen ratio, with SUV_{mean} r=0.53, P=0.003).

In terms of baseline cardiovascular risk indices, uptake of both tracers in the vasculature correlated with age (18F-FDG $SUV_{meanmax}$ r=0.48, P=0.037; 18F-fluoride SUV_{mean} r=0.59, P=0.007) and the cardiovascular risk score (18F-FDG $SUV_{meanmax}$ r=0.53, P=0.019; 18F-fluoride SUV mean r=0.65, P=0.002) but neither was associated with serum C-reactive protein concentration.

Table 7.5 | Plaque Analysis By CT And PET

	All Patients	
Calcium score		
Patients with AC CT usable for calcium score	24	
Carotid bifurcations analyzed for calcium score	48	
Agaston score, AU	164 (5–494)	
Log_{10}Agaston score	1.76±1.13	
Calcium volume, mm^3	150 (15.75–404)	
CT plaque analysis		
Patients with analyzable CT angiogram	17	
Internal carotid artery plaques analyzed	33	
CT diameter stenosis, %	50 (0–77)	
Wall-distal ICA lumen ratio, %	90 (54–173)	
Plaque burden, %	49.4±16.4	
Lipid/necrosis volume, mm^3	37.5 (8.6–79.5)	
Lipid/necrosis % volume	6.7 (2.4–15.8)	
Fibrofatty volume, mm^3	201 (96–313)	
Fibrofatty % volume	42.8±15.6	
Calcium volume, mm^3	211 (124–358)	
Calcium % volume	47.4±20.8	
^{18}F-Fluoride PET SUV_{mean}	1.69 (1.40–2.04)	
	r	*P* Value
vs CT Agatson score	0.79	<0.001
vs CT diameter stenosis	0.54	0.002
vs plaque burden	0.51	0.004
vs wall-distal ICA lumen ratio	0.53	0.003
vs lipid/necrosis volume	0.32	0.080
vs fibrofatty volume	0.29	0.126
vs calcium volume	0.72	<0.001
^{18}F-FDG PET SUV_{mean}	1.92±0.46	
	r	*P* Value
vs CT Agatson score	−0.14	0.469
vs CT diameter stenosis	−0.10	0.620
vs plaque burden	−0.03	0.873
vs wall-distal ICA lumen ratio	0.00	0.996
vs lipid/necrosis volume	−0.19	0.315
vs fibrofatty volume	−0.15	0.457
vs calcium volume	0.01	0.918

Parametric data presented as mean±SD. Nonparametric data presented as median (IQR). AC, attenuation correction; AU, arbitrary units; CT, computed tomography; FDG, fluorodeoxyglucose; ICA, internal carotid artery; IQR, interquartile range; PET, positron emission tomography; and SUV, standardized uptake value

7.6 Discussion

We have shown that the culprit plaques of patients with recent TIA or minor ischaemic strokes enhance with 18F-fluoride on PET/CT. Uptake was focal, readily identifiable, and discriminated between culprit and non-culprit. 18F-fluoride uptake was associated with high-risk plaque phenotype and predicted cardiovascular risk. In contrast, while 18F-FDG uptake was present in plaque and correlated with cardiovascular risk, it was more diffuse and prone to spillover and therefore less discriminatory. 18F-FDG also failed to correlate with established high-risk plaque morphological features.

We have previously shown that 18F-fluoride uptake is associated with increased intraplaque markers of cell death, pro-calcific proteins, inflammation, and high-risk features in the coronary circulation *in vivo* and the carotid system *ex vivo (*Chapter 5(117)). Here, we confirm our previous observations (chapter 6(200)) that this is explained by the ability of 18F-fluoride to report microcalcification. Why is this the case? Far from a passive and degenerative process, vessel mineralization is a controlled response to a variety of insults, particularly oxidized inflammatory lipid (as in the calcific response to tuberculosis infection where lipid-rich bacterial cell walls become oxidized through leukocyte action). It is therefore perhaps no surprise that direct links between atherosclerosis and the induction of extra-skeletal osteogenesis have been identified. (13,201) The presence of cellular necrosis and apoptosis(202) is also likely to potentiate this relationship further. Hydroxyapatite nanocrystals themselves may also further drive the inflammatory cycle by setting up a positive feedback loop of increasing calcification, increasing inflammation, and increasing cell death. (201) Furthermore, by accumulating in the surface of thin fibrous caps, microcalcifications may focally increase mechanical stress and thus promote structural cap failure and plaque rupture. (178,203,204) 18F-fluoride can demonstrate this pathologically important microscopic calcific response.

This is the first observation of 18F-fluoride uptake in necrotic brain tissue and merits consideration. Uptake of this and other bone metabolism markers has previously been observed in tissue necrosis. (203,205) This is likely to be because of cell membrane disruption with influx of calcium and formation of nanoscale calcium phosphate complexes. These offer a substrate to which 18F-fluoride can adsorb, allowing us to visualize the microcalcification associated with necrosis. We have also observed the same process in myocardial tissue post-infarction. (Figure 7.6).

Table 7.6 | 18F-Fluoride Uptake In A Patient With A Large Anterior ST-Elevation Myocardial Infarction

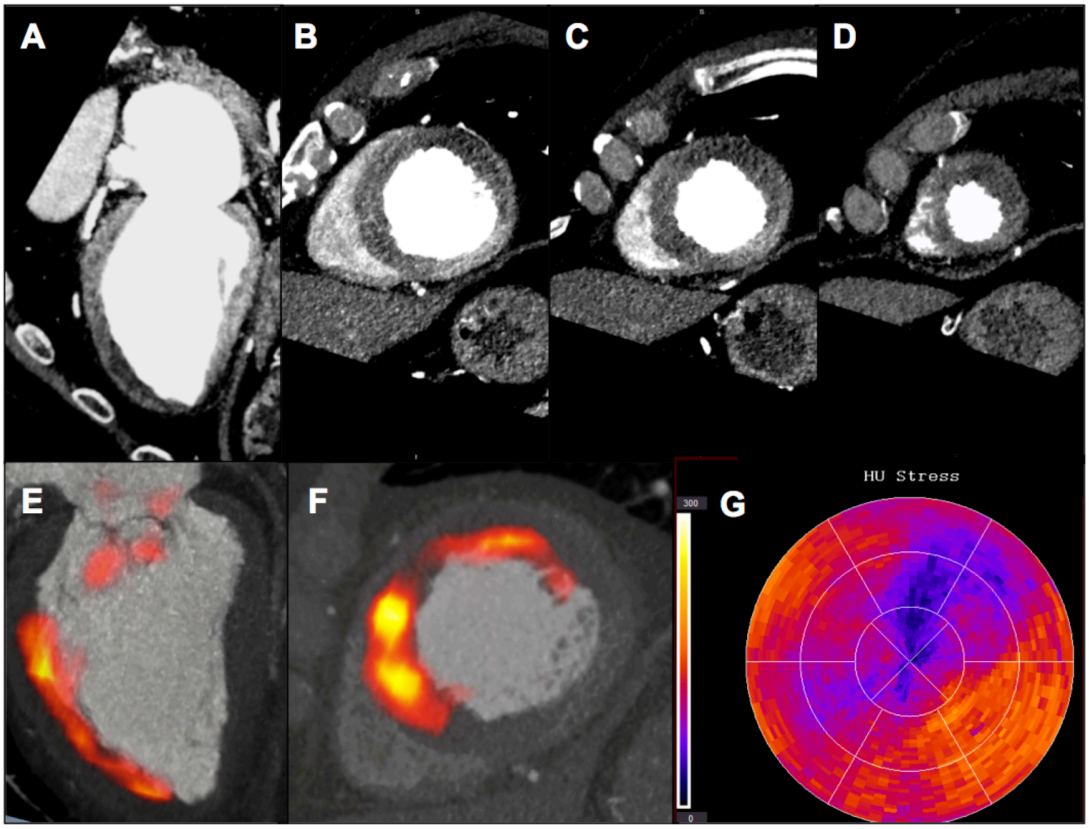

A-D: CT coronary angiogram in long axis (**A**) and short axis (**B-D**) reformats. Panels **E** and **F**: Fused 18F-fluoride PET CT image in long (**E**) and short (**F**) axis reformats. Panel **G**: 16 segment map of myocardial perfusion during stress. The hypoattenutating, hypoperfused infarcted areas visible on the CT angiogram and perfusion map can be seen to co-localise with intense 18F-fluoride uptake.

We confirmed identification of culprit plaque in 2 ways. First, we compared the culprit to the ideal internal control, the contralateral carotid artery (which is almost invariably diseased). Second, we compared the culprit against a valid external control; patients with a TIA or minor ischemic stroke not attributed to carotid plaque. This shows that 18F-fluoride may have real potential in helping to identify culprit plaque thus helping decision-making. This is exemplified by the case where a plaque with high uptake deemed non-culprit subsequently caused a fatal ischemic stroke (see figure 7.4j).

We compared uptake of 18F-fluoride with 18F-FDG. Unlike 18F-fluoride, overall, 18F-FDG uptake was not significantly higher in culprit lesions. Moreover, on a per-lesion basis, 18F-FDG failed to correlate with high-risk plaque morphological features, whereas 18F-fluoride uptake correlated with plaque burden, positive remodelling, and luminal stenosis: all established markers of plaque risk. Other studies have explored the utility of 18F-FDG alone in carotid atherosclerosis(71,130,195,198,206-208) and a few have directly compared clinical culprit with non-culprit plaques. (194,196,197) Our results are consistent with these previous findings with significant uptake noted in some but not all culprit plaques, in part because of spillover from adjacent muscle. Our observations are also influenced by the ubiquity of statin therapy, potentially blunting 18F-FDG uptake. We did, however, note that proximal carotid uptake correlated with cardiovascular risk indicating that 18F-FDG does reflect a major aspect of vessel pathobiology. As others suggest, (74,207) it may be that 18F-FDG better reflects generalized vascular inflammation and that the relationship between the tracer and a single advanced and acute plaque is more complicated. There are increasing data available concerning other more specific markers of inflammation, such as those targeting the macrophage-specific somatostatin receptor. (209) These will theoretically be less hampered by overspill.

Our findings confirm those of a smaller study of 9 patients by Quirce et al(107) that explored 18F-fluoride and 18F-FDG uptake in symptomatic patients. They

showed that 18F-fluoride uptake appeared to be higher in the symptomatic carotid and that 18-FDG uptake was non-discriminatory. Taken together with our current larger series, this suggests that 18F-fluoride has the potential to be a useful and robust clinical tool to identify culprit atherosclerotic plaque. Vascular 18F-fluoride imaging could therefore guide clinical management better than the current standard of care, and lead to trials of plaque-specific interventions that go beyond simple assessments of anatomic luminal stenosis severity.

7.6.1 Limitations

This was a small pilot observational study (recruitment is very challenging given the time pressure to intervene) and findings should be regarded as preliminary. The true utility of 18F-fluoride PET/CT will need to be evaluated by prospective studies with patients randomized to intervention based on imaging. 18F-fluoride PET/CT will need to be compared with other techniques(210) (in particular MR or PET/ MR) which have the advantages of improved soft tissue definition, reduced radiation, and lack of iodinated contrast.

We did not perform prolonged-delayed 18F-FDG imaging which some authors have suggested is advantageous. (211) We also acknowledge that quantitative vascular PET has some potential limitations because of the partial volume effects of small vascular structures. Finally, as vascular 18F-fluoride imaging is developed, consideration must be given to harmonizing acquisition and reconstruction protocols, (212) as well as achieving consensus on the uptake parameter of choice (SUV *versus* target to background ratio *versus* volumetric parameters) (213) and whether to use manual or automated methods to define ROI. This will reduce variation between scanners and research groups and permit meaningful multi-centre studies.

7.7 Conclusions

We have shown that 18F-fluoride PET/CT is able to identify culprit or high-risk carotid plaque. In comparison, 18F-FDG, the most widely used tracer in cardiovascular PET imaging, did not reliably identify culprit plaque and did not correlate with high-risk morphological features. 18F-fluoride PET has major potential to improve how we assess and manage the risk of stroke in patients with atherosclerosis.

Chapter 8 – Conclusions

8.1 Summary of Key Findings

This work has described the application of 18F-FDG and 18F-fluoride PET/CT imaging to both CAVD and atherosclerosis. Significant gains in our understanding of the mechanism of action of the 18F-fluoride isotope have been made and important validation of my group's previous findings has been demonstrated. I have also demonstrated in prospective studies that 18F-fluoride PET/CT provides important information about disease activity and clinical risk.

8.1.1 Mechanism of Action of 18F-Fluoride Uptake in Cardiovascular Tissue

Using electron microscopy, autoradiography, micro PET/CT and clinical PET/CT, I have shown that 18F-fluoride binds very small deposits of calcium apatite in cardiovascular tissue and is able to highlight this pathologically important phenomenon where, due to restrictions in resolution, other imaging modalities such as ultrasound, CT and MR cannot. 18F-Fluoride also appears to preferentially bind these tiny microcalcifications compared to large macroscopic calcium deposits that are more characteristic of a stable fibro-calcific plaque phenotype. This is due to the impenetrability of the large deposits to 18F-fluoride and a difference in available surface area for adsorption. In aortic valvular tissue, I have demonstrated that *in vivo* 18F-fluoride uptake correlates with immunohistochemical markers of active tissue mineralization.

I have also shown *in* and *ex vivo* that the binding characteristics of 18F-fluoride to cardiovascular calcification are highly favourable for imaging. Binding is highly specific, effectively irreversible and non-saturable (at relevant PET doses). 18F-fluoride has no metabolites making image analysis straightforward and I have confirmed that the isotope has highly favourable kinetics with a rapid clearance from the blood pool.

Taken together, these findings explain how 18F-fluoride behaves in cardiovascular tissue and supports the contention that the tracer is of significant potential utility in both CAVD and atherosclerosis imaging.

8.1.2 Prediction Of Disease Progression And Clinical Events In CAVD

In patients with CAVD, baseline valvular uptake 18F-fluoride uptake was correlated with the change in calcium score on CT at the one-year time point. This was the first demonstration of the prospective utility of 18F-fluoride in CAVD. Valvular 18F-FDG uptake did not correlate with either tissue markers of macrophage infiltration or indeed progression of disease at one-year as measured by change in CT calcium score.

With a larger cohort of patients available for analysis at the two-year follow up time point (n=99), I confirmed the one-year findings by showing that baseline valvular 18F-fluoride uptake predicted the rate of increase in CT calcium score as well as a variety of echocardiographic parameters of disease progression. 18F-fluoride uptake was also associated with clinical outcome after adjusting for age and sex. Patients with 18F-fluoride uptake higher than expected for a given CT calcium score were also noted to progress 3-times faster than those with lower than expected 18F-fluoride uptake. Valvular 18F-FDG uptake was also associated with disease progression in term of radiological and clinical progression but less so than 18F-fluoride.

These findings support the hypotheses that inflammation and microcalcification are important processes in CAVD progression and the 18F-fluoride PET/CT might have an interesting role to play in predicting disease progression as well as assessing response to new treatments targeted at either inflammation or calcification.

8.1.3 Identification of Culprit and High-Risk Plaque in the Carotid and Coronary Arteries

In a series of related studies, I have shown that increased arterial 18F-fluoride uptake is associated with atherosclerotic plaque rupture as well as histological and image-derived features of risk.

Ex vivo, clinically adjudicated culprit carotid plaques, excised during carotid endarterectomy procedures, all showed uptake of 18F-fluoride which localised to the site of plaque rupture. When compared to regions of plaque with low uptake, regions of high 18F-fluoride uptake were associated with increased staining for immunohistochemical markers of inflammation, micro-calcification and programmed cell death.

In vivo, 18F-fluoride uptake in clinically adjudicated coronary and carotid culprits was higher than in non-culprit controls. 18F-fluoride uptake was also associated with higher cardiovascular risk scores, increased levels of high-sensitivity troponin and image-derived markers of heightened plaque risk such as positive remodelling, the presence of a necrotic core, specked calcification and high plaque burden.

In both the coronary and carotid territories, 18F-FDG did not perform as well as 18F-fluoride. In the coronaries, myocardial uptake hampered analysis and, in the carotids, uptake was frequently similarly obscured by spill over from adjacent structures. Nevertheless, 18F-FDG was associated with validated parameters of cardiovascular risk, as previously published by other groups, but this association was not as strong as that seen with 18F-fluoride.

These findings support the notion that 18F-fluoride PET/CT may have a role to play in trying to identify culprit or high-risk atherosclerotic plaque. Given the high cost of PET/CT however, it is more likely that the major role will be in assessing *in vivo* biological response to new medical therapies in phase II trials;

a major potential cost benefit in an era where trials of new cardiovascular drugs usually require thousands of patients to be adequately powered.

8.2 Recent Literature

Since I finished collecting data, other groups have published related work that is worth briefly discussing here.

In 2016 Fiz and co-workers(214) published a retrospective analysis of patients who had undergone 18F-fluoride PET/CT for oncologic reasons. They re-analysed the scans and assessed aortic uptake. They found that 18F-fluoride uptake correlated with Framingham cardiovascular risk. These findings confirm ours and those of Morbelli(109) which were discussed in the introduction to this thesis.

More results from the CAMONA (Cardiovascular Molecular Calcification Assessed by 18F-fluoride PET/CT) study(133) were published in 2016. This was a prospective study of both 18F-FDG and 18F-fluoride cardiovascular PET/CT (n=139). In this report the authors present their initial cross-sectional findings as they pertained to cardiovascular risk. They noted that aortic calcium score and aortic 18F-fluoride uptake was strongly related to Framingham risk score. Interestingly they were not able to demonstrate a relation between Framingham risk and aortic 18F-FDG uptake. These results very much support those described in this thesis.

Oliveira-Santos and co-authors published a small (n=25) prospective study in 2017(215) of 18F-fluoride cardiovascular PET/CT. Supporting the data presented in this thesis, they showed an association between 18F-fluoride uptake (in any territory) and burden of cardiovascular risk. They also showed a relationship between 18F-fluoride uptake and thoracic fat volume, which is perhaps what one would expect but also further evidence that 18F-fluoride uptake is associated with established markers of cardiovascular risk.

Kitagawa *et al* published a paper in 2017(216) looking at coronary 18F-fluoride uptake in stable coronary patients. Again, their findings very much confirmed

ours, in that they demonstrated coronary 18F-fluoride uptake was associated with a wide array of relevant parameters including high risk features on CT coronary angiography, high cardiovascular risk scores, high plaque burden and others.

Finally, Lee *et al* published an important 18F-fluoride paper at the end of 2017. (217) This was a cross sectional study of 51 patients who underwent 18F-fluoride PET/CT prior to coronary catheterisation with IVUS and OCT. They divided lesions into those with high and low 18F-fluoride uptake and found those with high uptake were more likely to have high risk features on OCT and IVUS.

8.3 Limitations

Despite my encouraging findings, ultimately these data should be regarded as preliminary. Patients were recruited from a single centre and the numbers of subjects in the described trials cannot be regarded as large. As with all research, my findings will need to be repeated by others in order to be validated. As I have described in the previous section, some work has already been published supporting my data and conclusions, but no large trial has yet been done.

In terms of atherosclerosis, I have not proven the ability of 18F-fluoride to predict future events yet. I have shown that 18F-fluoride is able to highlight plaques that have either been proven to have ruptured or shown signs of risk, but to truly prove the worth of the technique, larger prospective studies of patients at risk of major adverse cardiovascular events will need to be done.

In CAVD, I have presented data showing that 18F-fluoride and 18F-FDG can predict disease progression and future clinical events. This doesn't yet prove 18F-fluoride's tractability as a surrogate marker of disease activity. In order to do so, further work demonstrating that the signal can be modulated by some agent or other will need to be done. It will also be important to show that the technique has added value and is cost effective compared to existing techniques such as echocardiography, cardiac magnetic resonance imaging and CT calcium scoring. Moreover, with the growing numbers of TAVI being performed, it will be important to investigate how the tracer performs with surgically and percutaneously implanted valves.

The resolution of positron emission tomography is fundamentally limited by the positron distance and to a lesser extent by other factors. This poses problems when imaging small volume structures such as atherosclerotic plaques and aortic valves. It is possible to get partial volume artefacts (and lose potential signal from a small object) when quantifying uptake. Coronary and respiratory

motion will clearly complicate this situation further when looking at the coronary arteries and the aortic valve.

Formidable barriers still exist to establishing PET/CT as a modality for "mass scanning" to assess cardiovascular risk with cost presenting the main problem. The platform itself remains expensive and limited in availability; although much the same arguments were made about MRI twenty years ago. The economic challenges are not merely limited to the hardware. A functioning PET service requires a staff of trained doctors, physicists, radiographers and others. The radiation safety measures required for free isotopes are significant and costly. For the vast majority of radioisotopes an on-site cyclotron and radiochemistry suite is also required and this represents a huge capital and continuing cost. Fortunately, the most common isotope, 18F-FDG, is frequently commercially available and it is likely that a simple novel isotope like 18F-fluoride would be a sensible investment choice for a commercial provider. In the acute setting (identifying potential culprits), additional challenges relating to easy availability of isotope and rapid access to the scanning platform will also need to be overcome.

Another problem that will need to be addressed in the future if the technique is to achieve broad appeal concerns the issue of fidelity of quantification and inter-scanner/centre comparability. There are several different commercially available PET systems. Each system is unique and will clearly not produce exactly the same data in the same patient. In addition, there are many parameters in a scan and these will vary from unit to unit. In order to ensure that data are comparable in future multi-centre studies, work on standardisation will need to be done. Finally, although it is the gold standard, fully quantitative PET as discussed in the introduction and methods is a difficult, expensive, slow and usually invasive technique. As such it is unsuitable for clinical use. A compromise is therefore made in clinical PET by using "semi-quantitative" methods such as the SUV that can be made on a statically acquired PET data set. This adds another layer of potential error to those already

discussed. The issue of accurate and reproducible quantification will be of particular importance when one considers that to make a clinical decision, a binary outcome is normally required of a test. A clear isotope uptake threshold (perhaps indexed to some factor or other) will need to be derived. It will be imperative to minimise inaccuracy and scanner/scanner variability prior to embarking on a full clinical use.

8.3 Future Directions

The work presented in this thesis has raised several questions and since completing data acquisition and publication, several grants have awarded based on the work presented. Here I briefly discuss the areas of future investigation.

8.3.1 Mutability Of 18F-Fluoride Uptake In CAVD

As has been discussed in the previous section, the true worth of 18F-fluoride PET/CT as an anatomically resolved marker of *in vivo* disease activity will be proven when it can be shown that the signal measured is actually changed by an agent that would be expected to do so. To this end, our research group applied for and was granted funding (British Heart Foundation FS/16/19/31982) to conduct SALTIRE 2 (Study Investigating the Effect of Drugs Used to Treat Osteoporosis on the Progression of Calcific Aortic Stenosis). (218) This single-centre, prospective, double-blind, randomised, placebo-controlled trial will randomly allocate 150 patients with CAVD to receive either a bisphosphonate, denosumab (an osteoprotegerin analogue) or a placebo. The study's objectives are to assess whether either of these agents can modulate the 18F-fluoride signal in the aortic valve and indeed arrest CAVD progression. Recruitment has completed and the study is in follow-up phase.

8.3.2 Predicting Events In Atherosclerosis

On a similar theme in atherosclerosis, the true value of 18F-fluoride PET/CT will gain much great traction if it can be shown that plaque uptake can predict future events. The PRE^{18}FFIR study (Prediction of Recurrent Events With 18F-fluoride) (219), was therefore designed and then funded by the Wellcome Trust. This is a large, multi-centre, prospective observational cohort study of patients hospitalised for acute myocardial infarction with proven multi-vessel coronary atherosclerosis. Patients will undergo 18F-fluoride PET/CT. The primary outcome will be cardiac death or non-fatal recurrent myocardial infarction at the 2-year follow-up time point. The main study objective will be to assess whether or not high baseline 18F-fluoride uptake is predictive of future

poor clinical outcome. Key second end-point will explore whether the tracer is able to identify the index culprit (validating our original findings) and whether high focal uptake can predict the myocardial territory affected by any future event.

8.3.3 Randomising Patients to an Investigational Strategy to Prove Worth

One of the frequently stated promises of advanced imaging for risk prediction is that it will permit individualised tailoring of therapy. Anti-thrombotic agents are a cornerstone of the treatment of atherosclerosis. They function by impairing platelet function and thus reducing the risk that an eroded or rupture plaque will lead to a thrombotic event. Inevitably they also increase the risk of clinically important bleeding. Many very large trials have been dedicated to fine tuning the correct amount of antiplatelet inhibition to offer patients in a variety of contexts; post myocardial infarction, post-percutaneous intervention, post-stroke, primary prevention, etc. Individualised anti-platelet prescribing based on imaging or other biomarker is not yet common practice. We applied for and were awarded grant funding to perform the DIAMOND (Dual Antiplatelet Therapy to Reduce Myocardial Injury) study. (220) In this single centre, randomized placebo-controlled study, 220 patients with established multivessel coronary heart disease will undergo coronary 18F-fluoride PET/CT. Patients will be parsed into low and high coronary uptake cohorts. Both cohorts will then be randomised separately to receive either aspirin and placebo or aspirin and ticagrelor. The primary outcome will be plasma high sensitivity troponin I (a marker of myocardial injury) at 30 days. The objective is to assess whether individualising anti-platelet therapy based on risk as measured by PET/CT can result in improved outcomes.

8.3.4 Utility of Combining PET and MR to Assess Cardiac Disease and Atherosclerosis

PET/CT and MR have strengths and limitations. We(221-223) and others have suggested that combining the two modalities to assess cardiovascular disease carries certain key advantages. With commercial PET/MR systems now on the market, exploring this hybrid combination is worthwhile. PET/CT carries a penalty in terms of radiation cost; much of which comes from CT; PET/MR would abrogate much of the radiation dose and make repeated examination (an important ability when monitoring chronic disease in the long-term) a more realistic proposal. In terms of plaque visualization and segmentation, although CT is able to achieve submillimetric spatial resolution in combination with a very short acquisition time, soft tissue contrast is poor and one dimensional (i.e. plaque segmentation is based purely on photon attenuation). CT atheroma imaging is also hampered by blooming artifact from dense calcification. Both these factors make visualization of the luminal and adventitial borders for region of interest analysis difficult. By comparison, MR with black-blood imaging offers superior soft tissue detail that provides excellent contrast at the adventitial and luminal borders. Furthermore, MR plaque analysis has been well validated and by exploring the T1 & T2 properties of the plaque (as well as using contrast enhance plaque imaging), more detail can be gleaned than with CT. PET/MR also offers the opportunity of permitting full motion correction for PET data; a crucial advantage in cardiac imaging where the cardiac and respiratory cycle complicate PET interpretation significantly.

Another major advantage of combining the two is that it permits excellent perfusion and functional imaging of the downstream tissues. For the carotid, performing brain image at the same acquisition permit a “one-stop-shop” approach. It may be that a combination of plaque factors (on PET and MR) combined with signs (or absence) of cerebral ischaemia would provide an extensive phenotypic panel that would be optimally able to assess risk in an individual. This of course is not limited to cerebral imaging but also the heart

(cardiac MR is well established and is probably now the gold standard for much structural imaging), the viscera and the peripheries.

Our group has been able to recently install a hybrid PET/MR platform. A key first study that has been funded by the BHF will recapitulate much of the work presented in chapter 7. The study will focus on patients with stroke, TIA and amaurosis fugax. A "one-stop-shop" 18F-fluoride PET/MR of the entire cephalic circulation will be performed (and then repeated at a later time-point) to assess whether more clinically important data can be gleaned from such an approach compared to the current standard practice. Plaque biology as assessed by PET will be compared to surgical specimens and also to trans-cranial doppler and MR brain and plaque imaging.

8.3.5 Other Pathologies

The potential utility of 18F-fluoride PET/CT is not limited to CAVD and atherosclerosis. During my thesis research, I undertook some *in vitro* experiments (presented in Chapter 3, Methods) with 18F-fluoride and aortic aneurysm tissue. I was able to show that aortic tissue bound 18F-fluoride. This work led to a joint British Heart Foundation and Medical Research Council funded SOFIA[3] trial. (224) In this prospective observational cohort study, 92 patients with abdominal aortic aneurysms in a surveillance program were scanned with 18F-fluoride PET/CT at baseline. They were then followed up clinically and by duplex ultrasound. Compared to patients with low uptake, those with high uptake showed higher aneurysm growth rates and a 3-fold increased risk of progressing to repair or rupture. These data have been published and will form the basis for a future randomised interventional trial.

8.4 Final Conclusions

18F-Fluoride PET/CT is a valuable for exploring disease activity in CAVD and atherosclerosis. The technique may represent an attractive method for assessing response to novel therapies. 18F-Fluoride PET/CT may also prove to have clinical utility. If it is confirmed that the isotope is able to identify high-risk and culprit plaque or patients, it will help achieve more guided therapy; an important goal in this era of precision medicine.

References

1. Buxton DB, Antman M, Danthi N, Dilsizian V, Fayad ZA, Garcia MJ, et al. Report of the National Heart, Lung, and Blood Institute Working Group on the Translation of Cardiovascular Molecular Imaging. Circulation. 2011 May 16;123(19):2157–63.

2. Nkomo VT, Gardin JM, Skelton TN, Gottdiener JS, Scott CG, Enriquez-Sarano M. Burden of valvular heart diseases: a population-based study. Lancet. 2006 Sep 16;368(9540):1005–11.

3. Eveborn GW, Schirmer H, Heggelund G, Lunde P, Rasmussen K. The evolving epidemiology of valvular aortic stenosis. the Tromsø study. Heart. 2013 Mar;99(6):396–400.

4. Schueler R, Hammerstingl C, Sinning J-M, Nickenig G, Omran H. Prognosis of octogenarians with severe aortic valve stenosis at high risk for cardiovascular surgery. Heart. 2010 Nov;96(22):1831–6.

5. Iung B, Baron G, Butchart EG, Delahaye F, Gohlke-Bärwolf C, Levang OW, et al. A prospective survey of patients with valvular heart disease in Europe: The Euro Heart Survey on Valvular Heart Disease. European Heart Journal. 2003 Jul;24(13):1231–43.

6. Dunning J, Gao H, Chambers J, Moat N, Murphy G, Pagano D, et al. Aortic valve surgery: marked increases in volume and significant decreases in mechanical valve use--an analysis of 41,227 patients over 5 years from the Society for Cardiothoracic Surgery in Great Britain and Ireland National database. J Thorac Cardiovasc Surg. 2011 Oct;142(4):776–782.e3.

7. Ludman PF, Moat N, de Belder MA, Blackman DJ, Duncan A, Banya W, et al. Transcatheter aortic valve implantation in the United Kingdom: temporal trends, predictors of outcome, and 6-year follow-up: a report from the UK Transcatheter Aortic Valve Implantation (TAVI) Registry, 2007 to 2012. Circulation. 2015 Mar 31;131(13):1181–90.

8. Dweck MR, Jones C, Joshi NV, Fletcher AM, Richardson H, White A, et al. Assessment of valvular calcification and inflammation by positron emission tomography in patients with aortic stenosis. Circulation. 2012 Jan 3;125(1):76–86.

9. Vesey AT, Dweck MR, Newby DE. PET/CT Imaging Of Inflammation And Calcification CAVD: Clinical Studies. In: Cardiovascular Imaging: Arterial and Aortic valve Inflammation and Calcification. 1st ed. Springer; pp. 201–23.

10. Pachulski RT, Chan KL. Progression of aortic valve dysfunction in 51 adult patients with congenital bicuspid aortic valve: assessment and

follow up by Doppler echocardiography. Heart. 1993 Mar 1;69(3):237–40.

11. Miller JD, Weiss RM, Heistad DD. Calcific aortic valve stenosis: methods, models, and mechanisms. Circulation Research. 2011 May 27;108(11):1392–412.

12. Beppu S, Suzuki S, Matsuda H, Ohmori F, Nagata S, Miyatake K. Rapidity of progression of aortic stenosis in patients with congenital bicuspid aortic valves. The American Journal of Cardiology. 1993 Feb;71(4):322–7.

13. Aikawa E, Nahrendorf M, Figueiredo J-L, Swirski FK, Shtatland T, Kohler RH, et al. Osteogenesis associates with inflammation in early-stage atherosclerosis evaluated by molecular imaging in vivo. Circulation. 2007 Dec 11;116(24):2841–50.

14. Demer LL, Tintut Y. Mineral exploration: search for the mechanism of vascular calcification and beyond: the 2003 Jeffrey M. Hoeg Award lecture. Vol. 23, Arteriosclerosis, thrombosis, and vascular biology. 2003. pp. 1739–43.

15. Zhu D, Mackenzie NCW, Farquharson C, MacRae VE. Mechanisms and clinical consequences of vascular calcification. Front Endocrinol (Lausanne). Frontiers; 2012;3:95.

16. New SEP, Aikawa E. Molecular Imaging Insights Into Early Inflammatory Stages of Arterial and Aortic Valve Calcification. Circulation Research. 2011 May 26;108(11):1381–91.

17. Otto CM, Kuusisto J, Reichenbach DD, Gown AM, O'Brien KD. Characterization of the early lesion of “degenerative” valvular aortic stenosis. Histological and immunohistochemical studies. Circulation. 1994 Aug;90(2):844–53.

18. Aikawa E, Otto CM. Look more closely at the valve: imaging calcific aortic valve disease. Circulation. 2012 Jan 3;125(1):9–11.

19. Garg V, Muth AN, Ransom JF, Schluterman MK, Barnes R, King IN, et al. Mutations in NOTCH1 cause aortic valve disease. Nature. 2005 Jul 17;437(7056):270–4.

20. Chen J-H, Chen WLK, Sider KL, Yip CYY, Simmons CA. β-catenin mediates mechanically regulated, transforming growth factor-β1-induced myofibroblast differentiation of aortic valve interstitial cells. Arteriosclerosis, Thrombosis, and Vascular Biology. 2011 Mar;31(3):590–7.

21. Kaden JJ, Bickelhaupt S, Grobholz R, Haase KK, Sarikoç A, Kiliç R, et al. Receptor activator of nuclear factor kappaB ligand and osteoprotegerin regulate aortic valve calcification. Journal of Molecular and Cellular Cardiology. 2004 Jan;36(1):57–66.

22. Vattikuti R, Towler DA. Osteogenic regulation of vascular calcification: an early perspective. American Journal of Physiology-Endocrinology and Metabolism. 2004 May;286(5):E686–96.

23. Cowell SJ, Newby DE, Prescott RJ, Bloomfield P, Reid J, Northridge DB, et al. A randomized trial of intensive lipid-lowering therapy in calcific aortic stenosis. N Engl J Med. 2005 Jun 9;352(23):2389–97.

24. Chan KL, Teo K, Dumesnil JG, Ni A, Tam J, for the ASTRONOMER Investigators. Effect of Lipid Lowering With Rosuvastatin on Progression of Aortic Stenosis: Results of the Aortic Stenosis Progression Observation: Measuring Effects of Rosuvastatin (ASTRONOMER) Trial. Circulation. 2010 Jan 18;121(2):306–14.

25. Rossebø AB, Pedersen TR, Boman K, Brudi P, Chambers JB, Egstrup K, et al. Intensive lipid lowering with simvastatin and ezetimibe in aortic stenosis. N Engl J Med. 2008 Sep 25;359(13):1343–56.

26. Pawade TA, Newby DE, Dweck MR. Calcification in Aortic Stenosis: The Skeleton Key. Journal of the American College of Cardiology. 2015 Aug 4;66(5):561–77.

27. Clavel M-A, Burwash IG, Pibarot P. Cardiac Imaging for Assessing Low-Gradient Severe Aortic Stenosis. JACC: Cardiovascular Imaging. 2017 Feb;10(2):185–202.

28. Dweck MR, Chin C, Newby DE. Small valve area with low-gradient aortic stenosis: beware the hard hearted. Journal of the American College of Cardiology. 2013 Dec 17;62(24):2339–40.

29. Clavel M-A, Dumesnil JG, Capoulade R, Mathieu P, Sénéchal M, Pibarot P. Outcome of patients with aortic stenosis, small valve area, and low-flow, low-gradient despite preserved left ventricular ejection fraction. Journal of the American College of Cardiology. 2012 Oct 2;60(14):1259–67.

30. Everett RJ, Tastet L, Clavel M-A, Chin CWL, Capoulade R, Vassiliou VS, et al. Progression of Hypertrophy and Myocardial Fibrosis in Aortic Stenosis. Circulation: Cardiovascular Imaging. 2018 Jun 18;11(6):e007451–21.

31. Herrington W, Lacey B, Sherliker P, Armitage J, Lewington S. Epidemiology of Atherosclerosis and the Potential to Reduce the Global Burden of Atherothrombotic Disease. Circulation Research. 2016 Feb 18;118(4):535–46.

32. Libby P, Hansson GK. Inflammation and immunity in diseases of the arterial tree: players and layers. Circulation Research. 2015 Jan 16;116(2):307–11.

33. Libby P. Inflammation in atherosclerosis. Nature. 2002 Dec;420(6917):868–74.

34. Libby P. Inflammation in Atherosclerosis. Arteriosclerosis, Thrombosis, and Vascular Biology. 2012 Aug 15;32(9):2045–51.

35. Galkina E, Ley K. Vascular adhesion molecules in atherosclerosis. Arteriosclerosis, Thrombosis, and Vascular Biology. 2007 Nov;27(11):2292–301.

36. Tabas I, Williams KJ, Boren J. Subendothelial Lipoprotein Retention as the Initiating Process in Atherosclerosis: Update and Therapeutic Implications. Circulation. 2007 Oct 16;116(16):1832–44.

37. Libby P, Ridker PM, Hansson GK. Progress and challenges in translating the biology of atherosclerosis. Nature. 2011 May 19;473(7347):317–25.

38. Brown MS, Goldstein JL. Heart Attacks: Gone with the Century? Science. 1996 May 3;272(5262):629–0.

39. Tall AR, Rader DJ. Trials and Tribulations of CETP Inhibitors. Circulation Research. 2018 Jan 5;122(1):106–12.

40. Björkbacka H. Multiple roles of Toll-like receptor signaling in atherosclerosis. Current Opinion in Lipidology. 2006 Oct;17(5):527–33.

41. Ogiku M, Kono H, Ishii K, Hosomura N, Fujii H. Role of Macrophage Colony-Stimulating Factor in Polymicrobial Sepsis According to Studies Using Osteopetrotic (op/op) Mice. Journal of Surgical Research. 2011 Jul;169(1):106–16.

42. Mach F, Sauty A, Iarossi AS, Sukhova GK, Neote K, Libby P, et al. Differential expression of three T lymphocyte-activating CXC chemokines by human atheroma-associated cells. J Clin Invest. 1999 Oct 15;104(8):1041–50.

43. Cao Z, Wara AK, Icli B, Sun X, Packard RRS, Esen F, et al. Kruppel-like factor KLF10 targets transforming growth factor-beta1 to regulate CD4(+)CD25(-) T cells and T regulatory cells. J Biol Chem. 2009 Sep 11;284(37):24914–24.

44. Ait-Oufella H, Salomon BL, Potteaux S, Robertson A-KL, Gourdy P, Zoll J, et al. Natural regulatory T cells control the development of atherosclerosis in mice. Nature Medicine. 2006 Feb 5;12(2):178–80.

45. Bouhlel MA, Derudas B, Rigamonti E, Dièvart R, Brozek J, Haulon S, et al. PPARγ Activation Primes Human Monocytes into Alternative M2 Macrophages with Anti-inflammatory Properties. Cell Metabolism. 2007 Aug;6(2):137–43.

46. Libby P. Molecular and cellular mechanisms of the thrombotic complications of atherosclerosis. J Lipid Res. 2009 Apr 3;50(Supplement):S352–7.

47. Tabas I. Macrophage death and defective inflammation resolution in atherosclerosis. Nature Reviews Immunology. 2010 Jan 1;10(1):36–46.

48. Libby P. Mechanisms of acute coronary syndromes and their implications for therapy. N Engl J Med. 2013 May 23;368(21):2004–13.

49. Demer LL, Tintut Y. Vascular Calcification: Pathobiology of a Multifaceted Disease. Circulation. 2008 May 27;117(22):2938–48.

50. New SEP, Goettsch C, Aikawa M, Marchini JF, Shibasaki M, Yabusaki K, et al. Macrophage-Derived Matrix Vesicles: An Alternative Novel Mechanism for Microcalcification in Atherosclerotic Plaques. Circulation Research. 2013 Jun 20;113(1):72–7.

51. New SEP, Aikawa E. Role of Extracellular Vesicles in De Novo Mineralization: An Additional Novel Mechanism of Cardiovascular Calcification. Arteriosclerosis, Thrombosis, and Vascular Biology. 2013 Jul 17;33(8):1753–8.

52. Virmani R, Burke AP, Farb A, Kolodgie FD. Pathology of the Vulnerable Plaque. Journal of the American College of Cardiology. 2006 Apr;47(8):C13–8.

53. Davies MJ. The pathophysiology of acute coronary syndromes. Heart. BMJ Publishing Group; 2000 Mar;83(3):361–6.

54. Kolodgie FD, Gold HK, Burke AP, Fowler DR, Kruth HS, Weber DK, et al. Intraplaque hemorrhage and progression of coronary atheroma. N Engl J Med. 2003 Dec 11;349(24):2316–25.

55. Vengrenyuk Y, Carlier S, Xanthos S, Cardoso L, Ganatos P, Virmani R, et al. A hypothesis for vulnerable plaque rupture due to stress-induced debonding around cellular microcalcifications in thin fibrous caps. Proc Natl Acad Sci USA. 2006 Oct 3;103(40):14678–83.

56. Maldonado N, Kelly-Arnold A, Vengrenyuk Y, Laudier D, Fallon JT, Virmani R, et al. A mechanistic analysis of the role of microcalcifications in atherosclerotic plaque stability: potential implications for plaque rupture. AJP: Heart and Circulatory Physiology. 2012 Sep 1;303(5):H619–28.

57. Hutcheson JD, Maldonado N, Aikawa E. Small entities with large impact: microcalcifications and atherosclerotic plaque vulnerability. Current Opinion in Lipidology. 2014 Oct;25(5):327–32.

58. Motoyama S, Kondo T, Sarai M, Sugiura A, Harigaya H, Sato T, et al. Multislice Computed Tomographic Characteristics of Coronary Lesions in Acute Coronary Syndromes. Journal of the American College of Cardiology. 2007 Jul;50(4):319–26.

59. Stone GW, Maehara A, Lansky AJ, de Bruyne B, Cristea E, Mintz GS, et al. A prospective natural-history study of coronary atherosclerosis. N Engl J Med. 2011 Jan 20;364(3):226–35.

60. Rothwell PM, Eliasziw M, Gutnikov SA, Fox AJ, Taylor DW, Mayberg MR, et al. Analysis of pooled data from the randomised controlled trials of endarterectomy for symptomatic carotid stenosis. The Lancet. 2003 Jan 11;361(9352):107–16.

61. Ibanez B, James S, Agewall S, Antunes MJ, Bucciarelli-Ducci C, Bueno H, et al. 2017 ESC Guidelines for the management of acute myocardial infarction in patients presenting with ST-segment elevation. European Heart Journal. 2017 Aug 26;39(2):119–77.

62. Ornello R, Degan D, Tiseo C, Di Carmine C, Perciballi L, Pistoia F, et al. Distribution and Temporal Trends From 1993 to 2015 of Ischemic Stroke Subtypes. Stroke. 2018 Mar 26;49(4):814–9.

63. Rajkumar CA, Nijjer SS, Cole GD, Al-Lamee R, Francis DP. Moving the Goalposts Into Unblinded Territory. Circulation: Cardiovascular Quality and Outcomes. 2018 Mar 12;11(3):e004665.

64. Al-Lamee R, Dehbi H-M, Tang K, Keeble T, Mielewczik M, Nijjer SS, et al. Percutaneous coronary intervention in stable angina (ORBITA): a double-blind, randomised controlled trial. The Lancet. 2018 Jan;391(10115):31–40.

65. Abbott AL. Medical (nonsurgical) intervention alone is now best for prevention of stroke associated with asymptomatic severe carotid stenosis: results of a systematic review and analysis. Stroke. 2009 Oct;40(10):e573–83.

66. Abbott AL, Adelman MA, Alexandrov AV, Barnett HJM, Beard J, Bell P, et al. Why the US Center for Medicare and Medicaid Services should not extend reimbursement indications for carotid artery angioplasty/stenting. Angiology. 2012 Nov;63(8):639–44.

67. Reivich M, Kuhl D, Wolf A, Greenberg J, Phelps M, Ido T, et al. Measurement of local cerebral glucose metabolism in man with 18F-2-fluoro-2-deoxy-d-glucose. Acta Neurol Scand, Supplc. 1977;64:190–1.

68. Rudd JHF. Imaging Atherosclerotic Plaque Inflammation With [18F]-Fluorodeoxyglucose Positron Emission Tomography. Circulation. 2002 May 20;105(23):2708–11.

69. Fayad ZA, Mani V, Woodward M, Kallend D, Abt M, Burgess T, et al. Safety and efficacy of dalcetrapib on atherosclerotic disease using novel non-invasive multimodality imaging (dal-PLAQUE): a randomised clinical trial. The Lancet. Elsevier; 2011 Oct;378(9802):1547–59.

70. Tawakol A, Migrino RQ, Bashian GG, Bedri S, Vermylen D, Cury RC, et al. In Vivo 18F-Fluorodeoxyglucose Positron Emission Tomography Imaging Provides a Noninvasive Measure of Carotid Plaque Inflammation in Patients. Journal of the American College of Cardiology. 2006 Nov;48(9):1818–24.

71. Tawakol A, Migrino RQ, Hoffmann U, Abbara S, Houser S, Gewirtz H, et al. Noninvasive in vivo measurement of vascular inflammation with F-18 fluorodeoxyglucose positron emission tomography. J Nucl Cardiol. 2005 May;12(3):294–301.

72. Kaim AH, Weber B, Kurrer MO, Gottschalk J, Schulthess Von GK, Buck A. Autoradiographic quantification of 18F-FDG uptake in experimental soft-tissue abscesses in rats. Radiology. 2002 May;223(2):446–51.

73. Babior BM. The respiratory burst of phagocytes. J Clin Invest. 1984 Mar;73(3):599–601.

74. Joshi F, Rosenbaum D, Bordes S, Rudd JHF. Vascular imaging with positron emission tomography. Journal of Internal Medicine. 2011 Aug;270(2):99–109.

75. Pedersen SF, Hag AMF, Klausen TL, Ripa RS, Bodholdt RP, Kjær A. Positron emission tomography of the vulnerable atherosclerotic plaque in man--a contemporary review. Clin Physiol Funct Imaging. 2014 Nov;34(6):413–25.

76. Folco EJ, Sheikine Y, Rocha VZ, Christen T, Shvartz E, Sukhova GK, et al. Hypoxia but not inflammation augments glucose uptake in human macrophages: Implications for imaging atherosclerosis with 18fluorine-labeled 2-deoxy-D-glucose positron emission tomography. Journal of the American College of Cardiology. 2011 Aug 2;58(6):603–14.

77. Tawakol A, Fayad ZA, Mogg R, Alon A, Klimas MT, Dansky H, et al. Intensification of statin therapy results in a rapid reduction in atherosclerotic inflammation: results of a multicenter fluorodeoxyglucose-positron emission tomography/computed tomography feasibility study. Journal of the American College of Cardiology. 2013 Sep 3;62(10):909–17.

78. Blau M, Ganatra R, Bender MA. 18 F-fluoride for bone imaging. Seminars in Nuclear Medicine. 1972 Jan;2(1):31–7.

79. Hawkins RA, Choi Y, Huang SC, Hoh CK, Dahlbom M, Schiepers C, et al. Evaluation of the skeletal kinetics of fluorine-18-fluoride ion with PET. Journal of Nuclear Medicine. 1992 May;33(5):633–42.

80. Messa C, Goodman WG, Hoh CK, Choi Y, Nissenson AR, Salusky IB, et al. Bone metabolic activity measured with positron emission tomography and [18F]fluoride ion in renal osteodystrophy: correlation with bone histomorphometry. J Clin Endocrinol Metab. 1993 Oct;77(4):949–55.

81. Schiepers C, Nuyts J, Bormans G, Dequeker J, Bouillon R, Mortelmans L, et al. Fluoride kinetics of the axial skeleton measured in vivo with fluorine-18-fluoride PET. Journal of Nuclear Medicine. 1997 Dec;38(12):1970–6.

82. Cook GJ, Lodge MA, Blake GM, Marsden PK, Fogelman I. Differences in skeletal kinetics between vertebral and humeral bone measured by 18F-fluoride positron emission tomography in postmenopausal women. J Bone Miner Res. 2000 Apr;15(4):763–9.

83. Cook GJR, Blake GM, Marsden PK, Cronin B, Fogelman I. Quantification of skeletal kinetic indices in Paget's disease using dynamic 18F-fluoride positron emission tomography. J Bone Miner Res. 2002 May;17(5):854–9.

84. Piert M, Zittel TT, Becker GA, Jahn M, Stahlschmidt A, Maier G, et al. Assessment of porcine bone metabolism by dynamic [18F]Fluoride Ion PET: Correlation with Bone Histomorphometry. Journal of Nuclear Medicine. 2001 Jul;42(7):1091–100.

85. Piert M, Zittel TT, Jahn M, Stahlschmidt A, Becker GA, Machulla H-J. Increased sensitivity in detection of a porcine high-turnover osteopenia after total gastrectomy by dynamic 18F-fluoride ion PET and quantitative CT. Journal of Nuclear Medicine. 2003 Jan;44(1):117–24.

86. Frost ML, Cook GJR, Blake GM, Marsden PK, Benatar NA, Fogelman I. A prospective study of risedronate on regional bone metabolism and blood flow at the lumbar spine measured by 18F-fluoride positron emission tomography. J Bone Miner Res. 2003 Dec;18(12):2215–22.

87. Frost ML, Fogelman I, Blake GM, Marsden PK, Cook G. Dissociation between global markers of bone formation and direct measurement of spinal bone formation in osteoporosis. J Bone Miner Res. 2004 Nov;19(11):1797–804.

88. Frost ML, Blake GM, Park-Holohan SJ, Cook GJR, Curran KM, Marsden PK, et al. Long-Term Precision of 18F-Fluoride PET Skeletal Kinetic Studies

in the Assessment of Bone Metabolism. Journal of Nuclear Medicine. 2008 Apr 15;49(5):700–7.

89. Frost ML, Cook GJR, Blake GM, Marsden PK, Fogelman I. The relationship between regional bone turnover measured using 18F-fluoride positron emission tomography and changes in BMD is equivalent to that seen for biochemical markers of bone turnover. J Clin Densitom. 2007 Jan;10(1):46–54.

90. Brenner W, Vernon C, Muzi M, Mankoff DA, Link JM, Conrad EU, et al. Comparison of different quantitative approaches to 18F-fluoride PET scans. Journal of Nuclear Medicine. 2004 Sep;45(9):1493–500.

91. Installé J, Nzeusseu A, Bol A, Depresseux G, Devogelaer J-P, Lonneux M. (18)F-fluoride PET for monitoring therapeutic response in Paget's disease of bone. Journal of Nuclear Medicine. 2005 Oct;46(10):1650–8.

92. Even-Sapir E, Mishani E, Flusser G, Metser U. 18F-Fluoride Positron Emission Tomography and Positron Emission Tomography/Computed Tomography. Seminars in Nuclear Medicine. 2007 Nov;37(6):462–9.

93. Ullmark G, Sörensen J, Nilsson O. Bone healing of severe acetabular defects after revision arthroplasty. Acta Orthop. 2009 Apr;80(2):179–83.

94. Sörensen J, Ullmark G, Långström B, Nilsson O. Rapid bone and blood flow formation in impacted morselized allografts: positron emission tomography (PET) studies on allografts in 5 femoral component revisions of total hip arthroplasty. Acta Orthop Scand. 2003 Dec;74(6):633–43.

95. Czernin J, Satyamurthy N, Schiepers C. Molecular Mechanisms of Bone 18F-NaF Deposition. Journal of Nuclear Medicine. 2010 Nov 23;51(12):1826–9.

96. Foldager CB, Bendtsen M, Bünger C. PET scanning for evaluation of bone metabolism. Acta Orthop. 2009 Dec;80(6):737–8.

97. Derlin T, Richter U, Bannas P, Begemann P, Buchert R, Mester J, et al. Feasibility of 18F-Sodium Fluoride PET/CT for Imaging of Atherosclerotic Plaque. Journal of Nuclear Medicine. 2010 May 25;51(6):862–5.

98. Derlin T, Toth Z, Papp L, Wisotzki C, Apostolova I, Habermann CR, et al. Correlation of Inflammation Assessed by 18F-FDG PET, Active Mineral Deposition Assessed by 18F-Fluoride PET, and Vascular Calcification in Atherosclerotic Plaque: A Dual-Tracer PET/CT Study. Journal of Nuclear Medicine. 2011 Jul 1;52(7):1020–7.

99. Derlin T, Wisotzki C, Richter U, Apostolova I, Bannas P, Weber C, et al. In Vivo Imaging of Mineral Deposition in Carotid Plaque Using 18F-Sodium Fluoride PET/CT: Correlation with Atherogenic Risk Factors. Journal of Nuclear Medicine. 2011 Feb 22;52(3):362–8.

100. Marincheva-Savcheva G, Subramanian S, Qadir S, Figueroa A, Truong Q, Vijayakumar J, et al. Imaging of the aortic valve using fluorodeoxyglucose positron emission tomography increased valvular fluorodeoxyglucose uptake in aortic stenosis. Journal of the American College of Cardiology. 2011 Jun 21;57(25):2507–15.

101. Dweck MR, Boon NA, Newby DE. Calcific aortic stenosis: a disease of the valve and the myocardium. Journal of the American College of Cardiology. 2012 Nov 6;60(19):1854–63.

102. Agatston AS, Janowitz WR, Hildner FJ, Zusmer NR, Viamonte M, Detrano R. Quantification of coronary artery calcium using ultrafast computed tomography. JAC. 1990 Mar 15;15(4):827–32.

103. Hyafil F, Messika-Zeitoun D, Burg S, Rouzet F, Benali K, Iung B, et al. Detection of 18Fluoride Sodium Accumulation by Positron Emission Tomography in Calcified Stenotic Aortic Valves. AJC. Elsevier Inc; 2012 Apr 15;109(8):1194–6.

104. Beheshti M, Saboury B, Mehta NN, Torigian DA, Werner T, Mohler E, et al. Detection and global quantification of cardiovascular molecular calcification by fluoro18-fluoride positron emission tomography/computed tomography--a novel concept. Hell J Nucl Med. 2011 May;14(2):114–20.

105. Li Y, Berenji GR, Shaba WF, Tafti B, Yevdayev E, Dadparvar S. Association of vascular fluoride uptake with vascular calcification and coronary artery disease. Nuclear Medicine Communications. 2012 Jan;33(1):14–20.

106. Dweck MR, Chow MWL, Joshi NV, Williams MC, Jones C, Fletcher AM, et al. Coronary Arterial 18F-Sodium Fluoride Uptake. JAC. Elsevier Inc; 2012 Apr 24;59(17):1539–48.

107. Quirce R, Martínez-Rodríguez I, De Arcocha Torres M, Jiménez-Bonilla JF, Banzo I, Rebollo M, et al. Contribution of 18F-sodium fluoride PET/CT to the study of the carotid atheroma calcification. Rev Esp Med Nucl Imagen Mol. 2013 Jan;32(1):22–5.

108. Blomberg BA, Thomassen A, Takx RAP, Vilstrup MH, Hess S, Nielsen AL, et al. Delayed sodium 18F-fluoride PET/CT imaging does not improve quantification of vascular calcification metabolism: results from the CAMONA study. J Nucl Cardiol. 2014 Apr;21(2):293–304.

109. Morbelli S, Fiz F, Piccardo A, Picori L, Massollo M, Pestarino E, et al. Divergent determinants of 18F–NaF uptake and visible calcium deposition in large arteries: relationship with Framingham risk score. Int J Cardiovasc Imaging. 2013 Dec 8;30(2):439–47.

110. North American Symptomatic Carotid Endarterectomy Trial Collaborators. Beneficial effect of carotid endarterectomy in symptomatic patients with high-grade carotid stenosis. N Engl J Med. 1991 Aug 15;325(7):445–53.

111. Patlak CS, Blasberg RG, Fenstermacher JD. Graphical evaluation of blood-to-brain transfer constants from multiple-time uptake data. J Cereb Blood Flow Metab. 1983 Mar;3(1):1–7.

112. Patlak CS, Blasberg RG. Graphical evaluation of blood-to-brain transfer constants from multiple-time uptake data. Generalizations. J Cereb Blood Flow Metab. 1985 Dec;5(4):584–90.

113. Dweck MR, Chow MWL, Joshi NV, Williams MC, Jones C, Fletcher AM, et al. Coronary Arterial 18F-Sodium Fluoride Uptake. JAC. 2012 Apr 24;59(17):1539–48.

114. Quarto C, Dweck MR, Murigu T, Joshi S, Melina G, Angeloni E, et al. Late gadolinium enhancement as a potential marker of increased perioperative risk in aortic valve replacement. Interactive CardioVascular and Thoracic Surgery. 2012 Jul;15(1):45–50.

115. Messika-Zeitoun D, Bielak LF, Peyser PA, Sheedy PF, Turner ST, Nkomo VT, et al. Aortic valve calcification: determinants and progression in the population. Arteriosclerosis, Thrombosis, and Vascular Biology. 2007 Mar;27(3):642–8.

116. Rosenhek R, Binder T, Porenta G, Lang I, Christ G, Schemper M, et al. Predictors of outcome in severe, asymptomatic aortic stenosis. N Engl J Med. 2000 Aug 31;343(9):611–7.

117. Joshi NV, Vesey AT, Williams MC, Shah ASV, Calvert PA, Craighead FHM, et al. 18F-fluoride positron emission tomography for identification of ruptured and high-risk coronary atherosclerotic plaques: a prospective clinical trial. Lancet. 2014 Feb 22;383(9918):705–13.

118. Dweck MR, Khaw HJ, Sng GKZ, Luo ELC, Baird A, Williams MC, et al. Aortic stenosis, atherosclerosis, and skeletal bone: is there a common link with calcification and inflammation? European Heart Journal. 2013 Jun;34(21):1567–74.

119. American College of Cardiology, American Heart Association Task Force on Practice Guidelines (Writing Committee to revise the 1998 guidelines for the management of patients with valvular heart disease), Society of

Cardiovascular Anesthesiologists, Bonow RO, Carabello BA, Chatterjee K, et al. ACC/AHA 2006 guidelines for the management of patients with valvular heart disease: a report of the American College of Cardiology/American Heart Association Task Force on Practice Guidelines (writing Committee to Revise the 1998 guidelines for the management of patients with valvular heart disease) developed in collaboration with the Society of Cardiovascular Anesthesiologists endorsed by the Society for Cardiovascular Angiography and Interventions and the Society of Thoracic Surgeons. Vol. 48, Journal of the American College of Cardiology. 2006. pp. e1–148.

120. Dweck MR, Jones C, Joshi NV, Fletcher AM, Richardson H, White A, et al. Assessment of valvular calcification and inflammation by positron emission tomography in patients with aortic stenosis. Circulation. 2012 Jan 3;125(1):76–86.

121. Dweck MR, Chow MWL, Joshi NV, Williams MC, Jones C, Fletcher AM, et al. Coronary arterial 18F-sodium fluoride uptake: a novel marker of plaque biology. Journal of the American College of Cardiology. 2012 Apr 24;59(17):1539–48.

122. Bland JM, Altman DG. Statistical methods for assessing agreement between two methods of clinical measurement. The Lancet. 1986 Feb 8;1(8476):307–10.

123. Derlin T, Tóth Z, Papp L, Wisotzki C, Apostolova I, Habermann CR, et al. Correlation of inflammation assessed by 18F-FDG PET, active mineral deposition assessed by 18F-fluoride PET, and vascular calcification in atherosclerotic plaque: a dual-tracer PET/CT study. J Nucl Med. 2011 Jul;52(7):1020–7.

124. Dweck MR, Joshi NV, Jenkins W, Jones C, Chow M, Fletcher A, et al. Assessment of calcification and inflammation with positron emission tomography in aortic stenosis and atherosclerosis. The Lancet. 2013 Feb;381:S11.

125. Derlin T, Toth Z, Papp L, Wisotzki C, Apostolova I, Habermann CR, et al. Correlation of Inflammation Assessed by 18F-FDG PET, Active Mineral Deposition Assessed by 18F-Fluoride PET, and Vascular Calcification in Atherosclerotic Plaque: A Dual-Tracer PET/CT Study. Journal of Nuclear Medicine. 2011 Jul 1;52(7):1020–7.

126. Derlin T, Wisotzki C, Richter U, Apostolova I, Bannas P, Weber C, et al. In vivo imaging of mineral deposition in carotid plaque using 18F-sodium fluoride PET/CT: correlation with atherogenic risk factors. J Nucl Med. 2011 Mar;52(3):362–8.

127. Narisawa S, Harmey D, Yadav MC, O'Neill WC, Hoylaerts MF, Millán JL. Novel Inhibitors of Alkaline Phosphatase Suppress Vascular Smooth Muscle Cell Calcification. J Bone Miner Res. 2007 Jul 16;22(11):1700–10.

128. Rosenhek R, Binder T, Porenta G, Lang I, Christ G, Schemper M, et al. Predictors of outcome in severe, asymptomatic aortic stenosis. N Engl J Med. 2000 Aug 31;343(9):611–7.

129. Toutouzas K, Drakopoulou M, Synetos A, Tsiamis E, Agrogiannis G, Kavantzas N, et al. In Vivo Aortic Valve Thermal Heterogeneity in Patients With Nonrheumatic Aortic Valve Stenosis. Journal of the American College of Cardiology. 2008 Aug;52(9):758–63.

130. Tawakol A, Migrino RQ, Bashian GG, Bedri S, Vermylen D, Cury RC, et al. In Vivo 18F-Fluorodeoxyglucose Positron Emission Tomography Imaging Provides a Noninvasive Measure of Carotid Plaque Inflammation in Patients. Journal of the American College of Cardiology. 2006 Nov;48(9):1818–24.

131. Ishimaru S, Tsujino I, Takei T, Tsukamoto E, Sakaue S, Kamigaki M, et al. Focal uptake on 18F-fluoro-2-deoxyglucose positron emission tomography images indicates cardiac involvement of sarcoidosis. European Heart Journal. 2005 Aug;26(15):1538–43.

132. Cheng VY, Slomka PJ, Ahlen M, Thomson LEJ, Waxman AD, Berman DS. Impact of carbohydrate restriction with and without fatty acid loading on myocardial 18F-FDG uptake during PET: A randomized controlled trial. J Nucl Cardiol. 2010 Apr;17(2):286–91.

133. Blomberg BA, de Jong PA, Thomassen A, Lam MGE, Vach W, Olsen MH, et al. Thoracic aorta calcification but not inflammation is associated with increased cardiovascular disease risk: results of the CAMONA study. Eur J Nucl Med Mol Imaging. 2016 Oct 29;44(2):249–58.

134. Osnabrugge RLJ, Mylotte D, Head SJ, Van Mieghem NM, Nkomo VT, LeReun CM, et al. Aortic Stenosis in the Elderly. Journal of the American College of Cardiology. 2013 Sep;62(11):1002–12.

135. Hyafil F, Messika-Zeitoun D, Burg S, Rouzet F, Benali K, Iung B, et al. Detection of 18Fluoride Sodium Accumulation by Positron Emission Tomography in Calcified Stenotic Aortic Valves. AJC. 2012 Apr 15;109(8):1194–6.

136. Dweck MR, Jenkins WSA, Vesey AT, Pringle MAH, Chin CWL, Malley TS, et al. 18F-sodium fluoride uptake is a marker of active calcification and disease progression in patients with aortic stenosis. Circulation: Cardiovascular Imaging. 2014 Mar;7(2):371–8.

137. Bonow RO, Carabello BA, Chatterjee K, de Leon AC, Freed MD, Gaasch WH, et al. 2008 focused update incorporated into the ACC/AHA 2006 guidelines for the management of patients with valvular heart disease: a report of the American College of Cardiology/American Heart Association Task Force on Practice Guidelines (Writing Committee to revise the 1998 guidelines for the management of patients with valvular heart disease). Endorsed by the Society of Cardiovascular Anesthesiologists, Society for Cardiovascular Angiography and Interventions, and Society of Thoracic Surgeons. Vol. 52, Journal of the American College of Cardiology. 2008. pp. e1–142.

138. Cannon CP, Brindis RG, Chaitman BR, Cohen DJ, Cross JT Jr, Drozda JP Jr, et al. 2013 ACCF/AHA Key Data Elements and Definitions for Measuring the Clinical Management and Outcomes of Patients With Acute Coronary Syndromes and Coronary Artery Disease. Journal of the American College of Cardiology. 2013 Mar;61(9):992–1025.

139. Authors/Task Force Members, Alfieri O, Andreotti F, Antunes MJ, Baron-Esquivias G, Borger MA, et al. Guidelines on the management of valvular heart disease (version 2012): The Joint Task Force on the Management of Valvular Heart Disease of the European Society of Cardiology (ESC) and the European Association for Cardio-Thoracic Surgery (EACTS). European Heart Journal. 2012 Oct 1;33(19):2451–96.

140. Clavel M-A, Pibarot P, Messika-Zeitoun D, Capoulade R, Malouf J, Aggarval S, et al. Impact of Aortic Valve Calcification, as Measured by MDCT, on Survival in Patients With Aortic Stenosis: Results of an International Registry Study. Journal of the American College of Cardiology. 2014 Sep 23;64(12):1202–13.

141. Utsunomiya H, Yamamoto H, Kitagawa T, Kunita E, Urabe Y, Tsushima H, et al. Incremental prognostic value of cardiac computed tomography angiography in asymptomatic aortic stenosis: Significance of aortic valve calcium score. International Journal of Cardiology. 2013 Oct;168(6):5205–11.

142. Clavel M-A, Messika-Zeitoun D, Pibarot P, Aggarwal SR, Malouf J, Araoz PA, et al. The complex nature of discordant severe calcified aortic valve disease grading: new insights from combined Doppler echocardiographic and computed tomographic study. Journal of the American College of Cardiology. 2013 Dec 17;62(24):2329–38.

143. la Iglesia de B, Potter JF, Poulter NR, Robins MM, Skinner J. Performance of the ASSIGN cardiovascular disease risk score on a UK cohort of patients from general practice. Heart. BMJ. 2011 Mar;97(6):491–9.

144. Naghavi M, Libby P, Falk E, Casscells SW, Litovsky S, Rumberger J, et al. From vulnerable plaque to vulnerable patient: a call for new definitions

and risk assessment strategies: Part I. Circulation. 2003 Oct 7;108(14):1664–72.

145. Virmani R, Kolodgie FD, Burke AP, Farb A, Schwartz SM. Lessons From Sudden Coronary Death : A Comprehensive Morphological Classification Scheme for Atherosclerotic Lesions. Arteriosclerosis, Thrombosis, and Vascular Biology. 2000 May 1;20(5):1262–75.

146. Rogers IS, Nasir K, Figueroa AL, Cury RC, Hoffmann U, Vermylen DA, et al. Feasibility of FDG imaging of the coronary arteries: comparison between acute coronary syndrome and stable angina. JACC: Cardiovascular Imaging. 2010 Apr;3(4):388–97.

147. Libby P, DiCarli M, Weissleder R. The Vascular Biology of Atherosclerosis and Imaging Targets. Journal of Nuclear Medicine. Society of Nuclear Medicine; 2010 May 10;51(Supplement_1):33S–37S.

148. Rogers IS, Tawakol A. Imaging of Coronary Inflammation with FDG-PET: Feasibility and Clinical Hurdles. Curr Cardiol Rep. 2011 Jan 28;13(2):138–44.

149. Rudd JHF, Myers KS, Bansilal S, Machac J, Rafique A, Farkouh M, et al. (18F)Fluorodeoxyglucose positron emission tomography imaging of atherosclerotic plaque inflammation is highly reproducible: implications for atherosclerosis therapy trials. Journal of the American College of Cardiology. 2007 Aug 28;50(9):892–6.

150. Wykrzykowska J, Lehman S, Williams G, Parker JA, Palmer MR, Varkey S, et al. Imaging of Inflamed and Vulnerable Plaque in Coronary Arteries with 18F-FDG PET/CT in Patients with Suppression of Myocardial Uptake Using a Low-Carbohydrate, High-Fat Preparation. Journal of Nuclear Medicine. 2009 Mar 16;50(4):563–8.

151. Cheng VY, Slomka PJ, Le Meunier L, Tamarappoo BK, Nakazato R, Dey D, et al. Coronary Arterial 18F-FDG Uptake by Fusion of PET and Coronary CT Angiography at Sites of Percutaneous Stenting for Acute Myocardial Infarction and Stable Coronary Artery Disease. Journal of Nuclear Medicine. 2012 Apr 2;53(4):575–83.

152. Thygesen K, Alpert JS, Simoons ML, Chaitman BR, Writing Group on the Joint ESC/ACCF/AHA/WHF Task Force for the Universal Definition of Myocardial Infarction, White HD, et al. Third universal definition of myocardial infarction. European Heart Journal 2012; 33(20). pp. 2551–67.

153. Williams G, Kolodny GM. Suppression of Myocardial 18F-FDG Uptake by Preparing Patients with a High-Fat, Low-Carbohydrate Diet. American Journal of Roentgenology. 2008 Feb;190(2):W151–6.

154. Calvert PA, Obaid DR, O'Sullivan M, Shapiro LM, McNab D, Densem CG, et al. Association Between IVUS Findings and Adverse Outcomes in Patients With Coronary Artery Disease. JACC: Cardiovascular Imaging. 2011 Aug;4(8):894–901.

155. Murray SW, Stables RH, Hart G, Palmer ND. Defining the magnitude of measurement variability in the virtual histology analysis of acute coronary syndrome plaques. European Heart Journal - Cardiovascular Imaging. 2013 Feb;14(2):167–74.

156. Stone GW, Maehara A, Lansky AJ, de Bruyne B, Cristea E, Mintz GS, et al. A Prospective Natural-History Study of Coronary Atherosclerosis. N Engl J Med. 2011 Jan 20;364(3):226–35.

157. Ehara S, Kobayashi Y, Yoshiyama M, Shimada K, Shimada Y, Fukuda D, et al. Spotty calcification typifies the culprit plaque in patients with acute myocardial infarction: an intravascular ultrasound study. Circulation. 2004 Nov 30;110(22):3424–9.

158. Mintz GS, Nissen SE, Anderson WD, Bailey SR, Erbel R, Fitzgerald PJ, et al. American College of Cardiology Clinical Expert Consensus Document on Standards for Acquisition, Measurement and Reporting of Intravascular Ultrasound Studies (IVUS). A report of the American College of Cardiology Task Force on Clinical Expert Consensus Documents. Journal of the American College of Cardiology. 2001; 37(5) pp. 1478–92.

159. García-García H, Mintz G, Lerman A, Vince G, Margolis P, van Es G-A, et al. Tissue characterisation using intravascular radiofrequency data analysis: recommendations for acquisition, analysis, interpretation and reporting. EuroIntervention. 2009 Jun;5(2):177–89.

160. Motoyama S, Sarai M, Harigaya H, Anno H, Inoue K, Hara T, et al. Computed tomographic angiography characteristics of atherosclerotic plaques subsequently resulting in acute coronary syndrome. Journal of the American College of Cardiology. 2009 Jun 30;54(1):49–57.

161. Kolh P, Wijns W, Danchin N, Di Mario C, Falk V, Folliguet T, et al. Guidelines on myocardial revascularization. European Journal of Cardio-Thoracic Surgery. 2010 Sep;38:S1–S52.

162. Burke AP, Farb A, Malcom GT, Liang Y-H, Smialek J, Virmani R. Coronary Risk Factors and Plaque Morphology in Men with Coronary Disease Who Died Suddenly. N Engl J Med. Massachusetts Medical Society; 1997 May;336(18):1276–82.

163. New SEP, Goettsch C, Aikawa M, Marchini JF, Shibasaki M, Yabusaki K, et al. Macrophage-Derived Matrix Vesicles: An Alternative Novel

Mechanism for Microcalcification in Atherosclerotic Plaques. Circulation Research. 2013 Jun 20;113(1):72–7.

164. Raggi P, Callister TQ, Shaw LJ. Progression of Coronary Artery Calcium and Risk of First Myocardial Infarction in Patients Receiving Cholesterol-Lowering Therapy. Arteriosclerosis, Thrombosis, and Vascular Biology. American Heart Association, Inc; 2004 Jul 1;24(7):1272–7.

165. McEvoy JW, Blaha MJ, DeFilippis AP, Budoff MJ, Nasir K, Blumenthal RS, et al. Coronary Artery Calcium Progression: An Important Clinical Measurement? Journal of the American College of Cardiology. 2010 Nov;56(20):1613–22.

166. Derlin T, Richter U, Bannas P, Begemann P, Buchert R, Mester J, et al. Feasibility of 18F-sodium fluoride PET/CT for imaging of atherosclerotic plaque. J Nucl Med. 2010 Jun;51(6):862–5.

167. Joshi NV, Vesey A, Newby DE, Dweck MR. Will 18F-Sodium Fluoride PET-CT Imaging Be the Magic Bullet for Identifying Vulnerable Coronary Atherosclerotic Plaques? Curr Cardiol Rep. 2014 Aug 8;16(9):521.

168. Doherty TM, Asotra K, Fitzpatrick LA, Qiao J-H, Wilkin DJ, Detrano RC, et al. Calcification in atherosclerosis: bone biology and chronic inflammation at the arterial crossroads. Proc Natl Acad Sci USA. 2003 Sep 30;100(20):11201–6.

169. Wu M, Rementer C, Giachelli CM. Vascular Calcification: An Update on Mechanisms and Challenges in Treatment. Calcif Tissue Int. 2013 Mar 1;93(4):365–73.

170. Johnson RC, Leopold JA, Loscalzo J. Vascular calcification: pathobiological mechanisms and clinical implications. Circulation Research. 2006 Nov 10;99(10):1044–59.

171. Budoff MJ, Shaw LJ, Liu ST, Weinstein SR, Tseng PH, Flores FR, et al. Long-Term Prognosis Associated With Coronary Calcification. Journal of the American College of Cardiology. 2007 May;49(18):1860–70.

172. London GM. Arterial media calcification in end-stage renal disease: impact on all-cause and cardiovascular mortality. Nephrology Dialysis Transplantation. 2003 Sep 1;18(9):1731–40.

173. Bastos Gonçalves F, Voûte MT, Hoeks SE, Chonchol MB, Boersma EE, Stolker RJ, et al. Calcification of the abdominal aorta as an independent predictor of cardiovascular events: a meta-analysis. Heart. 2012 Jun 5;98(13):988–94.

174. Chen W, Dilsizian V. Targeted PET/CT imaging of vulnerable atherosclerotic plaques: microcalcification with sodium fluoride and inflammation with fluorodeoxyglucose. Curr Cardiol Rep. 2013 Jun;15(6):364.

175. Fitzpatrick LA, Severson A, Edwards WD, Ingram RT. Diffuse calcification in human coronary arteries. Association of osteopontin with atherosclerosis. J Clin Invest. American Society for Clinical Investigation; 1994 Oct;94(4):1597–604.

176. Schmid K, McSharry WO, Pameijer CH, Binette JP. Chemical and physicochemical studies on the mineral deposits of the human atherosclerotic aorta. Atherosclerosis. 1980 Oct;37(2):199–210.

177. Kelly-Arnold A, Maldonado N, Laudier D, Aikawa E, Cardoso L, Weinbaum S. Revised microcalcification hypothesis for fibrous cap rupture in human coronary arteries. Proc Natl Acad Sci USA. 2013 Jun 25;110(26):10741–6.

178. Ewence AE, Bootman M, Roderick HL, Skepper JN, McCarthy G, Epple M, et al. Calcium phosphate crystals induce cell death in human vascular smooth muscle cells: a potential mechanism in atherosclerotic plaque destabilization. Circulation Research. 2008 Aug 29;103(5):e28–34.

179. Stary HC. Natural history of calcium deposits in atherosclerosis progression and regression. Z Kardiol. 2000;89 Suppl 2:28–35.

180. Ritman EL. Small-animal CT: Its difference from, and impact on, clinical CT. Nucl Instrum Methods Phys Res A. 2007 Oct;580(2):968–70.

181. Carlin S, Zhang H, Reese M, Ramos NN, Chen Q, Ricketts S-A. A comparison of the imaging characteristics and microregional distribution of 4 hypoxia PET tracers. J Nucl Med. Society of Nuclear Medicine; 2014 Mar;55(3):515–21.

182. Otsu N. A Threshold Selection Method from Gray-Level Histograms. IEEE Transactions on Systems, Man, and Cybernetics. 1979;9(1):62–6.

183. Li CH, Tam PKS. An iterative algorithm for minimum cross entropy thresholding. Pattern Recognition Letters. 1998 Jun;19(8):771–6.

184. Thevenaz P, Ruttimann UE, Unser M. A pyramid approach to subpixel registration based on intensity. IEEE Transactions on Image Processing. 1998;7(1):27–41.

185. Bolte S, Cordelières FP. A guided tour into subcellular colocalization analysis in light microscopy. J Microsc. 2006 Dec;224(Pt 3):213–32.

186. Loening AM, Gambhir SS. AMIDE: A Free Software Tool for Multimodality Medical Image Analysis. Mol Imaging. 2003 Jul 1;2(3):131–7.

187. Frost ML, Blake GM, Park-Holohan S-J, Cook GJR, Curran KM, Marsden PK, et al. Long-term precision of 18F-fluoride PET skeletal kinetic studies in the assessment of bone metabolism. Journal of Nuclear Medicine. 2008 May;49(5):700–7.

188. Lin J, Raghavan S, Fuerstenau DW. The adsorption of fluoride ions by hydroxyapatite from aqueous solution. Colloids and Surfaces. 1981 Dec;3(4):357–70.

189. Gasser P, Voegel JC, Gramain P. Surface reactions on hydroxyapatite in the presence of fluoride ions 1. Saturated and congruent conditions. Colloids and Surfaces A: Physicochemical and Engineering Aspects. 1993 Jul;74(2-3):275–86.

190. Richardson PD, Davies MJ, Born GV. Influence of plaque configuration and stress distribution on fissuring of coronary atherosclerotic plaques. The Lancet. 1989 Oct 21;2(8669):941–4.

191. Abedin M, Tintut Y, Demer LL. Vascular calcification: mechanisms and clinical ramifications. Arteriosclerosis, Thrombosis, and Vascular Biology. 2004 Jul;24(7):1161–70.

192. Chambers BR, Donnan GA. Carotid endarterectomy for asymptomatic carotid stenosis. Cochrane Stroke Group, editor. Cochrane Database Syst Rev. John Wiley & Sons, Ltd; 2005 Oct 19;273(4):CD001923.

193. Libby P. Inflammation in Atherosclerosis. Arteriosclerosis, Thrombosis, and Vascular Biology. 2012 Aug 15;32(9):2045–51.

194. Rudd JHF. Imaging Atherosclerotic Plaque Inflammation With [18F]-Fluorodeoxyglucose Positron Emission Tomography. Circulation. 2002 May 20;105(23):2708–11.

195. Fayad ZA, Mani V, Woodward M, Kallend D, Bansilal S, Pozza J, et al. Rationale and design of dal-PLAQUE: a study assessing efficacy and safety of dalcetrapib on progression or regression of atherosclerosis using magnetic resonance imaging and 18F-fluorodeoxyglucose positron emission tomography/computed tomography. American Heart Journal. 2011 Aug;162(2):214–221.e2.

196. Davies JR, Rudd JHF, Fryer TD, Graves MJ, Clark JC, Kirkpatrick PJ, et al. Identification of culprit lesions after transient ischemic attack by combined 18F fluorodeoxyglucose positron-emission tomography and high-resolution magnetic resonance imaging. Stroke. 2005 Dec;36(12):2642–7.

197. Marnane M, Merwick A, Sheehan OC, Hannon N, Foran P, Grant T, et al. Carotid plaque inflammation on 18F-fluorodeoxyglucose positron emission tomography predicts early stroke recurrence. Ann Neurol. 2012 May;71(5):709–18.

198. Tahara N, Kai H, Ishibashi M, Nakaura H, Kaida H, Baba K, et al. Simvastatin Attenuates Plaque Inflammation. Journal of the American College of Cardiology. 2006 Nov;48(9):1825–31.

199. Quirce R, Martínez-Rodríguez I, Banzo I, Jiménez-Bonilla J, Martínez-Amador N, Ibáñez-Bravo S, et al. New insight of functional molecular imaging into the atheroma biology: 18F-NaF and 18F-FDG in symptomatic and asymptomatic carotid plaques after recent CVA. Preliminary results. Clin Physiol Funct Imaging. 2016 Nov;36(6):499–503.

200. Irkle A, Vesey AT, Lewis DY, Skepper JN, Bird JLE, Dweck MR, et al. Identifying active vascular microcalcification by (18)F-sodium fluoride positron emission tomography. Nat Commun. 2015 Jul 7;6(1):7495.

201. Sage AP, Tintut Y, Demer LL. Regulatory mechanisms in vascular calcification. Nat Rev Cardiol. 2010 Jul 27;7(9):528–36.

202. Proudfoot D, Skepper JN, Hegyi L, Bennett MR, Shanahan CM, Weissberg PL. Apoptosis regulates human vascular calcification in vitro: evidence for initiation of vascular calcification by apoptotic bodies. Circulation Research. 2000 Nov 24;87(11):1055–62.

203. Maldonado N, Kelly-Arnold A, Vengrenyuk Y, Laudier D, Fallon JT, Virmani R, et al. A mechanistic analysis of the role of microcalcifications in atherosclerotic plaque stability: potential implications for plaque rupture. AJP: Heart and Circulatory Physiology. 2012 Sep 1;303(5):H619–28.

204. Bobryshev YV, Killingsworth MC, Lord RSA, Grabs AJ. Matrix vesicles in the fibrous cap of atherosclerotic plaque: possible contribution to plaque rupture. Journal of Cellular and Molecular Medicine. 2008 Oct;12(5B):2073–82.

205. Wang Y-F, Lin T-K, Chuang M-H. Myocardial Infarction: An Incidental Finding on Bone Scintigraphy. Tzu Chi Medical Journal. 2002 Feb 1;14(1):49–53.

206. Pedersen SF, Graebe M, Fisker Hag AM, Højgaard L, Sillesen H, Kjær A. Gene expression and 18FDG uptake in atherosclerotic carotid plaques. Nuclear Medicine Communications. 2010 May;31(5):423–9.

207. Moustafa RR, Izquierdo-Garcia D, Fryer TD, Graves MJ, Rudd JHF, Gillard JH, et al. Carotid plaque inflammation is associated with cerebral

microembolism in patients with recent transient ischemic attack or stroke: a pilot study. Circulation: Cardiovascular Imaging. 2010 Sep;3(5):536–41.

208. Figueroa AL, Subramanian SS, Cury RC, Truong QA, Gardecki JA, Tearney GJ, et al. Distribution of inflammation within carotid atherosclerotic plaques with high-risk morphological features: a comparison between positron emission tomography activity, plaque morphology, and histopathology. Circulation: Cardiovascular Imaging. 2012 Jan;5(1):69–77.

209. Pedersen SF, Sandholt BV, Keller SH, Hansen AE, Clemmensen AE, Sillesen H, et al. 64Cu-DOTATATE PET/MRI for Detection of Activated Macrophages in Carotid Atherosclerotic Plaques: Studies in Patients Undergoing Endarterectomy. Arteriosclerosis, Thrombosis, and Vascular Biology. 2015 Jul;35(7):1696–703.

210. Naylor AR, Sillesen H, Schroeder TV. Clinical and imaging features associated with an increased risk of early and late stroke in patients with symptomatic carotid disease. Eur J Vasc Endovasc Surg. 2015 May;49(5):513–23.

211. Blomberg BA, Akers SR, Saboury B, Mehta NN, Cheng G, Torigian DA, et al. Delayed time-point 18F-FDG PET CT imaging enhances assessment of atherosclerotic plaque inflammation. Nuclear Medicine Communications. 2013 Sep;34(9):860–7.

212. Huet P, Burg S, Le Guludec D, Hyafil F, Buvat I. Variability and uncertainty of 18F-FDG PET imaging protocols for assessing inflammation in atherosclerosis: suggestions for improvement. J Nucl Med. Society of Nuclear Medicine; 2015 Apr;56(4):552–9.

213. Mehta NN, Torigian DA, Gelfand JM, Saboury B, Alavi A. Quantification of atherosclerotic plaque activity and vascular inflammation using [18-F] fluorodeoxyglucose positron emission tomography/computed tomography (FDG-PET/CT). JoVE. 2012 May 2;(63):e3777–7.

214. Fiz F. Correlation between thoracic aorta 18F-natrium fluoride uptake and cardiovascular risk. World Journal of Radiology. 2016;8(1):82–9.

215. Oliveira-Santos M de, Castelo-Branco M, Silva R, Gomes A, Chichorro N, Abrunhosa A, et al. Atherosclerotic plaque metabolism in high cardiovascular risk subjects – A subclinical atherosclerosis imaging study with 18F-NaF PET-CT. Atherosclerosis. 2017 May;260:41–6.

216. Kitagawa T, Yamamoto H, Toshimitsu S, Sasaki K, Senoo A, Kubo Y, et al. 18 F-sodium fluoride positron emission tomography for molecular imaging of coronary atherosclerosis based on computed tomography analysis. Atherosclerosis. 2017 Aug;263:385–92.

217. Lee JM, Bang J-I, Koo B-K, Hwang D, Park J, Zhang J, et al. Clinical Relevance of 18F-Sodium Fluoride Positron-Emission Tomography in Noninvasive Identification of High-Risk Plaque in Patients With Coronary Artery Disease. Circulation: Cardiovascular Imaging. 2017 Nov 13;10(11):e006704.

218. Newby DE. Study Investigating the Effect of Drugs Used to Treat Osteoporosis on the Progression of Calcific Aortic Stenosis. (SALTIRE II). clinicaltrials.gov.

219. Newby DE. Prediction of Recurrent Events With 18F-Fluoride (PREFFIR). clinicaltrials.gov.

220. Newby DE. DIAMOND - Dual Antiplatelet Therapy to Reduce Myocardial Injury (DIAMOND). clinicaltrials.gov.

221. Vesey AT, Dweck MR, Fayad ZA. Utility of Combining PET and MR Imaging of Carotid Plaque. Neuroimaging Clin N Am. 2016 Feb;26(1):55–68.

222. Robson PM, Dey D, Newby DE, Berman D, Li D, Fayad ZA, et al. MR/PET Imaging of the Cardiovascular System. JACC: Cardiovascular Imaging. 2017 Oct;10(10 Pt A):1165–79.

223. Dweck MR, Puntmann VO, Vesey AT, Fayad ZA, Nagel E. MR Imaging of Coronary Arteries and Plaques. JACC: Cardiovascular Imaging. 2016 Mar;9(3):306–16.

224. Forsythe RO, Dweck MR, McBride OMB, Vesey AT, Semple SI, Shah ASV, et al. 18F-Sodium Fluoride Uptake in Abdominal Aortic Aneurysms: The SoFIA3 Study. Journal of the American College of Cardiology. 2018 Feb 6;71(5):513–23.

Appendices

Awards arising from this thesis

- Winner – Young Investigator Prize. British Cardiovascular Imaging Meeting. Edinburgh, UK. March 2018
- Winner – MR Angio Club International Travel Prize. Cincinatti, Ohio, USA. September 2015
- Winner – Roger Wadsworth Prize for the most significant contribution to cardiovascular research by a final year PhD student. Scottish Cardiovascular Forum, Edinburgh 2015.
- Winner – Best UK abstract. American Heart Association 2014 (for Valvular 18F-fluoride and 18F-fluorodeoxyglucose uptake predict disease progression and clinical outcome in patients with aortic stenosis)
- Runner up – British Journal of Surgery Prize. Vascular Society of Great Britain and Ireland AGM 2016
- Runner up – Sol Cohen Prize. Vascular Society of Great Britain and Ireland AGM 2016
- Runner up – British Journal of Surgery Prize. Vascular Society of Great Britain and Ireland AGM 2014
- Runner up – BMJ Research Paper of the Year 2014 (for 18F-fluoride positron emission tomography for identification of ruptured and high-risk coronary atherosclerotic plaques: a prospective clinical trial)

Selected Research Grants Arising From This Thesis And Related Work

- British Heart Foundation funded SALTIRE 2 trial(218)
- Wellcome Trust funded PREFFIR trial(219)
- Wellcome Trust and Astraeneca funded DIAMOND trial(220)
- British Heart Foundation and Medical Research Council funded SOFIA trial(224)
- British Heart Foundation Funded SAPPHIRE trial

Bibliography

Publications Arising Directly From This Thesis

- **Vesey AT**, Jenkins WS, Irkle A, Moss A, Sng G, Forsythe RO, Clark T, Roberts G, Fletcher A, Lucatelli C, Rudd JH, Davenport AP, Mills NL, Al-Shahi Salman R, Dennis M, Whiteley WN, van Beek EJ, Dweck MR, Newby DE. 18F-fluoride and 18F-fluorodeoxyglucose positron emission tomography after transient ischemic attack or minor ischemic stroke: case-control study. *Circulation: Cardiovascular Imaging*. 2017 Mar;10(3).

- **Vesey AT**, Dweck, MR, Fayad Z. Utility Of Combining PET And MRI Imaging Of Carotid Plaque. *Neuroimaging Clinics of North America*. 2016 Feb;26(1):55-68.

- **Vesey AT***, Jenkins WSA*, Shah ASV et al. Valvular 18F-fluoride and 18F-fluorodeoxyglucose uptake predict disease progression and clinical outcome in patients with aortic stenosis. *Journal of the American College of Cardiology* 66(10):1200-1201. 2015 (*joint first authorship).

- Irkle A, **Vesey AT**, Lewis DY et al. Identifying active vascular micro-calcification by 18F-sodium fluoride positron emission tomography. *Nature Communications* 2015 Jul 7;6:7495

- Joshi NV, **Vesey AT**, Williams MC, Shah AS, Calvert PA, Craighead FH, Yeoh SE, Wallace W, Salter D, Fletcher AM, van Beek EJ, Flapan AD, Uren NG, Behan MW, Cruden NL, Mills NL, Fox KA, Rudd JH, Dweck MR, Newby DE. 18F-fluoride positron emission tomography for identification of ruptured and high-risk coronary atherosclerotic plaques: a prospective clinical trial. *Lancet*. 2014 Feb 22;383(9918):705-13.

- Dweck MR, Jenkins WS, **Vesey AT**, Pringle MA, Chin CW, Malley TS, Cowie WJ, Tsampasian V, Richardson H, Fletcher A, Wallace WA, Pessotto R, van Beek EJ, Boon NA, Rudd JH, Newby DE. 18F-sodium fluoride uptake is a marker of active calcification and disease progression in patients with aortic stenosis. *Circulation: Cardiovascular Imaging*. 2014 Mar;7(2):371-8.

Publications Related To This Thesis

- Forsythe RO, Dweck MR, McBride OMB, **Vesey AT** *et al.* 18F-Sodium fluoride Uptake in Abdominal Aortic Aneurysms: The SoFIA3 Study. *Journal of the American College of Cardiology*. 2018 Feb 6;71(5):513-523.

- Anand A, Chin C, Shah ASV, Kwieciński J, **Vesey A**, Cowell J, Weber E, Kaier T, Newby DE, Dweck M, Marber MS, Mills NL. Cardiac myosin-binding protein C is a novel marker of myocardial injury and fibrosis in aortic stenosis. *Heart*. 2017

- Stoumpos S, Hennessy M, **Vesey AT**, Radjenovic A, Kasthuri R, Kingsmore DB, Mark PB, Roditi G. Ferumoxytol-enhanced magnetic resonance angiography for the assessment of potential kidney transplant recipients. *European Radiology*. 2018 Jan;28(1):115-123

- The MA3RS Study Trialists. Aortic Wall Inflammation Predicts Abdominal Aortic Aneurysm Expansion, Rupture and Need for Surgical Repair. *Circulation*. 2017 Aug 29;136(9):787-797

- Miller MR, Raftis JB, Langrish JP, McLean SG, Samutrtai P, Connell SP, Wilson S, **Vesey AT**, Fokkens PHB, Boere AJF, Krystek P, Campbell CJ, Hadoke PWF, Donaldson K, Cassee FR, Newby DE, Duffin R, Mills NL. Inhaled Nanoparticles Accumulate at Sites of Vascular Disease. *ACS Nano*. 2017 May 23;11(5):4542-4552.

- Cui L, Rashdan NA, Zhu D, Milne EM, Ajuh P, Milne G, Helfrich MH, Lim K, Prasad S, Lerman DA, **Vesey AT**, Dweck MR, Jenkins WS, Newby DE, Farquharson C, Macrae VE. End stage renal disease-induced hypercalcemia may promote aortic valve calcification via Annexin VI enrichment of valve interstitial cell derived-matrix vesicles. *Journal of Cellular Physiology*. 2017 Nov;232(11):2985-2995

- Chin CW, Everett RJ, Kwiecinski J, **Vesey AT** et al. Myocardial Fibrosis and Cardiac Decompensation in Aortic Stenosis. *Journal of the American College of Cardiology: Cardiovascular Imaging*. 2017 Nov;10(11):1320-1333.

- Jenkins WSA, **Vesey AT** et al. Cardiac Alpha-V Beta-3 Integrin Expression Following Acute Myocardial Infarction in Humans. *Heart* 2017 Apr;103(8):607-615.

- Zhu D, Hadoke PW, Wu J, **Vesey AT** et al. Ablation of the androgen receptor from vascular smooth muscle cells demonstrates a role for testosterone in vascular calcification. *Nature Science Reports*. 2016 Apr 20;6:24807.

- Ballantyne MD, Dakin R, Pinel K, **Vesey AT** et al. Smooth muscle enriched long non-coding RNA (SMILER) regulates cell proliferation. *Circulation* 2016 May 24;133(21):2050-65.

- Dweck MR, Puntman V, **Vesey AT**, Fayad ZA, Nagel E. Coronary Artery and Plaque Imaging with Cardiovascular Magnetic Resonance. *Journal of the American College of Cardiology: Cardiovascular Imaging*. 2016 Mar;9(3):306-16.

- Joshi NV, Toor I. Shah ASV, Carruthers K, **Vesey AT**, Alam SR, et al. Systemic Atherosclerotic Inflammation Following Acute Myocardial Infarction: Myocardial Infarction Begets Myocardial Infarction. *Journal of the American Heart Association*. 2015 Aug 27;4(9):e001956

- Adamson P, **Vesey AT**, Joshi et al. Salt in the Wound: 18F-fluoride positron emission tomography for identification of vulnerable coronary plaques Journal of Cardiovascular Diagnosis and Therapeutics. *Cardiovascular Diagnosis and Therapy*. 2015 Apr;5(2):150-5.

- McBride O, Berry C, Burns, Chalmers RTA, Doyle B, Forsythe R, Garden OJ, Goodman K, Graham C, Hoskins P, Holdsworth R, MacGillvray T, McKillop G, Murray G, Oatey K, Robson JMJ, Semple S, Stuart W, van Beek EJR, **Vesey AT**, Newby DE. Magnetic Resonance Imaging Using Ultrasmall Superparamagnetic Particles of Iron Oxide in Patients Under Surveillance for Abdominal Aortic Aneurysms to Predict Rupture or Surgical Repair: MRI for Abdominal Aortic Aneurysms to predict Rupture or Surgery: The MA3RS trial. *Open Heart*, 2(1), 2015.

- Stirrat C, **Vesey AT**, McBride O, Robson J, Alam S, Wallace W, et al. Ultra-small superparamagnetic particles of iron oxide in magnetic resonance imaging of cardiovascular disease. *Journal of Vascular Diagnostics* 2014 Oct; 99.

- Joshi NV, **Vesey A**, Newby DE, Dweck MR. Will 18F-Sodium fluoride PET-CT Imaging Be the Magic Bullet for Identifying Vulnerable Coronary Atherosclerotic Plaques? *Current Cardiology Reports*. 2014 Aug 8;16(9):521.

Publications Presented Within This Thesis In Published Format

18F-Sodium Fluoride Uptake Is a Marker of Active Calcification and Disease Progression in Patients With Aortic Stenosis

Marc R. Dweck, MD, PhD*; William S.A. Jenkins, MD*; Alex T. Vesey, MD; Mark A.H. Pringle, BSc; Calvin W.L. Chin, MD; Tamir S. Malley, MD; William J.A. Cowie, BSc; Vasiliki Tsampasian, MD; Hamish Richardson, BSc; Alison Fletcher, PhD; William A. Wallace, MD, PhD; Renzo Pessotto, MD; Edwin J.R. van Beek, MD, PhD; Nicholas A. Boon, MD; James H.F. Rudd, MD, PhD; David E. Newby, MD, PhD

Background—18F-Sodium fluoride (18F-NaF) and 18F-fluorodeoxyglucose (18F-FDG) are promising novel biomarkers of disease activity in aortic stenosis. We compared 18F-NaF and 18F-FDG uptake with histological characterization of the aortic valve and assessed whether they predicted disease progression.

Methods and Results—Thirty patients with aortic stenosis underwent combined positron emission and computed tomography using 18F-NaF and 18F-FDG radiotracers. In 12 patients undergoing aortic valve replacement surgery (10 for each tracer), radiotracer uptake (mean tissue/background ratio) was compared with CD68 (inflammation), alkaline phosphatase, and osteocalcin (calcification) immunohistochemistry of the excised valve. In 18 patients (6 aortic sclerosis, 5 mild, and 7 moderate), aortic valve computed tomography calcium scoring was performed at baseline and after 1 year. Aortic valve 18F-NaF uptake correlated with both alkaline phosphatase (r=0.65; P=0.04) and osteocalcin (r=0.68; P=0.03) immunohistochemistry. There was no significant correlation between 18F-FDG uptake and CD68 staining (r=−0.43; P=0.22). After 1 year, aortic valve calcification increased from 314 (193–540) to 365 (207–934) AU (P<0.01). Baseline 18F-NaF uptake correlated closely with the change in calcium score (r=0.66; P<0.01), and this improved further (r=0.75; P<0.01) when 18F-NaF uptake overlying computed tomography–defined macrocalcification was excluded. No significant correlation was noted between valvular 18F-FDG uptake and change in calcium score (r=−0.11; P=0.66).

Conclusions—18F-NaF uptake identifies active tissue calcification and predicts disease progression in patients with calcific aortic stenosis.

Clinical Trial Registration—URL: http://www.clinicaltrials.gov. Unique identifier: NCT01358513.

(*Circ Cardiovasc Imaging*. 2014;7:371-378.)

Key Words: aortic valve stenosis ■ calcification, physiologic ■ fluorodeoxyglucose F18 ■ inflammation ■ positron-emission tomography

The mechanisms underlying aortic stenosis (AS) remain incompletely understood, and the accurate prediction of disease progression remains a challenge.[1] Calcification and inflammation are thought to play key pathophysiological roles. Indeed, the amount of established calcium in the valve correlates with disease severity and predicts future adverse cardiovascular events.[2,3] Although computed tomography (CT) and echocardiography can provide measures of established valvular calcification, they cannot directly assess ongoing calcification activity, which is considered to be the main driver of disease progression.

Clinical Perspective on p 378

Recent reports have investigated 2 positron emission tomography (PET) radiotracers, 18F-sodium fluoride (18F-NaF) and 18F-fluorodeoxyglucose (18F-FDG), as measures of calcification activity and inflammation, respectively, in the aortic valve,[4] coronary arteries,[5,6] and major vessels.[7] 18F-FDG PET has become a widely used tool for the assessment of inflammation in the aorta and carotid arteries, with uptake correlating with macrophage burden.[8] Several studies have investigated its uptake in AS, although histological validation

Received September 27, 2013; accepted February 5, 2014.

From the Centre for Cardiovascular Science (M.R.D., W.S.A.J., A.T.V., M.A.H.P., C.W.L.C., T.S.M., W.J.A.C., V.T., R.P., N.A.B., D.E.N.) and Clinical Research Imaging Centre (M.R.D., W.S.A.J., A.T.V., C.W.L.C., H.R., A.F., E.J.R.v.B., D.E.N.), University of Edinburgh, Edinburgh, UK; Department of Pathology, Royal Infirmary of Edinburgh, Edinburgh, UK (W.A.W.); and Division of Cardiovascular Medicine, University of Cambridge, Cambridge, UK (J.H.F.R.).

*Drs Dweck and Jenkins contributed equally to this work.

Correspondence to Marc R. Dweck, MD, PhD, Centre for Cardiovascular Science, University of Edinburgh, 47 Little France Crescent, Edinburgh, UK, EH16 4TJ. E-mail MDweck@staffmail.ed.ac.uk

Circ Cardiovasc Imaging **is available at http://circimaging.ahajournals.org** **DOI: 10.1161/CIRCIMAGING.113.001508**

is lacking.[4,9] 18F-NaF has been used as a bone tracer for >40 years, displaying increased activity in conditions associated with increased bone metabolism such as Paget disease. In bone, it is thought to bind and then incorporate into exposed hydroxyapatite crystals via an exchange mechanism with hydroxyl groups to form fluoroapatite. Given that hydroxyapatite is also a key structural component of calcification in the aortic valve and vascular atheroma, it is presumed that similar mechanisms explain its accumulation in these tissues. However, this remains hypothetical. The principal aims of the present study were, therefore, to validate the use of 18F-NaF and 18F-FDG in AS by comparing in vivo radiotracer uptake with immunohistochemistry of calcification and inflammation in excised valvular tissue and to investigate whether either of these agents predicts disease progression at 1 year.

Methods

Patient Populations

Two cohorts of patients with AS were recruited into this study: (1) 12 patients undergoing valve replacement surgery, and (2) 18 patients with asymptomatic disease under surveillance at the Edinburgh Heart Center. The latter cohort was randomly selected for repeat scanning from a larger, previously described population who underwent baseline PET imaging.[4,5,10]

All patients were >50 years of age, and exclusion criteria included a normal aortic valve, insulin-dependent diabetes mellitus, end-stage renal failure, life expectancy of <2 years, and metastatic malignancy. Patients with severe AS were excluded from the cohort of patients under surveillance because of the potential for disease progression and symptom development before the follow-up 1-year scan. The study was performed in accordance with the Declaration of Helsinki and after local research ethics committee approval. All patients provided written informed consent before participating.

Baseline Assessment

All patients underwent full clinical assessment at baseline, and AS severity was assessed using Doppler and 2-dimensional echocardiography by means of the peak transvalvular velocity, mean gradient, and aortic valve area according to American Heart Association/American College of Cardiology guidelines.[11] Aortic sclerosis was defined as thickening of the aortic valve cusps in the absence of accelerated flow (<2 m/s) through the valve. Combined PET and CT scans of the aortic valve were performed using a hybrid scanner (Biograph mCT; Siemens Medical Systems, Erlangen, Germany) 60 minutes after administration of 125 MBq of 18F-NaF. Subsequently, a second PET/CT scan was performed using the same hybrid scanner 90 minutes after administration of 200 MBq of 18F-FDG. Glucose is a major energy source of the myocardium, so that intense 18F-FDG uptake frequently occurs, spilling over and contaminating the signal in the valve. We attempted to reduce myocardial uptake by asking patients to avoid carbohydrates for 24 hours before their 18F-FDG scan, thereby switching the myocardium from glucose to free fatty-acid metabolism. Myocardial 18F-FDG uptake was assessed within regions of interest (ROIs) placed in the basal septum of the left ventricle and classified as being adequately suppressed if mean standard uptake values were <5.0.[4] An ECG-gated breath-hold CT scan (noncontrast enhanced, 40 mA/rot [CareDose]; 100 kV) was performed for calculation of the aortic valve calcium score using dedicated analysis software (VScore; Vital Images, Minnetonka, MN) on axial scans.[12] Particular care was taken to differentiate valvular calcium from that in the aortic root and mitral valve annulus.[6] At 1-year follow-up, patients in the surveillance cohort underwent repeat clinical assessment and CT calcium scoring using the same protocol.

Quantification of Aortic Valve PET Activity

18F-NaF and 18F-FDG uptake in the aortic valve was quantified using an Osirix workstation (OsiriX version 3.5.1 64-bit; OsiriX Imaging Software, Geneva, Switzerland) as reported previously.[4,5] Briefly, fused PET-CT images were reoriented into the plane of the valve and circular ROIs drawn on adjacent 3-mm slices until the entire valve had been examined. For 18F-NaF, ROIs were placed around the perimeter of the valve while excluding the aortic root (whole-valve technique). To reduce the potential for myocardial 18F-FDG activity contaminating the aortic valve signal, ROIs for this tracer were drawn in the center of the valve as previously described (center-valve technique).[4,9] Within these ROIs, mean standard uptake values were calculated for each slice, averaged, and corrected for blood pool activity to provide mean tissue/background ratios. Mean tissue/background ratios were selected prospectively for subsequent comparisons with histology and disease progression because this measure was felt to best represent tracer uptake across the valve as a whole.

Distribution of 18F-NaF in the Aortic Valve Relative to Calcium Scoring

We undertook a voxel-by-voxel analysis comparing the distribution of calcium on CT with 18F-NaF uptake. ROIs were drawn around the valve, and each voxel was assessed for the presence of calcium (>130 HU) and increased 18F-NaF uptake (tissue/background ratio max >1.97 based on the highest uptake in the control cohort of our previous study)[4] using dedicated software MATLAB (Mathworks Inc, Natick, MA). We hypothesized that regions of completely novel calcium development might have an even more important effect on disease progression, and therefore we calculated the percentage of the valve with increased radiotracer uptake in the absence of underlying calcium on CT (% of PET-positive but CT-negative pixels).

Histological Assessment

In the patients undergoing aortic valve replacement, the aortic valve was removed at the time of operation, with care taken to preserve the integrity of the valve architecture. Samples were then fixed in 4% paraformaldehyde for 24 hours. Plaques were decalcified in EDTA for 10 days and embedded in paraffin, and 5-μm sections were prepared. Immunohistochemical staining for osteocalcin (antihuman mouse mAb ab13418; Abcam), CD68 (antihuman mouse clone PG-M1 m0876, DAKO), and tissue nonspecific alkaline phosphatase (TNAP; antihuman rabbit pAb CAT#LF PA50004; Abfrontier) was then undertaken after heat-induced epitope retrieval using a Citrate Buffer pH 6 (Novocastra Leica microsystems) in a decloaking chamber. Osteocalcin staining required no heat-induced epitope retrieval. Sections were stained using a Leica Vision Biosystems Bond×immunostaining robot. After blocking in peroxide for 10 minutes, sections were incubated with the specific antihuman antibodies for 2 hours at room temperature at the following dilutions: osteocalcin 1:200, TNAP 1:100, and CD68 1:100. All incubation steps were followed by washing in TBS/Tween. Sections for osteocalcin and CD68 were incubated for 15 minutes with prepolymer/postprimary followed by 15 minutes with polymer (HRP) for all antibodies before 3,3′-diaminobenzidine visualization and hematoxylin counterstain. Sections were dehydrated in graded ethanol and cleared in xylene before cover slipping in Pertex.

Images were taken on a Zeiss Axioskop2 fitted with an Axiocam MRc digital camera using Axiovision software. Tissue cross-sectional area on each section was manually delineated using Image Pro Plus 5 (Rockville, MD). Immunohistochemical staining for osteocalcin and TNAP was identified by visual assessment and quantified using automated color-based segmentation by a trained observer blinded to the PET data. Staining was expressed as a percentage of the total valve area. Macrophage infiltration using CD68 was assessed using a similar approach but with an object size set threshold applied at 20×10 pixels to limit counting to cell-sized objects. The density of cell staining in the valve tissue was expressed as cells per square millimeter. This technique was also used to identify cellular staining for TNAP and osteocalcin.

Reproducibility Studies

Interobserver reproducibility of the immunohistochemical data was investigated. Tissue staining with alkaline phosphatase, CD68, and

osteocalcin was quantified in 5 valves independently by 2 trained observers (W.S.A.J. and A.T.V.).

Autoradiography

Clinical PET systems have limited resolution. To gain further information about the precise localization of the 18F-NaF signal in aortic valve tissue, we undertook autoradiography. Nondecalcified valvular tissue was rapidly cooled in dry ice and then sectioned at 7-μm thickness using a cryostat (CM1520; Wetzlar, Germany). Sections for autoradiography were mounted on Superfrost slides (Gerhard Menzel, Braunschweig, Germany) before treatment with spray fixative. Sections were bathed in a solution of 18F-NaF at a concentration close to in vivo imaging concentrations (1 kBq/mL) for 60 minutes and then rinsed with PBS. A freshly blanked phosphor screen was then placed over the slides and an overnight exposure undertaken. The screen was then read using a FujiFilm FLA-5100 Fluorescent Image Analyser (Raytek Scientific Limited, Sheffield, UK). Sections adjacent to those used for autoradiography were stained for elemental phosphate (ie, calcium orthophosphate) using Von Kossa stain, and after surface decalcification in situ with Von Ebner solution, for TNAP and osteocalcin. Sections were then manually registered and examined for colocalization with 18F-NaF signal.

Statistical Methods

Continuous variables were assessed for normality both visually and using the D'Agostino-Pearson test. Variables were expressed as either mean±SD or median with interquartile ranges (IQRs) subject to whether they approximated a normal distribution. Categorical data were presented as n (%). The 95% normal range for differences between sets of immunohistochemical measurements (the limits of agreement) were estimated using Bland–Altman analysis by multiplying the SD of the mean difference by 1.96.[13] Intraclass correlation coefficients with 95% confidence intervals were calculated for interobserver variation. Baseline and follow-up calcium scores approximated a normal distribution and were compared using a paired *t* test. However, despite attempts at data transformation, the changes in calcium scores were not normally distributed, and correlations with CT progression data were assessed using Spearman correlation and linear regression analysis. We acknowledge the limitations in using linear regression in the context of a non-normal distribution. A 2-sided $P<0.05$ was regarded as statistically significant. Statistical analysis was performed with the use of Graph Pad Prism version 6.0 (GraphPad Software Inc, San Diego, CA).

Results

Histology Cohort

Twelve patients with symptomatic AS were recruited into the histology cohort (8 men; 76±6 years of age; peak aortic valve velocity, 4.6±0.9 m/s). Patients underwent PET scanning a median of 92 days before surgical aortic valve replacement. Eight patients received both 18F-NaF and 18F-FDG PET scans. In addition, 2 had a single 18F-NaF scan, whereas 2 more had a single 18F-FDG scan. Thus, 10 valves were available for the histological validation of each tracer. No patient had a significant perioperative complication (Table 1). Effective myocardial suppression of 18F-FDG activity was achieved in 40% (median myocardial standard uptake value, 5.4; IQR, 1.9–10.4).

Immunohistochemistry and Autoradiography

All valve samples displayed positive cellular staining for TNAP (225 cells/mm^2 valve tissue; IQR, 143–328), osteocalcin (130 cells/mm^2 valve tissue; IQR, 85–274), and CD68 (172 cells/mm^2 valve tissue; IQR, 73–271; Figure 1). Extensive TNAP and osteocalcin staining was also observed in the extracellular matrix, occupying approximately a sixth of the valve area sampled (17±5% and 17±7%, respectively).

On autoradiography, 18F-NaF uptake was observed to colocalize closely with staining for structural calcium phosphate, TNAP, and osteocalcin (Figure 1). However, signal was also clearly apparent in areas free of macroscopically visible calcium, thus highlighting the sensitivity of 18F-NaF in the detection of newly evolving calcification.

Reproducibility of Immunohistochemistry

Interobserver reproducibility was good for the quantification of osteocalcin and TNAP staining, as well as CD68 cell

Table 1. Baseline Characteristics of Progression Cohort

	Total	Aortic Sclerosis	Mild Aortic Stenosis	Moderate Aortic Stenosis
No.	18	6 (33)	7 (39)	5 (28)
Age, y	75 (71–79)	74 (70–78)	74 (69–80)	79 (70–83)
Men	15 (83)	4 (66)	7 (100)	4 (80)
Hypertension	13 (72)	3 (50)	5 (71)	5 (100)
Hyperlipidemia	12 (67)	4 (66)	5 (71)	3 (60)
Diabetes mellitus	5 (28)	1 (16)	4 (57)	0 (0)
Ischemic heart disease	13 (72)	4 (66)	6 (86)	3 (60)
Serum creatinine, μmol/L	92±29	85 (72–92)	91 (67–125)	84 (69–133)
Cigarette smoking	0 (0)	0 (0)	0 (0)	0 (0)
Peak aortic valve velocity, m/s	2.6 (1.8–3.1)	1.7 (1.6–1.8)	2.4 (2.1–2.6)	3.4 (3.2–3.6)
Aortic valve area, cm^2	1.68 (1.26–2.28)	1.92 (1.8–2.1)	1.63 (1.42–1.87)	1.03 (0.78–1.18)
Mean gradient, mm Hg	10.8 (7.0–16.5)	6.2 (4.8–7.0)	11.0 (9.3–14.0)	22.0 (18.8–27.2)
Aortic valve calcium score, AU	314 (193–540)	106 (13–204)	355 (211–536)	1167 (436–1472)
Time between CT scans, d	386 (377–409)	390 (375–408)	394 (376–426)	183 (360–399)
18F-FDG dose injected, MBq	193 (188–196)	193 (185–205)	191(185–194)	194 (190–206)
18F-NaF dose injected, MBq	123 (120–126)	124 (117–127)	123 (117–128)	123 (120–126)

Categorical displayed as total number (%). Median (interquartile range). CT indicates computed tomography; 18F-FDG, 18F-fluorodeoxyglucose; and 18F-NaF, 18F-sodium fluoride.

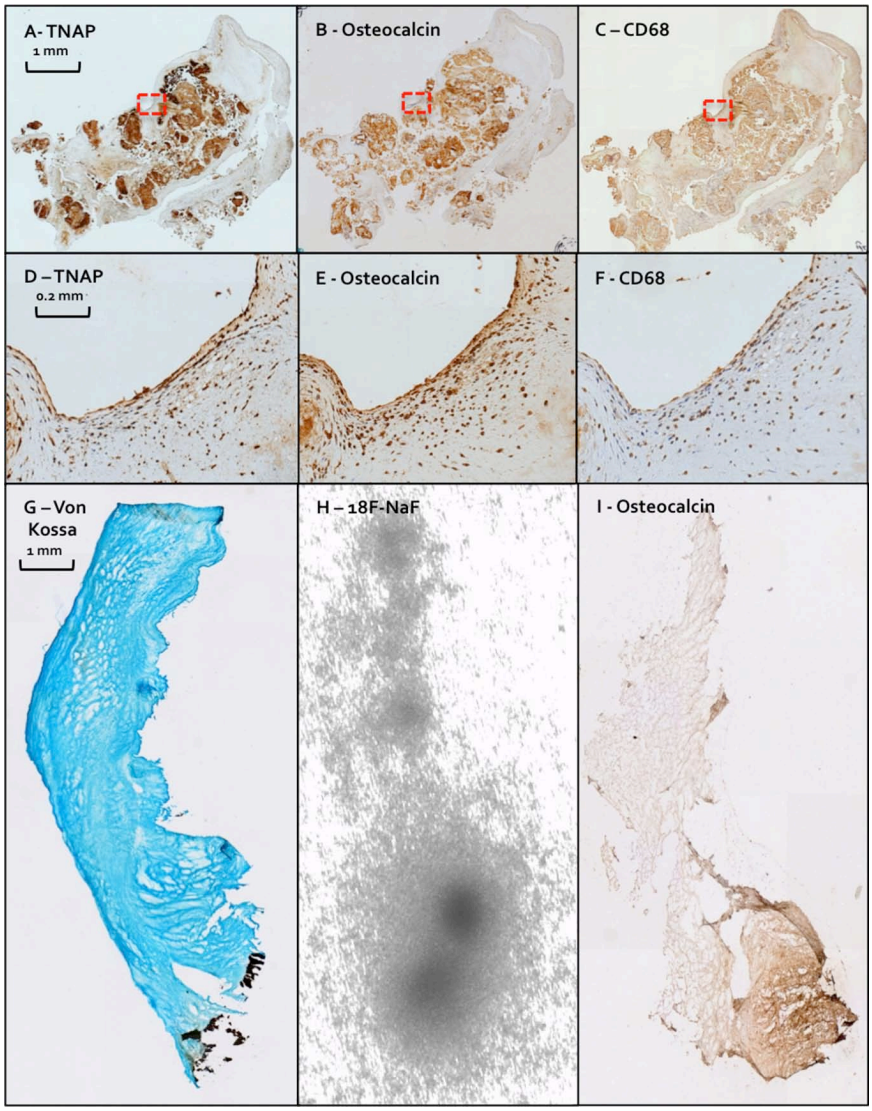

Figure 1. Histology and 18F-sodium fluoride (NaF) autoradiography of excised aortic valve tissue from patients with aortic stenosis. **A**–**F**, Fixed, decalcified, and paraffin-embedded aortic valve tissue after exposure to tissue nonspecific alkaline phosphatase (TNAP), osteocalcin, and CD68 antibodies. **A**–**C**, Widespread positive staining for TNAP, osteocalcin, and CD68 (magnification ×4) in the extracellular matrix, which is also observed on an individual cellular level (**D**–**F**, magnification ×20), respectively. **G**-**I**, Three adjacent and consecutive aortic valve leaflet sections displaying positive immunohistochemical staining for osteocalcin (**I**, magnification ×4) that colocalizes to areas of maximal 18F-NaF uptake on autoradiography (**H**). These likely represent areas of ongoing calcification activity, which extend beyond the areas of established calcium identified in black by Von Kossa stain (**G**, magnification ×4).

counting. All observations were characterized by an absence of fixed or proportional biases, narrow limits of agreement (−13.4% to 9.3%, −8.0% to 5.0%, and −7.9% to 9.6%, respectively), and interclass correlation coefficient values of 0.90 (0.35–0.99), 0.88 (0.60–0.97), and 0.99 (0.99–1.00), respectively (Tables 2 and 3).

Correlation With Radiotracer Uptake

There was a good correlation between in vivo valvular 18F-NaF uptake and both alkaline phosphatase (r=0.65 [95% confidence interval, 0.03–0.90]; P=0.04) and osteocalcin (r=0.68 [0.10–0.91]; P=0.03; Figure 2) staining of the excised tissue. In comparison, there was no association between 18F-FDG uptake and CD68 staining in the valve (r=–0.43; P=0.22).

Disease Progression

Of the 18 patients (75±6 years of age; 17 men; peak aortic-jet velocity, 2.6±0.9 m/s) reassessed at a median interval of 386 days (Table 1), 6 had aortic sclerosis, 7 had mild AS, and 5 had moderate AS. Effective myocardial suppression of 18F-FDG uptake was achieved in 66% (median myocardial standard uptake value, 3.6; IQR, 2.0–5.4).

A correlation was observed between baseline aortic valve calcium scores on CT and 18F-NaF activity on PET (r=0.74 [0.42–0.90]; P≤0.001). However, as described previously, the pattern of 18F-NaF uptake was distinct from the distribution of established calcium.[4,5,14] Indeed 18F-NaF uptake in the absence of underlying calcium occupied a median of 8.3% (IQR 1.6–23.4) of the total valve area, emphasizing that 18F-NaF provides distinct and complementary information to CT calcium scoring (Figure 1).

At 1 year, aortic valve calcium scores increased from 314 (193–540) to 365 (207–934) AU (P<0.01). Interestingly, these regions of novel calcium developed in much the same distribution as the observed baseline 18F-NaF uptake (Figure 3A and 3B). Indeed, we observed an excellent correlation between baseline valvular 18F-NaF PET uptake and the change in calcium score after 1 year (r=0.66 [0.27–0.86]; P=0.003; Figure 3C). This was similar to that observed for the current gold standard method of prediction: the baseline calcium score (r=0.58 [0.15–0.82]; P=0.01; Figure 3D) improved further when only increased 18F-NaF uptake in the absence of underlying CT macrocalcification was considered (r=0.75 [0.42–0.90];

Table 2. Histology Cohort Data

Baseline characteristics	
No.	12
Age, y	76±6
Men	9 (75)
Hypertension	8 (66)
Hyperlipidemia	5 (42)
Ischemic heart disease	4 (33)
Cigarette smoking	1 (8)
Diabetes mellitus	0 (0)
Serum creatinine, μmol/L	87±26
Peak aortic valve velocity (m/s)	4.6±0.9
Aortic valve area, cm^2	0.70 (0.53–0.97)
Mean gradient, mm Hg	48 (44–65)
Aortic valve calcium score, AU	5343 (3114–6292)
Aortic sclerosis	0 (0%)
Mild aortic stenosis	0 (0%)
Moderate aortic stenosis	3 (25%)
Severe aortic stenosis	9 (75%)
Time between 18F-NaF scan and AVR, d	92 (24–345)
Time between 18F-FDG scan and AVR, d	96 (23–331)
18F-FDG dose injected, MBq	200 (193–209)
18F-NaF dose injected, MBq	129 (119–132)
In vivo aortic valve PET data	
18F-NaF uptake (mean TBR)	2.15 (1.98–2.48)
18F-FDG uptake (mean TBR)	1.40 (1.31–1.76)

Categorical data are displayed as n (%). Normally distributed data are displayed as mean±SD. Non-normally distributed data are distributed as median (interquartile range). AVR indicates aortic valve replacement; FDG, fluorodeoxyglucose; NaF, sodium fluoride; PET, positron emission tomography; and TBR, tissue/background ratio.

P=0.01). No statistically significant correlation was observed between 18F-FDG uptake and the subsequent change in CT calcium score (*r*=–0.11 [–0.56 to 0.39]; *P*=0.66; Figure 3E).

Discussion

We provide the first preliminary evidence that valvular 18F-NaF uptake acts as a marker of calcification activity in patients with AS. Not only did uptake values demonstrate a correlation with histological markers of active calcification (TNAP and osteocalcin), but they were also a good predictor of the subsequent progression in aortic valve CT calcium scores at 1 year. In contrast, 18F-FDG uptake did not correlate with CD68 staining on histology or the progression in calcium scores. Our data indicate that 18F-NaF holds promise as a biomarker of disease activity in patients with AS.

The pathophysiology of AS is incompletely understood, delaying the development of biomarkers and effective medical therapies. Calcification and inflammation are thought to play a key pathological role,[1] so that noninvasive markers of their activity are of interest in better understanding the cause of this condition and in predicting disease progression.

Recent studies have investigated 18F-NaF PET as a marker of vascular calcification in AS[3] and atherosclerosis affecting the aorta,[7] coronary,[5,6] and carotid arteries.[15] However, this is the first study to provide histological validation of 18F-NaF uptake in vascular tissue. In bone, 18F-NaF is thought to incorporate onto the surface of hydroxyapatite crystal.[14] Given that hydroxyapatite is also a key component of vascular calcification, it too has been the presumed radiotracer target in AS and atherosclerosis. This hypothesis is supported by our autoradiography and immunohistochemical data, demonstrating a good correlation between 18F-NaF activity and osteocalcin staining: a well-recognized osteogenic protein that itself binds to hydroxyapatite.

Given that 18F-NaF binds to a structural component of vascular calcification, why then does it not simply label all regions of macrocalcification identified by CT? Indeed it is common for regions of dense calcium on CT to show no 18F-NaF uptake. This phenomenon is likely related to the available surface area of exposed hydroxyapatite crystal to which the 18F-fluoride ion can adsorb and the inactivity of established areas of calcification. 18F-NaF uptake is much greater at sites of evolving powdery microcalcification than established regions of field calcification in which the core of hydroxyapatite is internalized and, therefore, hidden from the 18F-NaF tracer. Thus, 18F-NaF binds more readily to regions of developing calcium and acts as a marker of calcification activity, providing distinct information to calcium scoring. In contrast, the latter quantifies regions of established macroscopic calcium in the valve but cannot

Table 3. Immunohistochemical Analysis

Histology	Osteocalcin	TNAP	CD68
No.	10	10	10
Mean valve area analyzed, mm^2	234±152	253±116	190±86
% staining of the valve	17±7	17±5	n/a
Positive cellular staining, cells/mm^2	130 (85–274)	225 (143–328)	172 (73–271)
Interobserver reproducibility			
Mean difference	–2.1%	–1.5%	0.8%
Limits of agreement	–13.4% to 9.3%	–8.0% to 5.0%	–7.9% to 9.6%
ICC	0.88 (0.60–0.97)	0.90 (0.35–0.99)	0.99 (0.99–1.00)

Categorical data are displayed as n (%). Normally distributed data are displayed as mean±SD. Non-normally distributed data are distributed as median (interquartile range). ICC as value (95% confidence interval). ICC indicates interclass correlation coefficient; n/a, not applicable; and TNAP, tissue nonspecific alkaline phosphatase.

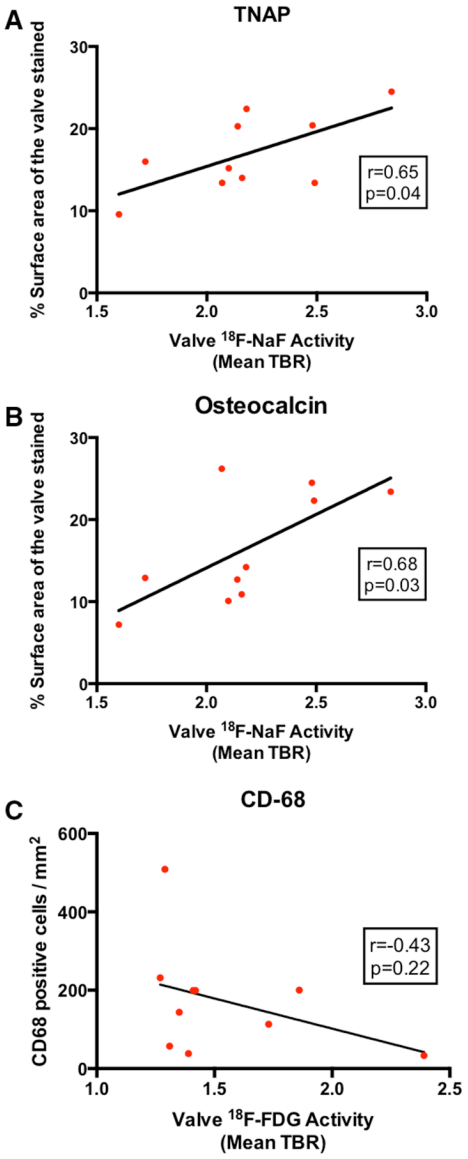

Figure 2. Correlations between in vivo aortic valve positron emission tomography (PET) activity and histological markers of calcification and inflammation. **A**, 18F-Sodium fluoride (NaF) vs tissue nonspecific alkaline phosphatase (TNAP). A good correlation was observed between the percentage aortic valve tissue staining for TNAP and the valvular 18F-NaF activity (mean tissue to background ratio [TBR]); r=0.65, P=0.04. **B**, 18F-NaF vs osteocalcin. Again a strong correlation was observed between the percentage surface area of the valve stained with osteocalcin and the aortic valve 18F-NaF PET activity (mean TBR); r=0.68, P=0.03. **C**, 18F-fluorodeoxyglucose (FDG) vs CD68. A poor correlation was observed between CD68 staining on immunohistochemistry and 18F-FDG PET activity in the aortic valve (mean TBR); r=–0.43, P=0.22.

inform whether the process of calcification is quiescent or active. Again this hypothesis is supported by our data. We have demonstrated a strong correlation between in vivo 18F-NaF uptake and staining for 1 of the key enzymes regulating mineralization: TNAP. This enzyme is expressed in the early stages of new calcium formation and is known to work by breaking down pyrophosphate: a potent inhibitor of mineralization.[16] Furthermore, as one would expect from a measure of activity, baseline 18F-NaF uptake closely correlated with the subsequent change in calcium score at 1 year. Indeed, 18F-NaF uptake performed as well as the current gold standard method of prediction, the degree of established calcium in the valve at baseline.[2,3] However, larger studies are now required to compare these 2 techniques, whereas calcium scoring may be easier to obtain; changes in the 18F-NaF PET signal are likely to occur more quickly, making it a more attractive technique with which to assess the early and more immediate effects of novel treatment strategies.

Interestingly, the pattern of 18F-NaF uptake may be important, with 18F-NaF uptake remote from established macrocalcification on CT offering the best prediction of calcium score progression in our cohort. The spatial resolution of PET/CT is ≈4 mm, and we acknowledge that the voxel-by-voxel analysis used to establish this observation is at the limit of resolution for PET imaging. Nevertheless, the strong correlation with progression is of interest and indicates that further investigation of the spatial distribution of 18F-NaF uptake is warranted.

The results of valvular 18F-FDG imaging were somewhat disappointing and surprising given previous data suggesting an important role for inflammation in AS.[17] Although correlations between 18F-FDG uptake and macrophage burden have previously been demonstrated in regions of aortic and carotid atheroma,[8] we were unable to replicate this with respect to the valve. There are several explanations for this discrepancy. The first is the close proximity of the valve to the myocardium. As discussed, avid uptake of 18F-FDG by the left ventricular myocardium can spill over into the aortic valve contaminating its signal. Unfortunately, despite the stringent dietary restrictions and center-valve analysis technique, it remains possible that myocardial contamination occurred, confounding the correlation with CD68 immunohistochemistry. Indeed poor myocardial suppression was achieved in the histology group, perhaps reflecting their advanced disease and symptomatic status. Alternative methods have been used to reduce further this myocardial uptake, including administration of heparin[18] and a high-fat drink before scanning.[19] However, these make the practicalities of scanning more difficult and have yet to show a clear advantage over dietary restrictions. An alternative explanation for the poor correlation with histology is that the aortic valve 18F-FDG signal relates to uptake by nonmacrophage cell types within the valve, such as osteoblasts, or is governed by external factors, such as hypoxia.[20] In this scenario, one might still expect 18F-FDG to predict disease progression, but once again this was not evident in our cohort. It would, therefore, seem that 18F-FDG holds less potential as a predictor of disease progression than 18F-NaF does, although it remains possible that longer periods of follow-up are required to detect such an association. Indeed on occasion, we also observed 18F-NaF activity that did not translate into a detectable change in calcium score at 1 year. AS is a slowly developing condition, so it is likely to take time for relatively low levels of 18F-NaF or 18F-FDG uptake to translate into new areas of macrocalcification detectable on CT imaging. Larger studies with longer follow-up are, therefore, required to address this issue, confirm our preliminary data, and assess whether 18F-NaF PET can predict disease progression with respect to echocardiographic parameters of valvular stenosis.

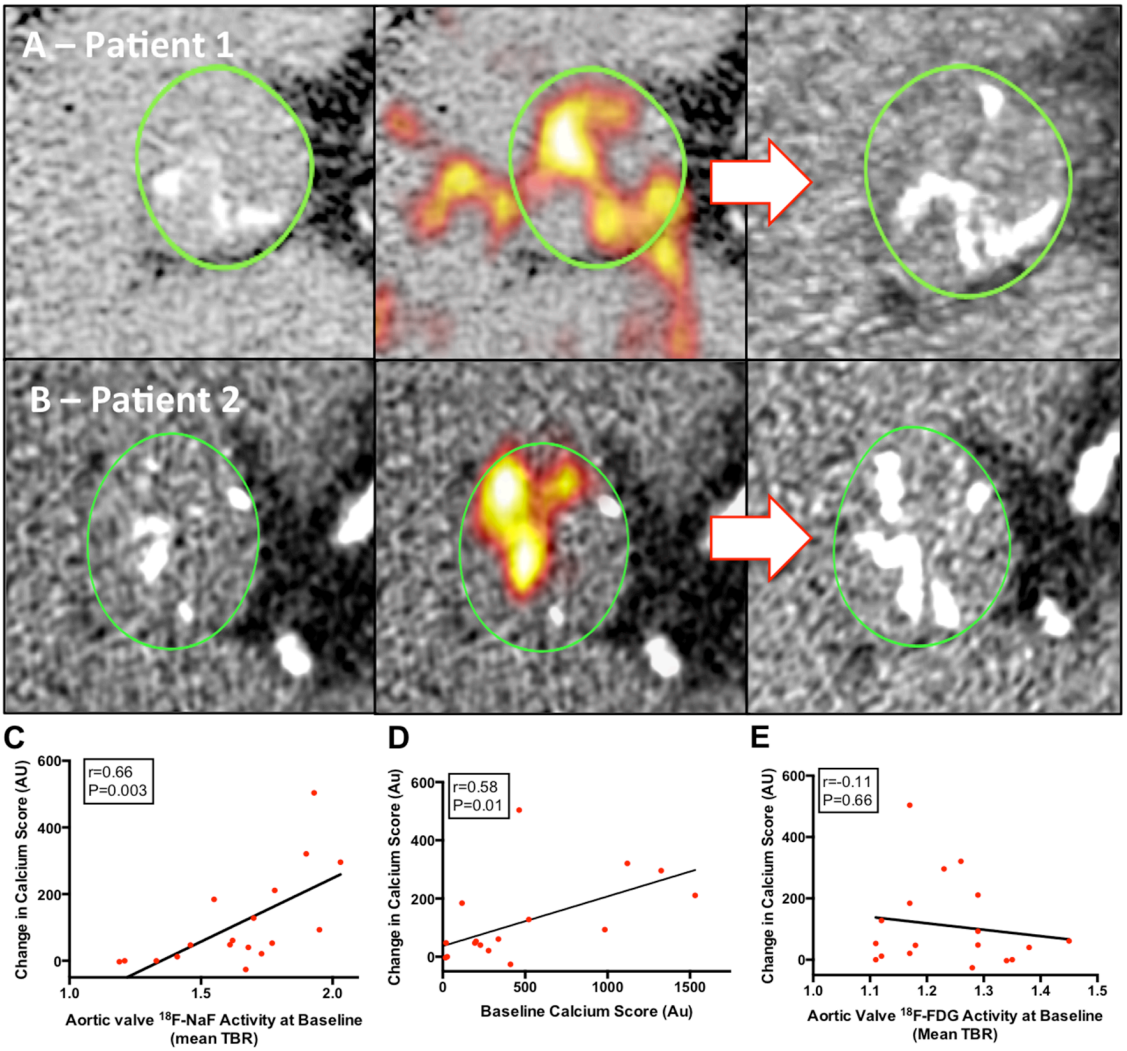

Figure 3. Change in aortic valve computed tomography (CT) calcium score and 18F-sodium fluoride (NaF) positron emission tomography (PET) activity after 1 year. **A** and **B**, Coaxial short axis views of the aortic valve from 2 patients with mild aortic stenosis (**top** and **bottom**). On baseline CT scans (**left**) established regions of macrocalcification appear white. Baseline fused 18F-NaF PET and CT scans (**middle**) show intense 18F-NaF uptake (red, yellow regions) both overlying and adjacent to existing calcium deposits on the CT. One-year follow-up CT scans (**right**) demonstrate increased calcium accumulation in much the same distribution as the baseline PET activity. **C**–**E**, Predictors of progression in aortic valve calcium score. An excellent correlation was observed between baseline 18F-NaF activity in the aortic valve and the subsequent change in calcium score at 1 year r=0.66, P<0.01 (**A**). This matched the current gold standard predictor of disease progression the baseline calcium score r=0.58, P=0.01 (**B**). By contrast, there was a poor correlation with 18F-fluorodeoxyglucose (FDG) activity in the valve r=–0.11, P=0.66 (**C**).

Conclusions

We provide the first preliminary data to support 18F-NaF as a marker of valve calcification activity in AS and as a potential method for predicting disease progression.

Acknowledgments

We acknowledge the support of staff at the Edinburgh Heart Centre at the Royal Infirmary of Edinburgh, the radiography and radiochemistry staff of the Clinical Research Imaging Centre, and the histology staff at the Queens Medical Research Institute.

Sources of Funding

The study was funded by the British Heart Foundation (PG/12/8/29371). Dr Dweck was supported by a fellowship and project grant from the British Heart Foundation (FS/10/026 & PG/12/8/29371). Dr Jenkins was supported by a British Heart Foundation scholarship scheme and fellowship grant (SS/CH/09/002/2636 and FS/12/84/29814). Drs Dweck, Jenkins, and Newby were supported by the British Heart Foundation (CH/09/002, FS/12/84/29814, SS/CH/09/002/2636, and FS/10/026). The work of Dr Rudd was supported by the Higher Education Funding Council for England, the British Heart Foundation, and the Cambridge National Institute for Health Research Biomedical Research Centre. Dr van Beek was supported by the Scottish Imaging Network—a Platform of Scientific Excellence. The Wellcome Trust Clinical Research Facility and the Clinical Research Imaging Centre are supported by the National Health Service Research Scotland through NHS Lothian.

Disclosures

None.

References

1. Quarto C, Dweck MR, Murigu T, Joshi S, Melina G, Angeloni E, Prasad SK, Pepper JR. Late gadolinium enhancement as a potential marker of increased perioperative risk in aortic valve replacement. *Interact Cardiovasc Thorac Surg*. 2012;15:45–50.

2. Messika-Zeitoun D, Bielak LF, Peyser PA, Sheedy PF, Turner ST, Nkomo VT, Breen JF, Maalouf J, Scott C, Tajik AJ, Enriquez-Sarano M. Aortic valve calcification: determinants and progression in the population. *Arterioscler Thromb Vasc Biol*. 2007;27:642–648.
3. Rosenhek R, Binder T, Porenta G, Lang I, Christ G, Schemper M, Maurer G, Baumgartner H. Predictors of outcome in severe, asymptomatic aortic stenosis. *N Engl J Med*. 2000;343:611–617.
4. Dweck MR, Jones C, Joshi NV, Fletcher AM, Richardson H, White A, Marsden M, Pessotto R, Clark JC, Wallace WA, Salter DM, McKillop G, van Beek EJ, Boon NA, Rudd JH, Newby DE. Assessment of valvular calcification and inflammation by positron emission tomography in patients with aortic stenosis. *Circulation*. 2012;125:76–86.
5. Dweck MR, Chow MW, Joshi NV, Williams MC, Jones C, Fletcher AM, Richardson H, White A, McKillop G, van Beek EJ, Boon NA, Rudd JH, Newby DE. Coronary arterial 18F-sodium fluoride uptake: a novel marker of plaque biology. *J Am Coll Cardiol*. 2012;59:1539–1548.
6. Joshi NVVA, Williams MC, Shah ASV, Calvert PA, Craighead FHM, Yeoh SE, Wallace WA, Salter D, Fletcher AM, van Beek EJR, Flapan AD, Uren NG, Behan MWH, Cruden NLM, Mills NL, Fox KAA, Rudd JHF, Dweck MR, Newby DE. 18F-Fluoride positron emission tomography identifies ruptured and high-risk coronary atherosclerotic plaques. *Lancet*. 2013;13:61754–61757.
7. Derlin T, Tóth Z, Papp L, Wisotzki C, Apostolova I, Habermann CR, Mester J, Klutmann S. Correlation of inflammation assessed by 18F-FDG PET, active mineral deposition assessed by 18F-fluoride PET, and vascular calcification in atherosclerotic plaque: a dual-tracer PET/CT study. *J Nucl Med*. 2011;52:1020–1027.
8. Tawakol A, Migrino RQ, Bashian GG, Bedri S, Vermylen D, Cury RC, Yates D, LaMuraglia GM, Furie K, Houser S, Gewirtz H, Muller JE, Brady TJ, Fischman AJ. *In vivo* 18F-fluorodeoxyglucose positron emission tomography imaging provides a noninvasive measure of carotid plaque inflammation in patients. *J Am Coll Cardiol*. 2006;48:1818–1824.
9. Marincheva-Savcheva G, Subramanian S, Qadir S, Figueroa A, Truong Q, Vijayakumar J, Brady TJ, Hoffmann U, Tawakol A. Imaging of the aortic valve using fluorodeoxyglucose positron emission tomography increased valvular fluorodeoxyglucose uptake in aortic stenosis. *J Am Coll Cardiol*. 2011;57:2507–2515.
10. Dweck MR, Khaw HJ, Sng GK, Luo EL, Baird A, Williams MC, Makiello P, Mirsadraee S, Joshi NV, van Beek EJ, Boon NA, Rudd JH, Newby DE. Aortic stenosis, atherosclerosis, and skeletal bone: is there a common link with calcification and inflammation? *Eur Heart J*. 2013;34:1567–1574.
11. Bonow RO, Carabello BA, Chatterjee K, de Leon AC Jr, Faxon DP, Freed MD, Gaasch WH, Lytle BW, Nishimura RA, O'Gara PT, O'Rourke RA, Otto CM, Shah PM, Shanewise JS, Smith SC Jr, Jacobs AK, Adams CD, Anderson JL, Antman EM, Fuster V, Halperin JL, Hiratzka LF, Hunt SA, Nishimura R, Page RL, Riegel B. ACC/AHA 2006 guidelines for the management of patients with valvular heart disease: a report of the American College of Cardiology/American Heart Association Task Force on Practice Guidelines (writing Committee to Revise the 1998 guidelines for the management of patients with valvular heart disease) developed in collaboration with the Society of Cardiovascular Anesthesiologists endorsed by the Society for Cardiovascular Angiography and Interventions and the Society of Thoracic Surgeons. *J Am Coll Cardiol*. 2006;48:e1–e148.
12. Cowell SJ, Newby DE, Burton J, White A, Northridge DB, Boon NA, Reid J. Aortic valve calcification on computed tomography predicts the severity of aortic stenosis. *Clin Radiol*. 2003;58:712–716.
13. Bland JM, Altman DG. Statistical methods for assessing agreement between two methods of clinical measurement. *Lancet*. 1986;1:307–310.
14. Derlin T, Richter U, Bannas P, Begemann P, Buchert R, Mester J, Klutmann S. Feasibility of 18F-sodium fluoride PET/CT for imaging of atherosclerotic plaque. *J Nucl Med*. 2010;51:862–865.
15. Derlin T, Wisotzki C, Richter U, Apostolova I, Bannas P, Weber C, Mester J, Klutmann S. *In vivo* imaging of mineral deposition in carotid plaque using 18F-sodium fluoride PET/CT: correlation with atherogenic risk factors. *J Nucl Med*. 2011;52:362–368.
16. Narisawa S, Harmey D, Yadav MC, O'Neill WC, Hoylaerts MF, Millán JL. Novel inhibitors of alkaline phosphatase suppress vascular smooth muscle cell calcification. *J Bone Miner Res*. 2007;22:1700–1710.
17. Toutouzas K, Drakopoulou M, Synetos A, Tsiamis E, Agrogiannis G, Kavantzas N, Patsouris E, Iliopoulos D, Theodoropoulos S, Yacoub M, Stefanadis C. *In vivo* aortic valve thermal heterogeneity in patients with nonrheumatic aortic valve stenosis the: first *in vivo* experience in humans. *J Am Coll Cardiol*. 2008;52:758–763.
18. Ishimaru S, Tsujino I, Takei T, Tsukamoto E, Sakaue S, Kamigaki M, Ito N, Ohira H, Ikeda D, Tamaki N, Nishimura M. Focal uptake on 18F-fluoro-2-deoxyglucose positron emission tomography images indicates cardiac involvement of sarcoidosis. *Eur Heart J*. 2005;26:1538–1543.
19. Cheng VY SP, Ahlen M, Thomson LEJ, Waxman AD, Berman DS. Impact of carbohydrate restriction with and without fatty acid loading on myocardial 18F-FDG uptake during PET: a randomized controlled trial. *J Nucl Cardiol*. 2010;17:286–291.
20. Folco EJ, Sheikine Y, Rocha VZ, Christen T, Shvartz E, Sukhova GK, Di Carli MF, Libby P. Hypoxia but not inflammation augments glucose uptake in human macrophages: implications for imaging atherosclerosis with 18fluorine-labeled 2-deoxy-D-glucose positron emission tomography. *J Am Coll Cardiol*. 2011;58:603–614.

CLINICAL PERSPECTIVE

Aortic stenosis is the most common form of valvular heart disease in the developed world; however, its rate of progression can vary greatly between patients, and as yet we lack effective medical therapies. Progressive valvular calcification is a key pathophysiological process driving aortic stenosis. Recent studies have suggested that the positron emission tomography (PET) tracer 18F-sodium fluoride (18F-NaF) can measure vascular calcification activity, although validation of this technique has previously been lacking. In this study, we sought to provide such validation, comparing aortic valve 18F-NaF uptake with both histological measures of calcification activity and the progression of aortic valve calcium scores on computed tomography. Ten patients scheduled for aortic valve replacement underwent 18F-NaF PET before their operation with valvular PET uptake, demonstrating a significant correlation with histological markers of calcification activity on the excised aortic valve tissue. In a separate cohort, we assessed 18 patients with calcific aortic valve disease who underwent 18F-NaF PET and computed tomography calcium scoring of the aortic valve both at baseline and after 1 year. Once again a good correlation was observed between the baseline PET uptake and change in calcium score. Our results are promising, providing the first preliminary validation of 18F-NaF as a marker of calcification activity in the aortic valve. More studies are now required to investigate 18F-NaF PET as a method for predicting disease progression in aortic stenosis and assessing the early efficacy of novel treatments aimed at reducing calcification activity in this condition.

JACC VOL. 66, NO. 10, 2015
SEPTEMBER 8, 2015:1198–205

Valvular ^{18}F-Fluoride and ^{18}F-Fluorodeoxyglucose Uptake Predict Disease Progression and Clinical Outcome in Patients With Aortic Stenosis

^{18}F-Fluoride is a positron emission tomography (PET) radiotracer that preferentially binds to regions of newly forming vascular microcalcifications beyond the resolution of computed tomography (CT) (1). ^{18}F-Fluorodeoxyglucose (^{18}F-FDG) has been widely used to measure vascular inflammation (2). This is the first prospective longitudinal study to investigate whether these tracers predict disease progression and clinical outcomes in aortic stenosis.

Patients age >50 years attending the outpatient department of the Edinburgh Heart Centre were approached for recruitment in this prospective cohort study alongside age- and sex-matched controls, as described previously (2). PET and CT were performed in 121 volunteers (age 72 ± 8 years; 68% men) with and without aortic valve disease (20 controls, 20 with aortic sclerosis, and 25 with mild, 33 with moderate, and 23 with severe aortic stenosis) using ^{18}F-fluoride (125 MBq) and ^{18}F-FDG (200 MBq). Uptake in the valve was measured using the most diseased segment tissue: background ratio, based upon averaging the mean standard uptake values in the 2 adjacent valve slices with the highest signal, corrected for blood-pool activity. Disease progression was assessed at 1 and 2 years using CT aortic valve calcium scoring and echocardiography. The primary clinical outcome endpoint was a composite of cardiovascular death and aortic valve replacement.

Ninety-nine participants (81%) returned for repeat clinical assessment and echocardiography at the 2-year time point (median 736 [interquartile range (IQR): 722 to 760] days from enrollment). Ninety-seven patients returned for repeat CT calcium scoring (10 scans were uninterpretable). Aortic valve calcium score increased by 61 (IQR: 5 to 226) AU/year, and aortic valve mean gradient increased by 0.7 (IQR: −0.2 to 2.9) mm Hg/year. After a median of 1,526 (IQR: 1,475 to 1,615) days, 29 patients had undergone aortic valve replacement, whereas 7 experienced cardiovascular death.

After 2 years, new valvular calcium on CT was visible in a similar distribution as the ^{18}F-fluoride activity on baseline PET imaging (Figure 1). Indeed, baseline ^{18}F-fluoride uptake correlated strongly with the subsequent rate of progression in aortic valve calcium score (Spearman $r = 0.80$; $p < 0.001$) and with echocardiographic measures of hemodynamic progression (mean gradient $r = 0.32$; $p = 0.001$). In an exploratory analysis, ^{18}F-fluoride emerged as an independent predictor of clinical outcome after age and sex adjustments (hazard ratio: 1.55; 95% CI: 1.33 to 1.81; $p < 0.001$). ^{18}F-FDG demonstrated moderate correlations with disease progression assessed by CT (Spearman $r = 0.43$; $p = 0.001$) and echocardiography (^{18}F-FDG $r = 0.30$; $p = 0.001$) and predicted clinical outcomes independently of age and sex (hazard ratio: 1.35; 95% CI: 1.16 to 1.58; $p < 0.001$).

There were strong associations between the baseline CT valvular calcium score and rate of change in calcium score (Spearman $r = 0.88$; 95% CI: 0.82 to 0.92; $p < 0.001$). Given the degree of collinearity between CT calcium scoring and ^{18}F-fluoride uptake in the valve (2), assessing whether ^{18}F-fluoride uptake provided incremental predictive information to CT was challenging. However, in a retrospective analysis using the regression line between the CT calcium score and ^{18}F-fluoride uptake as a cutoff, patients with aortic stenosis and higher than expected ^{18}F-fluoride uptake for a given CT calcium score progressed 3 times faster than participants with lower than expected uptake (median change in calcium score 315 [IQR: 127 to 492] AU/year vs. 99 [IQR: 51 to 290] AU/year, respectively; $p = 0.003$) Figures 1 and 2. When a similar analysis was performed for ^{18}F-FDG, no

FIGURE 1 Valvular ^{18}F-Fluoride Uptake Predicts the Progression of Calcification in Aortic Stenosis

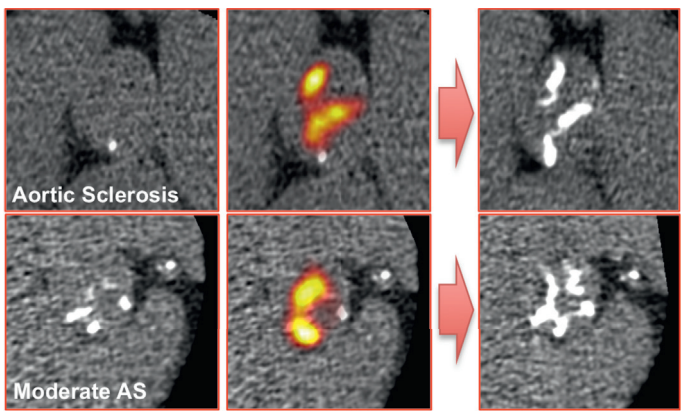

Two patients with calcific aortic valve disease. **(Left)** Baseline computed tomography (CT) images. **(Middle)** Fused positron emission tomography (PET)/CT images showing increased ^{18}F-fluoride valvular uptake **(red/yellow areas)**. **(Right)** Repeat CT scans after 2 years with new areas of macroscopic calcium **(white areas)** in a similar distribution to that of baseline PET uptake.

significant difference was observed (median change in calcium score: 231 [IQR: 79 to 446] AU/year vs. 124 [IQR: 61 to 321] AU/year; p = 0.14). Neither tracer offered independent prediction of clinical outcomes after correction for CT calcium scoring, perhaps reflecting the small number of events and again the collinearity between imaging parameters.

In conclusion we demonstrated that both ^{18}F-fluoride and ^{18}F-FDG predicted disease progression and adverse clinical outcomes in aortic stenosis. In particular, ^{18}F-fluoride provided excellent prediction of the change in CT calcium score, appearing to be of incremental value to baseline CT imaging. Larger studies are required to confirm the incremental predictive value of PET compared with CT. However, our data would support PET/CT as a novel method for measuring disease activity in aortic stenosis, with the ability to predict its natural history. This may be of particular value in studies investigating novel therapies, in which beneficial treatment effects are likely to be detected rapidly without the need for protracted follow-up. (Role of Active Valvular Calcification and Inflammation in Patients With Aortic Stenosis; NCT01358513)

*William S.A. Jenkins, MD
Alex T. Vesey, MD
Anoop S.V. Shah, MD, PhD
Tania A. Pawade, MD
Calvin W.L. Chin, MD
Audrey C. White, CRCS-AE
Alison Fletcher, PhD
Timothy R.G. Cartlidge, MD
Andrew J. Mitchell, MD
Mark A.H. Pringle, MD
Oliver S. Brown, BSc
Renzo Pessotto, MD
Graham McKillop, MD
Edwin J.R. Van Beek, MD, PhD
Nicholas A. Boon, MD
James H.F. Rudd, MD, PhD
*David E. Newby, MD, PhD
Marc R. Dweck, MD, PhD

*British Heart Foundation/University Centre for Cardiovascular Science
Room SU 305, Chancellor's Building
University of Edinburgh
49 Little France Crescent
Edinburgh EH16 4SB
Scotland
E-mail: williamjenkins@doctors.net.uk

http://dx.doi.org/10.1016/j.jacc.2015.06.1325

Please note: The authors have reported that they have no relationships relevant to the contents of this paper to disclose. Drs. Jenkins and Vesey contributed equally to this work. Drs. Newby and Dweck are joint senior authors.

FIGURE 2 ^{18}F-Flouride Uptake for a Given CT Calcium Score

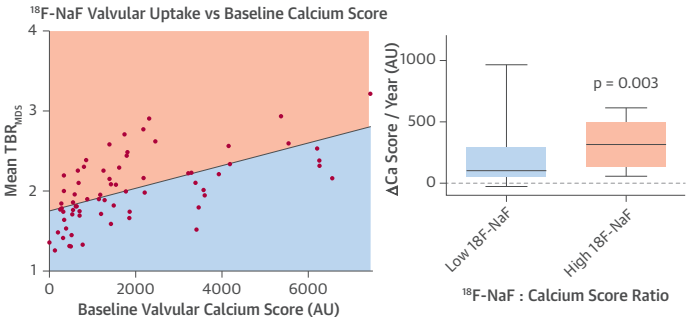

Patients with higher than expected ^{18}F-fluoride uptake for a given CT calcium score **(dots in red above regression line)** demonstrated disease progression rates 3-fold greater than those with lower than expected uptake **(dots in blue below regression line)**. The same was not true for ^{18}F-fluorodeoxyglucose. AS = aortic stenosis; TBR_{MDS} = most diseased segment tissue: background ratio; ^{18}F-NaF = ^{18}F-fluoride.

REFERENCES

1. Irkle A, Vesey AT, Lewis DY, et al. Identifying active vascular microcalcification by ^{18}F-sodium fluoride positron emission tomography. Nature Commun 2015;6:7495.

2. Dweck MR, Jones C, Joshi NV, et al. Assessment of valvular calcification and inflammation by positron emission tomography in patients with aortic stenosis. Circulation 2012;125:76–86.

Trends in Infective Endocarditis Incidence, Microbiology, and Valve Replacement in the United States From 2000 to 2011

The Devil Is in the Details

We read with great interest the paper by Pant et al. (1) regarding trends in infective endocarditis (IE) incidence using the Nationwide Inpatient Sample (NIS) database to address a nagging question that has rightfully garnered much attention and gravity: have recent changes in IE prophylaxis guidelines for dental procedures in this country and abroad resulted in an increase in IE incidence caused by viridans group streptococci (VGS)? As investigators who have previously used the NIS database (2,3), we pose 2 concerns to Pant et al. First, they unfortunately used ICD-9-CM codes that included enterococcal (04104) and non-VGS (038.2 *Streptococcus pneumoniae* septicemia, and

^{18}F-fluoride positron emission tomography for identification of ruptured and high-risk coronary atherosclerotic plaques: a prospective clinical trial

Nikhil V Joshi, Alex T Vesey, Michelle C Williams, Anoop S V Shah, Patrick A Calvert, Felicity H M Craighead, Su Ern Yeoh, William Wallace, Donald Salter, Alison M Fletcher, Edwin J R van Beek, Andrew D Flapan, Neal G Uren, Miles W H Behan, Nicholas L M Cruden, Nicholas L Mills, Keith A A Fox, James H F Rudd, Marc R Dweck, David E Newby**

Summary

Background The use of non-invasive imaging to identify ruptured or high-risk coronary atherosclerotic plaques would represent a major clinical advance for prevention and treatment of coronary artery disease. We used combined PET and CT to identify ruptured and high-risk atherosclerotic plaques using the radioactive tracers ^{18}F-sodium fluoride (^{18}F-NaF) and ^{18}F-fluorodeoxyglucose (^{18}F-FDG).

Methods In this prospective clinical trial, patients with myocardial infarction (n=40) and stable angina (n=40) underwent ^{18}F-NaF and ^{18}F-FDG PET-CT, and invasive coronary angiography. ^{18}F-NaF uptake was compared with histology in carotid endarterectomy specimens from patients with symptomatic carotid disease, and with intravascular ultrasound in patients with stable angina. The primary endpoint was the comparison of ^{18}F-fluoride tissue-to-background ratios of culprit and non-culprit coronary plaques of patients with acute myocardial infarction.

Findings In 37 (93%) patients with myocardial infarction, the highest coronary ^{18}F-NaF uptake was seen in the culprit plaque (median maximum tissue-to-background ratio: culprit 1·66 [IQR 1·40–2·25] *vs* highest non-culprit 1·24 [1·06–1·38], p<0·0001). By contrast, coronary ^{18}F-FDG uptake was commonly obscured by myocardial uptake and where discernible, there were no differences between culprit and non-culprit plaques (1·71 [1·40–2·13] *vs* 1·58 [1·28–2·01], p=0·34). Marked ^{18}F-NaF uptake occurred at the site of all carotid plaque ruptures and was associated with histological evidence of active calcification, macrophage infiltration, apoptosis, and necrosis. 18 (45%) patients with stable angina had plaques with focal ^{18}F-NaF uptake (maximum tissue-to-background ratio 1·90 [IQR 1·61–2·17]) that were associated with more high-risk features on intravascular ultrasound than those without uptake: positive remodelling (remodelling index 1·12 [1·09–1·19] *vs* 1·01 [0·94–1·06]; p=0·0004), microcalcification (73% *vs* 21%, p=0·002), and necrotic core (25% [21–29] *vs* 18% [14–22], p=0·001).

Interpretation ^{18}F-NaF PET-CT is the first non-invasive imaging method to identify and localise ruptured and high-risk coronary plaque. Future studies are needed to establish whether this method can improve the management and treatment of patients with coronary artery disease.

Funding Chief Scientist Office Scotland and British Heart Foundation.

Published **Online** November 11, 2013 http://dx.doi.org/10.1016/S0140-6736(13)61754-7

See **Online/Comment** http://dx.doi.org/10.1016/S0140-6736(13)61911-X

*These authors contributed equally

Centre for Cardiovascular Science, Clinical Research Imaging Centre, and Division of Pathology, University of Edinburgh, Edinburgh, UK (N V Joshi MD, A T Vesey MD, M C Williams MD, A S V Shah MD, F H M Craighead BSc, S E Yeoh, W Wallace MD, D Salter MD, A M Fletcher PhD, E J R van Beek PhD, N L Mills PhD, Prof K A A Fox MD, M R Dweck PhD, Prof D E Newby DSc)**; Edinburgh Heart Centre, Royal Infirmary of Edinburgh, Edinburgh, UK** (A D Flapan MD, N G Uren MD, M W H Behan MD, N L M Cruden PhD)**; and Division of Cardiovascular Medicine, University of Cambridge, Cambridge, UK** (P A Calvert PhD, J H F Rudd PhD)

Correspondence to:
Dr Nikhil Vilas Joshi, SU 305, Chancellors Building, University/BHF Centre for Cardiovascular Science, Little France Crescent, Edinburgh, UK
nikhil.joshi@ed.ac.uk

Introduction

Coronary atherosclerotic plaque rupture is the principal precipitant of acute myocardial infarction and an important cause of sudden cardiac death. Rupture is challenging to predict because most plaques are non-obstructive and are not identified by stress testing or coronary angiography.[1,2] Atherosclerotic lesions at risk of rupture have certain histopathological characteristics that include positive remodelling, microcalcification, and a large necrotic core.[1–3] The development of modern molecular imaging techniques targeted at these features could lead to the identification of such high-risk plaques in vivo and guide the development of novel treatment strategies.[4–7]

Combined PET and CT is a non-invasive imaging technique that brings functional molecular imaging together with precise anatomical information. We have recently reported preliminary PET-CT data using the tracer ^{18}F-sodium fluoride (^{18}F-NaF) as a marker of valvular and vascular calcification activity in patients with aortic stenosis.[7–9] Other studies have shown the usefulness of ^{18}F-flurodeoxyglucose (^{18}F-FDG) as a surrogate of vascular inflammation and macrophage burden.[6,10–13] We therefore investigated whether, compared with the current non-invasive gold standard of ^{18}F-FDG, ^{18}F-NaF uptake could identify ruptured and high-risk atherosclerotic plaques in patients with symptomatic coronary and carotid artery disease.

Methods

Patients

Patients were recruited from the Royal Infirmary of Edinburgh between February, 2012, and January, 2013, in three cohorts: 40 patients with acute ST-segment or non-ST-segment elevation myocardial infarction,[14] 40 patients with stable angina pectoris undergoing elective invasive coronary angiography, and 12 patients (nine evaluable)

undergoing carotid endartectomy for symptomatic carotid artery disease.[15]

Exclusion criteria were age younger than 50 years, insulin-dependent diabetes mellitus, women of childbearing age not receiving contraception, severe renal failure (serum creatinine >250 μmol/L), known contrast allergy, and inability to provide informed consent. Only patients older than 50 years were recruited in the study to reduce any long-term risks associated with radiation exposure. Uncontrolled diabetes and high blood glucose concentrations (>11 mmol/L) interfere with the quality of ^{18}F-FDG PET imaging because of the competition between glucose and ^{18}F-FDG for cellular entry. The convention is therefore to exclude such patients from vascular ^{18}F-FDG PET studies.[7,10,12,13]

All patients underwent a comprehensive baseline clinical assessment including evaluation of their cardiovascular risk factor profile. Plasma troponin I concentrations were measured in patients with stable angina using the ARCHITECT STAT high-sensitivity troponin I assay (Abbott Laboratories, Abbott Park, IL, USA; lower limit of detection 1·2 ng/L; 99th percentile diagnostic threshold 26 ng/L). Studies were done with the approval of the local research ethics committee, in accordance with the Declaration of Helsinki, and with the written informed consent of each participant.

Procedures

Patients with myocardial infarction and stable angina underwent ^{18}F-NaF and ^{18}F-FDG PET-CT, CT coronary angiography, and CT calcium scoring (appendix).[7] To minimise myocardial uptake, patients were instructed to adhere to a low-carbohydrate, high-protein, and high-fat diet for at least 24 h before undergoing ^{18}F-FDG PET-CT.

See Online for appendix

Electrocardiograph-gated PET images were reconstructed in diastole (50–75% of the R-R interval, Ultra-HD) using the Siemens Ultra-HD algorithm, fused with the CT coronary angiogram, and analysed by experienced observers blinded to the clinical diagnosis (NJ, MD, FC) using an OsiriX workstation (OsiriX version 5·5·1 64-bit; OsiriX Imaging Software, Geneva, Switzerland). Two-dimensional regions of interest were drawn around all major (diameter >2 mm) epicardial vessels on 3 mm axial slices just beyond the discernible adventitial border. The maximum standard uptake value (the decay corrected tissue concentration of the tracer divided by the injected dose per bodyweight) was measured and corrected for blood pool activity in the superior vena cava to provide tissue-to-background ratio (TBRs) measurements. Using this method, we have previously shown excellent reproducibility for ^{18}F-NaF TBR measurements in the coronary arteries with an intraclass correlation coefficient of 0·99.[7]

We used a previously established 95% lower reference limit to categorise coronary plaques into ^{18}F-NaF positive lesions (focal uptake with a TBR more than 25% higher than a proximal reference lesion) and negative plaques if these criteria were not achieved. This limit was based on our previous study, where plaques with high ^{18}F-NaF uptake had maximum TBRs that were 44% (95% CI 26–62) higher than a proximal quiescent reference lesion.[7] In patients with acute myocardial infarction, ^{18}F-NaF uptake in the culprit plaque was compared with the highest value in any of the non-culprit vessels.

Quantification of ^{18}F-FDG uptake was performed as for ^{18}F-NaF uptake but restricted to the proximal and mid-portions of the coronary arteries, and to regions where myocardial uptake and spillover could be confidently excluded.[7] Again, ^{18}F-FDG positive plaques were defined using the 25% threshold as described for ^{18}F-NaF. Effective myocardial suppression of ^{18}F-FDG was predefined as a standard uptake value of 5·0 or less in the basal ventricular septum (appendix) as per published data.[12]

In patients with stable angina, PET-CT imaging was prospectively used to direct greyscale and radiofrequency intravascular ultrasound (20 MHz Eagle Eye Platinum Catheters [Volcano Corp, San Diago, CA, USA], motorised pull-back 0·5 mm/s) to the ^{18}F-NaF positive and negative plaques. The interventional cardiologist acquiring the intravascular ultrasound data was blinded to the PET-CT status of the plaque.

Intravascular ultrasound analysis was done as described previously[16] using dedicated VIAS software (Volcano Image Analysis Software version 3.0) by operators blinded to the PET data. Regions of interest were drawn around the external elastic membrane and luminal borders, and plaque area and composition (dense calcium, necrotic core, fibro-fatty tissue, and fibrous tissue) calculated.[16–18] The presence of microcalcification (spotty calcification in the absence of acoustic shadowing on three or more consecutive frames) and the maximum frame necrotic core (the highest percentage of necrotic core on a single frame) were recorded.[19] The remodelling index was defined as the ratio between the external elastic membrane cross-sectional area of the lesion and a proximal reference region in the same vessel.[20] Plaques were classified as thin-cap fibroatheroma, thick-cap fibroatheroma, pathological intimal thickening, or fibrocalcific plaque as defined previously.[18,21]

CT analysis was done on a dedicated cardiovascular workstation (Vital Images, Minnetonka, MN, USA). Vessel-specific and total Agatston calcium scores were calculated as described previously.[7] An independent experienced and blinded observer (MW) determined the stenosis severity, plaque composition (calcified, non-calcified, mixed plaque), and presence of high-risk CT features (positive remodelling, microcalcification, necrotic core) according to standard definitions in plaques with and without increased ^{18}F-NaF activity.[22]

Intact atherosclerotic plaques were retrieved at the time of carotid endarterectomy and scanned using ex-vivo PET-CT to allow precise anatomical colocalisation of ^{18}F-NaF activity with pathological evidence of plaque rupture. Plaques were divided into ^{18}F-NaF positive and negative areas, and histological sections were assessed

using Movat's pentachrome and immunohistochemistry to investigate calcification activity (tissue non-specific alkaline phosphatase and osteocalcin), macrophage infiltration (CD68), and cell death (apoptosis, cleaved caspase 3; presence of necrotic core; appendix).

Statistical analysis

The primary endpoint of the study was the comparison of ^{18}F-fluoride tissue-to-background ratios of culprit and non-culprit coronary plaques of patients with acute myocardial infarction. The main secondary endpoints were comparative imaging and histological characterisation of ^{18}F-fluoride positive and negative atherosclerotic plaques in patients with coronary and carotid artery disease. Based on our previous data,[7] we required 36 patients with myocardial infarction to detect a difference of 0·23 in the tissue-to-background ratio between culprit and non-culprit plaques at 90% power and two-sided p<0·05. We recruited 40 patients to account for incomplete data and recruited a similar sized (n=40) comparator group of patients with stable angina.

Continuous data were tested for normality with the D'Agostino-Pearson omnibus test. Continuous parametric variables were expressed as mean (SD) and

	Myocardial infarction			Stable angina All (n=40)
	All (n=40)	STEMI (n=26)	NSTEMI (n=14)	
Age in years, mean (SD)	62 (8)	63 (9)	60 (8)	67 (8)
Men, n (%)	37 (93%)	24 (92%)	13 (93%)	36 (90%)
Body-mass index (kg/m^2), mean (SD)	28 (5)	27 (5)	30 (4)	30 (5)
Antecedent angina (active), n (%)	9 (23%)	5 (19%)	4 (29%)	40 (100%)
Heart rate (per min), mean (SD)*	56 (7)	56 (7)	56 (7)	59 (9)
Systolic blood pressure (mm Hg), mean (SD)	132 (21)	131 (20)	121 (21)	134 (14)
Diastolic blood pressure (mm Hg), mean (SD)	76 (9)	76 (9)	76 (8)	77 (10)
Cardiovascular history, n (%)				
Previous MI	5 (13%)	1 (4%)	4 (29%)	15 (38%)
Previous CVA/TIA	2 (5%)	1 (4%)	1 (7%)	4 (10%)
Previous PCI	5 (13%)	2 (8%)	3 (21%)	19 (48%)
Previous CABG	2 (5%)	2 (8%)	0	11 (28%)
Risk factors, n (%)				
Smoking habit (ex or current)	25 (63%)	19 (73%)	6 (43%)	24 (60%)
Non-insulin dependent diabetes	8 (20%)	7 (27%)	1 (7%)	13 (33%)
Hypertension	17 (43%)	11 (42%)	6 (43%)	36 (90%)
Hypercholesterolaemia	19 (48%)	11 (42%)	8 (57%)	39 (98%)
Medications, n (%)†				
Aspirin	40 (100%)	26 (100%)	14 (100%)	33 (83%)
Clopidogrel	39 (98%)	25 (96%)	14 (100%)	5 (13%)
Statin	39 (98%)	26 (100%)	13 (93%)	36 (90%)
β blocker	32 (80%)	20 (77%)	12 (86%)	28 (70%)
ACEI/ARB	35 (88%)	25 (96%)	10 (71%)	20 (50%)
Calcium channel blockers	2 (5%)	2 (8%)	0	16 (40%)
Other anti-hypertensive	3 (8%)	1 (4%)	2 (14%)	6 (15%)
Oral nitrates	1 (3%)	0	1 (7%)	15 (38%)
Serum biochemistry, mean (SD)				
Cholesterol (mmol/L)	4·7 (1·2)	4·7 (1·3)	4·8 (1·1)	3·9 (0·8)
HDL cholesterol (mmol/L)	1·1 (0·3)	1·1 (0·3)	1·0 (0·3)	1·1 (0·3)
LDL cholesterol (mmol/L)	2·9 (1·1)	2·8 (1·1)	3·1 (1·0)	2·1 (0·7)
Triglycerides (mmol/L)	1·6 (0·8)	1·7 (0·7)	1·5 (0·7)	1·6 (0·7)
Creatinine (μmol/L)	84 (27)	86 (29)	82 (24)	85 (23)
Coronary artery calcium score (Agatston units), median (IQR)	159 (42–456)	176 (45–474)	122 (26–442)	599 (60–1302)
Peak troponin concentration (ng/L), median (IQR)	32 300 (10 200–50 000)	11 200 (3300–50 000)	3800 (1000–9200)	

NSTEMI=non-ST elevation myocardial infarction. MI=myocardial infarction. CVA=cerebrovascular accident. TIA=transient ischaemic attack. PCI=percutaneous coronary intervention. ACEI=angiotensin converting enzyme inhibitor. ARB=angiotensin receptor blocker. CABG=coronary artery bypass graft. HDL=high-density lipoprotein. LDL=low-density lipoprotein. STEMI=ST-elevation myocardial infarction. *Heart rate at the time of CT coronary angiography. †Medications at the time of scan.

Table 1: **Baseline characteristics of patients with coronary artery disease**

compared using Student's *t* tests. Non-parametric data were presented as median (IQR) and compared using Mann-Whitney *U* test or Wilcoxon signed-rank test as appropriate. Fisher's exact test or chi-squared test was used for analysis of categorical variables. Statistical analysis was done with Graph Pad Prism version 5 (GraphPad Software, La Jolla, CA, USA). A two-sided p<0·05 was taken as statistically significant.

The study was registered with ClinicalTrials.gov number NCT01749254.

Role of the funding source

The funding source had no role in the study design (except through its external peer review process), data collection, data analysis, data interpretation, or writing of the report. All authors had access to the primary data and have final responsibility to submit for publication.

Results

Patients were predominantly middle-aged men and had multiple cardiovascular risk factors (table 1). They underwent both ^{18}F-NaF (60 [SD 9] min after 123 [SD 5] MBq) and ^{18}F-FDG (90 [7] min after 192 [11] MBq) PET-CT scanning within a median of 6 (IQR 3–9) days. The median duration between PET-CT scanning and coronary angiography was 7 (IQR 1–12) days. The total effective radiation dose from study participation was 13·7 (SD 3·0) mSv (conversion factor of 0·014 mSv/mGy.cm): ^{18}F-NaF (3·8 [SD 0·3] mSv) and ^{18}F-FDG (4·9 [0·5] mSv) PET-CT, CT coronary angiogram (3·7 [2·1] mSv), and calcium score (1·3 [0·5] mSv).

The culprit vessel was the left anterior descending artery in 17 (42%) patients, the left circumflex artery in seven (18%), and the right coronary artery in 16 (40%). Patients underwent ^{18}F-NaF scans 6 [IQR 3–10] days after hospitalisation for myocardial infarction (symptoms to ^{18}F-NaF scan, 8 [3–10] days). ^{18}F-NaF activity in the culprit plaque was 34% higher than the maximum activity recorded anywhere else in the coronary vasculature (maximum TBR 1·66 [1·40–2·25] *vs* 1·24 [1·06–1·38], p<0·0001; figures 1 and 2). In 37 of the 40 patients (93%), increased ^{18}F-NaF uptake was seen in the culprit plaque (figure 1; appendix). In the three patients without uptake, two were younger smokers (aged 50 and 52 years) and, in the third, the culprit lesion was adjudicated as the right coronary artery although focal increased activity was seen in the left circumflex artery. In five patients, increased ^{18}F-NaF activity was seen at multiple sites within the coronary circulation.

Predefined myocardial suppression of ^{18}F-FDG uptake was achieved in 28 (70%) patients (median myocardial standard uptake value 3·92 [IQR 2·71–5·55]). However, coronary ^{18}F-FDG uptake could not be distinguished from patchy myocardial uptake in 22 patients affecting 52% of vessel territories. Increased uptake of ^{18}F-FDG was observed in the culprit vessels of six (33%) of the remaining 18 patients. Overall, no significant differences could be shown between the maximum TBRs in the culprit plaques and those recorded elsewhere in the coronary vasculature (1·71 [IQR 1·40–2·13] *vs* 1·58 [1·28–2·01], p=0·34: figure 2) with a mean difference of 0·09 (95% CI –0·07 to 0·24).

The median duration between clinical symptoms and carotid endarterectomy was 17 [IQR 10–27] days (appendix). Carotid endarterectomy specimens (figure 3; appendix) were obtained for 12 patients, although three specimens could not be excised intact and were discarded. Ex-vivo ^{18}F-NaF PET-CT was undertaken in nine specimens and uptake was localised to the site of macroscopic plaque rupture in all patients (figure 3). Compared with sections of tissue without uptake (n=15), those with increased ^{18}F-NaF uptake (n=24) had increased calcification activity (tissue non-specific alkaline phosphatase 4·07% [SD 3·42] *vs* 0·76% [0·51], p<0·0001; osteocalcin 1·88% [IQR 0·58–4·10] *vs* 0·25% [0·11–0·58], p<0·0001), macrophage infiltration (CD68, 350 [IQR 172–840] *vs* 145 [24–362] cells/mm², p=0·013), and cell death (apoptosis, cleaved-caspase-3, 1·23% [0·69–1·91] *vs* 0·09% [0·04–1·38], p=0·005; necrotic core, 22/24 *vs* 4/15; p<0·0001; appendix).

Patients with stable angina were older (67 [SD 8] *vs* 62 [8] years, p=0·006) and had more severe coronary artery disease (coronary artery calcium score 599 [IQR 60–1302] *vs* 159 [42–456] Agatston units, p=0·006) than those with myocardial infarction (table 1). Focal ^{18}F-NaF uptake was noted in 18 patients (45%), which did not seem to be related to percutaneous coronary intervention and stent

Figure 1: **Focal ^{18}F-fluoride and ^{18}F-fluorodeoxyglucose uptake in patients with myocardial infarction and stable angina**

Patient with acute ST-segment elevation myocardial infarction with (A) proximal occlusion (red arrow) of the left anterior descending artery on invasive coronary angiography and (B) intense focal ^{18}F-fluoride (^{18}F-NaF, tissue-to-background ratios, culprit 2·27 versus reference segment 1·09 [108% increase]) uptake (yellow-red) at the site of the culprit plaque (red arrow) on the combined positron emission and computed tomogram (PET-CT). Corresponding ^{18}F-fluorodeoxyglucose PET-CT image (C) showing no uptake at the site of the culprit plaque (^{18}F-FDG, tissue-to-background ratios, 1·63 versus reference segment 1·91 [15% decrease]). Note the significant myocardial uptake overlapping with the coronary artery (yellow arrow) and uptake within the oesophagus (blue arrow). Patient with anterior non-ST-segment elevation myocardial infarction with (D) culprit (red arrow; left anterior descending artery) and bystander non-culprit (white arrow; circumflex artery) lesions on invasive coronary angiography that were both stented during the index admission. Only the culprit lesion had increased ^{18}F-NaF uptake (^{18}F-NaF, tissue-to-background ratios, culprit 2·03 versus reference segment 1·08 [88% increase]) on PET-CT (E) after percutaneous coronary intervention. Corresponding ^{18}F-fluorodeoxyglucose PET-CT showing no uptake either at the culprit (^{18}F-FDG, tissue-to-background ratios, culprit 1·62 versus reference segment 1·49 [9% increase]) or the bystander stented lesion. Note intense uptake within the ascending aorta. In a patient with stable angina with previous coronary artery bypass grafting, invasive coronary angiography (G) showed non-obstructive disease in the right coronary artery. Corresponding PET-CT scan (H) showed a region of increased ^{18}F-NaF activity (positive lesion, red line) in the mid-right coronary artery (tissue-to-background ratio, 3·13) and a region without increased uptake in the proximal vessel (negative lesion, yellow line). Radiofrequency intravascular ultrasound shows that the ^{18}F-NaF negative plaque (I) is principally composed of fibrous and fibrofatty tissue (green) with confluent calcium (white with acoustic shadow) but little evidence of necrosis. On the contrary, the ^{18}F-NaF positive plaque (J) shows high-risk features such as a large necrotic core (red) and microcalcification (white).

deployment (appendix). The maximum TBR for ^{18}F-NaF positive plaques was 1·90 [IQR 1·61–2·17] and for ^{18}F-NaF negative plaques was 1·02 [0·82–1·17]. ^{18}F-NaF positive plaques were predominantly (72% of patients) non-obstructive (<70% luminal stenosis) on coronary angiography and showed multiple high-risk features on radiofrequency intravascular ultrasound (positive remodelling [remodelling index 1·12 [IQR 1·09–1·19] *vs*

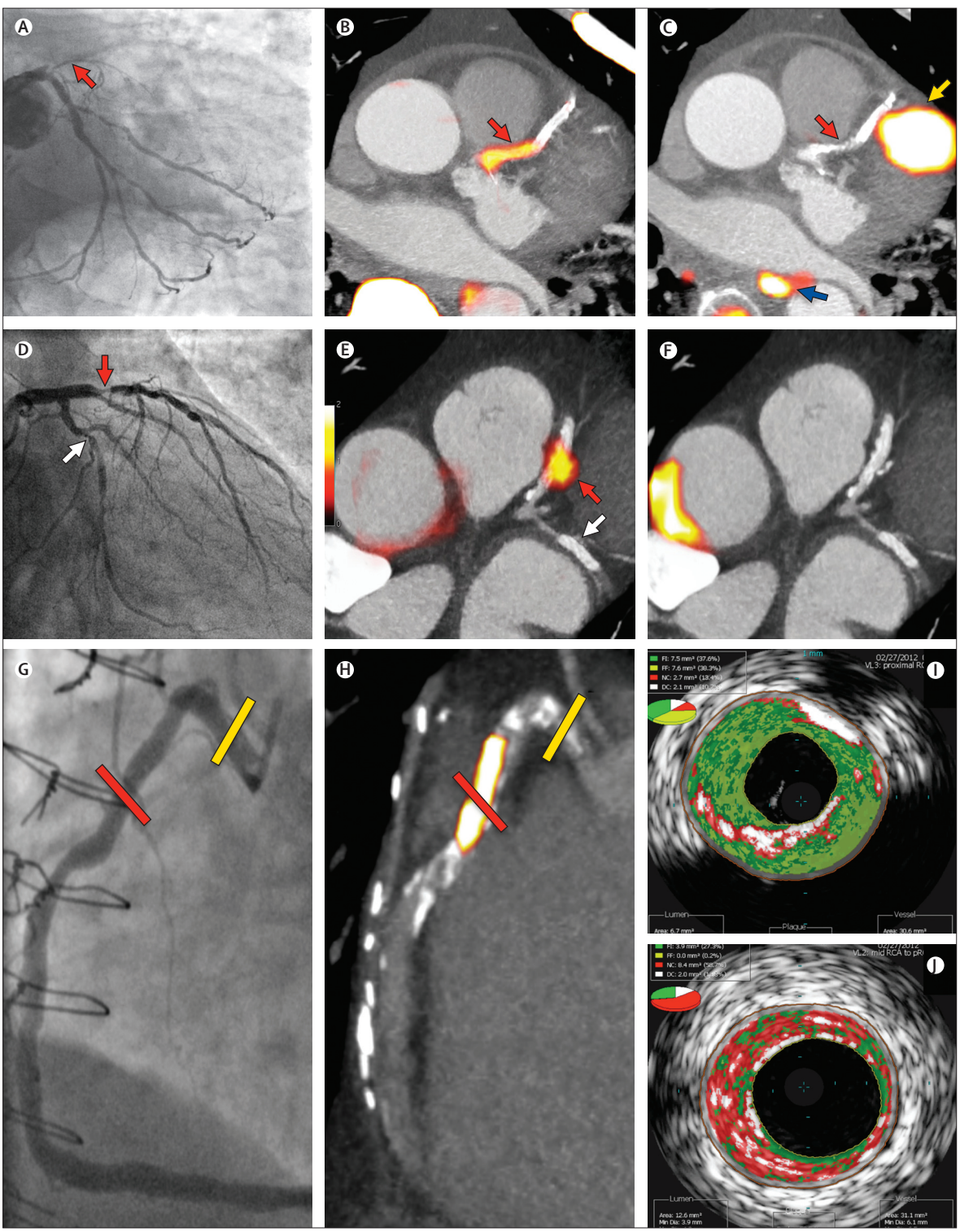

1·01 [0·94–1·06]; p<0·001, microcalcification (73 *vs* 21%, p=0·002) and necrotic core (24·6% [20·5–28·8] *vs* 18·0% [14·0–22·4]), p=0·001), with similar observations for CT (figure 1, table 2; appendix). Multivessel uptake was commonly seen: two-vessel uptake in six (15%) and three-vessel uptake in five (13%) patients. Patients with ^{18}F-NaF positive lesions had higher concentrations of plasma troponin at baseline (3·35 [IQR 2·35–10·20] *vs* 2·45 [1·85–4·02] ng/L; p=0·047), with one individual having a concentration (35 ng/L) above the 99th percentile diagnostic threshold.

Although predefined myocardial suppression of ^{18}F-FDG uptake was achieved in 34 (85%) patients (median myocardial standard uptake value 2·60 [IQR 1·83–3·83]), coronary ^{18}F-FDG uptake could not be confidently interpreted in 45% of vessel territories. Increased focal ^{18}F-FDG uptake was noted in just four patients: three at the site of recent coronary stenting and one at the ostium of a saphenous vein graft.

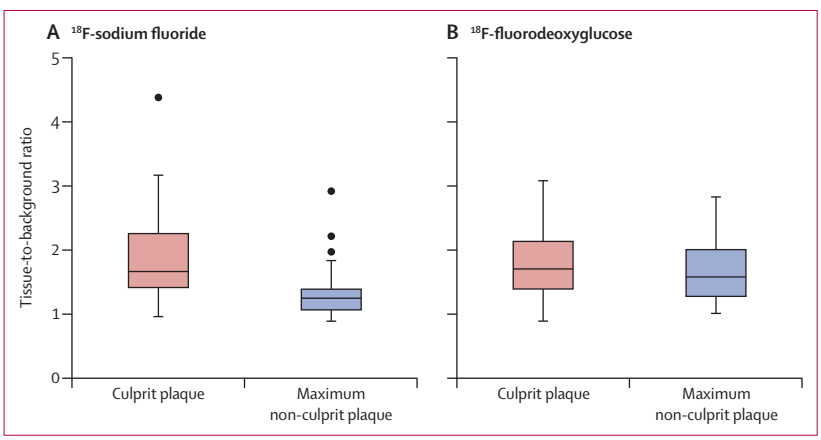

Figure 2: **^{18}F-fluoride and ^{18}F-fluorodeoxyglucose uptake in patients with myocardial infarction**
^{18}F-fluoride activity (maximum tissue-to-background ratio) was increased in the culprit plaque (red) compared with the maximum uptake in any of the non-culprit plaques (blue). By contrast, there was no difference in the activity of ^{18}F-fluorodeoxyglucose between these regions.

Discussion

We have shown that intense ^{18}F-NaF uptake localises to recent plaque rupture in patients with acute myocardial infarction and in those with symptomatic carotid disease. Moreover, in patients with stable coronary artery disease, ^{18}F-NaF uptake seems to identify coronary plaques with high-risk features on intravascular ultrasound. This technique holds major promise as a means of identifying high-risk and ruptured plaque, and potentially informing the future management and treatment of patients with stable and unstable coronary artery disease.

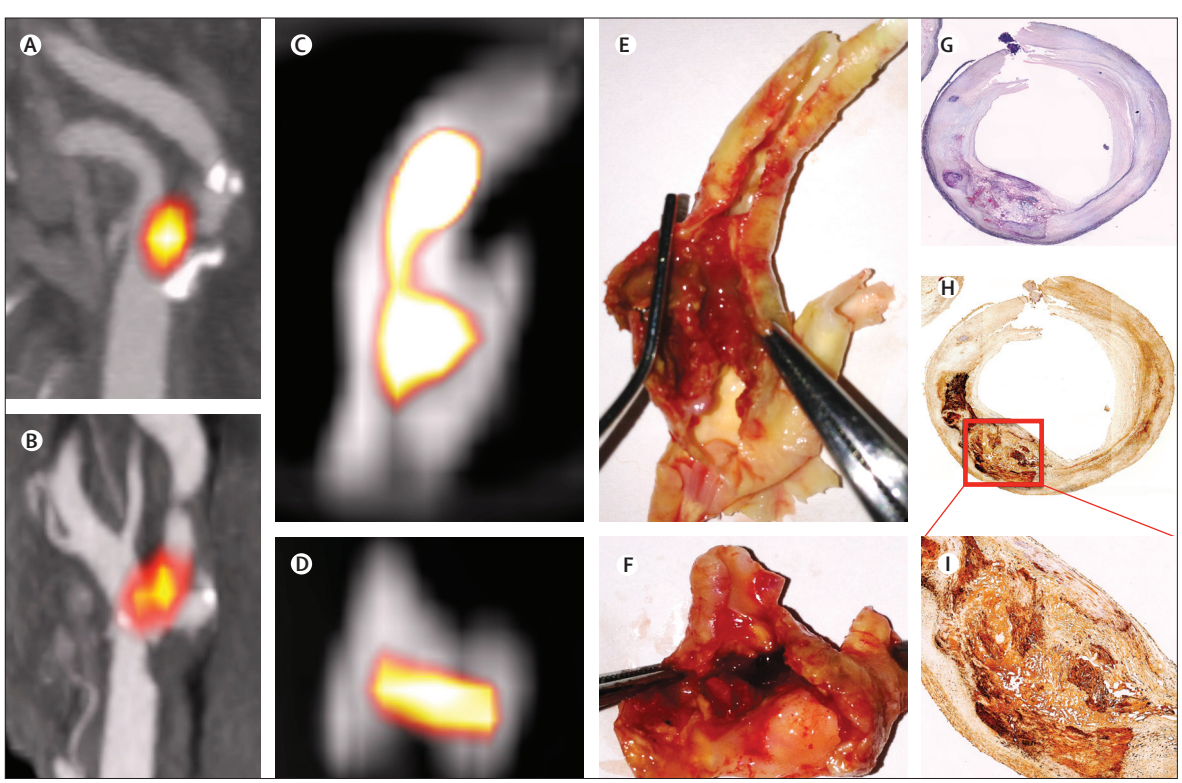

Figure 3: **Carotid ^{18}F-fluoride uptake and carotid plaque rupture**
In-vivo (A and B) and ex-vivo (C and D) positron emission and computed tomograms showing colocalisation of ^{18}F-fluoride (^{18}F-NaF) uptake (yellow-orange) to the site of plaque rupture with adherent thrombus on excised carotid endarterectomy tissue (E and F). Histology of the ^{18}F-NaF-positive region shows a large necrotic core (Movat's pentachrome, magnification 4×, G), within which increased staining for tissue non-specific alkaline phosphatase can be seen as a marker of calcification activity on immunohistochemistry (magnification 4×, H; magnification 10×, I).

Over 90% of our patients with myocardial infarction had increased ^{18}F-NaF uptake at the site of their culprit ruptured plaque, with TBR values that were a third higher than the maximum activity anywhere else in the coronary vasculature. These findings were not unique to the coronary circulation since we also noted increased focal ^{18}F-NaF uptake at the site of plaque rupture in all excised carotid endarterectomy specimens from patients with symptomatic carotid disease. However, we do acknowledge that this was not a universal finding. Of the three patients with myocardial infarction who had no uptake, two were younger smokers with only mild underlying irregularities on coronary angiography, implicating plaque erosion and thrombosis as the mechanism of their infarction rather than plaque rupture.[23] The third patient sustained an inferolateral non-ST segment elevation myocardial infarction and had a lesion stented in the right coronary artery. Increased ^{18}F-NaF activity was seen in the co-dominant circumflex artery that could have equally explained the clinical presentation, raising the intriguing possibility that ^{18}F-NaF might have a clinical role for patients in whom the culprit lesion is not readily apparent.

Focal regions of increased ^{18}F-NaF activity were seen in almost a half of our patients with stable coronary artery disease. To understand the mechanism of uptake in these patients, we sought to compare plaque characteristics of lesions with and without increased ^{18}F-NaF uptake. Because histology of the coronary arteries in this population is not feasible, we undertook greyscale and radiofrequency intravascular ultrasound, a widely used and validated process that provides detailed characterisation of plaque composition.[21] This method showed that lesions with increased ^{18}F-NaF uptake were associated with greater positive remodelling, more microcalcification, and a larger necrotic core. These findings were corroborated by, and consistent with, the findings of plaque analysis done with CT coronary angiography. Plasma troponin concentrations measured by a novel high-sensitivity assay were also higher in those patients with ^{18}F-NaF positive plaques than in patients with ^{18}F-NaF negative plaques, perhaps implicating subclinical plaque rupture with embolisation and microinfarction.

Why does ^{18}F-NaF bind to ruptured or high-risk plaque? Similar to the caseating granulomata of tuberculosis, atherosclerotic vascular calcification is a controlled cellular response to an intense, necrotic, and chronic inflammatory stimulus. Indeed, direct links between inflammatory cells and osteoblastic metaplasia in the vasculature are well described.[24,25] Hydroxyapatite is the central structural component of vascular calcification and is laid down during the earliest and most active stages of mineralisation:[24] hydroxyapatite nanocrystals nucleate, propagate, and mineralise the extracellular matrix. Fluoride ions are incorporated into the hydroxyapatite by ion exchange with hydroxyl groups at the crystal surface. This process is dependent on the crystal surface area that will be greatest in the earliest and most active nanocrystalline stages of mineralisation associated with plaque inflammation and necrosis. We believe that these processes are responsible for the observed ^{18}F-NaF uptake and is consistent with our data showing ^{18}F-NaF uptake in regions of necrosis, macrophage infiltration, apoptosis, microcalcification, and alkaline phosphatase and osteocalcin staining. Moreover, mathematical modelling indicates that microcalcification at the surface of thin-capped atheroma (figure 1) can intensify and double incident stresses.[26] Microcalcification is therefore not only a marker of acute plaque rupture but is implicated in its precipitation.

Coronary arterial calcification is considered pathognomonic of atherosclerosis and is a powerful independent risk predictor for cardiovascular events that can be further refined by the rapidity of its progression.[27,28] Why then not rely on CT coronary calcium scoring alone as a biomarker? Microcalcification cannot be detected on CT and confluent coronary macrocalcification develops slowly, taking many months or years to become apparent on CT, and can become dormant once inflammation in

	^{18}F-fluoride positive plaques (n=15)	^{18}F-fluoride negative plaques (n=24)	p
Lumen			
Area (mm²)	9·0 (5·7–13·5)	6·7 (4·7–9·7)	0·078
Minimal diameter (mm)	2·6 (1·7–3·1)	1·9 (1·7–2·6)	0·165
Maximum diameter (mm)	4·9 (4·1–5·3)	3·6 (3·1–4·6)	0·006
Vessel			
Area (mm²)	24·1 (17·2–27·1)	14·5 (11·9–18·1)	0·002
Minimal diameter (mm)	4·4 (3·4–5·2)	3·6 (3·0–4·1)	0·057
Maximum diameter (mm)	6·5 (6·0–7·1)	5·2 (4·7–5·9)	0·0001
Plaque			
Length (mm)	14·2 (6·2–23·5)	15·2 (6·7–25·0)	0·941
Volume (mm³)	152·9 (99·6–289·7)	91·0 (45·8–158·2)	0·032
Burden (%)*	55·6 (48·6–64·4)	54·2 (46·3–57·3)	0·174
Remodelling index	1·12 (1·09–1·19)	1·01 (0·94–1·06)	0·0004
Plaque composition			
Fibrous tissue (%)	51·0 (46·3–56·6)	58·1 (51·6–65·5)	0·015
Fibro-fatty (%)	10·9 (6·0–13·8)	12·6 (9·3–17·8)	0·092
Necrotic core (%)	24·6 (20·5–28·8)	18·0 (14·0–22·4)	0·001
Maximum frame necrotic core (%)†	35·5 (34·2–40·5)	29·2 (23·9–42·1)	0·009
Dense calcium (%)	12·6 (9·1–18·1)	10·2 (4·0–14·9)	0·092
Microcalcification, n (%)	11 (73%)	5 (21%)	0·002
Plaque classification, n (%)			
Thin-cap fibroatheroma	7 (47%)	4 (16%)	0·068
Thick-cap fibroatheroma	5 (33%)	9 (38%)	1·0
Pathological intimal thickening	0	7 (29%)	0·003
Fibrocalcific plaque	3 (20%)	4 (16%)	1·0

Data are median (IQR) unless otherwise stated. *Plaque burden calculation = (average vessel area – average lumen area) /average vessel area. †Maximum necrotic core in any single frame in the plaque.

Table 2: **Greyscale and radiofrequency intravascular ultrasound characteristics in ^{18}F-fluoride positive and negative plaques of patients with stable angina**

Panel: Research in context

Systematic review

We searched PubMed using variations of the keywords "high-risk plaques", "vulnerable plaques", "ruptured plaques", "^{18}F-fluorodeoxyglucose positron emission tomography", "^{18}F-fluoride positron emission tomography", and "coronary arteries". The search was restricted to human studies. We assessed the quality of the evidence specifically related to cardiovascular disease by reviewing the patient population studied and the methodology for the positron emission and CT imaging.

Non-invasive imaging of carotid plaque inflammation using ^{18}F-fluorodeoxyglucose positron emission tomography was reported by Rudd and colleagues in 2002.[11] Since then, this tracer has been validated and widely used as a surrogate of large vessel inflammation.[8,10] Increased ^{18}F-fluorodeoxyglucose in the coronary arteries has been described in patients with coexisting malignancy.[12,33,34] Since then, three prospective studies have examined the feasibility and reproducibility of assessing uptake of this tracer in the coronary vasculature.[6,7,13] Only two small studies (n=10–20)[6,13] have suggested that ^{18}F-fluorodeoxyglucose might identify some inflamed plaques in patients with recent myocardial infarction, although the largest study showed that in 50% of patients with acute myocardial infarction, there was no uptake of ^{18}F-fluorodeoxyglucose in the culprit plaque.[13]

Four retrospective studies in patients with cancer have recently reported cardiovascular uptake of ^{18}F-fluoride.[29,31,32,35] The aortic uptake of ^{18}F-NaF was first reported by Derlin and colleagues[29] and cardiac ^{18}F-fluoride uptake by Beheshti and colleagues.[31] We reported the coronary uptake of ^{18}F-NaF in a prospective clinical trial involving patients with aortic stenosis,[7,8] and these results were subsequently corroborated by Li and colleagues in their retrospective study of patients with cancer.[30] No study has prospectively assessed this tracer in patients with stable or unstable coronary artery disease or validated its activity against histology or invasive intracoronary imaging, such as intravascular ultrasound. There are no previous reports of ^{18}F-fluoride uptake in relation to plaque vulnerability or rupture.

Interpretation

There are currently no non-invasive imaging techniques that can identify high-risk and ruptured coronary atherosclerotic plaques in vivo in patients with coronary heart disease. For the first time, we have shown that ^{18}F-fluoride positron emission tomography can identify culprit and ruptured plaques in patients with myocardial infarction and symptomatic carotid disease. Moreover, histological characterisation demonstrates that ^{18}F-fluoride activity localises to regions of plaque rupture with evidence of increased inflammation, calcification activity, necrosis, and cell death. In patients with stable angina, ^{18}F-fluoride is associated with coronary plaques that have high-risk features on intravascular ultrasound, including positive remodelling, microcalcification, and necrosis. Given its ability to identify high-risk or ruptured coronary atherosclerotic plaque, this non-invasive imaging technique has the potential to change how we identify, manage, and treat patients with stable and unstable coronary artery disease. Further work is now needed to establish whether ^{18}F-fluoride positron emission tomography will provide a means of improving risk stratification, monitoring disease progression, guiding therapeutic interventions, and assessing novel anti-atherosclerotic therapies.

the plaque has subsided. By identifying areas of nascent and ongoing calcification activity, ^{18}F-NaF uptake allows us to detect regions of metabolically active plaque, thus providing complementary information to CT.[29–32] Indeed, we noted large areas of coronary CT calcium in the absence of increased ^{18}F-NaF uptake (figure 1) whereas other regions with minimal or no CT calcium had intense ^{18}F-NaF uptake (appendix) in keeping with previous observations in the aorta by Derlin and colleagues (panel).[29,32] Moreover, given that ^{18}F-NaF seems more closely aligned with the process of necrotic inflammation and plaque metabolic activity, we believe that it potentially offers major improvements to the prediction of cardiovascular risk compared with calcium scoring.

Our data have already established that ^{18}F-NaF identifies plaque with multiple high-risk features, but prospective studies are now needed in a broad range of patients to assess whether increased coronary ^{18}F-NaF activity will ultimately translate into future adverse events. If the results prove confirmatory then this technique has the potential to fundamentally alter the way we treat coronary artery disease: moving us away from the current framework based on lesion severity and ischaemia to one focused on plaque metabolism and inflammation. It could, for example, permit the identification of the vulnerable patient with single or multiple high-risk or silently ruptured plaques, providing an opportunity to treat and modify their risk to prevent future adverse cardiovascular events.

By contrast with ^{18}F-NaF, ^{18}F-FDG imaging was hampered by problems related to tracer uptake in the myocardium. Our stringent dietary recommendations resulted in suppression of myocardial activity in 70–85% of patients: a rate that compares favourably with previous studies (57–84%).[6,12,13] However, this suppression resulted in a patchy distribution of myocardial uptake that frequently obscured activity in one or more coronary vessels. Increased ^{18}F-FDG uptake might possibly occur in the culprit plaque and we failed to show this because of incomplete data or the delay in scanning. However, given its limitations, we believe that ^{18}F-FDG is unlikely to become sufficiently robust to permit its clinical application to the coronary circulation. Nevertheless, ^{18}F-FDG uptake remains an important measure of general vascular inflammation in the aorta and carotid arteries, providing complementary and distinct metabolic information to that of ^{18}F-NaF uptake.

We acknowledge that there are limitations of our study that include a lack of respiratory gating, potential partial volume artefacts, and the use of surrogate measures for coronary histology.[21] However, we believe that the totality of our comprehensive evidence using multiple approaches and imaging modalities provides a robust and cogent argument to support our contention that ^{18}F-fluoride uptake identifies vulnerable and high-risk plaques in patients with stable and unstable coronary heart disease. Further work is now needed to establish whether ^{18}F-NaF PET-CT will provide a clinically useful technique capable of improving risk stratification, monitoring disease progression, guiding therapeutic interventions, and assessing novel anti-atherosclerotic therapies.

Contributors

NVJ designed the study, undertook experiments, analysed results, and interpreted the data. ATV undertook experiments, analysed and interpreted the data, and prepared the report. MCW, ASVS, PAC, FHMC, SEY, AMF, EJRvB, and KAAF collected, analysed, and interpreted data, and prepared the report. ADF, NGU, MWHB, NLMC, and NLM collected the data and prepared the report. JHFR, MRD, and DEN contributed to the study design, supervision, and interpretation of data. DEN is the chief

investigator for the study and obtained funding for all studies. All authors participated in data interpretation. NVJ drafted the first and subsequent versions of this report with key input from MRD and DEN, and revisions from all authors, who reviewed and approved the final submitted report.

Conflicts of interest

NLM has received honoraria for Abbott Diagnostics and acted as a consultant for Abbott Diagnostics. The other authors declare that they have no conflicts of interest.

Acknowledgments

The study was funded by the Chief Scientist Office, Scotland (ETM/160) and the British Heart Foundation (PG/12/8/29371). MRD, NLM, and DEN are supported by the British Heart Foundation (CH/09/002, FS/10/024, FS/10/026). JHFR and PAC are part-funded by the NIHR Cambridge Biomedical Research Centre and the British Heart Foundation. The Wellcome Trust Clinical Research Facility and the Clinical Research Imaging Centre are supported by NHS Research Scotland (NRS) through NHS Lothian. We acknowledge the support of staff at the Edinburgh Heart Centre at the Royal Infirmary of Edinburgh, the radiography and radiochemistry staff of the Clinical Research Imaging Centre, and the histology staff at the Queens Medical Research Institute.

References

1 Naghavi M, Libby P, Falk E, et al. From vulnerable plaque to vulnerable patient: a call for new definitions and risk assessment strategies: part I. *Circulation* 2003; **108:** 1664–72.

2 Virmani R, Kolodgie FD, Burke AP, Farb A, Schwartz SM. Lessons from sudden coronary death: a comprehensive morphological classification scheme for atherosclerotic lesions. *Arterioscler Thromb Vasc Biol* 2000; **20:** 1262–75.

3 Virmani R, Burke AP, Farb A, Kolodgie FD. Pathology of the vulnerable plaque. *J Am Coll Cardiol* 2006; **47** (suppl)**:** C13–18.

4 Rogers IS, Tawakol A. Imaging of coronary inflammation with FDG-PET: feasibility and clinical hurdles. *Curr Cardiol Rep* 2011; **13:** 138–44.

5 Libby P, DiCarli M, Weissleder R. The vascular biology of atherosclerosis and imaging targets. *J Nucl Med* 2010; **51** (suppl 1)**:** 33S–37S.

6 Rogers IS, Nasir K, Figueroa AL, et al. Feasibility of FDG imaging of the coronary arteries: comparison between acute coronary syndrome and stable angina. *JACC Cardiovasc Imaging* 2010; **3:** 388–97.

7 Dweck MR, Chow MW, Joshi NV, et al. Coronary arterial 18F-sodium fluoride uptake: a novel marker of plaque biology. *J Am Coll Cardiol* 2012; **59:** 1539–48.

8 Dweck MR, Khaw HJ, Sng GK, et al. Aortic stenosis, atherosclerosis, and skeletal bone: is there a common link with calcification and inflammation? *Eur Heart J* 2013; **34:** 1567–74.

9 Dweck MR, Jones C, Joshi NV, et al. Assessment of valvular calcification and inflammation by positron emission tomography in patients with aortic stenosis. *Circulation* 2012; **125:** 76–86.

10 Tawakol A, Migrino RQ, Bashian GG, et al. In vivo 18F-fluorodeoxyglucose positron emission tomography imaging provides a noninvasive measure of carotid plaque inflammation in patients. *J Am Coll Cardiol* 2006; **48:** 1818–24.

11 Rudd JH, Warburton EA, Fryer TD, et al. Imaging atherosclerotic plaque inflammation with [18F]-fluorodeoxyglucose positron emission tomography. *Circulation* 2002; **105:** 2708–11.

12 Wykrzykowska J, Lehman S, Williams G, et al. Imaging of inflamed and vulnerable plaque in coronary arteries with 18F-FDG PET/CT in patients with suppression of myocardial uptake using a low-carbohydrate, high-fat preparation. *J Nucl Med* 2009; **50:** 563–68.

13 Cheng VY, Slomka PJ, Le Meunier L, et al. Coronary arterial ^{18}F-FDG uptake by fusion of PET and coronary CT angiography at sites of percutaneous stenting for acute myocardial infarction and stable coronary artery disease. *J Nucl Med* 2012; **53:** 575–83.

14 Thygesen K, Alpert JS, Jaffe AS, Simoons ML, Chaitman BR, White HD, and the Joint ESC/ACCF/AHA/WHF Task Force for the Universal Definition of Myocardial. Third universal definition of myocardial infarction. *Eur Heart J* 2012; **33:** 2551–67.

15 North American Symptomatic Carotid Endarterectomy Trial Collaborators. Beneficial effect of carotid endarterectomy in symptomatic patients with high-grade carotid stenosis. *N Engl J Med* 1991; **325:** 445–53.

16 Calvert PA, Obaid DR, O'Sullivan M, et al. Association between IVUS findings and adverse outcomes in patients with coronary artery disease: the VIVA (VH-IVUS in Vulnerable Atherosclerosis) Study. *JACC Cardiovasc Imaging* 2011; **4:** 894–901.

17 Murray SW, Stables RH, Hart G, Palmer ND. Defining the magnitude of measurement variability in the virtual histology analysis of acute coronary syndrome plaques. *Eur Heart J Cardiovasc Imaging* 2013; **14:** 167–74.

18 Stone GW, Maehara A, Lansky AJ, et al, and the PROSPECT Investigators. A prospective natural-history study of coronary atherosclerosis. *N Engl J Med* 2011; **364:** 226–35.

19 Ehara S, Kobayashi Y, Yoshiyama M, et al. Spotty calcification typifies the culprit plaque in patients with acute myocardial infarction: an intravascular ultrasound study. *Circulation* 2004; **110:** 3424–29.

20 Mintz GS, Nissen SE, Anderson WD, et al. American College of Cardiology clinical expert consensus document on standards for acquisition, measurement and reporting of intravascular ultrasound studies (IVUS). A report of the American College of Cardiology task force on clinical expert consensus documents. *J Am Coll Cardiol* 2001; **37:** 1478–92.

21 García-García HM, Mintz GS, Lerman A, et al. Tissue characterisation using intravascular radiofrequency data analysis: recommendations for acquisition, analysis, interpretation and reporting. *EuroIntervention* 2009; **5:** 177–89.

22 Motoyama S, Sarai M, Harigaya H, et al. Computed tomographic angiography characteristics of atherosclerotic plaques subsequently resulting in acute coronary syndrome. *J Am Coll Cardiol* 2009; **54:** 49–57.

23 Burke AP, Farb A, Malcom GT, Liang YH, Smialek J, Virmani R. Coronary risk factors and plaque morphology in men with coronary disease who died suddenly. *N Engl J Med* 1997; **336:** 1276–82.

24 Aikawa E, Nahrendorf M, Figueiredo JL, et al. Osteogenesis associates with inflammation in early-stage atherosclerosis evaluated by molecular imaging in vivo. *Circulation* 2007; **116:** 2841–50.

25 New SE, Goettsch C, Aikawa M, et al. Macrophage-derived matrix vesicles: an alternative novel mechanism for microcalcification in atherosclerotic plaques. *Circ Res* 2013; **113:** 72–77.

26 Vengrenyuk Y, Carlier S, Xanthos S, et al. A hypothesis for vulnerable plaque rupture due to stress-induced debonding around cellular microcalcifications in thin fibrous caps. *Proc Natl Acad Sci USA* 2006; **103:** 14678–83.

27 Raggi P, Callister TQ, Shaw LJ. Progression of coronary artery calcium and risk of first myocardial infarction in patients receiving cholesterol-lowering therapy. *Arterioscler Thromb Vasc Biol* 2004; **24:** 1272–77.

28 McEvoy JW, Blaha MJ, Defilippis AP, et al. Coronary artery calcium progression: an important clinical measurement? A review of published reports. *J Am Coll Cardiol* 2010; **56:** 1613–22.

29 Derlin T, Richter U, Bannas P, et al. Feasibility of 18F-sodium fluoride PET/CT for imaging of atherosclerotic plaque. *J Nucl Med* 2010; **51:** 862–65.

30 Li Y, Berenji GR, Shaba WF, Tafti B, Yevdayev E, Dadparvar S. Association of vascular fluoride uptake with vascular calcification and coronary artery disease. *Nucl Med Commun* 2012; **33:** 14–20.

31 Beheshti M, Saboury B, Mehta NN, et al. Detection and global quantification of cardiovascular molecular calcification by fluoro18-fluoride positron emission tomography/computed tomography—a novel concept. *Hell J Nucl Med* 2011; **14:** 114–20.

32 Derlin T, Tóth Z, Papp L, et al. Correlation of inflammation assessed by ^{18}F-FDG PET, active mineral deposition assessed by ^{18}F-fluoride PET, and vascular calcification in atherosclerotic plaque: a dual-tracer PET/CT study. *J Nucl Med* 2011; **52:** 1020–27.

33 Saam T, Rominger A, Wolpers S, et al. Association of inflammation of the left anterior descending coronary artery with cardiovascular risk factors, plaque burden and pericardial fat volume: a PET/CT study. *Eur J Nucl Med Mol Imaging* 2010; **37:** 1203–12.

34 Dunphy MP, Freiman A, Larson SM, Strauss HW. Association of vascular 18F-FDG uptake with vascular calcification. *J Nucl Med* 2005; **46:** 1278–84.

35 Janssen T, Bannas P, Herrmann J, et al. Association of linear (18) F-sodium fluoride accumulation in femoral arteries as a measure of diffuse calcification with cardiovascular risk factors: A PET/CT study. *J Nucl Cardiol* 2013; **20:** 569–77.

nature COMMUNICATIONS

ARTICLE

Received 15 Sep 2014 | Accepted 14 May 2015 | Published 7 Jul 2015

DOI: 10.1038/ncomms8495 OPEN

Identifying active vascular microcalcification by ^{18}F-sodium fluoride positron emission tomography

Agnese Irkle[1], Alex T. Vesey[2], David Y. Lewis[3], Jeremy N. Skepper[4], Joseph L.E. Bird[1], Marc R. Dweck[2], Francis R. Joshi[5], Ferdia A. Gallagher[3,6], Elizabeth A. Warburton[7], Martin R. Bennett[5], Kevin M. Brindle[3], David E. Newby[2], James H. Rudd[5] & Anthony P. Davenport[1]

Vascular calcification is a complex biological process that is a hallmark of atherosclerosis. While macrocalcification confers plaque stability, microcalcification is a key feature of high-risk atheroma and is associated with increased morbidity and mortality. Positron emission tomography and X-ray computed tomography (PET/CT) imaging of atherosclerosis using ^{18}F-sodium fluoride (^{18}F-NaF) has the potential to identify pathologically high-risk nascent microcalcification. However, the precise molecular mechanism of ^{18}F-NaF vascular uptake is still unknown. Here we use electron microscopy, autoradiography, histology and preclinical and clinical PET/CT to analyse ^{18}F-NaF binding. We show that ^{18}F-NaF adsorbs to calcified deposits within plaque with high affinity and is selective and specific. ^{18}F-NaF PET/CT imaging can distinguish between areas of macro- and microcalcification. This is the only currently available clinical imaging platform that can non-invasively detect microcalcification in active unstable atherosclerosis. The use of ^{18}F-NaF may foster new approaches to developing treatments for vascular calcification.

[1] Division of Experimental Medicine & Immunotherapeutics (EMIT), Department of Medicine, University of Cambridge, Cambridge, CB2 0QQ, UK. [2] Centre for Cardiovascular Science, University of Edinburgh, Edinburgh, EH16 4TJ, UK. [3] Cancer Research UK Cambridge Institute, University of Cambridge, Li Ka Shing Centre, Cambridge, CB2 0RE, UK. [4] Department of Physiology, Development and Neuroscience, Multi-Imaging Centre, University of Cambridge, Cambridge, CB2 3EG, UK. [5] Division of Cardiovascular Medicine, University of Cambridge, Cambridge, CB2 0QQ, UK. [6] Department of Radiology, Box 218 Level 5, University of Cambridge, Cambridge, CB2 0QQ, UK. [7] Department of Clinical Neurosciences, University of Cambridge, Cambridge, CB2 0QQ, UK. Correspondence and requests for materials should be addressed to A.P.D. (email: apd10@medschl.cam.ac.uk).

Vascular calcification is a complex pathological process pathognomonic of atherosclerosis[1–4]. Currently, the extent of macroscopic calcification can be determined by X-ray computed tomography (CT) imaging and this can be used clinically to predict cardiovascular morbidity and mortality[5–7].

Vessel mineralization is first marked by the appearance of calcified micro nodules which grow and coalesce into much larger macroscopic deposits[8]. The genesis of these micro nodules is principally mediated by a coordinated cellular pathway that shares similarities to active skeletal osteogenesis but may also involve a more passive process where a combination of high local concentrations of phosphates and phosphatidylserines from necrotic cells and an absence of calcification inhibitors results in the precipitation of calcium phosphate particles. It is likely that much of the mineral present is made up of hydroxyapatite, a crystalline form of calcium orthophosphate[9,10]. Although there is no universal size convention, emerging consensus categorizes micro- and macrocalcification based on nodules of <50 and $\geq 50\,\mu m$, respectively[11]. This distinction is important because although macrocalcification imparts plaque stability, microcalcification heralds the onset of vessel mineralization triggered by cell death and inflammation[8,12] and may itself be implicated in the aetiology of plaque rupture and major adverse cardiovascular events[13,14]. Detection of microcalcification is not possible with clinical CT systems that can only identify large areas of macrocalcification—$\sim$200–500 μm in diameter[10,15–17]. Furthermore, the rapid progression of existing vascular calcium is driven by on-going microcalcification, carries a poor prognosis and is not amenable to current medical therapies. As a consequence, the development of techniques to identify microcalcification is a major research goal with the potential for improving patient risk stratification and outcomes.

Positron emission tomography (PET)/CT imaging of atherosclerosis using ^{18}F-sodium fluoride (^{18}F-NaF) has recently been reported and, for the first time, has the potential to non-invasively identify high-risk microcalcification[18–21]. In patients with stable coronary artery disease, ^{18}F-NaF uptake correlates with CT coronary calcium scores although nearly half of the patients with very high scores have no ^{18}F-NaF uptake and increased ^{18}F-NaF uptake is often seen in the absence of calcification on CT. ^{18}F-NaF would therefore appear to provide distinct information to CT with potentially important clinical implications[20]. Recently, we have shown that ^{18}F-NaF uptake identifies culprit ruptured coronary plaques after myocardial infarction and, in carotid plaque, correlates with markers of active calcification and cell death[21]. Moreover, ^{18}F-NaF appears to identify high-risk coronary lesions in stable patients indicating that it may have a role in identifying vulnerable plaques at risk of rupture and in predicting myocardial infarction. In bone imaging, ^{18}F-NaF uptake involves the exchange of fluoride ions with hydroxyl groups in hydroxyapatite[22,23]; however, the mechanism underlying ^{18}F-NaF uptake in the vasculature has not been established. This is a major limitation that must be addressed before the nascent field of vascular ^{18}F-NaF PET imaging can progress.

The goal of the study was to characterize the selectivity, specificity and pharmacodynamics of ^{18}F-NaF uptake in vascular tissue in the human carotid atherosclerotic plaque. First, we performed electron probe X-ray microanalysis to measure ^{18}F-NaF presence directly in the areas of calcification identified by electron microscopy. Second, we studied the pharmacodynamic properties of ^{18}F-NaF adsorption to vascular calcification to characterize its potential as a clinical imaging agent. We correlated the extent of ^{18}F-NaF adsorption to vascular calcification and to cell-specific markers of atherosclerosis to exclude the possibility of ^{18}F-NaF binding to markers of inflammation, neovascularization and smooth muscle cells as opposed to solely calcified deposits. We next compared the ability of ^{18}F-NaF to penetrate carotid micro- and macrocalcifications using high-resolution phosphor-imaging autoradiography and light microscopy to understand ^{18}F-NaF-binding properties to these different forms of vascular calcifications. Finally, we compared clinical ^{18}F-NaF PET/CT images with μPET/μCT images of excised carotid endarterectomy specimens to develop a translational model of ^{18}F-NaF vascular uptake from bedside to bench and back and understand ^{18}F-NaF adsorption to vascular calcification on all three levels studied.

We propose a comprehensive translational model of ^{18}F-NaF pharmacological characteristics to vascular calcification in preclinical and clinical imaging systems. We conclude that ^{18}F-NaF PET/CT is the only currently available non-invasive clinical imaging platform that can detect microcalcification in active unstable human atherosclerosis.

Results

Electron microscopy analysis. We used an electron microprobe to measure directly the presence of non-radioactive fluoride within calcified and soft tissue areas of carotid endarterectomy specimens. We also used hydroxyapatite standards to confirm co-localization (see Supplementary Table 1). When tissues were preincubated with NaF, an energy-dispersive X-ray spectroscopic peak for fluoride was detectable and co-localized with regions of calcification (Fig. 1a). Microcalcifications showed greater levels of fluoride than macrocalcifications (F/Ca ratio: 0.59 ± 0.23 ($n = 10$, individual plaques) versus 0.37 ± 0.15 ($n = 7$, individual plaques), respectively, $P < 0.02$, ANOVA (analysis of variance) and Tukey Kramer *post hoc* test, Fig. 1b) and no tissue fluoride was observed in the absence of calcification (Fig. 1c). Thus, at the resolution of electron microscopy, fluoride co-localized to arterial calcification, with increased levels in the regions of microcalcification.

Pharmacodynamic and pharmacokinetic analyses. To confirm the specificity in pharmacological assays, we incubated carotid sections with a clinically relevant concentration (1×10^{-11} M) of ^{18}F-NaF for 1 h (ref. 21). As a control for nonspecific binding, adjacent sections were incubated at the same concentration of ^{18}F-NaF, but with an excess (4×10^{-4} M) of non-radioactive NaF. Phosphor-imaging autoradiography revealed a strong ^{18}F-NaF signal with negligible nonspecific binding and no ^{18}F-NaF binding in areas without calcification (Supplementary Fig. 1). Concentration–response curves were constructed by exposing carotid sections ($n = 5$) to increasing concentrations of ^{18}F-NaF (10^{-12}–10^{-7} M) for 1 h (refs 20,23). There was a positive linear correlation between the radioactivity and concentration of ^{18}F-NaF (Fig. 1d). We then performed association and dissociation binding experiments at a clinically relevant concentration (1×10^{-11} M; $n = 5$). There was a rapid and time-dependent exponential association and, following washing, a slow exponential dissociation from the plaque (Fig. 1e). The data were fitted to a one-site model, with an association rate constant (k_1) of $4.5 \pm 0.6 \times 10^9\,M^{-1}\,min^{-1}$ and a half-time for association of 14.3 ± 1.9 min. Dissociation was slow but detectable with a dissociation rate constant of $0.0027 \pm 0.0005\,min^{-1}$, a half-time for dissociation of 254 ± 43 min and an affinity constant (K_D) calculated from these kinetic data of 0.6 pM. The affinity constant is a measure of the strength of binding of ^{18}F-NaF to areas of calcification. The very high affinity is consistent with the comparatively low concentrations of radiolabelled ^{18}F-NaF required *in vitro* and *in vivo* to detect calcifications in tissues and demonstrates the sensitivity of the tracer.

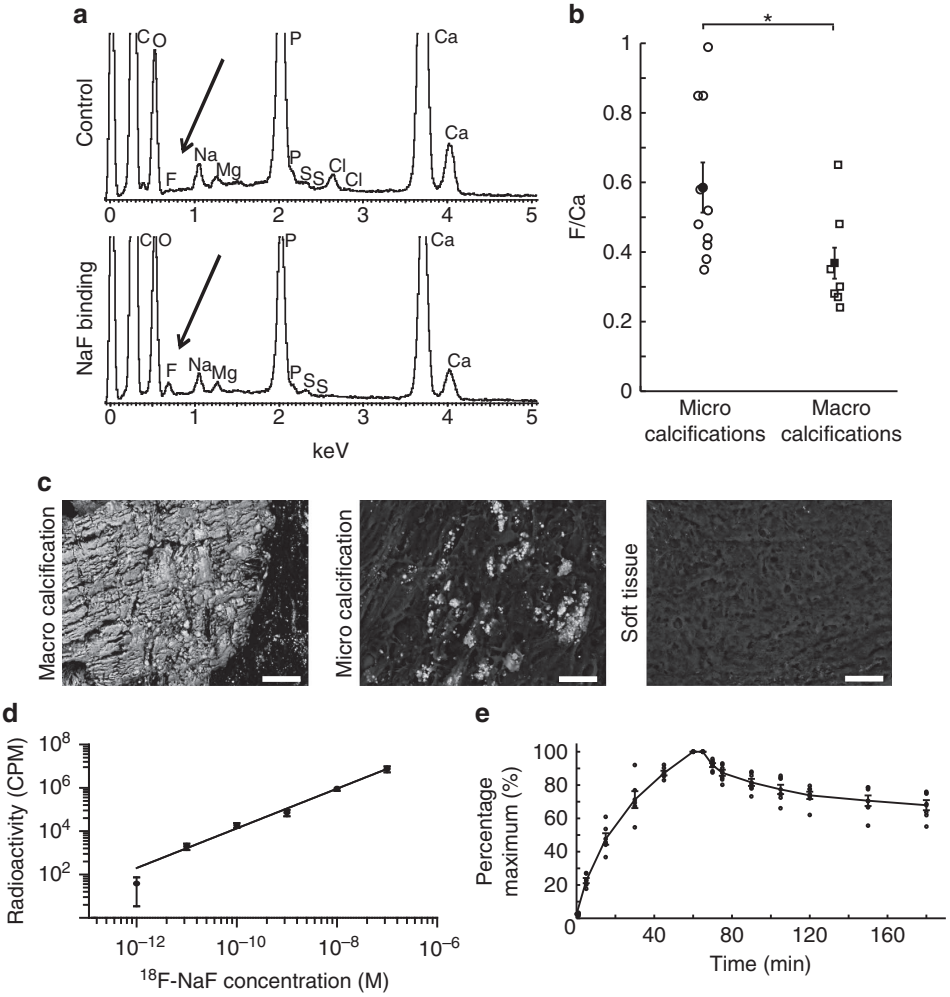

Figure 1 | F directly co-localizes with Ca in a concentration-dependent manner. (**a**) Fluoride peak is detected only in the calcified regions of those carotids that have been exposed to NaF. (**b**) The amount of fluoride adsorbed to microcalcifications (identified visually based on the size of nodules of <50 and manual measurements made) is significantly higher than macrocalcifications ($\geq 50\,\mu m$ to several mm; F/Ca in microcalcifications 0.59 ± 0.23, $n=10$ (circles); in macrocalcifications 0.37 ± 0.15, $n=7$ (squares)); $P<0.02$ using an ANOVA and Tukey Kramer *post hoc* test. (**c**) Representative images of macro- and microcalcifications and the soft tissue. F presence was detected only in the calcified regions. Scale bar, 50 µm. (**d**) ^{18}F-NaF binding to cryostat sections is linear over the clinically relevant concentration range from 1.0×10^{-12} to 1.0×10^{-7} ($y = 10^{(0.92*\log(x)+13)}$, $n=5$). (**e**) There is a fast exponential association and slow exponential dissociation of ^{18}F-NaF to the whole carotids over time. In all figures filled shapes show mean, error bars denote s.e.m.

We undertook dynamic PET analysis to explore the *in vivo* pharmacodynamic and pharmacokinetic properties of ^{18}F-NaF in five patients scheduled to undergo carotid endarterectomy for symptomatic disease (patient demographics both for dynamic scans and static scans described later are given in Supplementary Table 2. The SUV and TBR values of static and dynamic scans in table format are given in Supplementary Table 3 and in graphical format in Supplementary Fig. 2). There was clear carotid plaque uptake and Patlak analysis showed a good model fit with ^{18}F-NaF influx varying from 0.0005 to 0.007 ml cm^{-3} min^{-1} as compared with 0.05 to 0.08 ml cm^{-3} min^{-1} in the vertebral bodies (Supplementary Table 4 and Supplementary Fig. 3). No deviation of the data from the model was observed during the time course of these experiments although patients could only tolerate scanning for 75 min following tracer injection. Although very slow dissociation can be detected *in vitro*, this was too slow to detect during our imaging window *in vivo* and therefore is unlikely to be an important factor to take into account in clinical imaging. ^{18}F-NaF was rapidly eliminated from the plasma and showed a typical biexponential decay in keeping with immediate redistribution and then subsequent renal elimination (Supplementary Fig. 4). At 60 min from injection, plasma activity was 4–8% of its peak activity and excellent contrast between vascular tissue and blood pool was observed.

These complementary *ex vivo* and *in vivo* data demonstrate the favourable imaging properties of ^{18}F-NaF: an absence of metabolites, rapid ligand-binding site association with minimal dissociation and a rapid reduction in radiotracer background giving excellent tissue contrast resolution 1 h following its administration.

Immunohistochemical analysis. Vascular calcification is believed to occur in response to hypoxia, necrosis and chronic inflammation and has been linked with macrophage burden and neovascularization[3]. To test the cellular specificity of ^{18}F-NaF binding, we stained sequential sections with Alizarin Red (calcification marker) and antibodies for CD68 (macrophage marker), CD31 (endothelial cell marker of neovascularization) and smooth muscle actin (smooth muscle marker; $n=8$

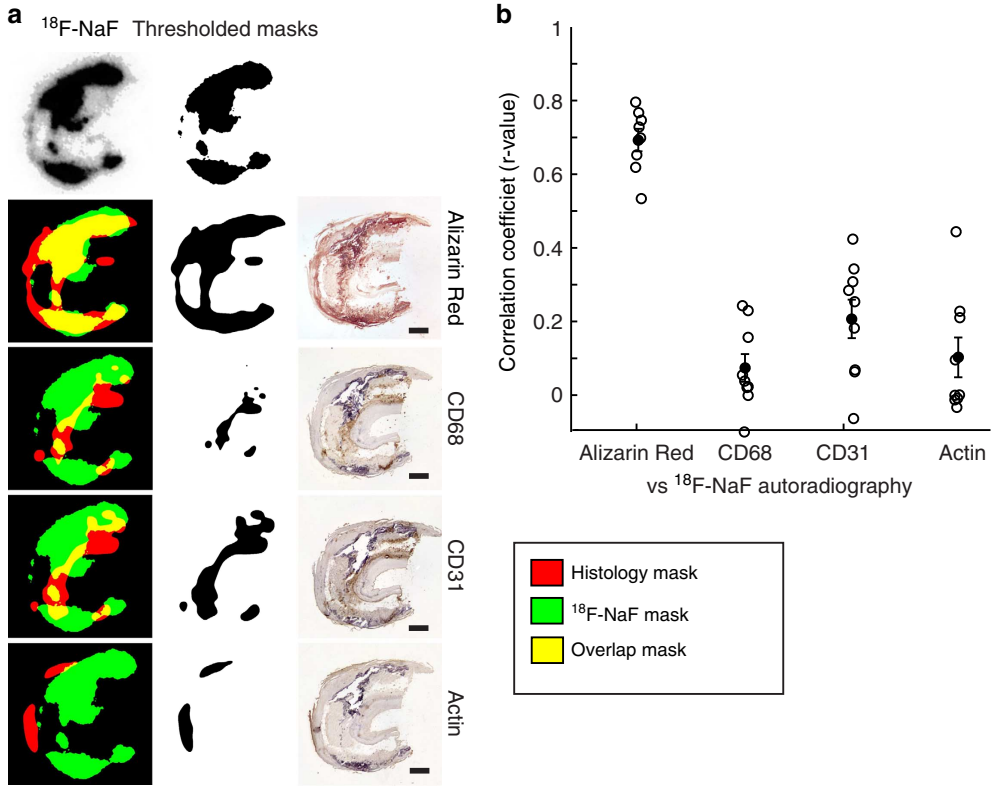

Figure 2 | ^{18}F-NaF uptake correlates with calcification but none of the histological inflammatory markers. (**a**) Representative images of ^{18}F-NaF autoradiography signal overlap with IHC-stained sequential sections. Green: ^{18}F-NaF signal, red: histology signal, yellow: overlap. Scale bar, 1 mm. (**b**) High correlation is observed between ^{18}F-NaF and Alizarin Red calcification staining, while low correlation is seen between ^{18}F-NaF autoradiography and inflammatory marker IHC signals.

individual plaques for each stain). We then filtered and applied an auto-threshold to both the ^{18}F-NaF radioactivity signal and each of the histological stains, and overlaid them to correlate the two signals (Fig. 2a). The only high correlation detected was between the ^{18}F-NaF signal and Alizarin Red calcification stain ($r = 0.69 \pm 0.03$, $n = 8$) indicating that ^{18}F-NaF specifically co-localizes to vascular calcification and not other upstream triggers to the calcific response (Fig. 2b).

Penetration by autoradiography/histology and μPET/μCT. We next compared areas of ^{18}F-NaF uptake with tissue micro- and macrocalcification. We first sectioned carotid plaques to remove barriers to penetration and incubated with 1×10^{-11} M ^{18}F-NaF for 1 h, followed by exposure to a phosphor-imaging screen. ^{18}F-NaF uptake correlated with calcification staining (Fig. 3a, macrocalcifications: closed arrowheads, microcalcifications: open arrowheads) and was observed across all regions of the calcific deposits (Fig. 3b). In contrast, if carotids were first incubated with ^{18}F-NaF and then sectioned, ^{18}F-NaF binding was only detected on the outer surface layer of macrocalcific deposits with the ligand unable to penetrate deeper (Fig. 3c,d, and Supplementary Fig. 5 for additional examples). Irrespective of presectioning of tissue, ^{18}F-NaF appeared to bind freely to regions of microcalcification and co-localized with histological staining for calcification (Fig. 3a–d). Using μPET/μCT, we saw similar results with ^{18}F-NaF binding only to the surface of macrocalcific deposits (Fig. 3e,f), matching the limits of penetration demonstrated with autoradiography.

One of the main aims of this work was to explain the previously observed differences between the PET and CT signals in the clinical setting. We chose to investigate this using preclinical μPET/μCT because of the higher spatial resolution that it offers (μPET, 900 μm; μCT, 30 μm). We hypothesized that the use of higher-resolution μPET/μCT would allow detection of microcalcifications. While microcalcifications identified on histology (Fig. 3g) were not detectable by μCT (Fig. 3i), they were identified by an increased ^{18}F-NaF μPET signal (Fig. 3j) that closely matched phosphor-imaging autoradiography (Fig. 3h). Finally, we further investigated ^{18}F-NaF penetration by examining the intensity and density of the μPET and μCT signals (where calcification was defined as ≥1,000 Hounsfield units (HU)) along 5–8-mm linear transects of atherosclerotic tissue (Fig. 3k–o). Once again there were clear differences in the signal produced by these two imaging techniques with increased ^{18}F-NaF activity on the surface of macroscopic calcium deposits that by contrast was not observed within their core.

Comparing clinical *in vivo* PET/CT and *ex vivo* μPET/μCT. We applied a novel approach to compare the *in vivo* and *ex vivo* imaging of carotid atherosclerotic plaque using co-registered clinical PET with CT, μPET with μCT and autoradiography with histology. In particular, we focused on the mismatch between the ^{18}F-NaF PET signal and CT identifiable calcification (Fig. 4).

We recruited four patients who were scanned with ^{18}F-NaF PET/CT before carotid endarterectomy (Fig. 4a). After surgery, we incubated the endarterectomy specimens with ^{18}F-NaF and imaged them with the μPET/μCT scanner (Fig. 4h). Finally, we again incubated the carotid endarterectomy specimens with ^{18}F-NaF and cryosectioned them to obtain autoradiography images and light microscope histology to detect areas of calcium (Fig. 4n). On the clinical PET/CT and μPET/μCT scans, we

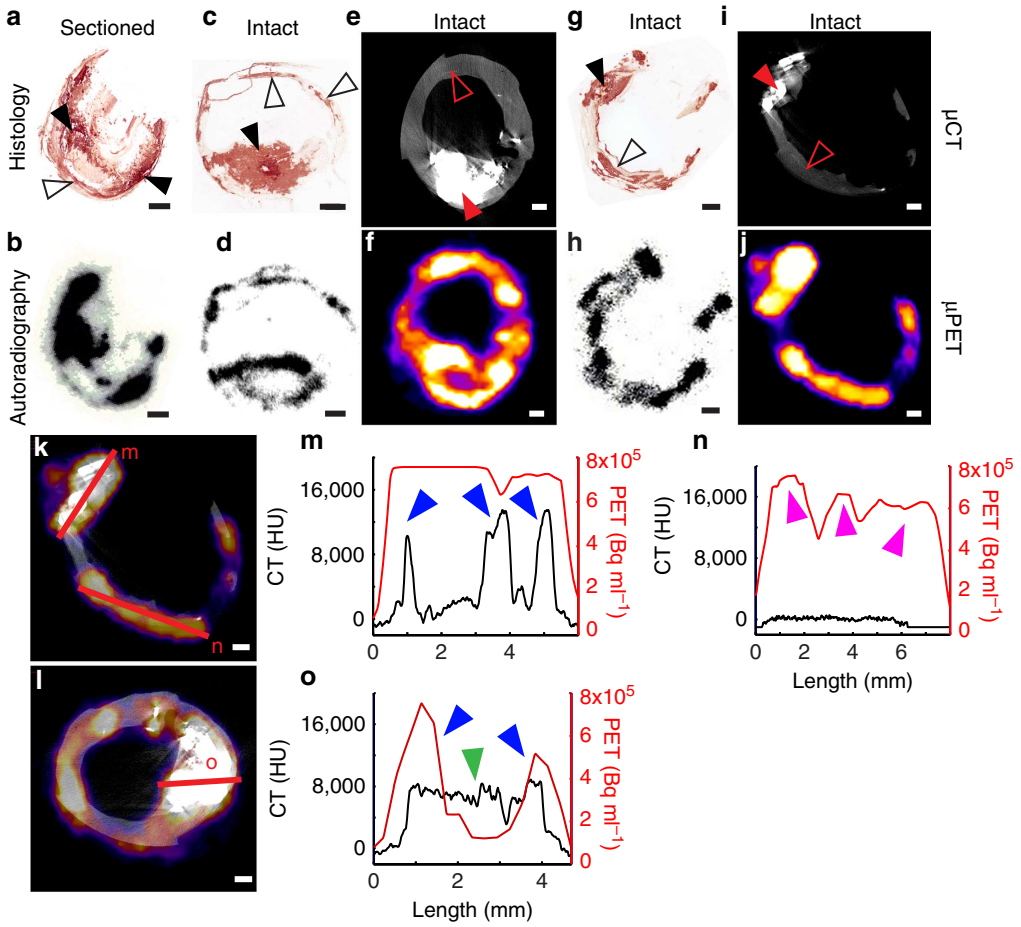

Figure 3 | ^{18}F-NaF signal detection depends on the sensitivity of the detection modality. (**a**,**b**) If the carotid is sectioned first and incubated in ^{18}F-NaF second, binding occurs to all macro- (closed arrowheads) and microcalcification (open arrowheads) surfaces. (**c**,**d**) However, if the carotid is incubated in ^{18}F-NaF first and then sectioned, ^{18}F-NaF is able to bind only to the surface level of macrocalcifications (closed arrowheads), while binding occurs to all microcalcifications (open arrowheads). (**e**,**f**) ^{18}F-NaF binding solely to the surface level of macrocalcifications can also be observed in a μPET/μCT scan, if the macrocalcification size is larger than μPET resolution. (**g**,**i**) Microcalcifications that are detected with Alizarin Red histology cannot be seen in a μCT scan, due to insufficient sensitivity. (**h**,**j**) Yet, ^{18}F-NaF μPET scan closely matches autoradiography signal and can detect microcalcifications. (**k**,**l**) μPET/μCT signal quantification by measuring the intensity of the ^{18}F-NaF μPET signal and the μCT density measure along the same transects. (**m**) ^{18}F-NaF binding can be observed throughout the three macrocalcification peaks due to macrocalcification size being smaller than μPET resolution (PET +/CT +, blue arrowheads); (**n**) Microcalcifications detected with ^{18}F-NaF μPET and autoradiography (see **h**) as well as Alizarin Red histology (see **g**) but not μCT (PET +/CT −, magenta arrowheads); (**o**) If macrocalcifications are larger than μPET resolution, ^{18}F-NaF binding solely around the surface level of macrocalcifications can be observed, similarly as in autoradiography (center green arrowhead PET −/CT +, blue arrowheads PET +/CT +). Scale bar, 1 mm.

confirmed differences in the distribution of calcium on CT and ^{18}F-NaF uptake on PET (Fig. 4c–g, for Fig. 4e–g corresponding three-dimensional (3D) Supplementary Movies 1–3). Regions of ^{18}F-NaF uptake were most commonly observed in the absence of calcium on CT, representing areas of microcalcification (PET + / CT −; Fig. 4b,i). In addition, there were also large CT-detected areas of macrocalcification that did not demonstrate concomitant ^{18}F-NaF uptake (PET − /CT +; Fig. 4b,g (for Fig. 4g, corresponding 3D Supplementary Movie 3)). These are likely to represent regions where nascent microcalcification is mild or absent.

The findings on μPET/μCT were similar to the clinical scans. Indeed the distribution of calcium detected with μCT closely matched that observed on the clinical CT although additional smaller areas of macrocalcification were also identified and resolved (Fig. 4j–m, corresponding 3D Supplementary Movies 4–7). The distribution of the ^{18}F-NaF signal was also similar although again it was more refined on the μPET compared with the clinical PET systems (Fig. 4j–l, corresponding 3D Supplementary Movies 4–6). Finally, histology and ^{18}F-NaF autoradiography provided the most sensitive method for the detection of tissue calcification (Fig. 4o–u). Histological staining with Alizarin Red confirmed that both μCT and clinical CT only detect regions of macrocalcification with extensive regions of microcalcification left unresolved by these techniques (Fig. 4p–u). By contrast, the ^{18}F-NaF signal detected by autoradiography was observed in a very similar distribution to that observed by the μPET (albeit providing better spatial resolution), with both able to resolve regions of microcalcification (Fig. 4r–u). For the number of patients used in the individual experiments, see Supplementary Table 5.

Discussion

For the first time, we demonstrate the specificity and sensitivity of ^{18}F-NaF adsorption to calcium deposits in human atherosclerotic vascular tissue and demonstrate that it can non-invasively detect areas of microcalcification indicative of nascent calcification and

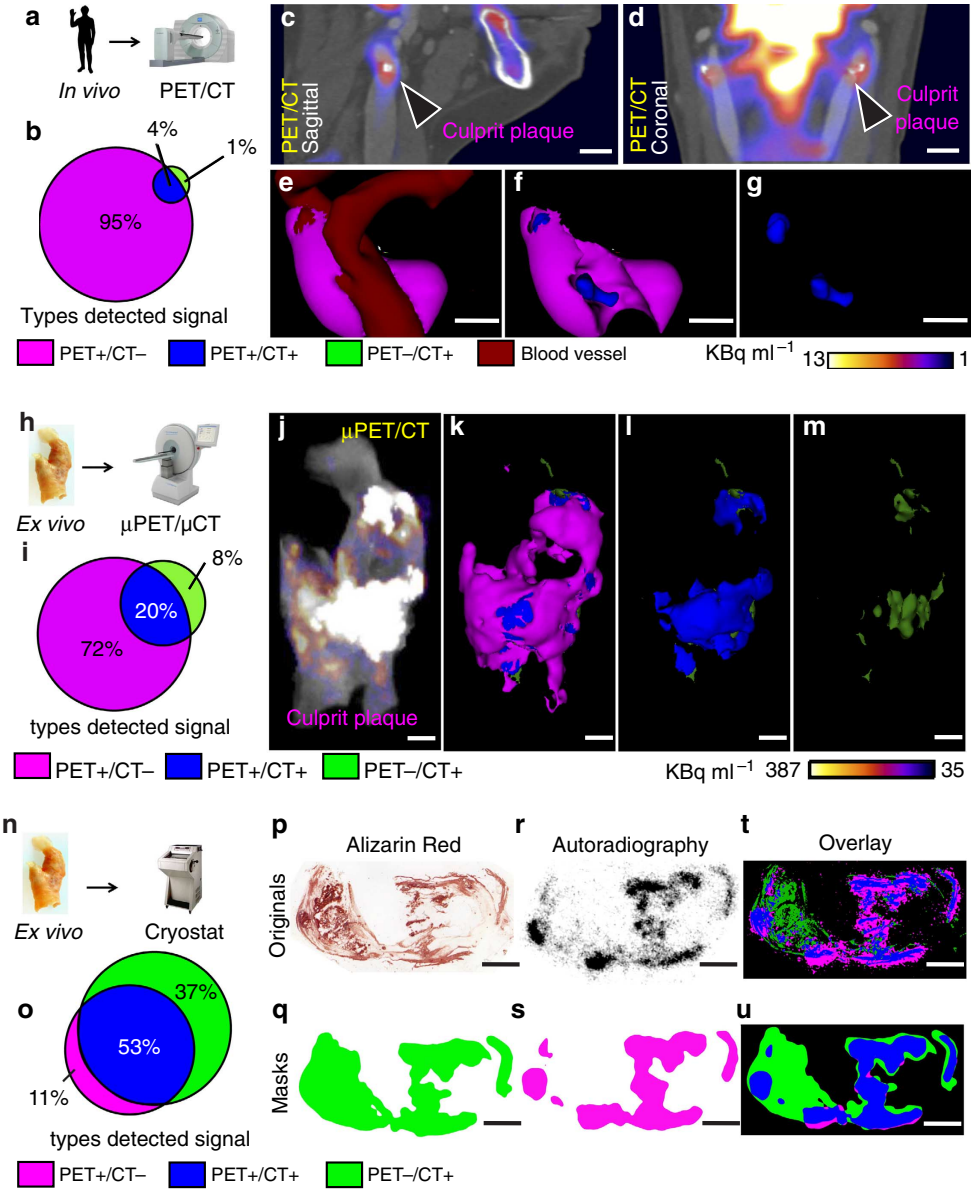

Figure 4 | High-resolution imaging reveals specificity of ^{18}F-NaF binding to vascular calcification. (**a**) Four symptomatic patients underwent clinical PET/CT imaging after injection of ^{18}F-NaF and before carotid endarterectomy. (**b**) Comparison of PET and CT signals. Although clinical PET spatial resolution is much less than CT, PET detects larger area than CT, demonstrating higher sensitivity. PET +/CT −: magenta, 95%, PET +/CT +: blue, 4%, PET −/CT +: green, 1%. (**c**,**d**) Clinical PET/CT scan with the culprit atheroma (arrowheads). Scale bar, 11 mm (**c**) Sagittal view; (**d**) Coronal view. (**e**–**g**) Analysis of the carotid *in vivo*, where PET signal (magenta) was detected using observer-independent Otsu histogram-based thresholding. PET signal is co-localized with CT vascular calcification (blue). CT-detected soft tissue is dark red. Scale bar, 7 mm. (**h**) After endarterectomy, carotids were recovered, incubated in ^{18}F-NaF and scanned in a μPET/μCT scanner. (**i**) Ratio of PET +/CT − area and CT + signals is smaller than in **b**, due to the higher μPET resolution, which results in more precise signal detection. PET +/CT −: magenta, 72%, PET +/CT +: blue, 20%, PET −/CT +: green, 8%. (**j**–**m**) *Ex vivo* images of the carotid from the same patient as in **c**–**g**. (**j**) μPET/μCT image without thresholding; (**k**–**m**) 3D thresholded μPET/μCT images. μPET signal (magenta), PET +/CT + (blue), PET −/CT + (green). (**n**) After μPET/μCT scan, carotids were incubated in ^{18}F-NaF and sectioned on cryostat. (**o**) Ratio between PET +/CT − and CT + regions indicates an even higher PET +/CT − resolution. PET +/CT −: magenta, 11%, PET +/CT +: blue, 53%, PET −/CT +: green, 37%. (**p**) Carotid from the same patient as in **c**–**g**, **j**–**m**. Alizarin Red detects both macro- and microcalcifications with the highest precision of all methods described here. (**q**) Alizarin Red image after Gaussian filter and Li thresholding, to match resolution to autoradiography image. (**r**) Autoradiography shows highly specific binding to all microcalcifications, but is not able to penetrate the deeper levels of macrocalcifications. (**s**) Autoradiography image after Gaussian filter and Li thresholding, to match resolution to the filtered Alizarin Red image. (**t**) Overlay of unfiltered histology and autoradiography images showing a high PET +/CT − signal, due to mismatch in resolution. (**u**) Overlay of filtered histology and autoradiography images shows matching signal resolution. Scale bar = 3 mm. 3D movies in Supplementary Data.

active unstable atherosclerosis. This unique and characteristic signal has implications and ramifications for the non-invasive clinical imaging of human atherosclerosis—a condition that represents the leading cause of death worldwide.

In bone, the binding of fluoride to areas of calcification is mediated through a chemical reaction with hydroxyapatite, a crystalline structure that is also the main component of vascular mineralization[22]. Using electron microprobe analysis, we have

shown for the first time that fluoride also closely co-localizes to pathological mineralization within vascular tissue. The precise target for NaF binding in living vasculature has been uncertain, as fluoride ions were not expected to have the selectivity as seen between ligands and their cognate receptors, and NaF could target molecules other than hydroxyapatite. Here we demonstrate that ^{18}F-NaF co-localizes to areas of nascent calcification and potentially provides a novel non-invasive biomarker of this high-risk pathology. Moreover, we observed that there is preferential adsorbing of fluoride to microcalcification, a clinically more significant manifestation of vascular mineralization. The extent of fluoride adsorption depends on the surface area of the mineral[24,25] and would be consistent with the proposal that the complex convex surface structure of microcalcifications allows more binding of fluoride than the relatively flat and smaller surface area of macrocalcification.

The association and dissociation of ^{18}F-NaF to carotid endarterectomy specimens showed an exponential rise and decay of signal, with excellent contrast between activity in vascular tissue and the blood pool observed as early as 60 min following injection. Studies in artificial chemical models have shown that fluoride binding to hydroxyapatite also occurs in an exponential binding reaction[24,25] and can be explained both by physico- and chemisorption[24]. This also appears as the most likely mechanism in human carotids but it is important to emphasize that not all calcification observed can be generalized to consist of hydroxyapatite. Previous clinical radiology reports have described an initial fluoride-bound water shell entrapment and a slow ion exchange[22]; however, no mechanistic studies to prove these assumptions have been published, at least to our knowledge. Therefore, we propose that our observations match the findings in artificial systems and the fluoride adsorption to hydroxyapatite in whole-carotid sections can be explained by physico- and chemisorption and the dissociation is a result of a washout, similar to what has been described in artificial systems[24].

The mechanism of early micronodular intimal atherosclerotic calcification is not yet clearly understood although its genesis has been linked to, amongst others factors, inflammatory macrophages, inflammatory lipids, apoptosis, neovascularization and phenotypically altered vascular smooth muscle cells[3]. We have demonstrated that ^{18}F-NaF binds specifically and sensitively to the final common pathway of precipitated micro nodules of pathological calcification (whether through active or passive mechanisms) and not directly to any of these putative earlier upstream triggers. This is in contrast to ^{18}F-fluorodexoyglucose, which although linked to activated macrophages in the vasculature, may lack sensitivity and specificity for identifying inflammation specific activation[26] and does not have the highly favourable pharmacokinetics of ^{18}F-NaF[26,27].

The main question we sought to answer was why does the ^{18}F-NaF clinical PET/CT imaging result in a signal mismatch between the two modalities? Specifically, why do some areas of macrocalcification show no uptake, while other areas without apparent calcification show high ^{18}F-NaF uptake? To address this, we used carotid endarterectomy sections and compared *ex vivo* and *in vivo* imaging approaches. Since vascular calcification consists predominantly of mineral and only a small amount of soft tissue, the architecture of the calcification in the *in vivo* and *ex vivo* environments was very similar. Using autoradiography, we were able to show that if the *ex vivo* carotid was first incubated in ^{18}F-NaF and then cryosectioned, ^{18}F-NaF only bound to the outer surface of the macrocalcifications. In contrast, microcalcifications had a greater surface area and no barriers to penetration of the tissues resulting in high levels of ^{18}F-NaF adsorption. This suggests that ^{18}F-NaF cannot penetrate into the deeper layers of macrocalcification. Since macrocalcifications have a large volume but small surface area, the detected radioactivity signal is proportionally smaller than microcalcifications with a small volume and large surface area. Microcalcifications are also dispersed in large numbers per given area of the tissue, again resulting in a disproportionally high signal compared with macrocalcifications. Furthermore, when sectioned carotid endarterectomy specimens were directly exposed to ^{18}F-NaF, uptake was this time observed also in the centre of macroscopic deposits that had now been made accessible to the tracer. We therefore conclude that the adsorption of ^{18}F-NaF to areas of calcification in carotid endarterectomy tissue is a measure of the available surface area accessible to the isotope. This is consistent with findings in the bone and explains the observed greater adsorption of ^{18}F-NaF to microcalcifications (Fig. 5a,b).

μPET/μCT scans of *ex vivo* carotids and their comparison with autoradiography revealed that μPET closely matches autoradiography. On the other hand, μCT was only able to detect macrocalcifications (Fig. 5c) and underestimated the extent of vascular microcalcification identified by Alizarin Red histology. Back-correlation of μPET/μCT *ex vivo* scans to clinical *in vivo* PET/CT scans showed similar results. Using clinical CT, it was possible to detect the larger macrocalcifications, and their shape closely matched the data acquired by μCT. In contrast, the ^{18}F-NaF uptake detected by the clinical and μPET co-localized with both underlying calcium deposits (PET+/CT+) and regions with no apparent calcification (PET+/CT−) as assessed on CT (Fig. 5d). For the latter situation, our histological studies showed that the PET signal was in fact binding to microcalcifications below the detection limit of clinical CT and μCT. We therefore conclude that areas of ^{18}F-NaF uptake are reporting underlying microcalcifications, which are undetectable by CT. Conversely, large CT-detected macrocalcifications that do not co-localize with ^{18}F-NaF PET uptake (PET−/CT+) might be considered to represent dormant areas where on-going mineralization, as evidenced by the presence of microcalcification, has ceased and atherosclerotic disease is quiescent. Indeed, more heavily calcified plaques have been reported to be particularly prevalent in more stable disease and are much less vulnerable to rupture[28,29].

In summary, using electron microprobe analysis, we have demonstrated for the first time that fluoride directly adsorbs to calcified areas in mineralized vascular tissue. We have shown that binding is highly specific since ^{18}F-NaF radioactivity is confined solely to calcification, with no localization to other soft tissues. Furthermore, we observed that ^{18}F-NaF signal is highly dependent on the surface area of the calcification, being able to adsorb only to the outer layer of macrocalcifications without deeper penetration. We replicated these findings on three levels—autoradiography, light microscopy, *in vivo* clinical PET/CT and *ex vivo* μPET/μCT. These characteristic position ^{18}F-NaF as a highly specific ligand for the detection of pathologically high-risk microcalcification and early unstable atherosclerotic disease. ^{18}F-NaF is an economical PET ligand that is easy to manufacture. If used clinically, ^{18}F-NaF uptake has the potential to identify microcalcification within high-risk plaques as well as determine the locations of plaque rupture. In addition, as a marker of nascent calcification, it could test the efficacy of pharmacological therapies targeting atherosclerosis or calcification in both the clinical and preclinical settings. Microcalcifications are also linked to other disease processes, such as breast cancer, prostate cancer and stroke. The main aim of this study was to understand the molecular mechanisms of ^{18}F-NaF uptake and not to define patients at risk. With data validating its co-localization with calcification, the potential now exists to evaluate these processes. Whether or not ^{18}F-NaF will be useful in stratifying risk of cardiovascular events remains to be demonstrated. Large-scale prospective investigations will be essential to determine the

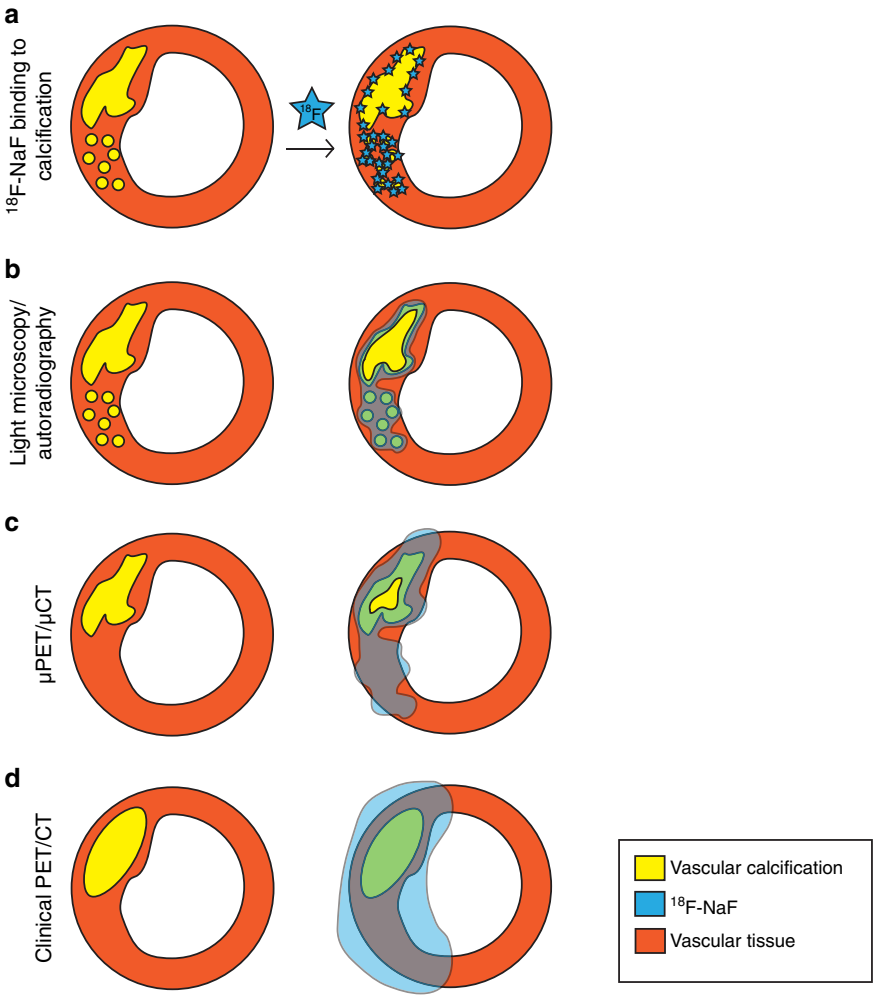

Figure 5 | Our model of ^{18}F-NaF binding to the vascular calcifications. (**a**) ^{18}F-NaF highly specifically binds to both micro- and macrocalcifications and the signal strength depends on the available surface area of these calcifications. (**b**) Schematic of histology/autoradiography vascular calcification detection. Alizarin Red histology results in the most definitive delineation of calcification, with the detection limit into the nanometre range. Phosphor screen autoradiography also has a much higher resolution compared with PET and μPET, resulting in accurate detection of calcifications. (**c**) Schematic of preclinical μPET/μCT vascular calcification detection. μCT detects macrocalcifications and their finer architecture. Proportionally less signal is detected on μCT than using histology, yet more than the clinical CT. μPET very precisely detects both macro and microcalcifications. In addition, if the macrocalcifications exceed μPET resolution, it is possible to observe ^{18}F-NaF binding to the outer surface of macrocalcifications. There are less PET −/CT + regions observed than using autoradiography but more than clinical PET/CT. (**d**) Schematic of clinical PET/CT vascular calcification detection. Here CT is able to detect gross macrocalcifications and PET detects both CT + and CT − calcifications. However, the signal is diffuse, resulting in much larger and therefore less precise PET + detections, as compared with the *ex vivo* imaging modalities described here.

prognostic value for ^{18}F-NaF role in risk stratification. Nevertheless, ^{18}F-NaF PET/CT holds promise and may have wide-ranging applications and become a valuable clinical tool to study active calcification across many disease areas and disciplines.

Methods

All chemicals were purchased form Sigma-Aldrich, Dorset, UK, unless stated otherwise.

Human tissues. The atherosclerotic intimal layers of human carotid arteries (further in text: carotids) were obtained with ethical approval and informed consent after endarterectomy surgeries (National Health Service Local Research Ethics Committee approval in Cambridge: 97/084, National Health Service West of Scotland Research Ethics Committee approval in Edinburgh: 12/WS/0227). The mean patient age was 71 ± 2 years and both male and female patient carotids were used. The tissue was collected immediately after the surgery and was fresh frozen in − 80 °C. It was kept frozen until the start of the experimental procedures. In clinical imaging, the concentration of the injected ^{18}F-NaF in plasma was calculated as approximately 1×10^{-11} M. Initial experiments were performed both on fresh carotids and carotids that had undergone a freeze-thaw cycle and no differences in ^{18}F binding were observed in terms of radioactivity penetration into macrocalcifications.

Electron microscopy. Frozen carotid tissue was placed in cryostat for 1 h to equilibrate to − 20 °C temperature. It was then immersed in Optimal Cutting Temperature compound (OCT) Embedding Matrix (CellPath, Powys, UK) and 30-μm thick, serial sections were cut on a Bright (Huntingdon, UK) cryostat. Sections were placed on custom-made Melinex discs (diameter: 12 mm) and allowed to dry. Discs were then frozen in − 80 °C temperature until the day of experiment. During the experiment, tissue sections were allowed to thaw and then incubated with 120 μl 0.01 M non-radioactive NaF for 2 h at room temperature. After incubation, sections were dipped in distilled H_2O three times and allowed to dry. The discs were stuck to 12.5 mm Cambridge style scanning electron microscope stubs and coated with carbon in an Edwards Auto 306 evaporative carbon coater. They were imaged in an FEI XL30 FEGSEM operated at 20 kV with secondary and backscattered electron detectors. Calcification was detected predominantly in the regions of intimal thickening and was designated micro- (spherical or near spherical deposits < 50 μm in diameter) or macrocalcification (where large regions between 50 μm and several mm in size were calcified).

Both types of calcification were analysed by energy-dispersive X-ray micro-analysis in 10 arteries. Spectra were collected using an Oxford Instruments SiLi atmospheric thin window detector running INCA software (ETAS Group, Stuttgart, Germany). Between 10 and 57 spectra were collected from both types of calcification (where present) for 100 s live time. As a control to assess nonspecific binding of F, spectra were also collected from regions of the arterial media where no backscattered electron signal for hydroxyapatite was present. The spectra were deconvolved in the INCA software and to estimate F/Ca only Ca and F spectra were input into the analysis. The quantitative data were expressed as atomic %. F/Ca was estimated by dividing the atomic % of F by the atomic % of Ca. Data are presented as means ± the s.e.m. and F/Ca between regions of micro- and macrocalcification was compared using an ANOVA and Tukey Kramer *post hoc* test.

Additional electron microscopy analysis was performed with commercial hydroxyapatite standards. Hydroxyapatite (2 mg) was incubated with 1 ml of 1% NaF on a rotator for 8 h or 4 days. The standards were then rinsed 10 times for 20 min in distilled water and air dried onto coverslips. They were mounted onto 12.5 mm Cambridge scanning electron microscope stubs, carbon coated and analysed in the same way as the cryostat sections. Control samples of hydroxyapatite standards were treated similarly as described above but the NaF incubation step was omitted. The hydroxyapatite analysed in the cryostat section is at least partially embedded/encapsulated in the tissue of the arteries and sections were coated in the same way with carbon to make them electrically conductive. As the carbon was added it was excluded from the analysis. Concentrations of O, P and Ca in the control hydroxyapatite are expressed in atomic per cent.

In the NaF-treated hydroxyapatite, no signal for Na was seen after extensive washes, and the concentrations of O, F, P and Ca were expressed as atomic per cent. Despite extensive washing, a clear signal for F was retained, indicating binding to the hydroxyapatite. In these control samples the interaction volume of the electron beam is expected to remain within hydroxyapatite alone whereas in the tissue sections a proportion of the interaction volume will also generate X-rays from the surrounding arterial tissue. Therefore the ratio of F/Ca was used to measure differences in F concentration between areas of macro- and micro-calcification.

^{18}F-NaF binding to cryostat cut carotid artery sections. For all experiments ^{18}F-NaF was synthesized by the Wolfson Brain Imaging Centre (WBIC) (Cambridge, UK). The typical activity was approximately 285 MBq.

Frozen whole carotids were placed in the cryostat for 1 h to equilibrate to −20 °C temperature. Tissue was then immersed in the OCT Embedding Matrix (CellPath, Powys, UK) and 20 μm thick, serial sections were cut on a Bright (Huntingdon, UK) cryostat. Sections were allowed to dry in room temperature and stored at −80 °C temperature until the start of the experiment.

The concentration of ^{18}F-NaF was detected using F^- electrode (Thermo Scientific, Loughborough, UK) and was then diluted to 1×10^{-11} M. For nonspecific binding detection, 20 μl of 0.1 M unlabelled NaF solution (Orion Ionplus F^- Standard, Thermo Scientific, Loughborough, UK) were added to an aliquot of the radioactive 1×10^{-11} M solution. Frozen tissue sections were allowed to thaw and washed with PBS for 10 min in room temperature. Adjacent sections were incubated either with ^{18}F-NaF or ^{18}F-NaF plus unlabelled NaF solutions for 1 h at room temperature. They were then washed in PBS 3 × 5 min and dipped in distilled H_2O. After drying, tissues were placed on a charged phosphor screen (Perkin Elmer, Waltham, Massachusetts) and left overnight. The following day screens were read using PerkinElmer's Cyclone Plus Phosphor Imager (Waltham, Massachusetts) and data were analysed with OptiQuant software (Packard Instrument, Meriden, Connecticut). Areas of micro- and macrocalcification were identified visually based on the size of nodules of <50 and ≥ 50 μm to several mm, respectively, and manual measurements made.

For concentration–response curve, the same method was used, except stock ^{18}F-NaF solution was split into serial dilutions from 10^{-12} to 10^{-7} M. After washing in PBS and dipping in distilled H_2O, tissues were wiped off the slides with filter paper, which was put into radioimmunoassay tubes and measured in the gamma counter (Packard Cobra II E5003, GMI, Ramsey, Minnesota).

^{18}F-NaF binding in whole-carotid arteries. Whole-carotid arteries were thawed in 5 ml PBS for 1 h, and then placed in 5 ml of 10^{-11} M ^{18}F-NaF solution for 1 h at room temperature. They were then washed in PBS 3 × 2 min, followed by a dip in distilled H_2O. Carotids were transferred to cryostat, immersed in OCT and allowed to freeze. Tissue was then cut into 20-μm serial sections, which were allowed to dry on microscopy slides. After drying, tissues were placed on a charged phosphor screen and left overnight.

For whole-carotid association and dissociation binding curves, the same method was used, except during association binding experiments, carotids were taken out from the 5 ml of 10^{-11} M ^{18}F-NaF tube at set time points—0, 5, 15, 30, 60 min, washed and measured in the gamma counter. For dissociation binding experiment, after the incubation in 5 ml of 10^{-11} M ^{18}F-NaF for 1 h, tissues were continuously washed in PBS for set amounts of time—0, 5, 10, 15, 30, 45, 60, 90, 120 min. Instead of cryostat cutting, arteries were placed in radioimmunoassay tubes and measured in the gamma counter.

Tissue staining. Tissue sections were cut on cryostat as described in section '^{18}F-NaF binding to cryostat cut carotid artery sections'.

Alizarin red staining. Alizarin Red staining (Alfa Aesar, Heysham, UK) was used for calcification detection in carotid arteries. In brief, cryosections were left to dry overnight. They were then fixed in acetone for 10 min at 4 °C and washed in PBS 2 × 5 min at room temperature. After washing, 300 μl Alizarin Red were applied to each section for 1 min. Tissue was then put in acetone for 1 min, followed by a wash in 50:50 acetone:xylene for 1 min and then left in xylene for at least 1 h.

Immunohistochemistry. Immunohistochemistry was used to detect multiple inflammatory tissue markers in cryosections. Tissue was left to dry overnight and the following day it was fixed in acetone at 4 °C for 10 min and washed in PBS 2 × 5 min at room temperature. Sections were blocked in 10% goat serum for 1 h and H_2O_2 for 5 min. Each blocking step was followed by washing in PBS for 2 × 5 min. Carotids were then incubated in primary antibody for 30 min at room temperature. Antibodies included CD68 (1:500, clone PG-M1), CD31 (1:20, clone JC70A) and Smooth Muscle Actin (1:500, clone 1A4) (all from Dako UK, Ely, UK). Labelled polymer-HRP anti-rabbit application and visualization with 3,3′-diaminobenzidine (DAB) was done using EnVision + System-HRP (DAB) kit (Dako UK, Ely, UK), following manufacturers specifications. Counterstain of 150 μl haemotoxylin was applied to each section and incubated for 1 min. Slide was then dipped six times in destain solution (1% HCl, 50% methanol, 49% distilled H_2O) and washed in tap water for 2 min. Afterwards tissue was quickly dehydrated in 1 min intervals through graded alcohols (30 to 70% to 100% to absolute alcohol 1 to absolute alcohol 2) and cleared in xylene for at least 1 h.

Section mounting. After staining, all tissues were mounted using DePeX mounting medium Gurr (VWR, Lutterworth, UK) and glass coverslips (Menzel-Gläser, Braunschweig, Germany). After hardening of the mounting solution, tissues were imaged using Wild Heerbrugg M3Z microscope (Leica, Heerbrugg, Switzerland).

μPET/μCT imaging of whole-carotid arteries. Whole-carotid arteries were removed from −80 °C freezer and thawed in 5 ml PBS at room temperature for 1 h. After thawing, tissues were placed in 1×10^{-9} M ^{18}F-NaF solution and incubated for 1 h. Tissues were then washed in PBS 3 × 2 min and dipped in distilled water. They were then placed in sealed plastic tubes. Tissue radioactivity was read using dose calibrator and they were then placed into the μPET/μCT scanner. Images were acquired over 30 min in list mode using a NanoScan PET/CT (Mediso, Budapest, Hungary). Data were reconstructed using a 3D ordered-subset expectation-maximization (OSEM) algorithm with eight iterations and six subsets using corrections for decay, dead time, random events, attenuation and scatter, the resulting image was isotropic with 300 μm voxels. Two sets of μCT were performed immediately after μPET acquisition, using high and low zoom (67.1 mm and 219 mm between object and source, respectively). Images were obtained by helical acquisition using a voltage, current and exposure time of 65 kVp, 123 μA and 1,100 ms. Images were reconstructed using a modified cone beam filtered-back projection method using a Butterworth filter producing a 22-μm and a 213-μm isotropic data set. μPET and μCT data were co-registered using previously established default shifts.

2D image processing and analysis. Two-dimensional image analysis was performed using open-source software ImageJ/Fiji (http://fiji.sc) (NIH, Bethesda, Maryland). Correlation between histology sections and autoradiography images was achieved by using thresholded binary images of the different signals. In addition, these thresholded images were filtered with Gaussian blur ($\sigma = 20$) and thresholded again, to create segmentation masks that overcome the issue of inherent resolution differences between histology and autoradiography signal detection processes[30].

Alizarin Red-stained calcification detection was performed using histogram-based Otsu automated thresholding method[31] and after Gaussian filter, it was processed using Li thresholding[32].

DAB-stained immunohistology sections were analysed using a colorimetric thresholding method. While calcification stains provided excellent signal-intensity to background ratio, this was not the case for immunohistochemistry. Therefore, a colour combination that only detected the brown DAB stain was set as the manual threshold value, irrespective of intensity. After Gaussian blurring, signal was detected using Li auto-thresholding method.

Autoradiography images were resized to match the size of the histology images. Then they were thresholded using Otsu method, Gaussian blurred and thresholded using Li method.

All two-dimensional histology images were subjected to background subtraction and histogram equalization.

Correlation between the various stained sections was accomplished using multiple ImageJ/Fiji plug-ins. The position of specimens between individual images was co-registred using TurboReg[33] plug-in. Although tissues had been exposed to acetone and alcohol fixation protocols, we did not observe prominent contraction

or shrinkage that would affect our data analysis. Images were then thresholded and turned into binary data as described above. Pearson's correlation coefficient was calculated using JACoP[34] plug-in. Overlapping images of histological and autoradiography signals were acquired using Co-localization Finder plug-in. The overlapped images were processed further to determine PET+/CT−, PET+/CT+ and PET−/CT+ regions in individual sections. Each colour corresponding to one of the three detection modalities was separated out and quantified using Analyze Particles command which counts the number of pixels in the binary segmented mask.

3D image processing and analysis. 3D images after data reconstruction were analysed using VivoQuant ver 1.23, (InviCRO, Boston, Massachusetts) software[35]. For μPET/μCT initially the files were cropped to reduce file size and remove experimental artifacts, such as the scanning panel and tube in which the carotid was placed. Once an image containing only the signals associated with the carotid was achieved, the colour intensities of both modalities were manually adjusted to match histology/autoradiography signals as close as possible. After that, Distance/Annotation function was selected and 5–8-mm linear transects were made across slides in the transversal plane of carotids. The raw data were then downloaded and graphs showing μCT densities and μPET units along the transect lines were later reconstructed with Matlab (Mathworks, Natick, Massachusetts) software. To quantify PET+/CT−, PET+/CT+ and PET−/CT+ regions on the 3D level, 3D ROI Tool function was selected. First, μPET data were thresholded using Otsu method, to delineate the extent of PET+ signal. On the μCT plane we defined densities over 1000 Hounsfield Units (HU) as calcifications. To detect PET+/CT+ signal, we selected PET+ delineated 3D area and used Global thresholding for ≥1,000 HU of the μCT data in this area. To detect PET−/CT+ areas, we selected all remaining μCT data and applied the ≥1,000 HU Global threshold. The raw data containing information about the different modality regions was downloaded and analysed with Microsoft Office Excel (Microsoft, Redmond, Washington).

Clinical PET/CT data were analysed by initially manually co-registering the PET, CT and CT angiogram using bones as anatomical landmarks of the three different modalities. Following this the images were zoomed in to the culprit plaque and was cropped around this area. The division into PET+/CT−, PET+/CT+ and PET−/CT+ regions was similar to as described for the μPET/μCT data. The only exception was that CT and CT angiogram CT+ regions were also detected using Otsu thresholding, to account for the inconsistencies of the amount of tracer injected and imaging time after ^{18}F-NaF injection.

Clinical PET/CT acquisition and dynamic analysis. Recruitment and scanning for the *in vivo* aspect of this study took place following approval from the local research ethics committee (National Health Service West of Scotland Research Ethics Committee approval in Edinburgh: 12/WS/0227) and in accordance with the Declaration of Helsinki. Patients with symptomatic carotid artery stenosis (scheduled to undergo carotid endarterectomy) ≥50% by NASCET criteria[36] were recruited from stroke and vascular surgery clinics at the Royal Infirmary of Edinburgh between January 2013 and April 2014. Exclusion criteria included a modified Rankin score of ≥3, insulin-dependent diabetes mellitus, women of child-bearing age not receiving contraception, severe chronic kidney disease (epidermal growth factor receptor $<30\,ml\,min^{-1}$ per $1.73\,m^2$), known iodine-based contrast allergy, prior ipsilateral carotid intervention, prior neck irradiation and inability to provide informed consent.

After giving their consent, patients underwent baseline clinical assessment before undergoing dynamic or ^{18}F-NaF PET/CT and CT carotid angiography with the use of a hybrid scanner (Biograph mCT, Siemens Medical Systems, Erlangen, Germany).

For static ^{18}F-NaF PET/CT, a target dose of 250 MBq of ^{18}F-NaF was administered intravenously. Scanning took place 60 min after injection. An attenuation-correction CT scan (non-enhanced, low dose 120 kV, 50 mAs) was then performed followed by PET imaging covering two bed positions with the first upper bed centred over the carotid bifurcation in 3D mode for 15 min per bed. Analysis was undertaken as described above.

In five patients, ^{18}F-NaF PET imaging was undertaken as a dynamic acquisition with the PET scanner in list mode. Three of these subjects underwent arterial blood sampling to directly assay the plasma arterial input function for model creation and to assess ^{18}F-NaF pharmacokinetics. An image-derived input function was utilized for modelling in the two patients that did not undergo arterial cannulation and sampling. The image-derived input function was generated by drawing regions of interest in the proximal carotid artery lumen. After the fitting of a soft neck collar to minimize movement, subjects were placed in the PET/CT scanner with intravenous and radial arterial catheters sited. An attenuation-correction CT scan (non-enhanced, low dose 120 kV, 50 mAs) was performed followed by PET imaging with the single bed centred over the carotid bifurcation. A target dose of 250 MBq of ^{18}F-NaF was then administered intravenously at the same time as scanning and blood sampling were initiated. Scanning took place for 75 min. Real-time whole-blood radioactivity was assayed using a calibrated Allogg ABSS V3 system (Allogg Technology, Mariefred, Sweden). In brief, whole arterial blood was sampled through a narrow bore polytetrafluoroethylene tube using a roller pump at a rate of $5\,ml\,min^{-1}$ before being drawn through a shielded scintillation-based detector. Counts were recorded using a data-logger. After 15 min, the pump was deactivated and 5 ml samples were drawn intermittently for the remaining 60 min. Decay corrected whole blood and plasma radioactivity was then assayed using a gamma counter. The fractional difference between whole blood and plasma radioactivity was then calculated to adjust the data for the first fifteen min from the Allogg device.

Following static and dynamic PET acquisitions, CT carotid angiograms were also undertaken (Care Dose 4D, 120 kV, 145 mA, rotation time 0.5 s, pitch 0.8).

Dynamic imaging data were reconstructed using the Siemens Ultra-HD algorithm (time of flight + True X) with corrections applied for attenuation, dead time, scatter and random coincidences. Imaging data were then parsed into the following time bins as per Hawkins and Frost[37,38] (12×10 s, 4×30 s, 12×240 s) and analysed on a PMOD workstation (PMOD v3.408, PMOD Technologies Ltd., Zurich, Switzerland).

For analysis, the image data were first reviewed for evidence of ^{18}F-NaF uptake, image quality and patient movement. The CT angiogram was scrutinized for plaque presence, location and characteristics. The PET data were then resliced as part of automated registration to the CT data. Volumes of interest were then generated by drawing regions of interest on sequential axial slices on the registered data sets. Volumes were drawn to separately incorporate internal carotid artery plaque (where present) and a vertebral body. Vertebral data were obtained as a comparator and also as a way of ensuring our data were commensurate with the work of others. Tissue activity curves were then generated and assessed.

Dynamic analysis of fluoride uptake in the bone has been well described. Since, our data and that of others shows that over the time course of a typical ^{18}F-PET/CT scan fluoride dissociation from calcified tissue is undetectably slow, the Patlak technique[39,40] may be used to gain an estimate for the net flux of fluoride (K_i) into a region of interest. Patlak derived K_i is calculated as follows:

$$\frac{Ct(t)}{Cb(t)} = Ki\frac{\int_0^t Cb(t)\mathrm{d}t}{Cb(t)} + V \qquad (1)$$

$C_t(t)$ is the activity concentration of ^{18}F-NaF at time t within the volume of interest, $C_b(t)$ is the blood activity concentration of ^{18}F-NaF at time t and V relates to the effective volume of distribution for ^{18}F-NaF. The Patlak plot is obtained by plotting $\frac{Ct(t)}{Cb(t)}$ against $Ki\frac{\int_0^t Cb(t)\mathrm{d}t}{Cb(t)}$ and calculating the slope of the regression line as given in equation (1).

This method has been extensively described and compared with multi-compartmental modelling with both techniques showing good agreement. To ensure equilibrium between the plasma and compartments had been achieved, we only plotted the data from 10 min onwards as described by Frost[38]. Patlak plots were generated for all carotid plaques and vertebra (see Supplementary Fig. 2 for a representative example and Supplementary Table 1). We also plotted directly measured plasma activity curves for illustration of the pharmacokinetics of ^{18}F-NaF (for a representative example, see Supplementary Fig. 3).

Data analysis. Numerical data analysis was performed using Microsoft Office Excel (Microsoft, Redmond, Washington), Matlab (Mathworks, Natick, Massachusetts) and Prism (GraphPad, San Diego, California) softwares. Written text was produced using Microsoft Office Word (Microsoft, Redmond, Washington) and figures were made using Adobe Illustrator CS5 (Adobe Systems, San Jose, California).

References

1. Doherty, T. M. *et al.* Calcification in atherosclerosis: Bone biology and chronic inflammation at the arterial crossroads. *Proc. Natl Acad. Sci. USA* **100,** 11201–11206 (2003).
2. Demer, L. L. & Tintut, Y. Mineral exploration: search for the mechanism of vascular calcification and beyond: the 2003 Jeffrey M. Hoeg Award lecture. *Arterioscler. Thromb. Vasc. Biol.* **23,** 1739–1743 (2003).
3. Johnson, R. C., Leopold, J. A. & Loscalzo, J. Vascular calcification—Pathobiological mechanisms and clinical implications. *Circ. Res.* **99,** 1044–1059 (2006).
4. Wu, M., Rementer, C. & Giachelli, C. M. Vascular calcification: an update on mechanisms and challenges in treatment. *Calcif. Tissue Int.* **93,** 365–373 (2013).
5. Budoff, M. J. *et al.* Long-term prognosis associated with coronary calcification: observations from a registry of 25,253 patients. *J. Am. Coll. Cardiol.* **49,** 1860–1870 (2007).
6. London, G. M. *et al.* Arterial media calcification in end-stage renal disease: impact on all-cause and cardiovascular mortality. *Nephrol. Dial. Transplant.* **18,** 1731–1740 (2003).
7. Goncalves, F. B. *et al.* Calcification of the abdominal aorta as an independent predictor of cardiovascular events: a meta-analysis. *Heart* **98,** 988–994 (2012).
8. Chen, W. & Dilsizian, V. Targeted PET/CT imaging of vulnerable atherosclerotic plaques: microcalcification with sodium fluoride and inflammation with fluorodeoxyglucose. *Curr. Cardiol. Rep.* **15,** 364 (2013).
9. Fitzpatrick, L. A., Severson, A., Edwards, W. D. & Ingram, R. T. Diffuse calcification in human coronary arteries. Association of osteopontin with atherosclerosis. *J. Clin. Invest.* **94,** 1597–1604 (1994).

10. Schmid, K., Mcsharry, W., Pameijer, C. & Binette, J. Chemical and physicochemical studies on the mineral-deposits of the human atherosclerotic aorta. *Atherosclerosis* **37,** 199–210 (1980).
11. Kelly-Arnold, A. *et al.* Revised microcalcification hypothesis for fibrous cap rupture in human coronary arteries. *Proc. Natl Acad. Sci. USA* **110,** 10741–10746 (2013).
12. New, S. E. P. *et al.* Macrophage-derived matrix vesicles: an alternative novel mechanism for microcalcification in atherosclerotic plaques. *Circ. Res.* **113,** 72–77 (2013).
13. Ewence, A. E. *et al.* Calcium phosphate crystals induce cell death in human vascular smooth muscle cells: a potential mechanism in atherosclerotic plaque destabilization. *Circ. Res.* **103,** e28–e34 (2008).
14. Hutcheson, J. D., Maldonado, N. & Aikawa, E. Small entities with large impact: microcalcifications and atherosclerotic plaque vulnerability. *Curr. Opin. Lipidol.* **25,** 327–332 (2014).
15. Stary, H. C. Natural history of calcium deposits in atherosclerosis progression and regression. *Z. Kardiol.* **89,** 28–35 (2000).
16. Aikawa, E. *et al.* Osteogenesis associates with inflammation in early-stage atherosclerosis evaluated by molecular imaging *in vivo*. *Circulation* **116,** 2841–2850 (2007).
17. Ritman, E. L. Small-animal CT: its difference from, and impact on, clinical CT. *Nucl. Instrum. Methods Phys. Res.A* **580,** 968–970 (2007).
18. McEvoy, J. W. *et al.* Coronary artery calcium progression: an important clinical measurement? A review of published reports. *J. Am. Coll. Cardiol.* **56,** 1613–1622 (2010).
19. Derlin, T. *et al.* Feasibility of 18F-sodium fluoride PET/CT for imaging of atherosclerotic plaque. *J. Nucl. Med.* **51,** 862–865 (2010).
20. Dweck, M. R. *et al.* Coronary arterial 18F-sodium fluoride uptake a novel marker of plaque biology. *J. Am. Coll. Cardiol.* **59,** 1539–1548 (2012).
21. Joshi, N. V. *et al.* 18F-fluoride positron emission tomography for identification of ruptured and high-risk coronary atherosclerotic plaques: a prospective clinical trial. *Lancet* **383,** 705–713 (2014).
22. Blau, M., Ganatra, R. & Bender, M. A. 18F-fluoride for bone imaging. *Semin. Nucl. Med.* **2,** 31–37 (1972).
23. Derlin, T. *et al.* Correlation of inflammation assessed by 18F-FDG PET, active mineral deposition assessed by 18F-Fluoride PET, and vascular calcification in atherosclerotic plaque: a dual-tracer PET/CT study. *J. Nucl. Med.* **52,** 1020–1027 (2011).
24. Lin, J., Raghavan, S. & Fuerstenau, D. The adsorption of fluoride ions by hydroxyapatite from aqueous-solution. *Colloids Surf.* **3,** 357–370 (1981).
25. Gasser, P., Voegel, J. & Gramain, P. Surface-reactions on hydroxyapatite in the presence of fluoride ions .1. Saturated and congruent conditions. *Colloids Surf. -Physicochem. Eng. Asp.* **74,** 275–286 (1993).
26. Folco, E. J. *et al.* Hypoxia but not inflammation augments glucose uptake in human macrophages: Implications for imaging atherosclerosis with 18fluorine-labeled 2-deoxy-D-glucose positron emission tomography. *J. Am. Coll. Cardiol.* **58,** 603–614 (2011).
27. Tawakol, A. *et al.* Noninvasive in vivo measurement of vascular inflammation with F-18 fluorodeoxyglucose positron emission tomography. *J. Nucl. Cardiol.* **12,** 294–301 (2005).
28. Richardson, P. Influence of plaque configuration and stress distribution on fissuring of coronary atherosclerotic plaques. *Lancet* **334,** 941–944 (1989).
29. Abedin, M., Tintut, Y. & Demer, L. L. Vascular calcification—mechanisms and clinical ramifications. *Arterioscler. Thromb. Vasc. Biol.* **24,** 1161–1170 (2004).
30. Carlin, S. *et al.* A comparison of the imaging characteristics and microregional distribution of 4 hypoxia PET tracers. *J. Nucl. Med.* **55,** 515–521 (2014).
31. Otsu, N. A threshold selection method from gray-level histograms. *IEEE Trans. Syst. Man Cybern* **9,** 62–66 (1979).
32. Li, C. H. & Tam, P. K. S. An iterative algorithm for minimum cross entropy thresholding. *Pattern Recognit. Lett.* **19,** 771–776 (1998).
33. Thevenaz, P., Ruttimann, U. E. & Unser, M. A pyramid approach to subpixel registration based on intensity. *IEEE Trans. Image Process* **7,** 27–41 (1998).
34. Bolte, S. & Cordelieres, F. P. A guided tour into subcellular colocalization analysis in light microscopy. *J. Microsc.* **224,** 213–232 (2006).
35. Loening, A. M. & Gambhir, S. S. AMIDE: a free software tool for multimodality medical image analysis. *Mol. Imaging* **2,** 131–137 (2003).
36. Ferguson, G. G. *et al.* The North American Symptomatic Carotid Endarterectomy Trial: surgical results in 1415 patients. *Stroke J. Cereb. Circ.* **30,** 1751–1758 (1999).
37. Hawkins, R. *et al.* Evaluation of the skeletal kinetics of fluorine-18-fluoride ion with Pet. *J. Nucl. Med.* **33,** 633–642 (1992).
38. Frost, M. L. *et al.* Long-term precision of F-18-fluoride PET skeletal kinetic studies in the assessment of bone metabolism. *J. Nucl. Med.* **49,** 700–707 (2008).
39. Patlak, C. S., Blasberg, R. G. & Fenstermacher, J. D. Graphical evaluation of blood-to-brain transfer constants from multiple-time uptake data. *J. Cereb. Blood Flow Metab.* **3,** 1–7 (1983).
40. Patlak, C. S. & Blasberg, R. G. Graphical evaluation of blood-to-brain transfer constants from multiple-time uptake data. Generalizations. *J. Cereb. Blood Flow Metab.* **5,** 584–590 (1985).

Acknowledgements

We thank Dr Janet Maguire and Rhoda Kuc for helpful discussions. We thank Robert Smith, Valentina Ferrari, Robert Bielik and other radiochemists at the University of Cambridge for supplying ^{18}F-NaF for our experiments. In addition, we acknowledge the surgeons and other members of the staff at the Addenbrooke's Hospital, Cambridge and Edinburgh Royal Infirmary for the provision of human tissue. We also acknowledge the contributions made by members of staff at the Clinical Research Imaging Centre in Edinburgh, in particular, Gemma Roberts, Tim Clark, Martin Connell, Dr Alison Fletcher and Professor Edwin Van Beek. J.H.R. is partly supported by the NIHR Cambridge Biomedical Research Centre, the British Heart Foundation, the Wellcome Trust and the Academy of Medical Sciences. This study was supported by the following grants: AI Wellcome Trust PhD Programme in Metabolic and Cardiovascular Disease Grant Number 096823/Z/11/Z, Wellcome Trust (WT103782AIA), British Heart Foundation (RG/10/007/28300, CH/09/002/26360, PG/12/8/29371, FS/14/78/31020), National Health Service Research Scotland and National Institute for Health Research Cambridge Biomedical Research Centre, Cancer Research UK 17242 and 16465.

Author contributions

A.I. designed the experiments, acquired and analysed data, wrote and revised the manuscript. A.T.V. designed and carried out the clinical research and analysed the data. A.T.V, M.R.D. and D.E.N. contributed to writing and manuscript revision. D.Y.L. with A.I. acquired μPET/CT data, contributed to data analysis, writing, and manuscript revision. J.N.S. carried out electron microscopy and associated data analysis and, contributed to writing and edited the manuscript. J.L.E.B. contributed to data acquisition. F.R.J, J.H.R., E.A.W., M.R.B., K.M.B and F.A.G provided interpretation and critical revision of the manuscript. A.P.D. conceived experimental design, analysis of the data, provided overall guidance, writing and critical revision of the manuscript. All authors have approved the final version of the manuscript.

Additional information

Supplementary Information accompanies this paper at http://www.nature.com/naturecommunications

Competing financial interests: The authors declare no competing financial interests.

Reprints and permission information is available online at http://npg.nature.com/reprintsandpermissions/

How to cite this article: Irkle, A. *et al.* Identifying active vascular microcalcification by ^{18}F-sodium fluoride positron emission tomography. *Nat. Commun.* 6:7495 doi: 10.1038/ncomms8495 (2015).

OPEN

^{18}F-Fluoride and ^{18}F-Fluorodeoxyglucose Positron Emission Tomography After Transient Ischemic Attack or Minor Ischemic Stroke

Case–Control Study

Alex T. Vesey, MD; William S. A. Jenkins, MD; Agnese Irkle, PhD; Alastair Moss, MD; Greg Sng, MD; Rachael O. Forsythe, MD; Tim Clark, MSc; Gemma Roberts, MSc; Alison Fletcher, PhD; Christophe Lucatelli, PhD; James H. F. Rudd, MD, PhD; Anthony P. Davenport, PhD; Nicholas L. Mills, MD, PhD; Rustam Al-Shahi Salman, MA, PhD; Martin Dennis, MD, PhD; William N. Whiteley, MD, PhD; Edwin J. R. van Beek, MD, PhD; Marc R. Dweck, MD PhD; David E. Newby, MD, PhD, DSc

Background—Combined positron emission tomography (PET) and computed tomography (CT) can assess both anatomy and biology of carotid atherosclerosis. We sought to assess whether ^{18}F-fluoride or ^{18}F-fluorodeoxyglucose can identify culprit and high-risk carotid plaque.

Methods and Results—We performed ^{18}F-fluoride and ^{18}F-fluorodeoxyglucose PET/CT in 26 patients after recent transient ischemic attack or minor ischemic stroke: 18 patients with culprit carotid stenosis awaiting carotid endarterectomy and 8 controls without culprit carotid atheroma. We compared standardized uptake values in the clinically adjudicated culprit to the contralateral asymptomatic artery, and assessed the relationship between radiotracer uptake and plaque phenotype or predicted cardiovascular risk (ASSIGN score [Assessing Cardiovascular Risk Using SIGN Guidelines to Assign Preventive Treatment]). We also performed micro PET/CT and histological analysis of excised plaque. On histological and micro PET/CT analysis, ^{18}F-fluoride selectively highlighted microcalcification. Carotid ^{18}F-fluoride uptake was increased in clinically adjudicated culprit plaques compared with asymptomatic contralateral plaques ($\log_{10}$standardized uptake value$_{mean}$ 0.29±0.10 versus 0.23±0.11, P=0.001) and compared with control patients ($\log_{10}$standardized uptake value$_{mean}$ 0.29±0.10 versus 0.12±0.11, P=0.001). ^{18}F-Fluoride uptake correlated with high-risk plaque features (remodeling index [r=0.53, P=0.003], plaque burden [r=0.51, P=0.004]), and predicted cardiovascular risk [r=0.65, P=0.002]). Carotid ^{18}F-fluorodeoxyglucose uptake appeared to be increased in 7 of 16 culprit plaques, but no overall differences in uptake were observed in culprit versus contralateral plaques or control patients. However, ^{18}F-fluorodeoxyglucose did correlate with predicted cardiovascular risk (r=0.53, P=0.019), but not with plaque phenotype.

Conclusions—^{18}F-Fluoride PET/CT highlights culprit and phenotypically high-risk carotid plaque. This has the potential to improve risk stratification and selection of patients who may benefit from intervention. **(*Circ Cardiovasc Imaging*. 2017;10:e004976. DOI: 10.1161/CIRCIMAGING.116.004976.)**

Key Words: carotid stenosis ■ fluorides ■ inflammation ■ nuclear medicine ■ phenotype ■ stroke

Although carotid endarterectomy reduces risk of ipsilateral stroke in people with symptomatic carotid artery stenosis, the number needed to treat to prevent one stroke is large,[1,2] especially in asymptomatic stenosis.[3] Furthermore, the pathological event that leads to cerebral thromboembolism (atherosclerotic plaque rupture) is not necessarily correlated with luminal stenosis severity.[4] Other pathological features, such as inflammation, cell death, and microcalcification, are important in driving both plaque formation and instability.[5–7] New imaging biomarkers of these processes are therefore needed to improve risk stratification and clinical

See Editorial by Tawakol et al
See Clinical Perspective

Received May 2, 2016; accepted January 12, 2017.

From the BHF Centre for Cardiovascular Science, University of Edinburgh, United Kingdom (A.T.V., W.S.A.J., A.M., G.S., R.O.F., N.L.M., E.J.R.v.B., M.R.D., D.E.N.); Division of Experimental Medicine and Immunotherapeutics, University of Cambridge, United Kingdom (A.I., J.R., A.P.D.); and Clinical Research Imaging Centre (T.C., G.R., A.F., C.L., E.J.R.v.B., M.R.D., D.E.N.) and Centre for Clinical Brain Sciences (R.A.-S.S., M.D., W.W.), University of Edinburgh, United Kingdom.

The Data Supplement is available at http://circimaging.ahajournals.org/lookup/suppl/doi:10.1161/CIRCIMAGING.116.004976/-/DC1.

Correspondence to Alex T. Vesey, MD, Centre for Cardiovascular Science, University of Edinburgh, Room SU 305, Chancellor's Bldg., 49 Little France Crescent, Edinburgh, EH16 4SB, United Kingdom. E-mail: avesey@staffmail.ed.ac.uk

decision-making. Such biomarkers could also assess the response of plaque biology to novel pharmacological interventions and provide a way of identifying culprit lesions in patients with multiple plaques.

Hybrid positron emission tomography and computed tomography (PET/CT) is a molecular imaging modality that has high sensitivity for noninvasive in vivo detection of radiolabeled biomolecules tuned to a variety of pathophysiological processes. In carotid atherosclerosis imaging, the most widely used tracer has been ^{18}F-fluorodeoxyglucose (^{18}F-FDG)[8–14]: Recently, we have described another radiotracer, ^{18}F-fluoride, in atherosclerosis imaging.[15,16] We[15–18] and others[19–23] have shown that this tracer has major potential in cardiovascular disease. ^{18}F-Fluoride can highlight culprit plaque in patients after myocardial infarction and high-risk plaques in patients with apparently stable coronary heart disease.[16] We have shown that this is because ^{18}F-fluoride can highlight areas of microcalcification indicative of necrotic atheroma.[24] The ability to identify high risk or culprit plaque in the cephalic circulation has the potential to improve risk stratification in patients at high risk of stroke with a view to more targeted interventions. Our study aims were to compare and contrast the identification of clinically adjudicated culprit and high-risk plaque at the carotid bifurcation using ^{18}F-fluoride and ^{18}F-FDG PET/CT.

Methods

Patient Population

Two cohorts of people with a recent transient ischemic attack (TIA) or minor ischemic stroke were recruited: a case cohort with a high-grade internal carotid artery stenosis (≥50% by North American Symptomatic Carotid Endarterectomy Trial[25] criteria for men, ≥70% for women) scheduled to undergo carotid endarterectomy and a control cohort in whom the cause of stroke was not attributed to carotid atheroma. Participants were recruited from outpatient clinics in National Health Service Lothian between January 2013 and June 2014 (for exclusion criteria, see Appendix in the Data Supplement). Research ethics committee approval (National Health Service West of Scotland Research Ethics Committee: 12/WS/0227) and the written and informed consent of all participants were obtained.

Baseline Assessment

Participants underwent clinical assessment at baseline including standard hematologic and biochemical indices. Serum C-reactive protein concentration was measured using the MULTIGENT CRP Vario assay on the high-throughput ARCHITECT system (Abbott Laboratories, Abbott Park, IL). Predicted cardiovascular risk was estimated using the ASSIGN score: a validated Scottish cardiovascular risk score that is similar to the Framingham risk score but includes additional factors, such as social deprivation and family history.[26]

PET/CT Protocol

Static ^{18}F-FDG PET/CT was acquired using a hybrid scanner (Biograph mCT, Siemens Medical Systems, Erlangen, Germany) 90 minutes after the intravenous administration of a target dose of 200 MBq. A rigid neck collar was fitted to minimize movement and standardize position. An attenuation-correction CT scan (nonenhanced, low dose 120 kV, 50 mAs) was then performed followed by PET acquisition covering 2 bed positions with the first upper bed centered over the carotid bifurcation in 3-dimensional mode for 20 minutes per bed. Patients were fasted for 6 hours before scanning.

^{18}F-Fluoride PET/CT was undertaken the subsequent day 60 minutes after administering 250 MBq ^{18}F-fluoride. A neck collar was

Table 1. Baseline Clinical Characteristics

	Stenosis Symptomatic	No Stenosis Symptomatic	*P* Value
n	18	8	
Age, y	71.7±12.3	66.1±12.5	0.30
Men, n (%)	12 (66.7)	4 (50)	0.67
BMI, kg·m^{-2}	26.2±5	27.3 (23.38–36)	0.40
Systolic blood pressure (mm Hg)	137±25	154±16	0.08
Diastolic blood pressure (mm Hg)	78±18	85±3.4	0.34
ASSIGN score	31±15.5	21.1±13.1	0.13
Presenting syndrome, n (%)			0.22
Stroke	8 (44)	6 (75)	
TIA/amaurosis fugax	10 (56)	2 (25)	
CEA side, right (%)	8 (44)		
Cardiovascular history, n (%)			
Coronary artery disease	10 (56)	2 (25)	0.22
Myocardial infarction	5 (28)	1 (13)	0.63
Risk factors, n (%)			
Hypertension	11 (61)	7 (88)	0.36
Diabetes	1 (6)	0	1
Hypercholesterolemia	13 (72)	5 (63)	0.67
Current smoker	6 (33)	2 (25)	0.67
Medication, n (%)			
Single antiplatelet therapy	14 (78)	6 (88)	1
Dual antiplatelet therapy	3 (17)	0	0.53
Anticoagulant	1 (6)	2 (25)	0.22
Statin	17 (94)	6 (75)	0.22
ACEi/AIIRB	7 (39)	2 (25)	0.20
Beta-antagonist	7 (39)	(131)	0.36
Calcium antagonist	7 (39)	2 (25)	0.67
Other antihypertensive	6 (39)	3 (38)	1
Hematology			
Hemoglobin, g/L	139.8±19	142.6±12.3	0.71
White cell count, ×10^9/L	8±1.4	6.4 (3.8–7.9)	0.06
Platelet count, ×10^9/L	259±64	273±63	0.60
Biochemistry			
Creatinine, mmol/L	88.5 (78–97.5)	76.8±13.5	0.07
Total cholesterol, mg/dL	117.9±34.8	181.7±54.1	0.81
C-reactive protein, mg/L*	3.1±2.6	2.4±3.5	0.66

Parametric data presented as mean±SD. Nonparametric data presented as median (IQR). Categorical data presented as number (%). ACE indicates angiotensin converting enzyme; AIIRB, angiotensin 2 receptor antagonists; BMI, body mass index; CAD, coronary artery disease; CEA, carotid endarterectomy; IQR, interquartile range; and transient ischemic attack.

*C-reactive protein values > 10 excluded as per AHA guidelines.

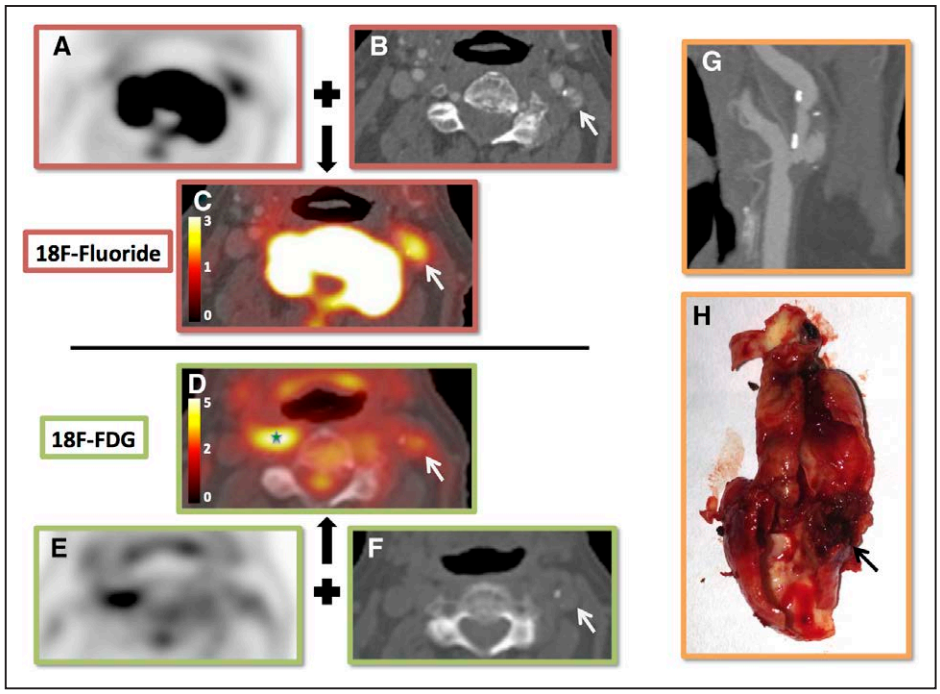

Figure 1. ^{18}F-Fluoride and ^{18}F-fluorodeoxyglucose (FDG) positron emission tomography of carotid arteries. Example of ^{18}F-fluoride (**A**, **B**, **C**) and ^{18}F-FDG (**D**, **E**, **F**) positron emission tomography (PET)/computed tomography (CT) of 1 patient before surgery for symptomatic carotid stenosis. **A**, ^{18}F-Fluoride PET axial slice. **B**, Registered CT angiogram axial slice. **C**, Fused PET/CT image. White arrow, Ruptured plaque showing ^{18}F-fluoride uptake. **D**–**F**, Same slice but with ^{18}F-FDG. Culprit shows uptake, but the contralateral side is obscured by uptake in the right longus colli (green star). An oblique computed tomography carotid angiogram reformat of the culprit (**G**). The operative specimen (**H**).

fitted and an attenuation-correction CT scan was performed. This was followed by PET acquisition covering 2 similar bed positions to the ^{18}F-FDG scan allowing 15 minutes per bed. A subset of 5 patients underwent fully dynamic ^{18}F-fluoride PET/CT with pharmacokinetic analysis as described previously.[24] Dynamic PET provides a quantitative assessment of uptake and these data were used to validate the semiquantitative static imaging data.

After PET acquisition, a CT carotid angiogram was performed without moving the subject (Care Dose 4D, 120 kV, 145 mA, rotation time 0.5 seconds, pitch 0.8. Contrast: 50 mL Niopam 370).

Static PET data were reconstructed using the Siemens UltraHD algorithm: ordered subset expectation maximization+point spread function modeling+time-of-flight; 2 iterations and 21 subsets; matrix size 200×200; 5 mm full-width half-maximum Gaussian smoothing. Dynamic PET data were similarly reconstructed but only using coincident events from the 60- to 75-minute time-bin. Dynamic data were analyzed as reported previously[24] and a K_i value was calculated using Patlak analysis.[27,28]

Tissue Collection, Micro PET/CT, and Histology

At the time of endarterectomy, plaques were collected immediately after excision, photographed, and snap frozen. A random selection (n=8) of specimens was analyzed by micro PET/CT and histology to explore ^{18}F-fluoride binding patterns (see Appendix in the Data Supplement for detailed methods).

Image Analysis

Positron Emission Tomography/Computed Tomography

Static analysis of ^{18}F-FDG and ^{18}F-fluoride uptake was performed on an OsiriX workstation (OsiriX version 3.5.1 64-bit; OsiriX Imaging Software, Geneva, Switzerland). PET/CT data were reviewed alongside the CT angiogram. Scans were qualitatively assessed for registration, image quality, patient movement, and visual evidence of radiotracer uptake. PET and CT data were individually and carefully manually coregistered by lining up fiducial markers apparent on both modalities (eg, cervical spine, mandible and hyoid on ^{18}F-fluoride imaging; skin, spinal cord, and brain on ^{18}F-FDG imaging). No formal inter-PET registration was performed. Three regions of interests (ROIs) were drawn on the carotid of interest on adjacent 3-mm axial slices. If a plaque was present, the ROIs were centered on the area of highest uptake. If there was no plaque, the uptake in the proximal 1 cm of internal carotid artery, just distal to the bifurcation was quantified. From these, standardized uptake values (SUVs; maximum, mean maximum, and mean) were recorded. Blood pool activity was determined from the average of 5 ROIs within the lumen of the superior vena cava to calculate target to background ratios.

Uptake in the proximal left common carotid artery was quantified to explore the relationships between arterial ^{18}F-FDG and ^{18}F-fluoride uptake in a site unaffected by an acute plaque event. Three ROIs were placed around this vessel and uptake was recorded.

Inter- and intraobserver reproducibility of ^{18}F-fluoride uptake measurements were determined using a random selection of 12 patients (24 carotids) by 2 experienced observers (A.T.V., G.S.) who were blinded to the clinical data during analysis.

Computed Tomography

The CT angiogram was assessed for image quality, plaque presence, location, and characteristics. Analysis was undertaken on a cardiovascular workstation (Vital Images, Minnetonka, MN). A blinded and experienced observer (A.V.) performed the semiautomated CT plaque analysis.

Statistical Analysis

Radiotracer uptake, expressed as mean and maximum SUV, was compared between the clinically adjudicated culprit carotid plaque and the contralateral side. Continuous variables are expressed as mean±standard deviation for normally distributed data and median (interquartile range) for skewed distributions. Skewed datasets underwent logarithmic transformation to normalize their distribution. Parametric (unpaired and paired *t*-tests) and nonparametric (Mann–Whitney *U* or Wilcoxon matched-pairs signed rank) tests were used for normally distributed and skewed data, respectively. Categorical

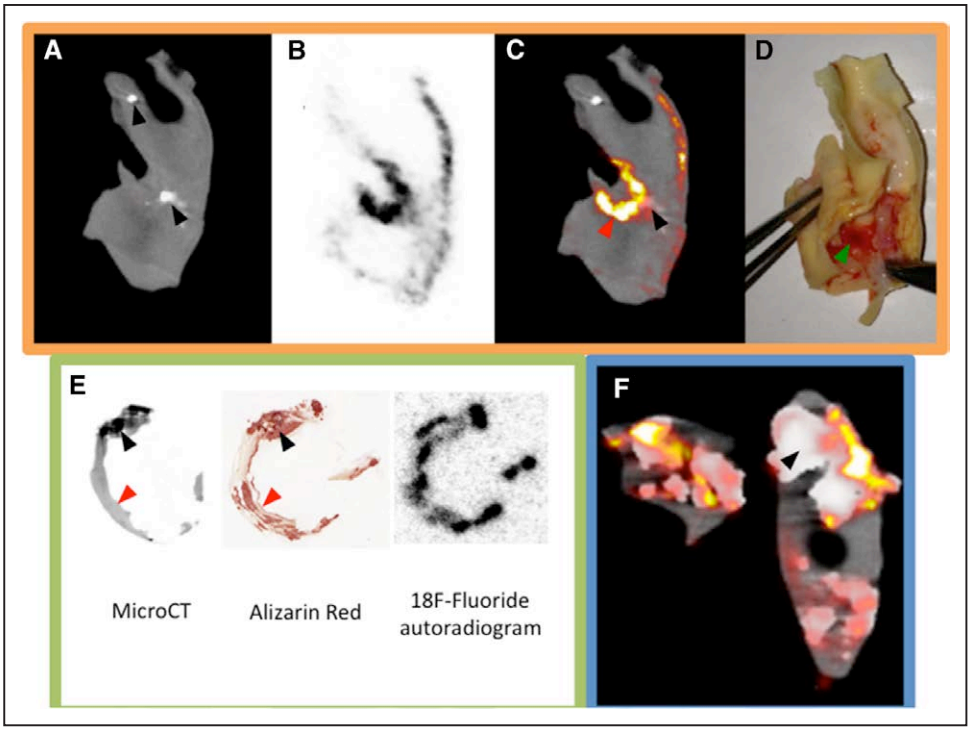

Figure 2. ^{18}F-Fluoride micro positron emission tomography (PET)/computed tomography (CT), autoradiography, and alizarin red staining. Two examples of ex vivo ^{18}F-fluoride micro PET/CT are shown (**A**–**D**, **F**). **A**, Coronal micro CT slice; **B**, corresponding micro PET; **C**, fused image; **D**, the plaque. Green arrow, Adherent thrombus over plaque rupture. Red arrow, Associated area of ^{18}F-fluoride uptake (microcalcification). Black arrows, Areas of macrocalcification showing comparatively little uptake (**A**, **C**, **F**). These examples show that ^{18}F-fluoride provides information of the presence of microcalcification and does not simply highlight all calcification. **E**, An example of micro CT slice registered to an alizarin red-stained section and the corresponding autoradiogram from a specimen that had been incubated whole in ^{18}F-fluoride. It can be seen that the tracer is unable to penetrate the deeper layers of macrocalcification (black arrow), but is able to highlight microcalcification beyond the resolution of even micro CT (red arrow), thus explaining the findings in the micro PET/CT images.

data are presented as n (%) and were compared using Fisher's exact or Chi-squared tests. Correlation was undertaken with either Pearson's r or Spearman's ρ subject to the normality of the variables tested. To quantify inter- and intraobserver reproducibility of ^{18}F-fluoride uptake measurement, the intraclass correlation coefficient was calculated and Bland-Altman analysis was undertaken.

Statistical analyses were performed with the use of SPSS version 18 (SPSS Inc, Chicago, IL) and Graph Pad Prism version 6.0 (GraphPad Software Inc, San Diego, CA). Statistical significance was defined as a 2-sided $P<0.05$.

Results

Study Population

We recruited 26 patients: 18 in the carotid endarterectomy cohort and 8 in the control cohort (Figure I in the Data Supplement). Baseline characteristics (Table 1) were similar in both cohorts. Twenty patients completed all the imaging techniques (Figure 1). A minority did not receive all scans because of the technical and feasibility challenges of completing our multimodality imaging protocol in the very short time frame before surgery. Actual doses and uptake times are specified in Table I in the Data Supplement. There were no adverse events during the study. There were 3 withdrawals.

Micro PET/CT and Histology

^{18}F-Fluoride was observed to selectively highlight areas of pathologically high-risk microcalcification (Figure 2 and Supplementary Movie I in the Data Supplement). Both on autoradiography and micro PET/CT, ^{18}F-fluoride was observed to bind avidly to areas of microcalcification but only to the surface of large volume stable macrocalcifications. Our previous studies[24] would suggest that this was because of the inability of the fluoride ion to penetrate to the deeper layers of a large crystalline mass (with a low surface-area-to-volume ratio). In contradistinction, the powdery deposits of microcalcification (not visible on CT) provide a large area (high surface-area-to-volume ratio) for the fluoride ion to bind.

Imaging

When comparing the ^{18}F-fluoride uptake on static imaging with full dynamic modeling, K_i was most strongly correlated with the SUV_{mean} (r=0.93 [95% confidence interval 0.64–0.99], P=0.001; Figure 3). There were no fixed or proportional biases in the SUV measurements within and between observers (Table II in the Data Supplement). These assessments also demonstrated high intraclass correlation coefficients (all >0.90).

Assessment of Uptake: Culprit Compared With Contralateral and Controls

^{18}F-Fluoride uptake was variably present in most plaques with all culprits showing uptake on visual assessment. In the large majority of patients undergoing carotid endarterectomy who were scanned (87%; 13/15), there was more visual uptake of ^{18}F-fluoride in the culprit compared with the contralateral

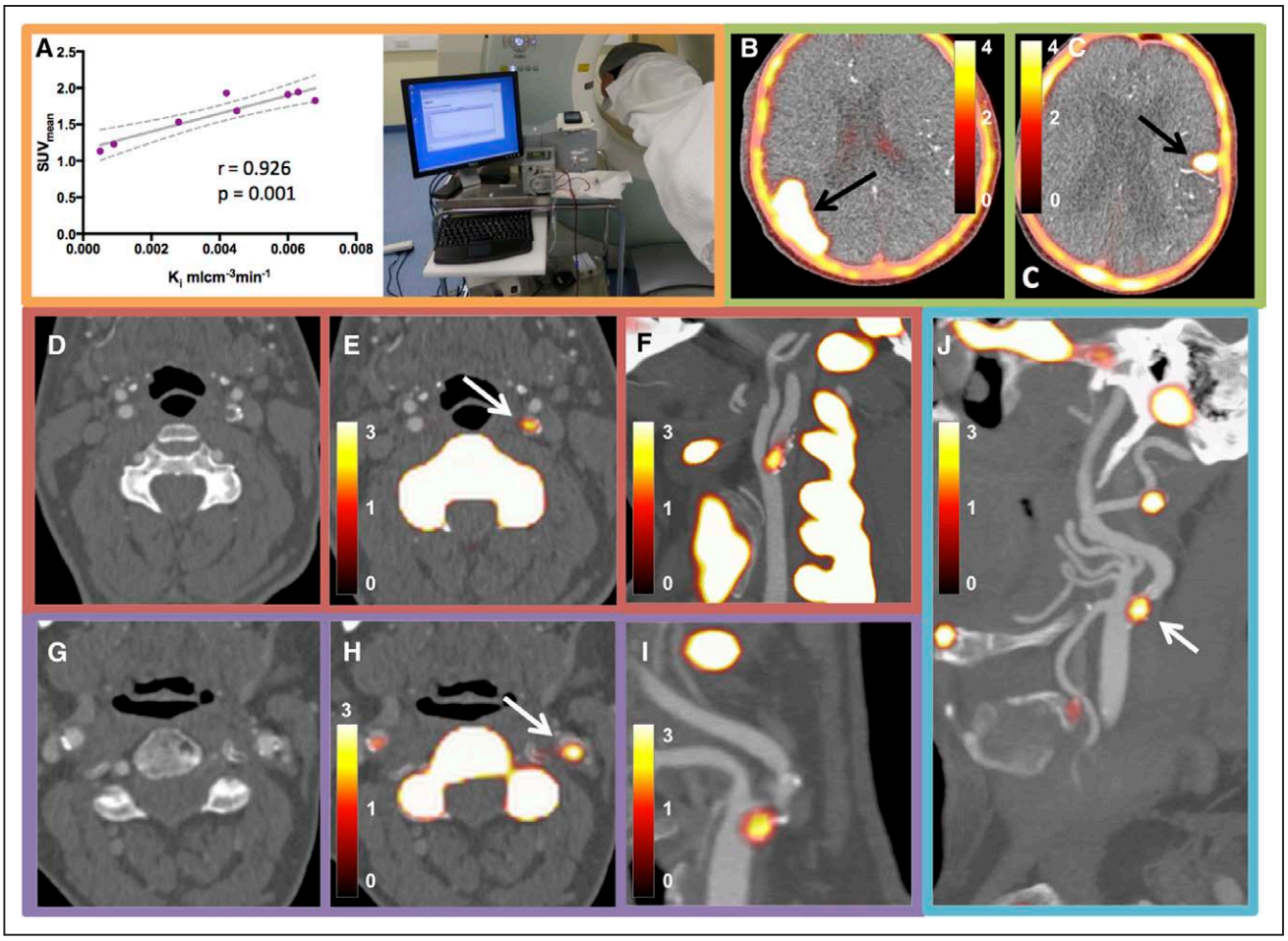

Figure 3. Dynamic positron emission tomography (PET) acquisition and examples of ^{18}F-fluoride uptake. **A**, Correlation between statically derived standardized uptake value (SUV)$_{mean}$ and dynamically measured K_i (dotted line is 95% confidence interval). Photograph shows a dynamic PET study in process. **B**, **C**, ^{18}F-Fluoride uptake into areas of cerebral infarction. **D**–**F**, From 1 patient. **D**, Axial image from computed tomography carotid angiogram; **E**, Fused axial ^{18}F-fluoride PET/computed tomography (CT; white arrow, culprit plaque); **F**, Oblique reconstruction. **G**–**I**, Similar reconstructions from a different patient. **J**, Obliquely reformatted PET/CT image from a patient who developed a fatal stroke (ipsilateral to the lesion marked by a white arrow) 2 weeks after this scan. The contralateral side, which had shown minimal uptake, had been deemed the culprit based on duplex assessment.

side. In the 2 patients without discriminatory uptake, there was heavy uptake bilaterally but more ^{18}F-fluoride uptake on the contralateral side. One patient had grossly ossified carotids and the second, at the time of surgery, was found to have a fibrous stenosis (low signal side) and was subsequently admitted with a fatal ischemic stroke on the contralateral side (high signal side, Figure 3J). ^{18}F-Fluoride uptake was focal and readily identifiable with excellent signal to background discrimination. Spillover from the hyoid bone, thyroid cartilage and cervical vertebrae occasionally made drawing ROI difficult, but only 1 vessel was rendered uninterpretable. On SUV analysis, the clinically adjudicated culprit showed higher uptake than either the paired contralateral ($\log_{10}$SUV$_{mean}$ 0.29±0.10 versus 0.23±0.11, P=0.001) or an unpaired control ($\log_{10}$SUV$_{mean}$ 0.29±0.10 versus 0.12±0.11, P=0.001) irrespective of the method of quantification (Table 2 and Figures 3 and 4).

Of note, in patients with a stroke in whom the imaging extended to encompass the affected territory of the brain (n=3), intense ^{18}F-fluoride uptake was noted in regions of cerebral infarction (SUV$_{mean}$ 4.8±1.98 versus SUV$_{mean}$ of 0.07±0.02 for contralateral noninfarcted brain, P<0.001; Figure 3B and 3C, Movie II in the Data Supplement).

Seven of the 16 culprit carotid plaques demonstrated clear and discernible increased ^{18}F-FDG uptake. However, this uptake was generally more diffuse than ^{18}F-fluoride and analysis was more frequently hampered by overspill from sternocleidomastoid, longus colli, tonsillar tissue, and the submandibular salivary glands (Figure 1). This rendered 5 vessels noninterpretable. In the remaining 4 culprit vessels, no increase in ^{18}F-FDG uptake could be observed. Overall on semiquantitative analysis, ^{18}F-FDG uptake was not higher in the clinically adjudicated culprit compared with either the paired contralateral (SUV$_{mean}$ 1.83±0.55 versus 1.81±0.46, P=0.269) or control vessels (SUV$_{mean}$ 1.83±0.55 versus 2.08±0.33, P=0.269) irrespective of the method of quantification (Table 2 and Figure 4).

Uptake Compared With Plaque Features and Baseline Characteristics

^{18}F-Fluoride uptake was correlated with several plaque characteristics on CT plaque analysis (Table 3). The strongest

Table 2. Radiotracer Uptake: Comparative Data

	Culprit Vessel	Contralateral Vessel	*P* Value for Culprit vs Contralateral	Control	*P* Value for Culprit vs Control
^{18}F-Fluoride					
SUV_{max}	2.56 (2.35–3.54)	2.18 (1.94–3.01)	*	1.78 (1.55–2.22)	*
$SUV_{meanmax}$	2.42 (2.24–3.24)	1.97 (1.78–2.74)	*	1.67 (1.41–2.08)	*
SUV_{mean}	1.92 (1.71–2.46)	1.64 (1.39–1.98)	*	1.41 (1.10–1.53)	*
TBR_{max}	2.75 (2.39–3.21)	2.42 (2.02–2.82)	*	2.44 (1.715–2.48)	*
$TBR_{meanmax}$	2.61 (2.24–2.90)	2.32 (1.74–2.58)	*	2.29 (1.61–2.37)	*
TBR_{mean}	1.96 (1.62–2.22)	1.71 (1.38–1.86)	*	1.67 (1.28–1.95)	*
$Log_{10}SUV_{max}$	0.44±0.14	0.38±0.16	0.013	0.25±0.09	<0.001
$Log_{10}SUV_{meanmax}$	0.42±0.13	0.34±0.15	0.005	0.22±0.10	<0.001
$Log_{10}SUV_{mean}$	0.29±0.10	0.23±0.11	0.001	0.12±0.11	<0.001
$Log_{10}TBR_{max}$	0.45±0.13	0.39±0.13	0.014	0.31±0.15	0.016
$Log_{10}TBR_{meanmax}$	0.43±0.13	0.35±0.12	0.005	0.28±0.15	0.014
$Log_{10}TBR_{mean}$	0.30±0.12	0.24±0.11	0.001	0.18±0.13	0.029
^{18}F-FDG					
SUV_{max}	2.32±0.78	2.32±0.77	0.675	2.61±0.53	0.375
$SUV_{meanmax}$	2.21±0.72	2.24±0.74	0.755	2.51±0.46	0.317
SUV_{mean}	1.83±0.55	1.81±0.46	0.346	2.08±0.33	0.269
TBR_{max}	1.88±0.31	1.81±0.31	0.496	1.86±0.27	0.848
$TBR_{meanmax}$	1.80±0.29	1.74±0.29	0.554	1.79±0.20	0.925
TBR_{mean}	1.49±0.19	1.44±0.19	0.358	1.48±0.10	0.922

Parametric data presented as mean±SD. Nonparametric data presented as median (IQR). FDG indicates fluorodeoxyglucose; SUV, standardized uptake value; TBR, target to background ratio; and IQR, interquartile range.
*Statistical testing performed on the normalized log_{10} transformed data.

correlation was with the Agatston score (SUV_{mean} r=0.72, P<0.001), although there were also strong correlations with high-risk features such as plaque burden (SUV_{mean} r=0.51, P=0.003) and positive remodeling (wall-distal internal carotid artery lumen ratio, with SUV_{mean} r=0.53, P=0.003).

In terms of baseline cardiovascular risk indices, uptake of both tracers in the vasculature correlated with age (^{18}F-FDG $SUV_{meanmax}$ r=0.48, P=0.037; ^{18}F-fluoride SUV_{mean} r=0.59, P=0.007) and the cardiovascular risk score (^{18}F-FDG $SUV_{meanmax}$ r=0.53, P=0.019; ^{18}F-fluoride SUV_{mean} r=0.65, P=0.002) but neither was associated with serum C-reactive protein concentration.

Discussion

We have shown that the culprit plaques of patients with recent TIA or minor ischemic strokes enhance with ^{18}F-fluoride on PET/CT. Uptake was focal, readily identifiable, and discriminated between culprit and nonculprit. ^{18}F-Fluoride uptake was associated with high-risk plaque phenotype and predicted cardiovascular risk. In contrast, while ^{18}F-FDG uptake was present in plaque and correlated with cardiovascular risk, it was more diffuse and prone to spillover and therefore less discriminatory. ^{18}F-FDG also failed to correlate with established high-risk plaque morphological features.

We have previously shown that ^{18}F-fluoride uptake is associated with increased intraplaque markers of cell death, procalcific proteins, inflammation, and high-risk features in the coronary circulation in vivo and the carotid system ex vivo.[16] Here, we confirm our previous observations[24] (which we have also recently reviewed[29]) that this is explained by the ability of ^{18}F-fluoride to report microcalcification. Why is this the case? Far from a passive and degenerative process, vessel mineralization is a controlled response to a variety of insults, particularly oxidized inflammatory lipid (as in the calcific response to tuberculosis infection where lipid-rich bacterial cell walls become oxidized through leukocyte action). It is therefore perhaps no surprise that direct links between atherosclerosis and the induction of extraskeletal osteogenesis have been identified.[30,31] The presence of cellular necrosis and apoptosis[32] is also likely to potentiate this relationship further. Hydroxyapatite nanocrystals themselves may also further drive the inflammatory cycle by setting up a positive feedback loop of increasing calcification, increasing inflammation, and increasing cell death.[30] Furthermore, by accumulating in the surface of thin fibrous caps, microcalcifications may focally increase mechanical stress and thus promote structural cap failure and plaque rupture.[7,33,34] ^{18}F-Fluoride can demonstrate this pathologically important microscopic calcific response.

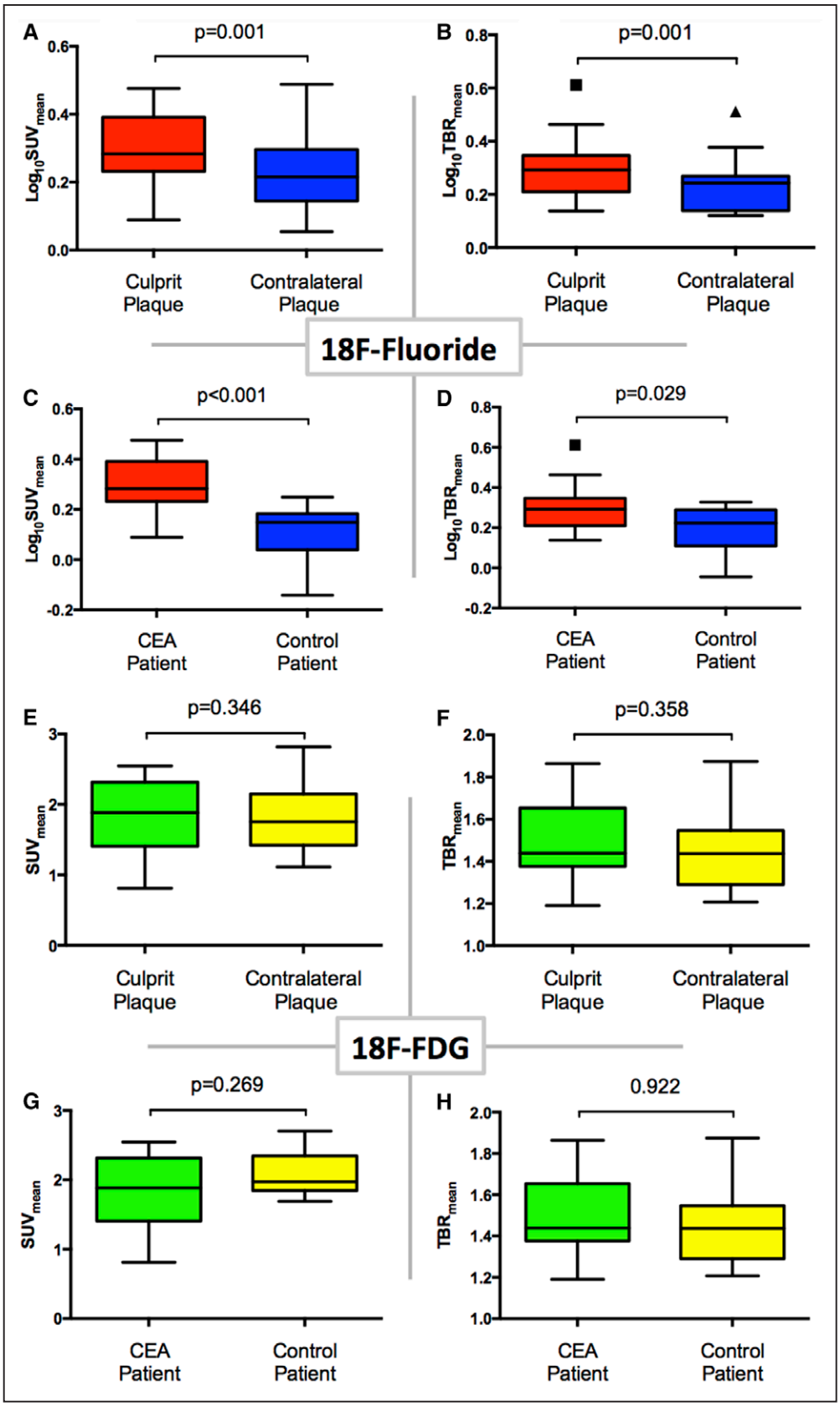

Figure 4. ^{18}F-Fluoride and ^{18}F-fluorodeoxyglucose (FDG) positron emission tomography (PET)/computed tomography uptake. Dynamic PET acquisition and examples of ^{18}F-fluoride uptake. Uptake in clinically adjudicated culprit vs contralateral and vs controls. Tukey box and whisker plots. **A**, **B**, ^{18}F-Fluoride uptake into culprit (red) and contralateral (blue) plaque using the standardized uptake value $(SUV)_{mean}$ and target to background ratio $(TBR)_{mean}$ measurements, respectively. **C**, **D**, Each demonstrate comparison in ^{18}F-fluoride uptake between carotid endarterectomy (CEA) patients (red) and controls (blue); uptake is reported by SUV_{mean} in **C** and TBR_{mean} in **D**. **E**–**H**, The same comparisons but using ^{18}F-FDG.

This is the first observation of ^{18}F-fluoride uptake in necrotic brain tissue and merits consideration. Uptake of this and other bone metabolism markers has previously been observed in tissue necrosis.[33,35] This is likely to be because of cell membrane disruption with influx of calcium and formation of nanoscale calcium phosphate complexes. These offer a substrate to which ^{18}F-fluoride can adsorb, allowing us to visualize the microcalcification associated with necrosis. We have also observed the same process in myocardial tissue postinfarction (Figure II in the Data Supplement).

We confirmed identification of culprit plaque in 2 ways. First, we compared the culprit to the ideal internal control, the contralateral carotid artery (which is almost invariably diseased). Second, we compared the culprit against a valid external control; patients with a TIA or minor ischemic stroke not attributed to carotid plaque. This shows that ^{18}F-fluoride may have real potential in helping to identify culprit plaque thus helping decision-making. This is exemplified by the case where a plaque with high uptake deemed nonculprit subsequently caused a fatal ischemic stroke.

We compared uptake of ^{18}F-fluoride with ^{18}F-FDG. Unlike ^{18}F-fluoride, overall, ^{18}F-FDG uptake was not significantly higher in culprit lesions. Moreover, on a per-lesion basis, ^{18}F-FDG failed to correlate with high-risk plaque morphological features, whereas ^{18}F-fluoride uptake correlated with plaque burden, positive remodeling, and luminal stenosis: all established markers of plaque risk. Other studies have explored the utility of ^{18}F-FDG alone in carotid atherosclerosis[9–11,14,36–39] and a few have directly compared clinical culprit with nonculprit plaques.[8,12,13] Our results are consistent with these previous findings with significant uptake noted in some but not all culprit plaques, in part because of spillover from adjacent muscle. Our observations are also influenced by the ubiquity of statin therapy, potentially blunting ^{18}F-FDG uptake. We did, however, note that proximal carotid uptake correlated with cardiovascular risk indicating that ^{18}F-FDG does reflect a major aspect of vessel pathobiology. As others suggest,[38,40] it may be that ^{18}F-FDG better reflects generalized vascular inflammation and that the relationship between the tracer and a single advanced and acute plaque is more complicated. There are increasing data available concerning other more specific markers of inflammation, such as those targeting the macrophage-specific somatostatin receptor.[41] These will theoretically be less hampered by overspill.

Our findings confirm those of a smaller study of 9 patients by Quirce et al[23] that explored ^{18}F-fluoride and ^{18}F-FDG uptake in symptomatic patients. They showed that ^{18}F-fluoride uptake appeared to be higher in the symptomatic carotid and that 18-FDG uptake was nondiscriminatory. Taken together with our current larger series, this suggests that ^{18}F-fluoride has the potential to be a useful and robust clinical tool to identify culprit atherosclerotic plaque. Vascular ^{18}F-fluoride imaging could therefore guide clinical management better than the current standard of care, and lead to trials of plaque-specific interventions that go beyond simple assessments of anatomic luminal stenosis severity.

Table 3. Plaque Analysis by CT and PET

	All Patients	
Calcium score		
Patients with AC CT usable for calcium score	24	
Carotid bifurcations analyzed for calcium score	48	
Agaston score, AU	164 (5–494)	
Log_{10}Agaston score	1.76±1.13	
Calcium volume, mm^3	150 (15.75–404)	
CT plaque analysis		
Patients with analyzable CT angiogram	17	
Internal carotid artery plaques analyzed	33	
CT diameter stenosis, %	50 (0–77)	
Wall-distal ICA lumen ratio, %	90 (54–173)	
Plaque burden, %	49.4±16.4	
Lipid/necrosis volume, mm^3	37.5 (8.6–79.5)	
Lipid/necrosis % volume	6.7 (2.4–15.8)	
Fibrofatty volume, mm^3	201 (96–313)	
Fibrofatty % volume	42.8±15.6	
Calcium volume, mm^3	211 (124–358)	
Calcium % volume	47.4±20.8	
^{18}F-Fluoride PET SUV_{mean}	1.69 (1.40–2.04)	
	r	*P* Value
vs CT Agatson score	0.79	<0.001
vs CT diameter stenosis	0.54	0.002
vs plaque burden	0.51	0.004
vs wall-distal ICA lumen ratio	0.53	0.003
vs lipid/necrosis volume	0.32	0.080
vs fibrofatty volume	0.29	0.126
vs calcium volume	0.72	<0.001
^{18}F-FDG PET SUV_{mean}	1.92±0.46	
	r	*P* Value
vs CT Agatson score	−0.14	0.469
vs CT diameter stenosis	−0.10	0.620
vs plaque burden	−0.03	0.873
vs wall-distal ICA lumen ratio	0.00	0.996
vs lipid/necrosis volume	−0.19	0.315
vs fibrofatty volume	−0.15	0.457
vs calcium volume	0.01	0.918

Parametric data presented as mean±SD. Nonparametric data presented as median (IQR). AC indicates attenuation correction; AU; arbitrary units; CT, computed tomography; FDG, fluorodeoxyglucose; ICA, internal carotid artery; IQR, interquartile range; PET, positron emission tomography; and SUV, standardized uptake value.

Limitations

This was a small pilot observational study (recruitment is very challenging given the time pressure to intervene) and findings should be regarded as preliminary. The true utility of ^{18}F-fluoride PET/CT will need to be evaluated by prospective studies with patients randomized to intervention based on imaging. ^{18}F-Fluoride PET/CT will need to be

compared with other techniques[42] (in particular MR or PET/MR) which have the advantages of improved soft tissue definition, reduced radiation, and lack of iodinated contrast. We did not perform prolonged-delayed ^{18}F-FDG imaging which some authors have suggested is advantageous.[43] We also acknowledge that quantitative vascular PET has some potential limitations because of the partial volume effects of small vascular structures. Finally, as vascular ^{18}F-fluoride imaging is developed, consideration must be given to harmonizing acquisition and reconstruction protocols,[44] as well as achieving consensus on the uptake parameter of choice (SUV versus target to background ratio versus volumetric parameters[45]) and whether to use manual or automated methods to define ROI. This will reduce variation between scanners and research groups and permit meaningful multicenter studies.

Conclusion

We have shown that ^{18}F-fluoride PET/CT is able to identify culprit or high-risk carotid plaque. In comparison, ^{18}F-FDG, the most widely used tracer in cardiovascular PET imaging, did not reliably identify culprit plaque and did not correlate with high-risk morphological features. ^{18}F-Fluoride PET has major potential to improve how we assess and manage the risk of stroke in patients with atherosclerosis.

Acknowledgments

We acknowledge the help and support of the vascular surgical staff at the Royal Infirmary of Edinburgh and the radiography and radiochemistry staff of the Clinical Research Imaging Centre.

Sources of Funding

Dr Vesey and the study were funded by program grants from the British Heart Foundation (PG12/8/29371) and Chest Heart and Stroke Scotland (R13/A147). Dr Jenkins, Vesey, Dweck, and Newby are supported by the British Heart Foundation (FS/14/78/31020, CH/09/002) and the Wellcome Trust (WT103782AIA). Dr Dweck is the recipient of the Sir Jules Thorn Biomedical Research Award 2015. The Wellcome Trust Clinical Research Facility and the Clinical Research Imaging Centre are supported by National Health Service (NHS) Research Scotland (NRS) through NHS Lothian. Dr Beek is supported by the Scottish Imaging Network—a Platform of Scientific Excellence (SINAPSE). Dr Rudd is part-supported by the National Institute for Health Research Cambridge Biomedical Research Centre, the British Heart Foundation, and the Wellcome Trust.

Disclosures

None.

References

1. Rothwell PM, Eliasziw M, Gutnikov SA, Fox AJ, Taylor DW, Mayberg MR, Warlow CP, Barnett HJ; Carotid Endarterectomy Trialists' Collaboration. Analysis of pooled data from the randomised controlled trials of endarterectomy for symptomatic carotid stenosis. *Lancet*. 2003;361:107–116.
2. Rerkasem K, Rothwell PM. Carotid endarterectomy for symptomatic carotid stenosis. *Cochrane Database Syst Rev* 2011; CD001081.
3. Chambers BR, Donnan GA. Carotid endarterectomy for asymptomatic carotid stenosis. *Cochrane Database Syst Rev* 2005; CD001923.
4. Stone GW, Maehara A, Lansky AJ, de Bruyne B, Cristea E, Mintz GS, Mehran R, McPherson J, Farhat N, Marso SP, Parise H, Templin B, White R, Zhang Z, Serruys PW; PROSPECT Investigators. A prospective natural-history study of coronary atherosclerosis. *N Engl J Med*. 2011;364:226–235. doi: 10.1056/NEJMoa1002358.
5. Libby P. Inflammation in atherosclerosis. *Arterioscler Thromb Vasc Biol*. 2012;32:2045–2051. doi: 10.1161/ATVBAHA.108.179705.
6. Libby P. Mechanisms of acute coronary syndromes and their implications for therapy. *N Engl J Med*. 2013;368:2004–2013. doi: 10.1056/NEJMra1216063.
7. Ewence AE, Bootman M, Roderick HL, Skepper JN, McCarthy G, Epple M, Neumann M, Shanahan CM, Proudfoot D. Calcium phosphate crystals induce cell death in human vascular smooth muscle cells: a potential mechanism in atherosclerotic plaque destabilization. *Circ Res*. 2008;103:e28–e34. doi: 10.1161/CIRCRESAHA.108.181305.
8. Rudd JH, Warburton EA, Fryer TD, Jones HA, Clark JC, Antoun N, Johnström P, Davenport AP, Kirkpatrick PJ, Arch BN, Pickard JD, Weissberg PL. Imaging atherosclerotic plaque inflammation with [18F]-fluorodeoxyglucose positron emission tomography. *Circulation*. 2002;105:2708–2711.
9. Tawakol A, Migrino RQ, Bashian GG, Bedri S, Vermylen D, Cury RC, Yates D, LaMuraglia GM, Furie K, Houser S, Gewirtz H, Muller JE, Brady TJ, Fischman AJ. *In vivo* 18F-fluorodeoxyglucose positron emission tomography imaging provides a noninvasive measure of carotid plaque inflammation in patients. *J Am Coll Cardiol*. 2006;48:1818–1824. doi: 10.1016/j.jacc.2006.05.076.
10. Tawakol A, Migrino RQ, Hoffmann U, Abbara S, Houser S, Gewirtz H, Muller JE, Brady TJ, Fischman AJ. Noninvasive *in vivo* measurement of vascular inflammation with F-18 fluorodeoxyglucose positron emission tomography. *J Nucl Cardiol*. 2005;12:294–301.
11. Fayad ZA, Mani V, Woodward M, Kallend D, Bansilal S, Pozza J, Burgess T, Fuster V, Rudd JH, Tawakol A, Farkouh ME. Rationale and design of dal-PLAQUE: a study assessing efficacy and safety of dalcetrapib on progression or regression of atherosclerosis using magnetic resonance imaging and 18F-fluorodeoxyglucose positron emission tomography/computed tomography. *Am Heart J*. 2011;162:214–221.e2. doi: 10.1016/j.ahj.2011.05.006.
12. Davies JR, Rudd JH, Fryer TD, Graves MJ, Clark JC, Kirkpatrick PJ, Gillard JH, Warburton EA, Weissberg PL. Identification of culprit lesions after transient ischemic attack by combined 18F fluorodeoxyglucose positron-emission tomography and high-resolution magnetic resonance imaging. *Stroke*. 2005;36:2642–2647. doi: 10.1161/01.STR.0000190896.67743.b1.
13. Marnane M, Merwick A, Sheehan OC, Hannon N, Foran P, Grant T, Dolan E, Moroney J, Murphy S, O'Rourke K, O'Malley K, O'Donohoe M, McDonnell C, Noone I, Barry M, Crowe M, Kavanagh E, O'Connell M, Kelly PJ. Carotid plaque inflammation on 18F-fluorodeoxyglucose positron emission tomography predicts early stroke recurrence. *Ann Neurol*. 2012;71:709–718. doi: 10.1002/ana.23553.
14. Tahara N, Kai H, Ishibashi M, Nakaura H, Kaida H, Baba K, Hayabuchi N, Imaizumi T. Simvastatin attenuates plaque inflammation: evaluation by fluorodeoxyglucose positron emission tomography. *J Am Coll Cardiol*. 2006;48:1825–1831. doi: 10.1016/j.jacc.2006.03.069.
15. Dweck MR, Chow MW, Joshi NV, Williams MC, Jones C, Fletcher AM, Richardson H, White A, McKillop G, van Beek EJ, Boon NA, Rudd JH, Newby DE. Coronary arterial 18F-sodium fluoride uptake: a novel marker of plaque biology. *J Am Coll Cardiol*. 2012;59:1539–1548. doi: 10.1016/j.jacc.2011.12.037.
16. Joshi NV, Vesey AT, Williams MC, Shah AS, Calvert PA, Craighead FH, Yeoh SE, Wallace W, Salter D, Fletcher AM, van Beek EJ, Flapan AD, Uren NG, Behan MW, Cruden NL, Mills NL, Fox KA, Rudd JH, Dweck MR, Newby DE. 18F-fluoride positron emission tomography for identification of ruptured and high-risk coronary atherosclerotic plaques: a prospective clinical trial. *Lancet*. 2014;383:705–713. doi: 10.1016/S0140-6736(13)61754-7.
17. Dweck MR, Jones C, Joshi NV, Fletcher AM, Richardson H, White A, Marsden M, Pessotto R, Clark JC, Wallace WA, Salter DM, McKillop G, van Beek EJ, Boon NA, Rudd JH, Newby DE. Assessment of valvular calcification and inflammation by positron emission tomography in patients with aortic stenosis. *Circulation*. 2012;125:76–86. doi: 10.1161/CIRCULATIONAHA.111.051052.
18. Dweck MR, Jenkins WS, Vesey AT, Pringle MA, Chin CW, Malley TS, Cowie WJ, Tsampasian V, Richardson H, Fletcher A, Wallace WA, Pessotto R, van Beek EJ, Boon NA, Rudd JH, Newby DE. 18F-sodium fluoride uptake is a marker of active calcification and disease progression in patients with aortic stenosis. *Circ Cardiovasc Imaging*. 2014;7:371–378. doi: 10.1161/CIRCIMAGING.113.001508.
19. Beheshti M, Saboury B, Mehta NN, Torigian DA, Werner T, Mohler E, Wilensky R, Newberg AB, Basu S, Langsteger W, Alavi A. Detection and global quantification of cardiovascular molecular calcification by fluoro18-fluoride positron emission tomography/computed tomography–a novel concept. *Hell J Nucl Med*. 2011;14:114–120.
20. Hyafil F, Messika-Zeitoun D, Burg S, Rouzet F, Benali K, Iung B, Vahanian A, Le Guludec D. Detection of 18fluoride sodium accumulation

by positron emission tomography in calcified stenotic aortic valves. *Am J Cardiol*. 2012;109:1194–1196. doi: 10.1016/j.amjcard.2011.11.060.
21. Li Y, Berenji GR, Shaba WF, Tafti B, Yevdayev E, Dadparvar S. Association of vascular fluoride uptake with vascular calcification and coronary artery disease. *Nucl Med Commun*. 2012;33:14–20. doi: 10.1097/MNM.0b013e32834c187e.
22. Quirce R, Martínez-Rodríguez I, De Arcocha Torres M, Jiménez-Bonilla JF, Banzo I, Rebollo M, Revilla MA, Palacio E, Rubio-Vassallo A, Ortega-Nava F, Del Castillo-Matos R, Carril JM. Contribution of 18F-sodium fluoride PET/CT to the study of the carotid atheroma calcification. *Rev Esp Med Nucl Imagen Mol*. 2013;32:22–25. doi: 10.1016/j.remn.2012.08.003.
23. Quirce R, Martínez-Rodríguez I, Banzo I, Jiménez-Bonilla J, Martínez-Amador N, Ibáñez-Bravo S, López-Defilló J, Jiménez-Alonso M, Revilla MA, Carril JM. New insight of functional molecular imaging into the atheroma biology: 18F-NaF and 18F-FDG in symptomatic and asymptomatic carotid plaques after recent CVA. Preliminary results. *Clin Physiol Funct Imaging*. 2016;36:499–503. doi: 10.1111/cpf.12254.
24. Irkle A, Vesey AT, Lewis DY, Skepper JN, Bird JL, Dweck MR, Joshi FR, Gallagher FA, Warburton EA, Bennett MR, Brindle KM, Newby DE, Rudd JH, Davenport AP. Identifying active vascular microcalcification by (18)F-sodium fluoride positron emission tomography. *Nat Commun*. 2015;6:7495. doi: 10.1038/ncomms8495.
25. North American Symptomatic Carotid Endarterectomy Trial Collaborators. Beneficial effect of carotid endarterectomy in symptomatic patients with high-grade carotid stenosis. *N Engl J Med*. 1991;325:445–453.
26. de la Iglesia B, Potter JF, Poulter NR, Robins MM, Skinner J. Performance of the ASSIGN cardiovascular disease risk score on a UK cohort of patients from general practice. *Heart*. 2011;97:491–499. doi: 10.1136/hrt.2010.203364.
27. Patlak CS, Blasberg RG, Fenstermacher JD. Graphical evaluation of blood-to-brain transfer constants from multiple-time uptake data. *J Cereb Blood Flow Metab*. 1983;3:1–7. doi: 10.1038/jcbfm.1983.1.
28. Patlak CS, Blasberg RG. Graphical evaluation of blood-to-brain transfer constants from multiple-time uptake data. Generalizations. *J Cereb Blood Flow Metab*. 1985;5:584–590. doi: 10.1038/jcbfm.1985.87.
29. Dweck MR, Aikawa E, Newby DE, Tarkin JM, Rudd JH, Narula J, Fayad ZA. Noninvasive molecular imaging of disease activity in atherosclerosis. *Circ Res*. 2016;119:330–340. doi: 10.1161/CIRCRESAHA.116.307971.
30. Sage AP, Tintut Y, Demer LL. Regulatory mechanisms in vascular calcification. *Nat Rev Cardiol*. 2010;7:528–536. doi: 10.1038/nrcardio.2010.115.
31. Aikawa E, Nahrendorf M, Figueiredo JL, Swirski FK, Shtatland T, Kohler RH, Jaffer FA, Aikawa M, Weissleder R. Osteogenesis associates with inflammation in early-stage atherosclerosis evaluated by molecular imaging in vivo. *Circulation*. 2007;116:2841–2850. doi: 10.1161/CIRCULATIONAHA.107.732867.
32. Proudfoot D, Skepper JN, Hegyi L, Bennett MR, Shanahan CM, Weissberg PL. Apoptosis regulates human vascular calcification *in vitro*: evidence for initiation of vascular calcification by apoptotic bodies. *Circ Res*. 2000;87:1055–1062.
33. Maldonado N, Kelly-Arnold A, Vengrenyuk Y, Laudier D, Fallon JT, Virmani R, Cardoso L, Weinbaum S. A mechanistic analysis of the role of microcalcifications in atherosclerotic plaque stability: potential implications for plaque rupture. *Am J Physiol Heart Circ Physiol*. 2012;303:H619–H628. doi: 10.1152/ajpheart.00036.2012.
34. Bobryshev YV, Killingsworth MC, Lord RS, Grabs AJ. Matrix vesicles in the fibrous cap of atherosclerotic plaque: possible contribution to plaque rupture. *J Cell Mol Med*. 2008;12:2073–2082. doi: 10.1111/j.1582-4934.2008.00230.x.
35. Wang Y-F, Lin T-K, Chuang M-H. Myocardial infarction: an incidental finding on bone scintigraphy. *Tzu Chi Med J*. 2002;14:49–53.
36. Graebe M, Pedersen SF, Borgwardt L, Højgaard L, Sillesen H, Kjaer A. Molecular pathology in vulnerable carotid plaques: correlation with [18]-fluorodeoxyglucose positron emission tomography (FDG-PET). *Eur J Vasc Endovasc Surg*. 2009;37:714–721. doi: 10.1016/j.ejvs.2008.11.018.
37. Pedersen SF, Graebe M, Fisker Hag AM, Højgaard L, Sillesen H, Kjaer A. Gene expression and 18FDG uptake in atherosclerotic carotid plaques. *Nucl Med Commun*. 2010;31:423–429. doi: 10.1097/MNM.0b013e32833767e0.
38. Moustafa RR, Izquierdo-Garcia D, Fryer TD, Graves MJ, Rudd JH, Gillard JH, Weissberg PL, Baron JC, Warburton EA. Carotid plaque inflammation is associated with cerebral microembolism in patients with recent transient ischemic attack or stroke: a pilot study. *Circ Cardiovasc Imaging*. 2010;3:536–541. doi: 10.1161/CIRCIMAGING.110.938225.
39. Figueroa AL, Subramanian SS, Cury RC, Truong QA, Gardecki JA, Tearney GJ, Hoffmann U, Brady TJ, Tawakol A. Distribution of inflammation within carotid atherosclerotic plaques with high-risk morphological features: a comparison between positron emission tomography activity, plaque morphology, and histopathology. *Circ Cardiovasc Imaging*. 2012;5:69–77. doi: 10.1161/CIRCIMAGING.110.959478.
40. Joshi F, Rosenbaum D, Bordes S, Rudd JH. Vascular imaging with positron emission tomography. *J Intern Med*. 2011;270:99–109. doi: 10.1111/j.1365-2796.2011.02392.x.
41. Pedersen SF, Sandholt BV, Keller SH, Hansen AE, Clemmensen AE, Sillesen H, Højgaard L, Ripa RS, Kjær A. 64Cu-DOTATATE PET/MRI for detection of activated macrophages in carotid atherosclerotic plaques: studies in patients undergoing endarterectomy. *Arterioscler Thromb Vasc Biol*. 2015;35:1696–1703. doi: 10.1161/ATVBAHA.114.305067.
42. Naylor AR, Sillesen H, Schroeder TV. Clinical and imaging features associated with an increased risk of early and late stroke in patients with symptomatic carotid disease. *Eur J Vasc Endovasc Surg*. 2015;1–11.
43. Blomberg BA, Akers SR, Saboury B, Mehta NN, Cheng G, Torigian DA, Lim E, Del Bello C, Werner TJ, Alavi A. Delayed time-point 18F-FDG PET CT imaging enhances assessment of atherosclerotic plaque inflammation. *Nucl Med Commun*. 2013;34:860–867. doi: 10.1097/MNM.0b013e3283637512.
44. Huet P, Burg S, Le Guludec D, Hyafil F, Buvat I. Variability and uncertainty of 18F-FDG PET imaging protocols for assessing inflammation in atherosclerosis: suggestions for improvement. *J Nucl Med*. 2015;56:552–559. doi: 10.2967/jnumed.114.142596.
45. Mehta NN, Torigian DA, Gelfand JM, Saboury B, Alavi A. Quantification of atherosclerotic plaque activity and vascular inflammation using [18-F] fluorodeoxyglucose positron emission tomography/computed tomography (FDG-PET/CT). *J Vis Exp*. 2012:e3777–e3777.

CLINICAL PERSPECTIVE

Stroke remains the leading global cause of disability and is responsible for huge healthcare costs. It is commonly caused by thromboembolism from extracranial atherosclerotic plaque. In addition to medical therapy, invasive carotid artery intervention (by endarterectomy or stenting) has a role in reducing the chances of subsequent stroke. However, intervention itself is associated with significant risk and the decision to proceed with surgery is still based principally on stenosis severity, an outdated parameter. This report shows that by selectively demonstrating intraplaque microcalcification, a pathologically high-risk process that reflects ongoing inflammation and cell death, ^{18}F-fluoride PET/CT may be able to identify plaque at particular risk of causing future stroke. The technique, as part of a multimodal risk stratification strategy, may help to ensure the appropriate planning of surgical intervention. This would potentially avoid unnecessary surgery on quiescent yet tightly stenosed plaques and conversely permit the identification and removal of high-risk plaques that currently do not meet criteria for intervention. ^{18}F-Fluoride PET/CT also offers the possibility of noninvasively assessing the response to existing or novel pharmacological agents permitting the personalization of therapy to maximize benefit and minimize risk of complications.